

Universität  
Rostock



Traditio et Innovatio

Virial coefficients of hard, anisotropic  
particles in Euclidean spaces of various  
dimensionality

**Cumulative Dissertation**

to

obtain the academic degree

*doctor rerum naturalium (Dr. rer. nat.)*

of the Faculty of Mathematics and Natural Sciences

at the University of Rostock

submitted by

**Markus Kulossa**

born on 4 August 1997 in Nauen

ORCID: 0000-0002-9064-2685

Rostock, March 2025

This dissertation was researched and written at the Institute of Chemistry of the University of Rostock, at the chair of Physical Chemistry in the research group of Professor Joachim Wagner in the time between October 2021 and March 2025.

**Referees:**

Professor Joachim Wagner  
Institute of Chemistry  
University of Rostock

Professor Roland Roth  
Institute for Theoretical Physics  
Eberhard Karl University of Tübingen

Professor Rolf Schilling  
Institute of Physics  
Johannes Gutenberg University Mainz

Date of submission: 07 March 2025  
Date of scientific colloquium: 15 July 2025

## Abstract

In this work, virial coefficients of hard, anisotropic particles in various-dimensional Euclidean spaces are calculated. Using the Brunn-Minkowski theorem, exact values for the second virial coefficients of arbitrary convex bodies and their binary mixtures can be obtained in arbitrary dimensions of space. Therefore, in two-, three-, and four-dimensional spaces second virial coefficients of uniaxial solids of revolution and regular polytopes are calculated based on their geometric measures, including higher-dimensional solids of revolution with singularities in their surface curvature. Using these, for selected geometries in arbitrary-dimensional spaces new theorems are derived and proven. For the calculation of virial coefficients up to the eighth order, optimized Monte Carlo simulations are used and extended to four- and higher-dimensional spaces. The obtained highly accurate numerical results can be used in the virial equation of state for the description of the isotropic phase of such systems. For all virial coefficients, a direct relation to the excess part of the averaged excluded volume in dependence on the dimensionality of space can be observed, allowing the interpolation of the data via heuristic low-order polynomials. An overview of the manuscripts [1–4], published as part of this dissertation is given and placed in the scientific context.

## Übersicht

Die vorliegende Arbeit beschäftigt sich mit der Berechnung von Virialkoeffizienten harter, anisotroper Körper in euklidischen Vektorräumen verschiedener Dimensionalität. Unter Anwendung des Brunn-Minkowski-Theorems ist die exakte Berechnung der zweiten Virialkoeffizienten für beliebige, konvexe Körper sowie für binäre Mischungen dieser in beliebig-dimensionalen Räumen möglich. Dazu werden exemplarisch für den zwei-, drei- und vier-dimensionalen Raum systematisch zweite Virialkoeffizienten für uniaxiale Rotationskörper und reguläre Polytope mit Hilfe ihrer geometrischen Kenngrößen berechnet, insbesondere für höher-dimensionale Rotationskörper mit Singularitäten in deren Oberflächenkrümmung. Für ausgewählte Geometrien werden daraus neue Theoreme für beliebig-dimensionale Räumen erhalten und bewiesen. Für die Berechnung weiterer Virialkoeffizienten bis zur einschließlich achten Ordnung werden verschiedene, optimierte Monte-Carlo-Simulationen verwendet und auf vier- und höher-dimensionale Räume übertragen. Die dabei erhaltenen, hochgenauen numerischen Ergebnisse ermöglichen den direkten Zugang zu Zustandsdaten der isotropen Phase solcher Systeme über die Virialzustandsgleichung. Für alle berechneten Virialkoeffizienten wird in Abhängigkeit der Dimensionalität des Raumes eine direkte, universelle Abhängigkeit vom Exzessanteil des gemittelten Ausschlussvolumens beobachtet, was die Interpolation der Daten über heuristische Polynome niedriger Ordnung ermöglicht. Die im Rahmen der kumulativen Dissertation publizierten Manuskripte [1–4] werden zusammengefasst und in den wissenschaftlichen Rahmen eingeordnet.

## **Declaration of Authorship**

I hereby declare under oath that I have completed this dissertation independently and have composed it without outside assistance. Furthermore, I have not used anything other than the resources and sources stated. Where I have taken sections from these works in terms of content or text, I have identified this appropriately.

Rostock, 7 March 2025

---

Markus Kulossa

## Acknowledgments

In this section I would like to express my gratitude to all people who supported me during the time working on my doctoral thesis. Firstly, I want to thank **Professor Joachim Wagner** for the opportunity to conduct my research in his group and his encouragement to work independently on this project with realizing my own ideas and for gathering the required funding. I would also like to express my gratitude for the invested time in my scientific education and for writing the scientific papers with me together. Beside that, I am grateful for the willingness to review my thesis.

I also want to thank **all other reviewers** for their willingness to spend their time on my work. I would also like to thank **Dr. Philipp Marienhagen** and **Daniel Weidig** for the successful collaborations and the pleasant time during my entire stay in this group. I am additionally grateful to **Professor Achill Schürmann**, **Valentin Dannenberg**, **Professor Giorgio Cinacchi** and **Professor Salvatore Torquato** for fruitful discussions and private scientific communications that enriched my research and the content of this thesis. All people who made it possible to present my research at conferences in front of an international audience are acknowledged, too.

Furthermore, I want to thank the entire research group and all in the department of physical chemistry who contributed to a pleasant and welcoming environment during the time working on my thesis. Special thanks go to **Dr. Joel Diaz Maier**, **Paul Tümmeler**, and in particular **Alexandra Bumann**. Finally, I would like to thank my family and friends for their continuous support during the entire time.



# Contents

<b>List of Symbols</b>	<b>vii</b>
<b>1 Introduction</b>	<b>1</b>
1.1 Motivation . . . . .	1
1.2 Model systems and methods for calculating their virial coefficients . . . . .	2
1.3 Aim and outline of this thesis . . . . .	3
<b>2 Theoretical background</b>	<b>5</b>
2.1 Virial series . . . . .	5
2.1.1 Graph theory . . . . .	6
2.1.2 Analytical calculation of virial coefficients . . . . .	9
2.1.3 Numerical calculation of virial coefficients . . . . .	10
2.2 Euclidean space of arbitrary dimension . . . . .	12
2.3 Geometry of selected solids . . . . .	14
2.3.1 Uniaxial solids of revolution . . . . .	14
2.3.2 Polytopes . . . . .	15
<b>3 Results and Discussion</b>	<b>18</b>
3.1 Analytical calculation of second virial coefficients for anisotropic solids . . . . .	18
3.1.1 Exclusion volume of two convex solids . . . . .	18
3.1.2 Geometric measures of convex solids . . . . .	20
3.1.3 Second virial coefficients for uniaxial solids of revolution . . . . .	25
3.1.4 Second virial coefficients for convex polytopes . . . . .	28
3.2 Numerical calculation of virial coefficients for hard particles . . . . .	30
3.2.1 Algorithms for overlap detection of anisotropic solids . . . . .	30
3.2.2 Implementation of the numerical Monte Carlo integration . . . . .	31
3.2.3 Anisotropic particles in two-dimensional space . . . . .	31
3.2.4 Anisotropic particles in three-dimensional space . . . . .	33
3.2.5 Anisotropic particles in four-dimensional space . . . . .	35
3.3 Equation-of-state data and phase behavior . . . . .	37
<b>4 Summary and Outlook</b>	<b>39</b>
<b>5 Publications</b>	<b>41</b>
5.1 Publication I - Virial coefficients of hard hyperspherocylinders in $\mathbb{R}^4$ : Influence of the aspect ratio . . . . .	43
5.2 Publication II - Virial coefficients of hard, homonuclear dumbbells in two- to four-dimensional Euclidean spaces . . . . .	51
5.3 Publication III - Virial coefficients of hard, two-dimensional, convex particles up to the eighth order . . . . .	67

5.4 Publication IV - Geometric measures of uniaxial solids of revolution in higher-dimensional Euclidean spaces and their relation to the second virial coefficient .	85
<b>List of Figures</b>	<b>103</b>
<b>List of Tables</b>	<b>105</b>
<b>References</b>	<b>107</b>
<b>Appendix</b>	<b>115</b>
<b>A Geometric measures for selected particle geometries</b>	<b>115</b>
<b>B Analytical values for virial coefficients of hard bodies</b>	<b>118</b>
<b>C Numerical results for virial coefficients of hard bodies</b>	<b>121</b>

# List of Symbols

## Greek symbols

$\alpha = (B_2^* - 1)/(2^{D-1} - 1)$	normalized mutual excess excluded volume per particle
$\beta_D = D \kappa_D$	surface area of a $D$ -dimensional unit ball
$\Gamma(z)$	gamma function
$\gamma$	integrand of a configuration integral
$\gamma(P, F)$	external angle for a $k$ -face $F$ of a polytope $P$
$\gamma_{\text{ref}}$	reference integrand
$\delta_P$	dihedral angle of a regular polytope $P$
$\eta$	volume fraction
$\eta_c$	critical volume fraction for isotropic phase transitions
$\vartheta$	angular coordinate
$\vartheta_c$	critical opening angle
$\kappa_D = \pi^{D/2}/\Gamma(1 + D/2)$	volume of a $D$ -dimensional unit ball
$\nu$	aspect ratio
$\rho$	sampling distribution
$\rho_{\text{new}}$	new sampling distribution
$\rho_{\text{old}}$	old sampling distribution
$\varrho$	particle number density
$\sigma$	contact distance
$\sigma_c$	core contact distance
$\phi$	angular coordinate
$\phi_i$	general angular coordinate
$\varphi$	angular coordinate
$\chi$	angular coordinate
$\underline{\Psi}$	rotation matrix
$\psi$	rotation angle

## Latin symbols

$A$	arbitrary component
$a$	edge length of a polytope, arbitrary real unit of a quaternion
$B$	arbitrary component
$B_2^{\text{mix}}$	second virial coefficient of a mixture
$B_n$	virial coefficient of order $n$
$B_n^* = B_n/V_{\text{P}}^{n-1}$	reduced virial coefficient of order $n$
$\tilde{B}_n = B_n/B_2^{n-1}$	reduced virial coefficient of order $n$
$\mathcal{B}^D$	$D$ -dimensional unit ball
$b$	arbitrary real unit of a quaternion
$\mathbb{C}$	set of complex numbers
$c$	arbitrary real unit of a quaternion
$c_G$	weight of a graph $G$
$D$	dimensionality
$d$	arbitrary real unit of a quaternion
$E(k)$	complete elliptic integral of the second kind
$e_{ij} = f_{ij} + 1$	Ree-Hoover $e$ -function
$F$	arbitrary $k$ -face of a polytope
${}_2F_1(a,b,c; z)$	Gaussian hypergeometric function
$f_{ij} = \exp\left[-\frac{U_{ij}}{k_{\text{B}}T}\right] - 1$	Mayer $f$ -function
$F_k$	$k$ -face of a polytope $F \in \mathcal{F}_k(P)$
$\mathcal{F}_k(P)$	set of $k$ -faces for a polytope $P$
$G$	graph
$g_G$	number of isomorphic permutations of a graph $G$
$\mathbb{H}$	set of quaternions
$h$	height
$H_{\text{P}}$	mean curvature of a particle
$h_{p,q}$	$\sqrt{4N_1(\{p,q\}) + 1} - 1$
$\mathcal{H}^i(P)$	$i$ -dimensional Hausdorff measure of a polytope $P$
$\underline{\mathbf{I}}_{\text{P}}$	first fundamental form
$\underline{\mathbf{II}}_{\text{P}}$	second fundamental form
$I$	arbitrary integral
$i$	index
$\text{i}$	imaginary unit
$I_{\text{ref}}$	arbitrary reference integral
$I_x(a,b)$	regularized incomplete beta function
$j$	index
$\text{j}$	imaginary unit
$K$	arbitrary convex solid
$k$	index

$k$	imaginary unit
$K(k)$	complete elliptic integral of the first kind
$k_B$	Boltzmann constant
$\mathcal{K}^D$	set of convex solids in $\mathbb{R}^D$
$L$	center-to-center distance, arbitrary convex solid
$m$	number of components in a mixture
$M_P$	integral mean curvature of a particle
$\mathcal{M}_i^L$	set of labeled Mayer graphs with $i$ nodes
$\mathcal{M}_i^U$	set of unlabeled Mayer graphs with $i$ nodes
$n$	order of virial coefficient
$N(P,F)$	normal cone
$N_k$	number of $k$ -faces $F_k$ for a polytope $P$
$n_{\max}$	maximum order of known virial coefficients
$N_T$	number of considered spanning trees
$P$	arbitrary polytope
$p$	pressure, element of a Schläfli symbol
$P_{\text{acc}}$	acceptance probability
$P_i$	arbitrary particle with label $i$
$\{p_1, p_2, \dots, p_{D-1}\}$	general Schläfli symbol
$\{p, q, r, \dots\}$	Schläfli symbol
$\mathcal{P}^D$	set of regular, convex $D$ -polytopes
$q$	quaternion, element of a Schläfli symbol
$q_i$	quaternion with label $i$
$\mathbb{R}^D$	$D$ -dimensional Euclidean space
<b><math>\mathbf{R}</math></b>	rotation matrix
<b><math>\mathbf{R}_L</math></b>	left isoclinic rotation matrix
<b><math>\mathbf{R}_R</math></b>	right isoclinic rotation matrix
$\mathbf{r}_i$	position vector of the center of particle $i$
$\mathbf{r}_{ij} = \mathbf{r}_j - \mathbf{r}_i$	center-to-center distance vector from particle $i$ to particle $j$
$r$	radial coordinate, element of a Schläfli symbol
$r(z)$	meridian curve in cylindrical coordinates
$r_{\text{cap}}$	radius of a spherical segment
$r_{\text{eq}}$	equatorial radius
$R_i$	principal radius of curvature
$r_i$	radius with index $i$
$\bar{R}_P$	mean radius of curvature of a particle
$\mathcal{R}_i^L$	set of labeled Ree-Hoover graphs with $i$ nodes
$\mathcal{R}_i^U$	set of unlabeled Ree-Hoover graphs with $i$ nodes
$d^D S$	$D$ -dimensional surface element
$S_G$	configuration integral of graph $G$
$S_P$	total surface area of a particle

$S'_P$	lateral surface area of a particle
$T$	temperature
$U$	potential energy
$U_{ij}$	pair potential between particles $i$ and $j$
$\mathbf{v}$	arbitrary vector in $\mathbb{R}^4$
$\mathbf{v}'$	arbitrary vector in $\mathbb{R}^4$ after rotation
$V_{\text{ex}}$	orientation-averaged excluded volume
$V_i(K)$	$i$ th intrinsic volume of $K$
$V_P$	volume of a particle
$\mathcal{W}_P$	Weingarten map
$w$	Cartesian coordinate
$W_i(K)$	$i$ th quermassintegral of $K$
$\bar{w}_P$	mean width of a particle
$x$	Cartesian coordinate
$x_i$	general Cartesian coordinate, number fraction of component $i$
$y$	Cartesian coordinate
$Z = p/(\rho k_B T)$	compressibility factor
$z$	Cartesian coordinate
$z_{\text{max}}$	maximum $z$ -coordinate
$z_{\text{min}}$	minimum $z$ -coordinate

# 1 Introduction

## 1.1 Motivation

During the past decades, soft matter science emerged as a field of increasing interest for investigating the fundamentals and applications of condensed matter at the interface between chemistry, statistical mechanics, material science, and biophysics. Therefore, a broad range of systems is studied, including colloids, liquid crystals, polymers, glasses, foams, gels, and active matter. Today, the presence of such materials is ubiquitous in a wide variety of areas, e.g., liquid crystal displays (LCD), cosmetics, or biomedical tissues. Beside experimental studies including scattering techniques, microscopy, and rheology, these systems are also modeled in computer simulations and theoretical investigations gaining insights into their thermodynamic properties, i.e., self-organization and phase behavior.

The model system studied the most, is the many-particle system of hard spheres [5]. Hard particles are defined as impenetrable with an infinitely repulsive potential for overlapping configurations and exhibit no interactions otherwise. Thus, their phase behavior is solely driven by entropy as excluded volume effects with the volume fraction as control parameter. For colloidal hard-sphere suspensions, freezing as the self-assembling with phase transitions from a fluid into crystalline and glassy phases can be observed with increasing volume fraction [6]. Using density functional theory (DFT) by employing free energy calculations and fundamental measure theory [7], the structure and thermodynamics of an equilibrium fluid can be predicted based on the excess free energy. The virial equation of state (VEOS) provides access to closed expressions for the free energy, where the compressibility factor, denoting deviations from an ideal gas, is expanded in powers of the particle number density or the volume fraction respectively [8]. Therefore, expansion coefficients  $B_n$ , known as virial coefficients of order  $n$ , account for the influence of intermolecular interactions in clusters with  $n$  particles. With the inevitable need to know the virial coefficients of a given many-particle system, only a finite number can be provided, e.g., for hard spheres up to  $B_{12}$  [9–11]. The remaining virial coefficients of higher order have to be approximated, e.g., for hard spheres with the Carnahan-Starling method [12]. Therefore, a sequence with as many virial coefficients as possible has to be provided.

Starting with the seminal work of Onsager, observing an isotropic-nematic phase transition for infinitely thin hard rods [13], a significant interest in the influence of the particle shape on the thermodynamics of a many-particle system arises. The phase diagrams for a vast amount of particle geometries in  $\mathbb{R}^3$  and  $\mathbb{R}^2$  are studied using free energy calculations and computer simulations [14]. This includes ellipsoids [15, 16], spherocylinders [17, 18], cylinders [19], lenses [20–22], polyhedra [23–25], dumbbells [26–28], and bowl shaped particles [29–34] in  $\mathbb{R}^3$  and ellipses [35], stadia [36], rectangles [37–39], and circular arcs [40–43] in  $\mathbb{R}^2$ . Complementarily, additional experimentally observed phase diagrams [44, 45] and computed equation-of-state data [46–49] are reported for respective geometries. Generalizing fundamental measure theory to non-spherical (anisometric) particles [50, 51], a free energy functional can be obtained. For solids of revolution, this can be simplified [52, 53], enabling the prediction of nematic and smectic phase transitions [54, 55]. To obtain the VEOS for anisometric particles, often Parson's

approach is used, which accounts excluded volume effects solely relying on the second virial coefficient of the particle and rescaling the Carnahan-Starling virial coefficients of spheres [56]. An improved agreement with numerical equation-of-state data can be obtained by considering more virial coefficients of a given particle geometry with respect to truncation effects [57, 58]. Therefore, virial coefficients  $B_n$  with  $n \geq 2$  for a given particle geometry in the respective dimension of space have to be determined. Since for hard particles excluded volume effects are based on their geometric measures, additional insights into jamming phenomena and closed packings at respectively higher volume fractions can be gained, too [59–62], with relevance for granular materials [63].

## 1.2 Model systems and methods for calculating their virial coefficients

Modeling many-particle systems, their interactions are often described by a simple hard-body potential. Therewith, this potential  $U$  is exactly pairwise additive

$$U = \sum_i \sum_{j>i} U_{ij} \quad (1)$$

with a pair potential

$$U_{ij} = \begin{cases} \infty & : P_i \cap P_j \neq \emptyset \\ 0 & : P_i \cap P_j = \emptyset \end{cases} \quad (2)$$

for two arbitrary particles  $P_i$  and  $P_j$ .

Starting with the works of van der Waals, Boltzmann, and Jäger [64–67], exact values for the virial coefficients up to fourth order are derived from the grand canonical partition function for hard,  $D$ -dimensional spheres in arbitrary even-dimensional Euclidean spaces [68] and odd-dimensional Euclidean spaces up to  $D = 11$  [69]. For hard, non-spherical convex particles in  $\mathbb{R}^3$ , exact values for their second virial coefficients can be derived by the Isihara-Hadwiger theorem [70–72], only requiring the geometric measures volume  $V_P$ , total surface area  $S_P$ , and mean radius of curvature  $\bar{R}_P$  of the individual particles [73]. These formulations are also extended to arbitrary convex particles in two-dimensional Euclidean spaces  $\mathbb{R}^2$ , where analogously only their two-dimensional volume (area) and surface area (perimeter) are required. Also for concave dumbbells in  $\mathbb{R}^2$  and  $\mathbb{R}^3$ , explicit expressions for their second virial coefficients are already provided [74–76]. For other concave geometries, in general the second virial coefficient has to be calculated numerically in the respective space by the orientation-averaged excluded volume using computer simulations [77]. Also,  $B_3$  and  $B_4$  for anisometric particles and  $B_n$  with  $n > 4$  in general for arbitrarily shaped particles (including spheres) have to be determined numerically so far, employing Monte Carlo (MC) methods and graph theory, pioneered by Metropolis *et al.* 70 years ago [78, 79].

Using MC simulations, numerical results for virial coefficients up to the eighth order of hard spheres in  $\mathbb{R}^3$  and hard disks in  $\mathbb{R}^2$  are reported over several decades due to the availability of advancing computational resources [80–84]. Initiated by Ree and Hoover [85], virial coefficients

of hyperspheres in higher-dimensional Euclidean spaces are simultaneously reported up to the eighth order, too [86–89]. Using graph isomorphism [90,91] and adapted simulation techniques the ninth and tenth virial coefficients of hard,  $D$ -dimensional spheres are obtained [92,93], whereas for higher orders other computational methods are implemented [9–11].

For hard, anisometric particles, the computation of virial coefficients is in general more demanding, since the pair potential [Eq. (2)] additionally depends on the relative orientation of the particles. For solids in  $\mathbb{R}^3$ , virial coefficients for various particle geometries are provided [57,58,84,94–106], where due to the introduction of Mayer sampling [107,108] their numerical uncertainties reduced significantly during the last decades. There, Mayer-sampling Monte Carlo (MSMC) simulations are originally used to compute virial coefficients for other interaction potentials, referring to the corresponding virial coefficients with hard-body potential as a reference system. Recently, MSMC simulations have also been adapted to calculate Boyle temperatures of Lennard-Jones fluids [109], allowing for the calculation of the respective virial coefficients without the need of a reference integral. For hard, two-dimensional, anisometric particles, certainly less virial coefficients have been computed [110–115]. These were at most up to the fifth order and have higher relative uncertainties. In a higher-dimensional Euclidean space  $\mathbb{R}^D$  with  $D > 3$ , virial coefficients of any anisometric particles (without fixed orientations) have previously to this work not been published.

### 1.3 Aim and outline of this thesis

Aim of this thesis is the calculation of virial coefficients for hard, anisometric particles with various geometric shapes in two-, three-, and especially higher-dimensional Euclidean spaces. Therefore, the detailed influence of the specific particle geometry is studied with the main purpose to provide so far unknown virial coefficients and a minor priority to reduce uncertainties of already known virial coefficients for given particle shapes. To obtain the virial coefficients, an optimized MSMC simulation can be used [58], enabling their accurate calculations up to the eighth order without the need of graph canonization etc. [10]. Beside the adaptation of the dimension of space with the corresponding (random) translation and rotation of particles, the key step for the calculation of virial coefficients for hard, anisometric particles is the development of an algorithm to detect particle overlaps for a given particle configuration depending on their geometry [Eq. (2)]. Furthermore, the Isihara-Hadwiger theorem [70–72] for the analytical calculation of  $B_2$  for hard, convex particles in Euclidean spaces  $\mathbb{R}^3$  is studied with its extension to  $\mathbb{R}^2$  [113,116] and especially higher-dimensional Euclidean spaces [117,118]. The derived theorems can then be applied to analytically calculate second virial coefficients of convex, uniaxial solids of revolution and polytopes, particularly examining the influence of singularities in their surface curvatures. If the second virial coefficient of a given many-particle system is known with sufficiently high accuracy, beside improving the virial equation of state, that virial coefficient can also be used as an intrinsic reference to calculate higher-ordered virial coefficients employing MSMC simulations [58]. Computations of virial coefficients for anisotropic particles are exemplarily studied in detail in  $\mathbb{R}^4$  with an extension to higher-dimensional spaces being straightforward. Additionally, the second virial coefficient for a system of many identical hard

particles quantifies the sphericity of the particle's geometry, too.

This work is organized as follows: After a brief introduction about the fundamentals of virial theory and graph theory, analytical and numerical methods to calculate virial coefficients of hard particles are given in more detail in Sec. 2, including a geometric description of the Euclidean space  $\mathbb{R}^D$  and the shapes of the embedded particles. Afterwards, an overview of the results of this thesis is given in Sec. 3, where all relevant additional data is for convenience attached in the appendix of the manuscript, expanded by complementary results taken from the literature. Then, the work is summarized in Sec. 4, including a brief perspective of the topic. Finally, the scientific papers published as part of this dissertation are presented in Sec. 5. A total of four publications are provided [1–4], all written as first author.

In Publication I, virial coefficients  $B_n$  are provided for anisotropic particles in a high-dimensional Euclidean space  $\mathbb{R}^D$  with  $D > 3$  for the first time. They are calculated numerically for hyperspherocylinders up to  $B_6$  employing Mayer-sampling Monte Carlo simulations. Then, in Publication II, the first calculations of virial coefficients up to  $B_8$  for a concave geometry in a high-dimensional space is followed, where a comparison with the analog geometries in lower space dimensions is included. In Publication III, the virial coefficients up to the eighth order for various convex solids are calculated in the two-dimensional Euclidean space  $\mathbb{R}^2$ , exemplarily showing the results of ellipses for the virial equation of state within the boundary of the isotropic phase. Finally, in Publication IV, so far unknown explicit analytical expressions for second virial coefficients of various four-dimensional, uniaxial solids of revolution with singularities in their surface curvatures are provided, compared with previously reported expressions for other geometries, and extended to arbitrary dimensions.

## 2 Theoretical background

### 2.1 Virial series

Many-particle fluids consisting of particles without positional and orientational order embody isotropic phases. This accounts for gases, supercritical fluids, or liquid crystals at sufficiently high temperatures or low particle number densities, respectively. For their thermodynamic characterization, an adequate equation of state is required. Starting from the ideal gas with a simplified equation of state at sufficiently small pressure  $p$  and high temperature  $T$ , real gases and supercritical fluids can be described by the virial equation of state (VEOS), originally proposed by Kamerlingh Onnes as a heuristic expansion in powers of the particle number density  $\varrho$  with the compressibility factor

$$Z = \frac{p}{\varrho k_{\text{B}} T} = 1 + \sum_{n=2}^{\infty} B_n \varrho^{n-1} = 1 + \sum_{n=2}^{\infty} B_n^* \eta^{n-1} \quad (3)$$

accounting for the departure from the ideal gas [119]. The coefficients  $B_n$ , in general depending on the temperature  $T$ , are the virial coefficients of order  $n$ , initially serving to correct experimental equation-of-state data for real gases of non-spherical molecules (e.g.:  $\text{H}_2$ ,  $\text{N}_2$ ,  $\text{CO}_2$ , or  $\text{CH}_4$ ) and spherical noble gases at low temperature [120, 121]. Using statistical mechanics, Mayer and Goeppert Mayer were able to derive the virial series solely from the grand canonical partition function with the virial coefficient  $B_n$  considering the interactions in  $n$ -particle clusters [122, 123], enabling Born the merger with the previously heuristic virial equation of state [124].

Employing the volume fraction  $\eta = \varrho V_{\text{P}}$ , the virial series can be rewritten using reduced virial coefficients

$$B_n^* = \frac{B_n}{V_{\text{P}}^{n-1}} \quad (4)$$

normalized to powers of the volume of the individual particles  $V_{\text{P}}$ . In this form, the virial coefficients are independent of the size of the particles and instead only characterized by their shape. Assuming additive pairwise interactions for a many-particle system in  $\mathbb{R}^D$ , its virial coefficients  $B_n$  of order  $n$  can, for sufficiently small number densities  $\varrho$  and high temperatures  $T$ , be derived from the grand canonical partition function as

$$B_n = \frac{1-n}{n!} \int \cdots \int \left[ \sum_{G \in \mathcal{M}_n^L} \prod_{ij \in G} f_{ij} \right] d^D \mathbf{r}_{12} \cdots d^D \mathbf{r}_{1n}, \quad (5)$$

with  $f_{ij}$  being the Mayer  $f$ -function

$$f_{ij} = \exp \left[ -\frac{U_{ij}}{k_{\text{B}} T} \right] - 1 \quad (6)$$

for a corresponding pair potential  $U_{ij}$  of two particles  $i$  and  $j$  [125]. Here,  $\mathbf{r}_{ij} = \mathbf{r}_j - \mathbf{r}_i$  is the

distance vector between the centers of both particles  $\mathbf{r}_i$  and  $\mathbf{r}_j$ , whereas the products of Mayer  $f$ -functions are represented through graphs  $G$  (cf. Sec. 2.1.1).

Graphs  $G$ , that contribute to  $B_n$ , are those with  $n$  nodes (vertices) that are undirected and biconnected [126]. They form the set of labeled Mayer graphs  $\mathcal{M}_n^L$ . Thus, the virial coefficients  $B_n$  can for orders  $n \leq 4$  be written as

$$B_2 = -\frac{1}{2} \int f_{12} d^D \mathbf{r}_{12}, \quad (7)$$

$$B_3 = -\frac{1}{3} \iint f_{12} f_{13} f_{23} d^D \mathbf{r}_{12} d^D \mathbf{r}_{13}, \quad (8)$$

$$B_4 = -\frac{1}{8} \iiint [f_{12} f_{14} f_{23} f_{34} + f_{12} f_{13} f_{24} f_{34} + f_{13} f_{14} f_{23} f_{24} + f_{12} f_{13} f_{14} f_{23} f_{34} \\ + f_{12} f_{14} f_{23} f_{24} f_{34} + f_{12} f_{13} f_{23} f_{24} f_{34} + f_{12} f_{13} f_{14} f_{23} f_{24} + f_{12} f_{13} f_{14} f_{24} f_{34} \\ + f_{13} f_{14} f_{23} f_{24} f_{34} + f_{12} f_{13} f_{14} f_{23} f_{24} f_{34}] d^D \mathbf{r}_{12} d^D \mathbf{r}_{13} d^D \mathbf{r}_{14}, \quad (9)$$

whereas for  $n > 4$  the number of contributing graphs, or the cardinality of  $\mathcal{M}_n^L$  respectively, increases dramatically (cf. Sec. 2.1.1, Tab. 1).

Note, that for hard particles (solids), where the pair potential can also be written as

$$U_{ij} = \begin{cases} \infty & : |\mathbf{r}_{ij}| < \sigma \\ 0 & : |\mathbf{r}_{ij}| \geq \sigma \end{cases}, \quad (10)$$

the representation of the many-body potential  $U$  through sums of pair potentials is exact [cf. Eqs. (1) and (2)]. Here,  $\sigma$  is the contact distance, which in general depends for anisometric particles of a given configuration on  $\hat{\mathbf{r}}_{ij}$  and the relative orientations of the particles. Using Eq. (6), the Mayer  $f$ -function for two solids simplifies to  $f_{ij} = -1$  if  $|\mathbf{r}_{ij}| < \sigma$  and  $f_{ij} = 0$  otherwise. Thus, the virial coefficients of hard-body systems are independent of the temperature  $T$ . Also, as seen by Eqs. (7) and (8), for solids in arbitrary-dimensional Euclidean spaces, the second and third virial coefficients are always non-negative with  $B_2 \geq 0$  and  $B_3 \geq 0$ . Oppositely, for virial coefficients of order  $n \geq 4$ , negative virial coefficients are possible.

For other potentials, e.g., square well, Lennard-Jones, or dispersion interactions, negative second and third virial coefficients are possible, resulting from attractive particle interactions. Also, Eq. (1) possibly remains an approximation and the virial coefficients depend on the temperature of the system. For systems with dispersion interactions, non-additive contributions to the virial coefficients have to be considered, too [127–130].

### 2.1.1 Graph theory

For the calculation of virial coefficients, especially for orders  $n > 3$ , fundamental graph theory emerged as an indispensable tool, generally modeling abstract objects and their interactions. These objects, here particles, are modeled as nodes (vertices), where two nodes can be connected by an edge (line), representing their interaction, here the Mayer  $f$ -function. A set of nodes and edges form a graph  $G$ . The number of edges linking a node to other nodes defines its degree

where a loop, an edge that connects a node to itself, contributes twice. If a graph consists of nodes that all have a degree of zero, the graph is empty and the nodes are isolated. If a graph contains edges connecting two vertices asymmetrically, it is a directed graph. Directing edges are only linking vertices along their orientation while undirected edges connect vertices in both directions. If a graph only consists of nodes and undirected edges, the graph is undirected itself. Graphs with nodes directly connected by multiple edges to other nodes or to themselves are referred to as multigraphs, otherwise they are simple graphs. Graphs which have nodes that can be connected to themselves through edges without using a single edge multiple times are circuit graphs. If in addition only starting and ending node are equal and the trail of edges has a length of at least three, the graph has a cycle. In Fig. 1, examples for cyclic graphs with three nodes are displayed.

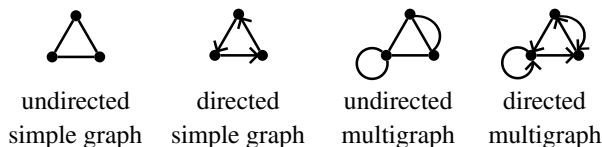


Fig. 1: Examples for cyclic graphs with three nodes.

Focusing on undirected simple graphs, a total of  $2^{i(i-1)/2}$  different graphs with  $i$  nodes exist. In Fig. 2, these  $2^6$  graphs are shown for simple graphs with  $i = 4$  nodes. If all nodes are connected through edges and other nodes, a graph is connected. Connected graphs, where by removing one node with adjacent edges the graphs remains connected, are called biconnected graphs. Otherwise, the graph is singly-connected (articulated) and becomes disconnected by removing the articulation point. E.g., is articulated, but not biconnected. If a graph gets disconnected by removing a single edge, this edge is referred to as a bridge. The graph for which each pair of nodes is connected by a unique edge is known as the complete graph with  $i$  nodes and  $i(i-1)/2$  edges. Undirected connected graphs without cycles are known as trees. Nodes in a tree with degree one are known as leaves. A subgraph of an undirected graph  $G$  that is a tree and includes all nodes of  $G$  is called a spanning tree. Using Cayley's formula [131], the number of labeled spanning trees for the complete graph with  $i$  nodes is  $i^{i-2}$ . Thus, 16 spanning trees result for the complete graph with four nodes in Fig. 2. Removing edges of a tree, a disjoint union of trees results, known as forest. Vice versa, if a forest gets connected, a tree results.

Applying graph theory in chemistry and physics, virial coefficients can be calculated by representing the configuration integral through products of Mayer  $f$ -functions, summarized in graphs  $G$  with  $G \in \mathcal{M}_n^L$ . Starting from Eqs. (7), (8), and (9), the virial coefficients up to the fourth order can be rewritten as

$$B_2 = -\frac{1}{2} \int f_{12} d^D \mathbf{r}_{12} = -\frac{1}{2} \text{---}, \quad (11)$$

$$B_3 = -\frac{1}{3} \iint f_{12} f_{13} f_{23} d^D \mathbf{r}_{12} d^D \mathbf{r}_{13} = -\frac{1}{3} \triangle, \quad (12)$$

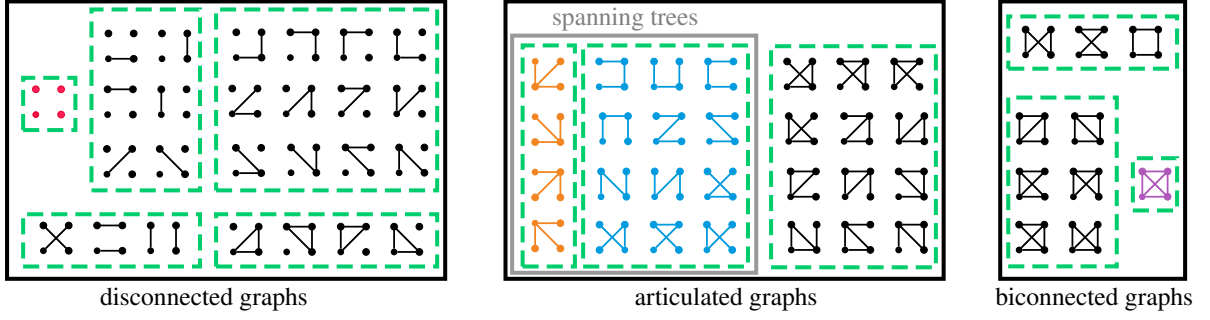


Fig. 2: The 64 undirected simple graphs with four nodes. Color-highlighted are the empty graph (red), the 16 spanning trees with three or two leaves (orange or blue), and the complete graph (violet). Isomorphic graphs are bounded by a dashed green box.

$$\begin{aligned}
B_4 &= -\frac{1}{8} \left[ \square + \boxtimes + \boxtimes + \boxtimes + \boxtimes + \boxtimes + \boxtimes + \boxtimes + \boxtimes + \boxtimes \right] \\
&= -\frac{1}{8} \left[ 3 \square + 6 \boxtimes + 1 \boxtimes \right], \tag{13}
\end{aligned}$$

considering all biconnected graphs with  $n$  nodes.

For virial coefficients with sufficiently high order, it is possible to summarize isomorphic graphs and only consider topologically distinct graphs [Eq. (13)]. Two graphs are isomorphic to each other, if they have the same canonical representation, i.e., the same connectivity for all nodes disregarding their labeling [90, 91, 132, 133], as seen in Fig. 2. Let  $g_G$  be the number of isomorphic permutations for a graph  $G$  and  $S_G$  the corresponding configuration integral for this graph, then

$$B_n = \frac{1-n}{n!} \sum_{G \in \mathcal{M}_n^U} g_G S_G \tag{14}$$

results for the calculation of the virial coefficient of order  $n$  [Eq. (5)]. Here,  $\mathcal{M}_n^U$  is the set of unlabeled (topologically distinct) Mayer graphs with  $n$  nodes. These graphs are displayed only by their edges and without their nodes in this manuscript [cf. Eq. (13)].

Since for virial coefficients  $B_n$  with increasing order  $n$  the number of biconnected graphs increases dramatically (Tab. 1), a reformulation of the Mayer graphs is required for the calculation of higher-ordered virial coefficients. Using the function  $e_{ij} = f_{ij} + 1$ , introduced by Ree and Hoover [80, 81, 134], all graphs can be represented as complete graphs with nodes being connected either by  $f$ -bonds or  $e$ -bonds. Therewith, Mayer graphs can be rewritten as a combination of Ree-Hoover graphs, e.g., for the not-fully connected, unlabeled graphs with four nodes [Eq. (13)]

$$\boxtimes = \iiint f_{12} f_{13} f_{14} f_{23} f_{34} (e_{24} - f_{24}) d^D \mathbf{r}_{12} d^D \mathbf{r}_{13} d^D \mathbf{r}_{14} = \boxtimes - \boxtimes \tag{15}$$

Tab. 1: Cardinality of the sets of labeled and unlabeled Mayer graphs ( $\mathcal{M}_i^L, \mathcal{M}_i^U$ ) and respectively Ree-Hoover graphs ( $\mathcal{R}_i^L, \mathcal{R}_i^U$ ) with  $i$  nodes [11, 92, 93].

$i$	$\#\mathcal{M}_i^L$	$\#\mathcal{M}_i^U$	$\#\mathcal{R}_i^L$	$\#\mathcal{R}_i^U$
2	1	1	1	1
3	1	1	1	1
4	10	3	4	2
5	238	10	68	5
6	11 368	56	3 053	23
7	1 014 888	468	297 171	171
8	166 537 616	7 123	56 671 216	2 606
9	50 680 432 112	194 066	21 286 987 064	81 564
10	29 107 809 374 336	9 743 542		4 980 756
11	32 093 527 159 296 128	900 969 091		

and

$$\square = \iiint f_{12} f_{14} f_{23} f_{34} (e_{13} - f_{13}) (e_{24} - f_{24}) d^D \mathbf{r}_{12} d^D \mathbf{r}_{13} d^D \mathbf{r}_{14} = \text{red square} - 2 \text{black square} + \text{white square}, \quad (16)$$

with  $e$ -bonds colored in red. Hence, Eq. (13) can be rewritten as

$$B_4 = -\frac{1}{8} [3 \text{red square} - 2 \text{black square}] = -\frac{1}{8} [\text{red square} + \text{black square} + \text{red square} - 2 \text{black square}], \quad (17)$$

using unlabeled or labeled Ree-Hoover graphs  $G$  with  $G \in \mathcal{R}_n^U$  or  $G \in \mathcal{R}_n^L$  for  $n = 4$  nodes. In general, the number of graphs to consider is reduced by about 65% for  $n > 3$  with this reformulation (Tab. 1). Conversely to labeled Mayer graphs, Ree-Hoover graphs  $G$  have to be considered with their respective weights  $c_G$  [cf. Eq. (17)], which have to be calculated, too [80]. This results in

$$B_n = \frac{1-n}{n!} \sum_{G \in \mathcal{R}_n^L} c_G S_G \quad (18)$$

for the virial coefficient of order  $n$ . For hard bodies, the calculation of virial coefficients is further simplified using Ree-Hoover graphs, since for a given configuration of particles always  $f_{ij} e_{ij} = 0$  results. Subsequently, only one graph with a non-zero contribution to the respective virial coefficient is obtained for a respective particle configuration. For this graph, all Mayer  $f$ -functions give  $f_{ij} = -1$  ( $P_i \cap P_j \neq \emptyset$ ) and all Ree-Hoover  $e$ -functions give  $e_{ij} = 1$  ( $P_i \cap P_j = \emptyset$ ).

### 2.1.2 Analytical calculation of virial coefficients

Virial coefficients  $B_n$  with sufficiently low order  $n$  can, for solids with an accessible contact distance  $\sigma$  [Eq. (10)], be calculated analytically by their configuration integrals [Eq. (5)]. For

the simplest model of  $D$ -dimensional spheres in  $\mathbb{R}^D$ , a reduced second virial coefficient

$$B_2^* = \frac{B_2}{V_P} = 2^{D-1} \quad (19)$$

results. In addition, the third virial coefficient of hyperspheres can be written as

$$\tilde{B}_3 = \frac{B_3}{B_2^2} = \frac{4\Gamma(1 + \frac{D}{2})}{\sqrt{\pi}\Gamma(\frac{1+D}{2})} \int_0^{\pi/3} \sin^D \phi \, d\phi \quad (20)$$

in arbitrary-dimensional Euclidean spaces  $\mathbb{R}^D$  [135]. Also, analytical expressions for the fourth virial coefficients of hard hyperspheres are available for arbitrary even-dimensional Euclidean spaces and odd-dimensional Euclidean spaces with  $D \leq 11$  [68, 69, 136].

For anisotropic particles, the analytical calculation of virial coefficients is more complicated in general, since the average contact distance over all relative particle positions and orientations is required. If the hard particles are identical, arbitrary convex solids  $K$  in  $\mathbb{R}^3$ , their second virial coefficient  $B_2$  can, as independently shown by Isihara and Hadwiger [70–72], be obtained analytically by

$$B_2(K) = V_P(K) + S_P(K) \bar{R}_P(K), \quad (21)$$

using the geometric measures volume  $V_P$ , total surface area  $S_P$ , and mean radius of curvature  $\bar{R}_P$  of a single particle. This is referred to as Isihara-Hadwiger theorem. Similarly, for arbitrary convex figures in  $\mathbb{R}^2$ , the general expression

$$B_2(K) = V_P(K) + \frac{1}{2} S_P(K) \bar{R}_P(K) = V_P(K) + \frac{S_P^2(K)}{4\pi} \quad (22)$$

results [113, 116]. Starting with the known results for hyperspheres, an extension of the Isihara-Hadwiger theorem to arbitrary higher-dimensional Euclidean spaces  $\mathbb{R}^D$  is reported in the literature [117]. As part of this dissertation, this expression for  $B_2$  appeared to be incorrect in general, being a rigorous lower limit with a correct result only for hyperspheres. After private communication, the authors published an already prepared correction [118].

For concave solids, no general analytical expression for their virial coefficients is available so far. Nevertheless, for homonuclear and heteronuclear dumbbells in  $\mathbb{R}^2$  and  $\mathbb{R}^3$ , closed analytical expressions for  $B_2$  have been reported [74–76, 137].

### 2.1.3 Numerical calculation of virial coefficients

With limited analytical expressions for the configuration integrals of virial coefficients  $B_n$ , the remaining calculations have to be performed numerically, employing computer simulations. Starting with the seminal works of Metropolis *et al.* [78, 79], Monte Carlo simulations can be used to obtain virial coefficients of up to the eighth order for arbitrary hard particles, employing Mayer and Ree-Hoover graphs summarized in previously prepared lookup tables [10, 80, 81, 83].

A significant improvement on the accurate numerical calculation of virial coefficients for hard particles results from the introduction of Mayer sampling [107]. Starting from the general umbrella sampling method, an integral  $I$  can be calculated with

$$I = I_{\text{ref}} \frac{\langle \gamma / \rho \rangle_{\rho}}{\langle \gamma_{\text{ref}} / \rho \rangle_{\rho}} \quad (23)$$

relative to an already known reference integral  $I_{\text{ref}}$  with corresponding integrands  $\gamma$  and  $\gamma_{\text{ref}}$ . For Mayer-sampling Monte Carlo (MSMC) simulations, the sampling distribution  $\rho = |\gamma|$  is selected. Each simulation step is then accepted by a probability  $P_{\text{acc}} = \min(1, \rho_{\text{new}} / \rho_{\text{old}})$ , with  $\rho_{\text{new}}$  being the distribution of the step to be accepted and  $\rho_{\text{old}}$  the distribution of the previous step. Therefore, at the beginning of each simulation an acceptance ratio  $P_{\text{acc}} \approx 50\%$  is tuned in by a step-parameter in an equilibration phase which is then set as constant for the determination of the averages in Eq. (23) in a followed production run.

By selecting an appropriate reference system, being part of the phase space of the investigated system, it is then possible to numerically obtain unknown virial coefficients of a selected many-particle system relative to the virial coefficients of the reference system. Beside the initial application to calculate virial coefficients of spheres with other interaction potentials relative to known virial coefficients of hard spheres [107], hard spheres can be selected additionally as a reference system to obtain virial coefficients of hard, anisotropic particles in the same dimensional space. The more similar system and reference system are with their corresponding integrals, the more efficient is the MSMC simulation. For hard, uniaxial solids of revolution, virial coefficients can usually be obtained with high accuracy for geometries with aspect ratios  $1/5 < \nu < 5$  using virial coefficients of the same order of hard spheres as a reference system. For highly anisotropic particles, however, similar anisotropic particles (e.g., spheroids with  $\nu = 2$ ) have to be selected as a reference system to obtain reliable results.

Furthermore, virial coefficients of lower order can for a system of interest be selected as a reference integral to calculate higher-order virial coefficients [107]. Besides the accurate numerical computation of higher-order virial coefficients of hard hyperspheres, this intrinsic reference allows for the accurate numerical computation of higher-order virial coefficients for anisotropic particles, too, since the influence of a different geometry of the reference system is eliminated. The reference integral for the calculation of  $B_n$  with  $n \geq 3$  can thus be written as

$$I_{\text{ref}} = N_{\text{T}} (-2B_2)^{n-1} \quad (24)$$

using the second virial coefficient as a reference with  $N_{\text{T}}$  spanning trees with  $n$  nodes (Fig. 1) [58]. To the reference integrand  $\gamma_{\text{ref}}$  the  $n$  spanning trees with  $n - 1$  leaves and one node of degree  $n$  usually contribute by far the most. Thus, as an approximation it is sufficient to only consider these  $n$  out of  $n^{n-2}$  spanning trees for the reference system [58]. Therewith, virial coefficients up to the eighth order of hard, anisotropic particles can be calculated using binary stored spanning trees and Ree-Hoover graphs with their respective weights [2, 3, 58].

With currently accessible computer hardware it is usually not possible to binary store all labeled Ree-Hoover graphs  $G \in \mathcal{R}_n^L$  with their weights  $c_G$  for  $n \geq 9$  in the computer memory before a simulation. Thus, more complex computational techniques are required for the calculation of higher-ordered virial coefficients. For the ninth and tenth virial coefficients of hard bodies, canonical representations of graphs and graph isomorphism can be used [10,92,93,104,138], whereas for  $n > 10$  other methods are required [9–11]. Due to the complexity of the calculation, virial coefficients  $B_n$  with  $n \geq 10$  have not been computed for any anisotropic particle geometry so far.

## 2.2 Euclidean space of arbitrary dimension

Beside the fundamental two- and three-dimensional Euclidean spaces  $\mathbb{R}^2$  and  $\mathbb{R}^3$  with

$$\begin{pmatrix} x \\ y \end{pmatrix} = \begin{pmatrix} r \cos \varphi \\ r \sin \varphi \end{pmatrix} \quad \text{and} \quad \begin{pmatrix} x \\ y \\ z \end{pmatrix} = \begin{pmatrix} r \sin \vartheta \cos \varphi \\ r \sin \vartheta \sin \varphi \\ r \cos \vartheta \end{pmatrix}, \quad (25)$$

other Euclidean spaces  $\mathbb{R}^D$  of arbitrary positive integer dimension  $D$  can be defined using Cartesian or polar coordinates

$$\begin{pmatrix} x_1 \\ x_2 \\ \vdots \\ x_{D-1} \\ x_D \end{pmatrix} = \begin{pmatrix} r \cos \phi_1 \\ r \sin \phi_1 \cos \phi_2 \\ \vdots \\ r \sin \phi_1 \cdots \sin \phi_{D-2} \cos \phi_{D-1} \\ r \sin \phi_1 \cdots \sin \phi_{D-2} \sin \phi_{D-1} \end{pmatrix} \quad (26)$$

with the volume element

$$\prod_{i=1}^D dx_i = r^{D-1} dr \prod_{i=1}^{D-1} \sin^{i-1} \phi_{D-i} d\phi_{D-i} \quad (27)$$

and  $\phi_{D-1} \in [0, 2\pi]$ , as well as  $\phi_1, \phi_2, \dots, \phi_{D-2} \in [0, \pi]$ , based on the dot products of the vectors defining the Euclidean space. Therefore, the four-dimensional Euclidean space  $\mathbb{R}^4$  can be defined as

$$\begin{pmatrix} w \\ x \\ y \\ z \end{pmatrix} = \begin{pmatrix} r \sin \vartheta \sin \chi \cos \varphi \\ r \sin \vartheta \sin \chi \sin \varphi \\ r \sin \vartheta \cos \chi \\ r \cos \vartheta \end{pmatrix} = \begin{pmatrix} r(z) \sin \chi \cos \varphi \\ r(z) \sin \chi \sin \varphi \\ r(z) \cos \chi \\ z \end{pmatrix}, \quad (28)$$

relabeling the coordinates where in general  $\phi_1$  is denoted as  $\vartheta$  and  $\phi_{D-1}$  as  $\varphi$  in each dimension. Additionally, beside Cartesian and polar coordinates, the corresponding  $D$ -dimensional cylindrical coordinates can be obtained.

Regarding the four-dimensional Euclidean space  $\mathbb{R}^4$ , a vector  $\mathbf{v}$  can be rotated via a rotation matrix  $\underline{\mathbf{R}}$  using Hamiltonian quaternions  $q$  with

$$q = a + bi + cj + dk \quad (a, b, c, d \in \mathbb{R}; \quad i^2 = j^2 = k^2 = ijk = -1) \quad (29)$$

which consist of one real part and three imaginary parts. The quaternion number system  $\mathbb{H}$  is the extension of the complex number system  $\mathbb{C}$  with  $\mathbb{C} \subset \mathbb{H}$ . When operating with quaternions, it has to be taken into account that multiplication is not commutative, giving  $q_1 q_2 \neq q_2 q_1$  in general.

For the rotation of a vector  $\mathbf{v}$  in  $\mathbb{R}^4$  with  $r$ ,  $\varphi$ ,  $\chi$ , and  $\vartheta$  [Eq. (28)], a left isoclinic rotation matrix  $\underline{\mathbf{R}}_L$  or a right isoclinic rotation matrix  $\underline{\mathbf{R}}_R$  with

$$\underline{\mathbf{R}}_L = \begin{pmatrix} a & -b & c & -d \\ b & a & -d & -c \\ -c & d & a & -b \\ d & c & b & a \end{pmatrix} \quad \text{and} \quad \underline{\mathbf{R}}_R = \begin{pmatrix} a & -b & c & d \\ b & a & -d & c \\ -c & d & a & b \\ -d & -c & -b & a \end{pmatrix} \quad (30)$$

can be used [139].

For a counterclockwise rotation around the angle  $\psi$  using the left isoclinic rotation matrix,

$$\mathbf{v}' = \underline{\mathbf{R}}_L \underline{\Psi}(\psi) \underline{\mathbf{R}}_L^T \mathbf{v} \quad (31)$$

results for the vector after the rotation. Here, at first the vector  $\mathbf{v}$  is aligned via  $\underline{\mathbf{R}}_L^T$  with

$$d = \sin \vartheta \sin \chi \cos \varphi, \quad (32a)$$

$$c = \sin \vartheta \sin \chi \sin \varphi, \quad (32b)$$

$$b = \sin \vartheta \cos \chi, \quad (32c)$$

$$a = \cos \vartheta \quad (32d)$$

to the positive direction of the  $z$ -axis and then via

$$\underline{\Psi}(\psi) = \begin{pmatrix} \cos \psi_1 & -\sin \psi_1 & 0 & 0 \\ \sin \psi_1 & \cos \psi_1 & 0 & 0 \\ 0 & 0 & \cos \psi_2 & -\sin \psi_2 \\ 0 & 0 & \sin \psi_2 & \cos \psi_2 \end{pmatrix} \quad (33)$$

rotated around the angle  $\psi$ , before finally getting rotated back via  $\underline{\mathbf{R}}_L$  [1]. For  $\underline{\Psi}(\psi)$ , the relation  $\psi_1 = \psi_2$  results for left isoclinic rotations and  $\psi_1 = -\psi_2$  for right isoclinic rotations [139].

Note, that, independent of the dimension of space, a rotation is always executed in a plane around a rotational invariant element. Therefore, quaternions can also be used for rotations in  $\mathbb{R}^3$ , where the rotation is around an invariant axis. This has various applications, especially in robotics where due to the high numerical accuracy and simple operations a high precision results in the technical implementation. For rotations in Euclidean spaces  $\mathbb{R}^D$  with  $D > 4$ ,

other, computationally more demanding methods are required, where, e.g., the Aguilera-Perez algorithm [140] can be used, whose computational time scales with the number of dimensions  $D$ .

## 2.3 Geometry of selected solids

### 2.3.1 Uniaxial solids of revolution

For modeling hard, anisotropic particles, one of the most common types of geometries are uniaxial solids of revolution. Their shape can solely be defined by their meridian curve  $r(z)$ , describing the distance of the surface to the rotational invariant  $z$ -axis. Therefore, a  $D$ -dimensional cylindrical coordinate system for  $\mathbb{R}^D$  is preferred for such solids. Since in Euclidean spaces of higher dimensions ( $D > 3$ ) a rotation is always in a plane around a  $(D - 2)$ -dimensional invariant element, an additional rotational invariance exist for uniaxial solids of revolution. Furthermore, in addition to the meridian curve, the aspect ratio  $\nu$  as the ratio of the height of the solid in respect to the elongated axis to the width in respect to each remaining axis can be used to characterize their specific geometry. Defining the size of a particle by its radius, various solids of revolution can be defined by their meridian curve  $r(z)$ . A selection of geometries investigated in this work is summarized in Fig. 3 with their corresponding meridian curves given in Appendix A, Tab. A-1.

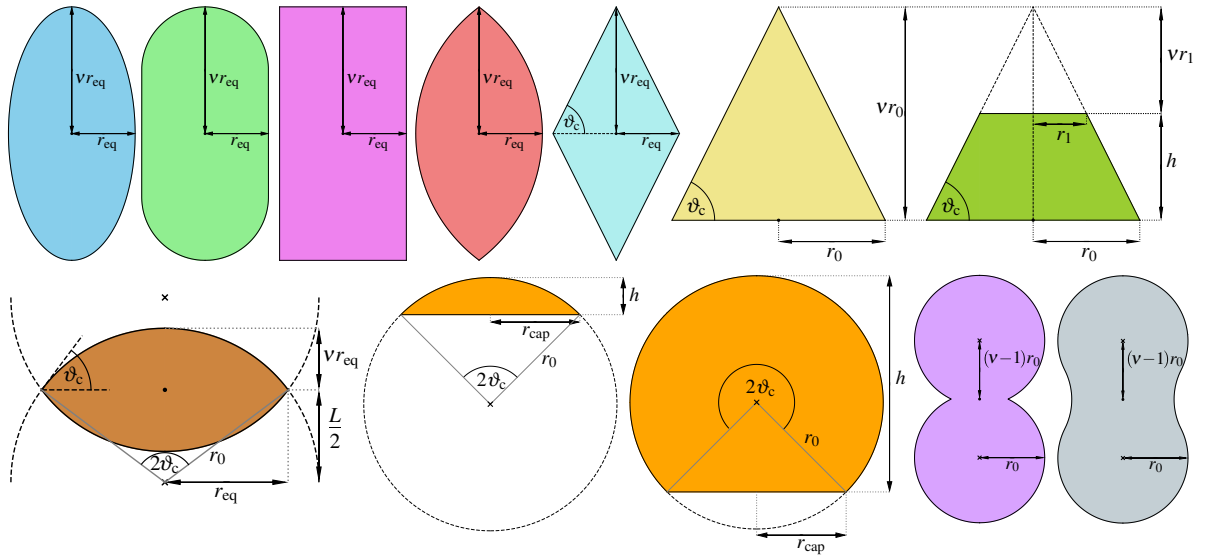


Fig. 3: Two-dimensional sections of selected uniaxial solids or revolution in this work, FLTR: Ellipsoid, spherocylinder, cylinder, spindle, doublecone, cone, truncated cone, lens, spherical segment ( $\vartheta_c < \pi/2$ ), spherical segment ( $\vartheta_c > \pi/2$ ), homonuclear dumbbell, peanut [2, 4].

The generalization of these geometries from two- and three-dimensional Euclidean spaces to arbitrary higher-dimensional Euclidean spaces is straightforward, using their meridian curves and hypercylindrical coordinates [Eq. (28)]. The  $D$ -dimensional volume (hypervolume)  $V_P$  of

a solid in  $\mathbb{R}^D$  can in general be calculated with

$$V_P = \kappa_{D-1} \int_{z_{\min}}^{z_{\max}} r^{D-1}(z) dz, \quad (34)$$

with

$$\kappa_D = \frac{\beta_D}{D} = \frac{\pi^{D/2}}{\Gamma(1 + D/2)} \quad (35)$$

being the volume of a  $D$ -dimensional unit ball  $\mathcal{B}^D$  and  $\beta_D$  its corresponding  $(D-1)$ -dimensional surface area (hypersurface area). The  $(D-1)$ -dimensional lateral surface area (lateral hypersurface area) of a solid can in general be calculated by

$$S'_P = \beta_{D-1} \int_{z_{\min}}^{z_{\max}} r^{D-2}(z) [1 + \dot{r}^2(z)]^{1/2} dz \quad (36)$$

where for uniaxial solids of revolution with  $r(z_{\min}) = r(z_{\max}) = 0$  the lateral hypersurface area  $S'_P$  is equal to the total hypersurface area  $S_P$  [4].

### 2.3.2 Polytopes

Beside uniaxial solids of revolution, mainly polytopes are used for modeling anisotropic particles. Each polytope  $P$  can be characterized by its sets of proper  $k$ -faces  $\mathcal{F}_k(P)$  with  $k = 0, 1, \dots, D-1$  and the external angle  $\gamma(P, F)$  for each  $k$ -face  $F$  of  $P$ . Denoting  $F \in \mathcal{F}_k(P)$  as  $F_k$  for any  $k$ -face  $F$  of a polytope  $P$ ,  $F_0$  is commonly referred to as vertex,  $F_1$  as edge,  $F_2$  as face, and  $F_{D-1}$  as facet. Furthermore,  $F_3$  is referred to as cell,  $F_{D-2}$  as ridge, and  $F_{D-3}$  as peak. Additionally,  $F_D$  represents the polytope  $P$  itself as an improper  $k$ -face. Writing  $N_k(P)$  for the cardinality  $\#\mathcal{F}_k(P)$ , the Euler characteristic

$$\sum_{k=0}^{D-1} (-1)^k N_k(P) = 1 + (-1)^{D-1} \quad (37)$$

results for any convex polytope in  $\mathbb{R}^D$ . The external angle  $\gamma$  of each  $k$ -face  $F$  of a polytope  $P$  can be written as

$$\gamma(P, F) = \frac{\mathcal{H}^{D-k}(N(P, F) \cap \mathcal{B}^D)}{\kappa_{D-k}}, \quad (38)$$

using the normal cone  $N(P, F)$  and the  $D$ -dimensional unit ball  $\mathcal{B}^D$  with the  $(D-k)$ -dimensional Hausdorff measure  $\mathcal{H}^{D-k}$  of their intersection [141, 142]. There, the cases

$$\sum_{F \in \mathcal{F}_0(P)} \gamma(P, F) = 1, \quad \gamma(P, F_{D-1}) = \frac{1}{2}, \quad \gamma(P, F_D) = 1 \quad (39)$$

for vertices, facets, and the polytope itself ( $F_D \equiv P$ ) can be deduced for arbitrary convex polytopes.

If all  $k$ -faces of a polytope have a transitive symmetry, the polytope itself is regular if all  $k$ -faces are regular  $k$ -dimensional polytopes, too. Hence, all  $k$ -faces and their external angles are respectively identical for a regular polytope. Let  $\mathcal{P}^D$  be the set of different types of regular, convex polytopes in  $\mathbb{R}^D$ . For  $P \in \mathcal{P}^D$ , the external angle of a ridge  $\gamma(P, F_{D-2})$  can be rewritten as

$$\gamma(P, F_{D-2}) = \frac{\pi - \delta_P}{2\pi} \quad (40)$$

with  $\delta_P$  being the dihedral angle of the polytope. Also, each regular  $D$ -dimensional polytope ( $D$ -polytope) can be characterized by its Schläfli symbol  $\{p_1, p_2, \dots, p_{D-1}\}$  or  $\{p, q, r, \dots\}$  [143]. Only one type of 1-polytope exist, the line segment  $\{\}$  with length  $a$ . Oppositely, infinite many types of regular, convex polygons (2-polytopes) exist, with  $\{p\}$  denoting the Schläfli symbol and  $p$  being the number of its vertices and edges of length  $a$ .

The five types of regular, convex polyhedra  $P \in \mathcal{P}^3$  are known as the platonic solids  $\{p, q\}$  with faces of type  $\{p\}$  and vertex figures of type  $\{q\}$  [143]. They are shown in Fig. 4 and their dihedral angles  $\delta_P$  can be written as

$$\delta_{\{p,q\}} = 2 \arcsin \left[ \frac{\cos \left( \frac{\pi}{q} \right)}{\sin \left( \frac{\pi}{p} \right)} \right] \quad (41)$$

in dependence on their Schläfli symbols [143].



Fig. 4: The five Platonic solids tetrahedron  $\{3,3\}$ , cube  $\{4,3\}$ , octahedron  $\{3,4\}$ , dodecahedron  $\{5,3\}$ , and icosahedron  $\{3,5\}$ .

For regular 4-polytopes (polychora), a total of six convex types exist: 5-cell  $\{3,3,3\}$  (also called 4-simplex), 8-cell  $\{4,3,3\}$  (also referred to as 4-cube or tesseract), 16-cell  $\{3,3,4\}$  (also known as 4-dimensional cross-polytope), 24-cell  $\{3,4,3\}$ , 120-cell  $\{5,3,3\}$ , and 600-cell  $\{3,3,5\}$ . Each regular, convex polychoron  $\{p,q,r\}$  has cells of type  $\{p,q\}$ , 2-faces of type  $\{p\}$ , edge figures of type  $\{r\}$ , and vertex figures of type  $\{q,r\}$ . While 5-cell, 8-cell, 16-cell, 120-cell, and 600-cell are the analog geometries for the five platonic solids tetrahedron, cube, octahedron, dodecahedron, and icosahedron in  $\mathbb{R}^4$ , the 24-cell is an additional regular, convex polytope which is unique in this dimension of space. In higher-dimensional Euclidean spaces  $\mathbb{R}^D$  with  $D > 4$ , only three types of regular, convex  $D$ -polytopes exist:  $D$ -simplex,  $D$ -cube, and  $D$ -dimensional cross-polytope. Their characteristic Schläfli symbols, numbers of  $k$ -faces and dihedral angles

are summarized in Tab. 2.

Tab. 2: Schläfli symbol  $\{p_1, \dots, p_{D-1}\}$ , number of  $k$ -faces  $N_k$ , and dihedral angle  $\delta_P$  for the three regular, convex  $D$ -polytopes in arbitrary-dimensional Euclidean spaces  $\mathbb{R}^D$  [143].

Name	Schläfli symbol	$N_k$	$\delta_P$
Simplex	$\{3, 3, 3, \dots, 3\} = \{3^{D-1}\}$	$\binom{D+1}{k+1}$	$\arccos\left(\frac{1}{D}\right)$
Cube	$\{4, 3, 3, \dots, 3\} = \{4, 3^{D-2}\}$	$2^{D-k} \binom{D}{k}$	$\frac{\pi}{2}$
Cross-polytope	$\{3, 3, 3, \dots, 4\} = \{3^{D-2}, 4\}$	$2^{k+1} \binom{D}{k+1}$	$\arccos\left(\frac{2-D}{D}\right)$

### 3 Results and Discussion

#### 3.1 Analytical calculation of second virial coefficients for anisotropic solids

##### 3.1.1 Exclusion volume of two convex solids

For particles purely interacting as hard bodies, their second virial coefficient is directly related to their orientation-averaged excluded volume. For two solids with fixed orientation, the exclusion volume is the volume inaccessible for the center of the second body in the vicinity of the first one. Averaging for anisotropic particles over all relative particle orientations, the orientation-averaged excluded volume  $V_{\text{ex}}$  with the corresponding second virial coefficient

$$B_2 = \frac{V_{\text{ex}}}{2} \quad (42)$$

as orientation-averaged excluded volume per particle can be obtained in arbitrary-dimensional Euclidean spaces  $\mathbb{R}^D$ . E.g., the excluded area in  $\mathbb{R}^2$  for two hexagons is shown in Fig. 5.

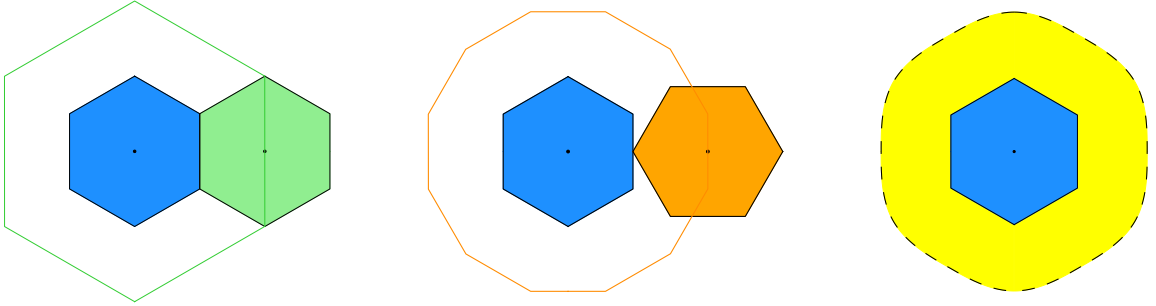


Fig. 5: Excluded area for parallel-oriented (green) and anti-parallel-oriented (orange) hexagons as the area inside the solid lines with the orientation-averaged excluded area  $V_{\text{ex}}$  as the area inside the dashed line.

For two arbitrary convex solids  $K$  and  $L$  in  $\mathbb{R}^D$ , the rotation-averaged excluded volume  $V_{\text{ex}}$  can be calculated analytically by the Brunn-Minkowski theorem with

$$V_{\text{ex}}(K, L) = \frac{1}{\kappa_D} \sum_{i=0}^D \binom{D}{i} W_i(K) W_{D-i}(L), \quad (43)$$

using quermassintegrals  $W_i$  of order  $i$  as geometric measures for each convex solid [118, 142, 144]. The  $i$ th quermassintegral  $W_i(K)$  of a convex body  $K$  with  $i = 0, 1, \dots, D$  is the mixed volume of  $(D - i)$  copies of  $K$  and  $i$  copies of the  $D$ -dimensional unit ball  $\mathcal{B}^D$ . Specific quermassintegrals are related to other common geometric measures [117, 118, 142, 144, 145], e.g.,

$$W_0(K) = V_{\text{P}}(K), \quad (44a)$$

$$W_1(K) = \frac{S_{\text{P}}(K)}{D}, \quad (44b)$$

$$W_2(K) = \frac{M_{\text{P}}(K)}{D} = \frac{1}{D} \oint H_{\text{P}}(K) d^{D-1}S, \quad (44c)$$

$$W_{D-1}(K) = \bar{R}_P(K) \kappa_D = \frac{\bar{w}_P(K)}{2} \kappa_D, \quad (44d)$$

$$W_D(K) = \kappa_D, \quad (44e)$$

with  $V_P$  denoting the volume,  $S_P$  the total surface area,  $M_P$  the surface integral over the mean curvature  $H_P$ ,  $\bar{R}_P$  the mean radius of curvature, and  $\bar{w}_P$  the mean width of the convex particle. Alternatively, independent of the dimension of space in which the convex body is embedded into, the  $i$ th intrinsic volume

$$V_i(K) = \binom{D}{i} \frac{W_{D-i}(K)}{\kappa_{D-i}} \quad (45)$$

of a convex body  $K$  can be used instead of the corresponding quermassintegral [146].

For many-particle systems consisting of hard, convex particles, all identical in size and shape, the Brunn-Minkowski theorem [Eq. (43)] with Eq. (42) and  $K \equiv L$  can be used to obtain the second virial coefficient  $B_2$  for particles in arbitrary-dimensional Euclidean spaces  $\mathbb{R}^D$ , resulting with Eqs. (44) in Eq. (22) for  $\mathbb{R}^2$  and in the Isihara-Hadwiger theorem [Eq. (21)] for  $\mathbb{R}^3$ . In the four-dimensional Euclidean space  $\mathbb{R}^4$ , analogously

$$B_2(K) = V_P(K) + S_P(K) \bar{R}_P(K) + \frac{6}{\pi^2} W_2^2(K) \quad (46)$$

can be obtained [1]. The previously proposed general expression

$$B_2(K) = V_P(K) + \frac{2^{D-1} - 1}{D} S_P(K) \bar{R}_P(K) \quad (47)$$

for arbitrary convex solids in  $\mathbb{R}^D$  by Torquato and Jiao [117], however, is just a rigorous lower bound, giving the correct results only in the limiting case of hyperspheres [118].

Since the Brunn-Minkowski theorem with Eq. (43) is defined for two arbitrary convex particles in general, the second cross virial coefficient  $B_2(A, B)$  of a binary mixture with components  $A$  and  $B$  can analytically be obtained, too, if  $A, B \in \mathcal{K}^D$ . Therefore, with the second virial coefficients of the pure components  $B_2(A)$  and  $B_2(B)$ , the second virial coefficient of a binary mixture  $B_2^{\text{mix}}$  with

$$B_2^{\text{mix}}(A, B) = x_A^2 B_2(A) + 2x_A x_B B_2(A, B) + x_B^2 B_2(B) \quad (48)$$

can be calculated analytically in dependence on the number fractions  $x_A$  and  $x_B$  for arbitrary hard, convex particles in  $\mathbb{R}^D$ , if all quermassintegrals  $W_i$  are known for  $A$  and  $B$ . In addition, the general extension to second virial coefficients of mixtures with  $m$  components as

$$B_2^{\text{mix}} = \sum_{i=1}^m \sum_{j=1}^m x_i x_j B_2(i, j) \quad (49)$$

is straightforward [147].

### 3.1.2 Geometric measures of convex solids

To calculate the second virial coefficient of a many-particle system consisting of an arbitrary number of distinguishable hard, convex particles in  $\mathbb{R}^D$ , only their individual geometric measures in form of quermassintegrals  $W_i$  or intrinsic volumes  $V_i$  are required. Since uniaxial solids of revolution and polytopes are the most common types of geometries for modeling anisotropic particles, general and specific expressions for their quermassintegrals are derived [4, 118].

For uniaxial solids of revolution with continuous surface curvatures in  $\mathbb{R}^D$ , their quermassintegrals  $W_0$  and  $W_1$  can directly be obtained in dependence on their meridian curve  $r(z)$  using Eqs. (44a) and (44b) by calculating their volume  $V_P$  and total surface area  $S_P$  [Eqs. (34) and (36)], while  $W_D$  is already given as the volume of a  $D$ -dimensional unit ball [Eq. (35)]. For the remaining quermassintegrals, the principal curvatures or the reciprocal principal radii of curvature are required. The principal curvatures of a solid can be obtained as the eigenvalues of its Weingarten map  $\underline{\mathcal{W}}_P$  (also known as shape operator) with

$$\underline{\mathcal{W}}_P = \underline{\mathbf{I}}_P^{-1} \underline{\mathbf{II}}_P \quad (50)$$

where  $\underline{\mathbf{I}}_P$  denote the first and  $\underline{\mathbf{II}}_P$  the second fundamental form of the solid's surface [4, 73]. For solids of revolution, this results for the Weingarten map in a main diagonal matrix with  $D - 1$  elements where thus the eigenvalues are directly accessible, giving

$$R_i = \begin{cases} \pm r(z) [1 + \dot{r}^2(z)]^{1/2} & : 1 \leq i \leq D - 2 \\ \mp \frac{1}{\ddot{r}(z)} [1 + \dot{r}^2(z)]^{3/2} & : i = D - 1 \end{cases} \quad (51)$$

for their principal radii of curvature in dependence on their meridian curve  $r(z)$  [4, 73].

Using the principal radii of curvature, quermassintegrals  $W_i$  with  $i \geq 1$  can then be rewritten as surface integrals, e.g., in  $\mathbb{R}^4$  as

$$W_1 = \frac{1}{4} \oint d^3S, \quad (52a)$$

$$W_2 = \frac{1}{4} \oint \frac{1}{3} \left[ \frac{1}{R_1} + \frac{1}{R_2} + \frac{1}{R_3} \right] d^3S, \quad (52b)$$

$$W_3 = \frac{1}{4} \oint \frac{1}{3} \left[ \frac{1}{R_1 R_2} + \frac{1}{R_1 R_3} + \frac{1}{R_2 R_3} \right] d^3S, \quad (52c)$$

$$W_4 = \frac{1}{4} \oint \frac{1}{R_1 R_2 R_3} d^3S, \quad (52d)$$

or in general by the recursive relation

$$W_i = \begin{cases} \frac{1}{D} \oint d^{D-1}S & : i = 1 \\ \frac{1}{D} \oint \frac{1}{\binom{D-1}{i-1}} \left[ \sum_{j=1}^{D-i+1} a_{D-i+1,j} \right] d^{D-1}S & : 2 \leq i \leq D \end{cases} \quad (53)$$

with

$$a_{i,j} = \begin{cases} \frac{1}{R_j} & : i = D - 1 \\ \frac{1}{R_j} \sum_{k=j+1}^{i+1} a_{i+1,k} & : i \leq D - 2 \end{cases} \quad (54)$$

and

$$\begin{aligned} d^{D-1}S &= \left[ \prod_{i=1}^{D-1} R_i \right] \left[ \prod_{j=1}^{D-1} \sin^{j-1} \phi_{D-j} d\phi_{D-j} \right] \\ &= r^{D-2}(z) [1 + \dot{r}^2(z)]^{1/2} \left[ \prod_{i=1}^{D-2} \sin^{i-1} \phi_{D-i} d\phi_{D-i} \right] dz \end{aligned} \quad (55)$$

for the surface element [4]. Here, the mean curvature  $H_P$  is written as

$$H_P = \frac{1}{D-1} \sum_{i=1}^{D-1} \frac{1}{R_i} \quad (56)$$

[Eqs. (44c) and (52b)] and the mean radius of curvature  $\bar{R}_P$  as

$$\bar{R}_P = \frac{1}{\beta_D} \oint \frac{1}{D-1} \left[ \sum_{i=1}^{D-1} R_i \right] \prod_{j=1}^{D-1} \sin^{j-1} \phi_{D-j} d\phi_{D-j} \quad (57)$$

[Eqs. (44d) and (52c)].

Using the provided equations, all quermassintegrals for convex solids of revolution with continuous surface curvature can be calculated in dependence on their meridian curve  $r(z)$ . For the geometries selected in this work, i.e., hyperspheres, uniaxial hyperellipsoids of revolution (hyperspheroids), and prolate hyperspherocylinders the obtained expressions are summarized in Tab. A-2 (Appendix A), which agree with the expressions provided in the literature [118,144]. Therefore, the Gaussian hypergeometric function  ${}_2F_1(a,b,c;z)$ , related to the complete elliptic integral of the first kind  $K(k)$  and the complete elliptic integral of the second kind  $E(k)$  by

$$K(k) = \frac{\pi}{2} {}_2F_1\left(\frac{1}{2}, \frac{1}{2}, 1; k^2\right), \quad E(k) = \frac{\pi}{2} {}_2F_1\left(-\frac{1}{2}, \frac{1}{2}, 1; k^2\right), \quad (58)$$

is used for the quermassintegrals of uniaxial hyperellipsoids. For oblate solids of revolution with  $\nu \rightarrow 0$ , a  $(D-1)$ -dimensional spherical plate results in  $\mathbb{R}^D$ . Its general quermassintegrals are given in Tab. A-2 too, which can also be obtained using the intrinsic volumes  $V_i$  of a  $(D-1)$ -dimensional sphere with the corresponding quermassintegrals in  $\mathbb{R}^{D-1}$  [118].

For uniaxial solids of revolution with discontinuities in their surface curvatures, e.g., hypercylinders, hypercones, hyperspindles, or hyperlenses, additional contributions to the quermassintegrals  $W_i$  with  $1 \leq i \leq D-1$  have to be considered. Firstly, for uniaxial solids of revolution with  $r(z_{\max}) \neq 0$  or  $r(z_{\min}) \neq 0$ , the top or the bottom of the solid is covered by

half a spherical hyperplate with the additional contribution of half its quermassintegral to the respective quermassintegral of the solid. Thus, the general expression for the quermassintegrals of cylinders can be obtained, giving the result shown in Tab. A-2. Furthermore, in general, zero-dimensional singularities or  $(D-2)$ -dimensional singularities might occur in the hypersurface curvatures of uniaxial solids of revolution, e.g., the apical singularities of hyperspindles or the equatorial singularities of hyperlenses. Due to the symmetry of the solid, other-dimensional singularities in the surface curvature do not occur for a uniaxial solid of revolution.

To calculate the contribution of a  $(D-2)$ -dimensional singularity  $W_i''$  to the quermassintegral of a convex solid of revolution, e.g., an equatorial singularity for a hyperlens, the meridian curve of the geometry can continuously be replaced by a hypertorus in the vicinity of the singularity [Fig. 6 (left)] [4, 73]. For the limit of an infinitely thin hypertorus, the contribution of the equatorial singularity

$$W_i'' = \kappa_{D-1} \frac{i-1}{D} r_{\text{eq}}^{D-i} \int_{\vartheta_c}^{\pi-\vartheta_c} \sin^{i-2} \vartheta \, d\vartheta \quad : \quad 1 \leq i \leq D-1 \quad (59)$$

results in dependence on the critical angle  $\vartheta_c$  to the total quermassintegral  $W_i$  with  $W_i'$  being the previously calculated contribution of the parts with continuous surface curvature using the principal radii of curvature of the solid [4]. Finally, if a uniaxial solid of revolution has a zero-dimensional singularity with  $r(z) = 0$  in its surface curvature, where for convex solids only apices with  $r(z_{\text{max}}) = 0$  or  $r(z_{\text{min}}) = 0$  are possible, the contribution to the quermassintegral  $W_i'''$  can be derived by continuously replacing the meridian curve by a hypersphere segment in the vicinity of the apex [Fig. 6 (right)] [4, 73]. For the limit of an infinitely small hypersphere segment, a vanishing contribution of the apical singularity  $W_i'''$  to the total quermassintegral  $W_i$  results, regardless of the specific geometrical shape. Therefore, only  $(D-2)$ -dimensional singularities contribute to the quermassintegrals  $W_i$  with  $2 \leq i \leq D-1$  of convex, uniaxial solids of revolution, depending on their critical angles  $\vartheta_c$  which are compiled for the selected geometries of this work in Tab. 3.

Tab. 3: Critical angles  $\vartheta_c$  of  $D$ -dimensional, uniaxial solids of revolution with singularities in their surface curvatures contributing to  $W_i$ .

	Cylinder	Lens	Spherical segment	Doublecone Cone	Truncated cone
$\vartheta_c$	$\frac{\pi}{2}$	$\arccos\left(\frac{1-\nu^2}{1+\nu^2}\right)$	$\arccos\left(1 - \frac{h}{r_0}\right)$	$\arccos\left(\frac{1}{\sqrt{1+\nu^2}}\right)$	$\arccos\left(\frac{r_0-r_1}{\sqrt{h^2+(r_0-r_1)^2}}\right)$

For uniaxial solids of revolution with  $r(z_{\text{max}}) \neq 0$  or  $r(z_{\text{min}}) \neq 0$ , only half of the contribution using Eq. (59) has to be considered for a singularity in the surface curvature, while the other half of the contribution is replaced with half the contribution of a spherical hyperplate. Note, that for the contribution of the top singularity of a truncated hypercone the sign of the contribution

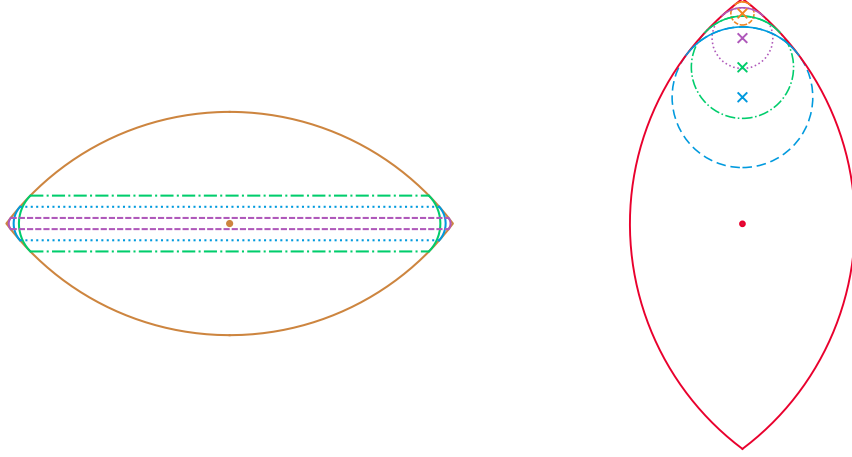


Fig. 6: Left: Continuous completion of a hyperlens by a hypertorus at the vicinity of the equator [4]. Right: Continuous completion of a hyperspindle by a hypersphere segment at the vicinity of the upper apex [4].

$W_i''$  has to be reversed or the critical angle  $\vartheta_c$  has to be adapted accordingly [4, 73]. With the derived expressions, all quermassintegrals for convex, uniaxial solids of revolution in  $\mathbb{R}^4$  can be obtained, including geometries with apical and equatorial singularities. Results can also be obtained for arbitrary dimensions with the general expressions for doublecones and cones given in Tab. A-2 (Appendix A). For the remaining geometries spindle, lens, spherical segment, and truncated cone, also expressions for arbitrary dimensions could be obtained while exemplarily the results for four-dimensional solids of revolution in  $\mathbb{R}^4$  are displayed in Tab. A-3 (Appendix A).

While the geometric measures for two- and three-dimensional spindles, lenses, spherical segments, doublecones, cones, and truncated cones have been previously reported in the literature [73], general expressions for the quermassintegrals of the four- and higher-dimensional analog geometries have not been provided in the literature before. For hyperspherical segments with  $h \leq r_0$ , concise formulas for volume  $V_P$  and lateral surface area  $S_P'$  are reported by Li [148], giving

$$W_0 = \frac{\kappa_D}{2} r_0^D I_{r_{\text{cap}}^2/r_0^2} \left( \frac{D+1}{2}, \frac{1}{2} \right), \quad (60a)$$

$$W_1 = \frac{\kappa_D}{2} r_0^{D-1} I_{r_{\text{cap}}^2/r_0^2} \left( \frac{D-1}{2}, \frac{1}{2} \right) + \frac{\kappa_{D-1}}{D} r_{\text{cap}}^{D-1} \quad (60b)$$

for opening angles  $\vartheta_c \leq \pi/2$  with  $I_x(a,b)$  being the regularized incomplete beta function. For hyperspherical segments with  $h > r_0$  and  $\vartheta_c \geq \pi/2$ , analogously

$$W_0 = \frac{\kappa_D}{2} r_0^D \left[ 2 - I_{r_{\text{cap}}^2/r_0^2} \left( \frac{D+1}{2}, \frac{1}{2} \right) \right], \quad (61a)$$

$$W_1 = \frac{\kappa_D}{2} r_0^{D-1} \left[ 2 - I_{r_{\text{cap}}^2/r_0^2} \left( \frac{D-1}{2}, \frac{1}{2} \right) \right] + \frac{\kappa_{D-1}}{D} r_{\text{cap}}^{D-1} \quad (61b)$$

can be obtained.

While for a convex, uniaxial solid of revolution its geometric measures are determined by its meridian curve, for an arbitrary convex polytope  $P$  its geometric measures are set on its  $k$ -faces  $F \in \mathcal{F}_k$  and its external angles. The intrinsic volumes  $V_i$  [Eq. (45)] of an arbitrary convex polytope  $P$  in  $\mathbb{R}^D$  can for  $i = 0, 1, \dots, D$  be written as

$$V_i(P) = \sum_{F \in \mathcal{F}_i(P)} \gamma(P, F) \mathcal{H}^i(F) \quad (62)$$

with  $\gamma(P, F)$  being the external angle of  $P$  at its face  $F$  and  $\mathcal{H}^i(F)$  the  $i$ -dimensional Hausdorff measure of the latter in  $\mathbb{R}^D$  [142]. For regular, convex polytopes, the external angles and Hausdorff measures are identical for all  $i$ -faces, thus the intrinsic volumes simplify to

$$V_i(P) = N_i(P) \gamma(P, F) \mathcal{H}^i(F) \quad (63)$$

with  $F$  being any  $i$ -face of  $P$ . Using Eq. (40) with  $F_{D-2}$  being a ridge  $F \in \mathcal{F}_{D-2}(P)$ , the second quermassintegral of a regular, convex polytope can be rewritten as

$$W_2(P) = \frac{\pi - \delta_P}{D(D-1)} N_{D-2}(P) V_P(F_{D-2}) \quad (64)$$

in dependence on the dihedral angle  $\delta_P$  and the  $(D-2)$ -dimensional volume of the ridges. Also, the quermassintegral  $W_{D-1}$  can be rewritten as

$$W_{D-1}(P) = \frac{\kappa_{D-1}}{D} N_1(P) \gamma(P, F_1) a \quad (65)$$

with  $F_1$  being an edge  $F \in \mathcal{F}_1(P)$  of length  $a$ .

Using Eq. (62), the geometric measures of any convex polytope can be obtained, where general results for the intrinsic volumes of regular simplices, cubes, and cross-polytopes are already reported in the literature [118, 141, 149, 150] and summarized in Tab. A-2 (Appendix A). For the remaining regular, convex polytopes in  $\mathbb{R}^D$  with  $D \leq 4$ , their intrinsic volumes or quermassintegrals have to be calculated individually. For regular polygons and polyhedra all geometric measures are already available [117], using Eqs. (62), (38), and (64) with the dihedral angle  $\delta_P$  given by Eq. (41). For regular, convex 4-polytopes, an analog expression of the dihedral angles can be obtained in dependence on the Schläfli symbols  $\{p, q, r\}$ , where

$$\delta_{\{p, q, r\}} = 2 \arcsin \left[ \frac{\cos\left(\frac{\pi}{r}\right) \sin\left(\frac{\pi}{p}\right)}{\sin\left(\frac{\pi}{h_{p, q}}\right)} \right] \quad (66)$$

with

$$h_{p, q} = \sqrt{4N_1(\{p, q\}) + 1} - 1 \quad (67)$$

results. Therewith,  $W_2$  of a regular, convex 4-polytope can be obtained using Eq. (64) and for

the calculation of  $W_3$ , Eq. (65) with the external angle

$$\gamma(P, F_1) = \frac{r}{2\pi} \arccos \left[ \frac{\cos\left(\frac{\pi}{q}\right)}{\sin\left(\frac{\pi}{p}\right)} \right] - \frac{r-2}{4} \quad (68)$$

for a regular, convex 4-polytope  $P$  with  $\{p, q, r\}$  can be used. Thus, all geometric measures for  $P \in \mathcal{P}^4$  can be obtained with the results for the remaining geometries summarized in Tab. A-3 (Appendix A).

### 3.1.3 Second virial coefficients for uniaxial solids of revolution

Using the Brunn-Minkowski theorem with the provided expressions for the quermassintegrals of uniaxial solids of revolution in dependence on their meridian curve  $r(z)$ , reduced second virial coefficients  $B_2^*$  can be calculated analytically in Euclidean spaces  $\mathbb{R}^D$ , allowing to compare the influence of the detailed particle shape on  $B_2^*$  among the dimensions of space. In Fig. 7,  $B_2^*$  is shown for hard particles with moderate anisotropy in  $\mathbb{R}^2$  and  $\mathbb{R}^4$ .

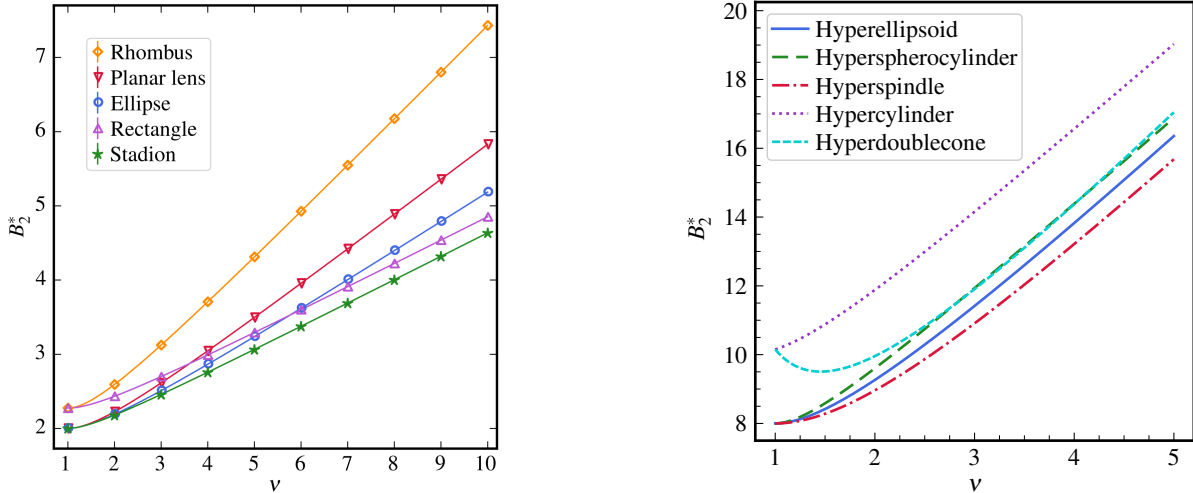


Fig. 7: Left: Reduced second virial coefficients  $B_2^*$  for anisotropic solids with aspect ratios  $\nu$  in  $\mathbb{R}^2$  [3]. Right: Reduced second virial coefficients  $B_2^*$  of prolate, uniaxial solids of revolution with inversion symmetry and aspect ratios  $\nu$  in  $\mathbb{R}^4$  [4].

As seen in Fig. 7,  $D$ -dimensional spherocylinders, ellipsoids, and spindles approach for  $\nu \rightarrow 1$  spheres with  $B_2^* = 2^{D-1}$ . Similar to solids of revolution in  $\mathbb{R}^3$  [73], with increasing aspect ratio  $\nu \gg 1$  the reduced second virial coefficient linearly depends on the aspect ratio with  $B_2^* \propto \nu$  [4]. For oblate, uniaxial solids of revolution, the inverse relation  $B_2^*(\nu \ll 1) \propto \nu^{-1}$  can be observed in  $\mathbb{R}^D$  where for  $\nu \rightarrow 0$  all uniaxial solids of revolution approach spherical hyperplates [4]. For high aspect ratios  $\nu \rightarrow \infty$ , as shown in Fig. 8 (left) for  $\mathbb{R}^4$ , all geometries approach hard needles where for spherocylinders and cylinders the smallest values for  $B_2^*$  out of the selected geometries result, with a vanishing contribution of the capping hyperspheres to  $B_2^*$  for spherocylinders. In addition, for aspect ratios  $\nu \rightarrow \infty$ , hyperdoublecones have the highest values for  $B_2^*$  out of the selected geometries in  $\mathbb{R}^2, \mathbb{R}^3, \mathbb{R}^4$ , whereas for planar spindles and spindles  $B_2^*$  is higher than for

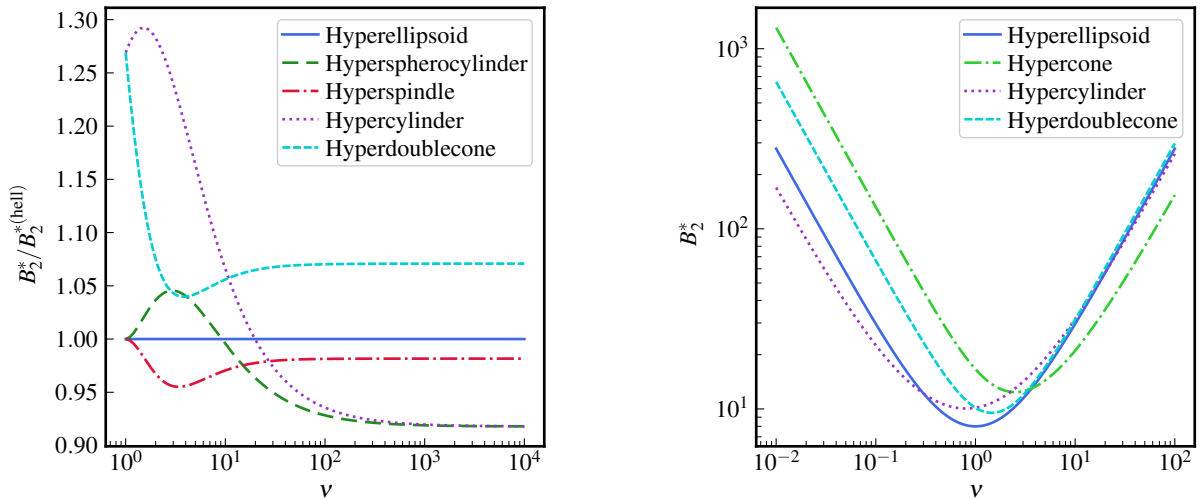


Fig. 8: Left: Reduced second virial coefficients  $B_2^*$  of prolate, uniaxial solids of revolution with aspect ratios  $\nu \geq 1$  in  $\mathbb{R}^4$ , normalized to corresponding values of uniaxial hyperellipsoids  $B_2^{*(\text{hell})}$  [4]. Right: Reduced second virial coefficients  $B_2^*$  of uniaxial solids of revolution defined for prolate and oblate aspect ratios  $\nu$  in  $\mathbb{R}^4$  [4].

ellipses and ellipsoids [3, 73] in  $\mathbb{R}^2$  and  $\mathbb{R}^3$ , but smaller for hyperspindles than for hyperellipsoids in  $\mathbb{R}^4$  [4]. Due to the additional symmetry of the solid,  $B_2^*$  becomes more similar for highly prolate, uniaxial solids of revolution with increasing dimensions of space. Conversely, for oblate geometries with  $\nu \rightarrow 0$ , larger differences for ratios of  $B_2^* \propto \nu^{-1}$  arise [4, 73]. In Fig. 8 (right) the reduced second virial coefficients for uniaxial solids of revolution defined for prolate and oblate aspect ratios  $\nu$  in  $\mathbb{R}^4$  are displayed.

For uniaxial hyperellipsoids of revolution, the parity  $B_2^*(\nu) = B_2^*(\nu^{-1})$  is observed in  $\mathbb{R}^4$  [4], as for spheroids in  $\mathbb{R}^3$  [73]. Using the Brunn-Minkowski theorem with the general quermassintegrals for this geometry, the parity is proven in this work for arbitrary-dimensional Euclidean spaces  $\mathbb{R}^D$  [4]. Also, for four-dimensional doublecones and cylinders with aspect ratio  $\nu = 1$ , the reduced second virial coefficients  $B_2^*$  are identical in  $\mathbb{R}^4$ . This can trivially be observed for the analog two-dimensional rhombi and rectangles in  $\mathbb{R}^2$  too, where for  $\nu \rightarrow 1$  both geometries approach hard squares [3]. This non-trivial identity is unique for the four-dimensional Euclidean space  $\mathbb{R}^4$ . The result for  $B_2^*$  of cylinders with  $\nu = 1$  exceeds the result for  $B_2^*$  of doublecones with  $\nu = 1$  in  $\mathbb{R}^3$ , whereas for higher dimensions  $D > 4$  the results for  $D$ -dimensional doublecones with  $\nu = 1$  exceed those of the corresponding cylinders. This is shown in Fig. 9 (left).

By carefully studying the general expression for the quermassintegrals  $W_i$  of  $D$ -dimensional spherocylinders in  $\mathbb{R}^D$  (Tab. A-2, Appendix A), the simplified expression

$$B_2^{*(\text{scyl})} = 2^{D-1} + 2^{D-3} \left( \frac{S_P \bar{R}_P}{V_P} - D \right) = 2^{D-1} \left[ 1 + \frac{D-1}{D} \frac{\kappa_{D-1}}{\kappa_D} \frac{(\nu-1)^2}{2(\nu-1) + \frac{\kappa_D}{\kappa_{D-1}}} \right] \quad (69)$$

for the reduced second virial coefficient of this geometry is obtained from the Brunn-Minkowski theorem in dependence on at most three of its proper  $D$  geometric measures for arbitrary-

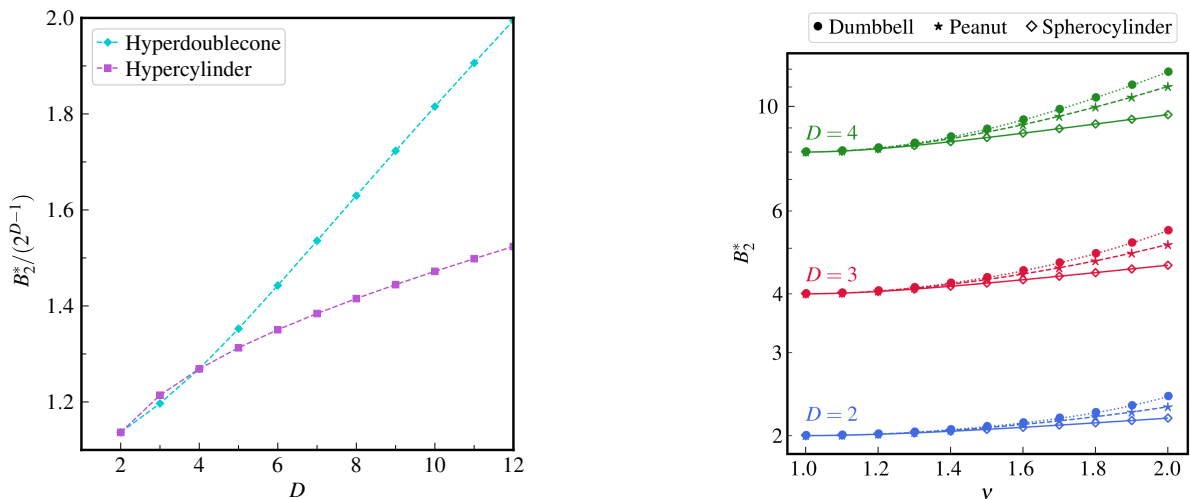


Fig. 9: Left: Reduced second virial coefficients  $B_2^*$  of  $D$ -dimensional doublecones and cylinders with aspect ratio  $\nu = 1$  in  $\mathbb{R}^D$  [4]. The dashed lines serve as a guide to the eye. Right: Reduced second virial coefficients  $B_2^*$  of  $D$ -dimensional homonuclear dumbbells, peanut-shaped particles and spherocylinders with aspect ratio  $\nu$  in  $\mathbb{R}^D$  [2].

dimensional Euclidean spaces with the respective aspect ratio  $\nu$  of the solid [4]. For the limit of hyperspheres with  $\nu \rightarrow 1$ , again, the commonly known result  $B_2^* = 2^{D-1}$  is obtained [Eq. (69)], while in the opposite limit of an infinitely long hyperspherocylinder

$$\lim_{\nu \rightarrow \infty} \frac{B_2^{*(\text{scyl})}}{\nu} = 2^D \frac{D-1}{8\sqrt{\pi}} \frac{\Gamma\left(\frac{D}{2}\right)}{\Gamma\left(\frac{D+1}{2}\right)} \quad (70)$$

results, with the proportionality  $B_2^* \propto \nu$  for highly anisotropic, prolate solids of revolution. Since for high aspect ratios the contribution of the hyperhemispherical parts of a hyperspherocylinder to  $B_2^*$  become negligible, this is the limit for hypercylinders, too.

While for convex solids analytical results for  $B_2$  can be obtained based on their quermass-integrals, no general analytical expressions are available for  $B_2$  of arbitrary concave solids. However, in  $\mathbb{R}^2$  for planar, homonuclear dumbbells [74], planar, heteronuclear dumbbells, and multimers of fused hard disks [75] and in  $\mathbb{R}^3$  for homonuclear dumbbells [76], explicit analytical results for  $B_2$  are reported in the literature. In this work, a corresponding expression for hyperdumbbells with  $1 \leq \nu \leq 2$  in  $\mathbb{R}^4$  is derived. For homonuclear hyperdumbbells in  $\mathbb{R}^4$  with volume

$$V_P^{(\text{hdb})} = \frac{\pi r_0^4}{6} \left[ 6 \arcsin(\nu - 1) + 3\pi + (-4\nu^3 + 12\nu^2 - 2\nu - 6) (2\nu - \nu^2)^{1/2} \right] \quad (71)$$

[Eq. (34)], the second virial coefficient  $B_2$  can be calculated by

$$B_2^{(\text{hdb})} = \frac{\pi^2}{4} \sigma_c^4 + 8 \int_{\sigma_c}^{2\nu r_0} r^3 \int_0^{\frac{\pi}{2}} \sin^2 \vartheta_r \int_0^{\frac{\pi}{2}} \sin^2 \vartheta_2 \int_0^\pi f(r, \vartheta_r, \vartheta_2, \chi_2) \sin \chi_2 d\chi_2 d\vartheta_2 d\vartheta_r dr, \quad (72)$$

with

$$\sigma_c = r_0(2 + 4\nu - 2\nu^2)^{1/2} \quad (73)$$

being the contact distance of the core where for any angular configuration at  $r < \sigma_c$  an overlap of two particles with corresponding contact function  $f(r, \vartheta_r, \vartheta_2, \chi_2) = 1$  results [2]. Here, the inner most integration can be performed using the critical cosines  $\cos \chi_{2,c}$  at the contact distances of the hyperdumbbells. The remaining integration has to be performed numerically, e.g., employing adaptive Gauss-Kronrod algorithms, resulting in highly accurate, semi-analytical values for the second virial coefficients of four-dimensional, homonuclear dumbbells.

Defining a  $D$ -dimensional, peanut-shaped particle with the meridian curve shown in Tab. A-1 (Appendix A), an additional concave solid of revolution with an overlap criterion identical to that of a homonuclear hyperdumbbell with the same radius and aspect ratio results. Thus, the second virial coefficients  $B_2(\nu)$  and reduced virial coefficients  $\tilde{B}_n(\nu) = B_n(\nu)/B_2^{n-1}(\nu)$  are identical for these particles whereas the reduced virial coefficients  $B_n^*(\nu)$  only differ by powers of the ratio of their respective volumes  $V_P$  [2]. The results for  $B_2^* = B_2/V_P$  of  $D$ -dimensional dumbbells and peanut-shaped particles in  $\mathbb{R}^D$  are shown in Fig. 9 (right), compared to the results for corresponding spherocylinders. As expected, with  $\nu \rightarrow 1$  being the limit of  $D$ -spheres,  $B_2^*$  increases with rising aspect ratio  $\nu$ , while for each  $\nu$  the reduced second virial coefficient  $B_2^*$  decreases for the particles with the increasing volume of the respective shape, as the geometries are encapsulated subsets.

### 3.1.4 Second virial coefficients for convex polytopes

With the provided analytical expressions for all quermassintegrals of all regular, convex  $D$ -polytopes  $P \in \mathcal{P}^D$ , their second virial coefficients can be obtained using the Brunn-Minkowski theorem. For the only regular 1-polytope, the line segment with Schläfli symbol  $\{\}$ ,  $B_2^*(\{\}) = 1$  results. For regular, convex polygons with Schläfli symbol  $\{p\}$ , the general expression

$$B_2^*(\{p\}) = 1 + \frac{p}{\pi \cot\left(\frac{\pi}{p}\right)}$$

can be obtained with  $\lim_{p \rightarrow \infty} B_2^*(\{p\}) = 2$  for hard disks. The values of  $B_2^*$  for regular  $p$ -gons with  $p \leq 11$  are summarized in Tab. A-9 (Appendix B). As expected,  $B_2^*$  decreases with increasing number of edges of the polygon. Due to the Alexandrov-Fenchel inequality [142], the reduced second virial coefficient for any convex body  $K$  is  $B_2^*(K) \geq 2^{D-1}$  with equality only for the limit of a  $D$ -dimensional sphere.

Similarly,  $B_2^*$  can be calculated for all five regular, convex polyhedra with the results provided in Tab. A-9, too. The reduced second virial coefficient  $B_2^*$  can be used to quantify the sphericity of an arbitrary solid. As seen, not the number of vertices, but the number of facets determines how spherical a regular, convex polyhedron is. These results can also be compared to  $B_2^*$  of the remaining four isotoxal (edge-transitive) polyhedra: Cuboctahedron, rhombic dodecahedron, icosidodecahedron, and rhombic triacontahedron. For each of these, the dihedral angles are

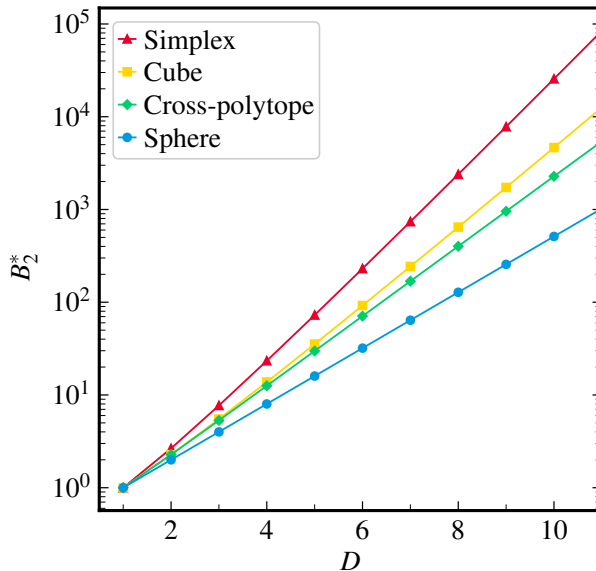


Fig. 10: Reduced second virial coefficients  $B_2^*$  of hyperspheres and the three regular, convex polytopes in arbitrary-dimensional Euclidean spaces  $\mathbb{R}^D$  for  $D \leq 11$ . The solid lines serve as guide to the eye.

identical for all edges. Thus, their geometric measures can be calculated, using Eqs. (62) and (40) with their reduced second virial coefficients summarized in Tab. A-9 (Appendix B). The obtained values for  $B_2^*$  of the quasi-regular polyhedra and their dual geometries are significantly smaller than the results of the platonic solids they are based on, due to the increasing sphericity of each solid.

Next,  $B_2^*$  is calculated for the six regular, convex polychora  $P \in \mathcal{P}^4$  (Tab. A-9, Appendix B), where so far unknown results for the 24-cell, 120-cell, and 600-cell are obtained. Again,  $B_2^*$  decreases with increasing number of facets for a regular, convex polychoron. Extending the calculations to arbitrary higher-dimensional Euclidean spaces  $\mathbb{R}^D$  with  $D > 4$ , the results for the three existing regular, convex  $D$ -polytopes are displayed in Fig. 10 and compared to  $D$ -spheres. Note, that the values printed in [118] for simplices and cross-polytopes with  $D \geq 3$  are flawed due to typos in the formulas for their quermassintegrals  $W_i$ . For the correct expressions see [141, 149, 150] or Tab. A-2 (Appendix A). As seen in Fig. 10, the sphericity of a regular, convex polytope increases with the number of facets and not with the number of vertices in arbitrary-dimensional Euclidean spaces  $\mathbb{R}^D$ .

Generalizing the geometry of a  $D$ -dimensional cube by elongating the length of an axis  $a$  by the ratio  $\nu$ , a  $D$ -dimensional squared rectangular cuboid (quadratic pillar) with  $V_P = \nu a^D$  and all axes being perpendicular towards each other results. Its general quermassintegrals  $W_i$  are provided in the literature [118] and can be rewritten by the expression displayed in Tab. A-2 (Appendix A). While for the limit  $\nu \rightarrow 1$  a hypercube results, a quadratic hyperplate can be obtained for  $\nu \rightarrow 0$ . Using this expression for  $W_i$ , the general parity  $B_2^*(\nu) = B_2^*(\nu^{-1})$  results for this geometry in arbitrary dimensions  $D$ , too, similar to uniaxial hyperellipsoids of revolution. E.g., for the squared rectangular cuboid in  $\mathbb{R}^3$ , the reduced second virial coefficient

can be written as

$$B_2^{*(\text{qp})} = \frac{7}{2} + \nu + \frac{1}{\nu} \quad (74)$$

with  $\lim_{\nu \rightarrow \infty} [B_2^{*(\text{qp})}/\nu] = \lim_{\nu \rightarrow 0} [\nu B_2^{*(\text{qp})}] = 1$  for infinitely long and short aspect ratios.

## 3.2 Numerical calculation of virial coefficients for hard particles

### 3.2.1 Algorithms for overlap detection of anisotropic solids

For the numerical calculation of virial coefficients by means of Monte Carlo integration, a reliable algorithm for the contact detection of the respective particle geometries at any possible particle configuration in  $\mathbb{R}^D$  is required. For hard,  $D$ -dimensional spheres and fusions of them, e.g., homonuclear dumbbells [2], this is straightforward by using the center-to-center distances for all pairs of spheres. Thus, for geometries without a simple mathematical overlap detection procedure, these shapes are out of necessity often approximated by combinations of fused hard spheres [151]. Also, for peanut-shaped particles, the same algorithm as for homonuclear dumbbells with identical size and aspect ratio can be used [2].

For hyperspherocylinders, the contact detection can in general be reduced to the determination of the shortest distance between two one-dimensional rods in  $\mathbb{R}^D$  [1, 152]. If this minimum distance is less than the sum of the radii of the respective spherocylinders, the latter overlap, otherwise they do not.

For general ellipsoids (and thus also spheroids) in  $\mathbb{R}^3$ , the well established Perram-Wertheim algorithm can be employed for an overlap detection [153]. While in general algorithms for  $\mathbb{R}^3$  can be applied to their analog geometries in  $\mathbb{R}^2$  by restricting the positions and orientations of the particles into a fixed plane, the overlap algorithm for ellipsoids can be generalized to hyperellipsoids in  $\mathbb{R}^D$ , too [3, 154, 155]. Here, a hyperellipsoid is defined by its shape matrix and the configuration of two hyperellipsoids by a polynomial function  $f(\lambda)$  with  $0 \leq \lambda \leq 1$ . If  $\exists : f(\lambda) \leq 0$ , the two hyperellipsoids do not overlap, otherwise they do.

For convex polytopes, the hyperplane separation theorem (or its generalization the Hahn-Banach separation theorem) can be used to detect overlaps in arbitrary space dimensions [156]. In general, two non-overlapping convex solids in  $\mathbb{R}^D$  are separated by hyperplanes. For convex polytopes the detection of a possible hyperplane of separation simplifies, as at least one facet of a polytope has to be in such a hyperplane [3, 157]. For concave geometries, other overlap algorithms are required, often using shape approximations or (triangular) tessellations [157].

The adaptation of overlap algorithms for other anisotropic particle geometries from  $\mathbb{R}^3$  to higher-dimensional spaces is usually more complicated. For lenses in  $\mathbb{R}^3$ , with a lens defined by the section of two spheres with identical radius giving a circular equatorial singularity (Fig. 3), overlap routines are already reported in the literature [58, 158]. Therefore, three possible types of overlap configurations have to be detected: sphere-sphere, sphere-circle, and circle-circle overlaps. While sphere-sphere and sphere-circle overlaps can straightforwardly be extended to hyperlenses in higher dimensions, the overlap detection between two circular disks in  $\mathbb{R}^3$  [159] is

already surprisingly complex. An extension to spherical plates in higher dimensions is possible, but relies at the state of this work on respectively highly computationally demanding, numerical minimization routines of non-injective functions with multiple parameters.

Besides lenses, overlap algorithms for other geometries in  $\mathbb{R}^3$ , e.g., cylinders [19, 160] or spindles, can be developed. Particularly interesting is the reported contact detection for superellipsoids [161–163]. With this type of geometry a variety of convex shapes can be formed and analyzed, including doublecones, cylinders, cuboids, and square bipyramids.

### 3.2.2 Implementation of the numerical Monte Carlo integration

In this work, virial coefficients are calculated up to the eighth order for hard particles of various geometries in the two-, three-, and four-dimensional Euclidean space, using Mayer-sampling Monte Carlo simulations. For the calculations of the second virial coefficients, hard,  $D$ -dimensional spheres with  $B_2^* = 2^{D-1}$  [Eq. (19)] are used as a reference system. For convex solids, the obtained numerical results are compared with available analytical expressions, serving as a validation for the used simulation technique. For concave geometries without analytical results for  $B_2$  (hyperdumbbells [2]), the results of the respective Monte Carlo simulations are compared and validated with values obtained by numerical Gauss-Kronrod integration. The reduced second virial coefficient of a many-particle system with a respective particle geometry is then used as an intrinsic reference to calculate the higher-ordered virial coefficients  $B_3$  up to  $B_8$  for this geometry. Therefore,  $n$  spanning trees with  $n - 1$  leaves and one node of degree  $n - 1$  are used for the reference system [Eq. (24), Fig. 2].

For the numerical calculation of  $B_2$  up to  $B_6$ , a simulation with a total of 16 parallel runs, each with  $5 \times 10^{10}$  steps with a previous equilibration phase of  $10^7$  steps, is typically used. With the latter an acceptance rate for each step is set to  $\approx 50\%$ . To obtain  $B_7$  and  $B_8$  for hard solids in  $\mathbb{R}^4$  and hard, homonuclear dumbbells in  $\mathbb{R}^D$ , the number of steps is increased to  $4 \times 10^{11}$  to reduce the uncertainties of the results while for the remaining systems again  $5 \times 10^{10}$  steps are used. The uncertainty of the results is the standard error based on the deviation between the 16 independent runs. To calculate  $B_n$ , in each step of a Monte Carlo simulation  $n$  particles are randomly translated and rotated in  $\mathbb{R}^D$ . The center and the orientation of the first particle define the origin and the direction of the coordinate system. For the translation and rotation, polar coordinates are used with the corresponding angular coordinates  $\varphi$ ,  $\vartheta$ , and  $\chi$  [Eqs. (25) and (28)], where each angular coordinate  $\phi_{D-i}$  [Eq. (26)] has to be randomly generated, weighted by  $\sin^{i-1}(\phi_{D-i})$  [1].

### 3.2.3 Anisotropic particles in two-dimensional space

Firstly, the influence of the detailed particle geometry on higher-ordered virial coefficients  $B_n^*$  with  $n > 2$  is investigated in  $\mathbb{R}^2$ . Therefore, based on statistical mechanics or scaled particle theory (SPT) respectively, a characteristic shape parameter  $\alpha$  can be defined as the normalized

mutual excess excluded volume per particle [116, 164], which can be written as

$$\alpha = \frac{B_2 - V_P}{(2^{D-1} - 1)V_P} = \frac{B_2^* - 1}{2^{D-1} - 1} \quad (75)$$

for arbitrary anisotropic particles and space dimensions in general [2]. In  $\mathbb{R}^2$ , less particle geometries have been investigated in respect to their virial coefficients compared to anisotropic particles in  $\mathbb{R}^3$ . Only for fused disks, stadia, ellipses, and rectangles some virial coefficients are available in the literature, limited up to order  $n \leq 5$  [111–115].

As part of this work, virial coefficients up to  $B_8^*$  of planar, homonuclear dumbbells, stadia, ellipses, planar spindles (lenses), rectangles, and rhombi with various aspect ratios  $\nu$  are provided [2, 3], summarized in Tabs. A-11 to A-17 in Appendix C. Therefore, Mayer-sampling Monte Carlo simulations have been employed, starting with the numerical calculation of  $B_2^*$  based on the developed overlap algorithms. The obtained numerical results are, within the uncertainty, in perfect agreement with the analytically known results [2, 3], exemplarily shown for planar dumbbells in Fig. 11 (left), validating the employed simulation technique.

The virial coefficients of orders  $n > 3$  can then efficiently be calculated using  $B_2^*$  of the respective geometry as an intrinsic reference, resulting in highly accurate values in agreement with numerical results using  $B_n^*$  of hard disks as a reference. Resulting reduced virial coefficients  $\tilde{B}_n = B_n/B_2^{n-1}$  of planar dumbbells, stadia, and ellipses are exemplarily shown in Figs. 11 (right) and 12. Overall, the obtained numerical results are all in agreement with previously reported results from the literature. In addition to more accurate results for the virial coefficients up to the fifth order, new virial coefficients are derived systematically up to  $B_8^*$ , including planar spindles and rhombi as two geometries that have not specifically been investigated before. Note, that planar spindles and lenses in  $\mathbb{R}^2$  are identical geometries whereas for higher dimensions  $D > 2$  different geometries result, based on their defined meridian curves [Tab. A-1, Appendix A].

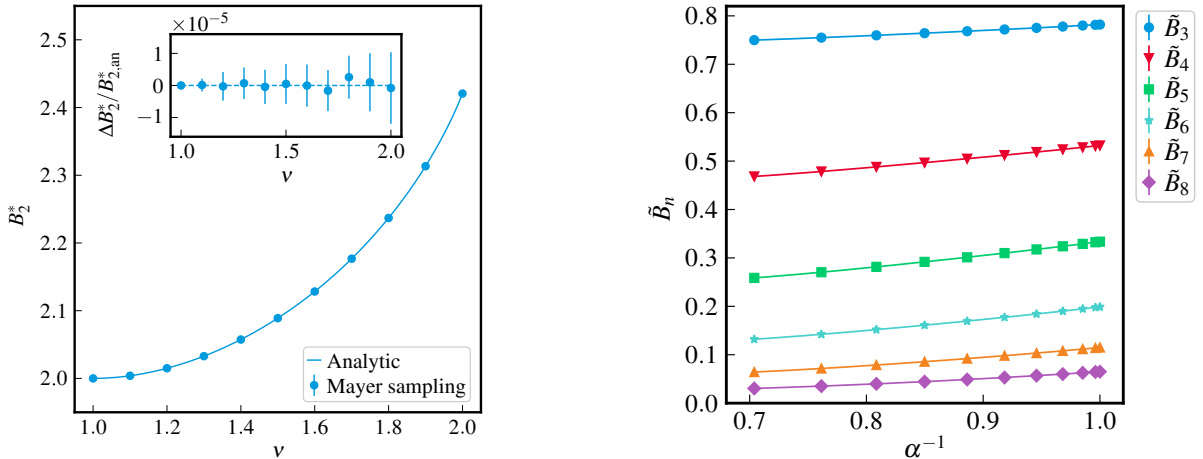


Fig. 11: Left: Reduced second virial coefficients  $B_2^*$  of planar dumbbells in dependence on the aspect ratio  $\nu$  with deviations  $\Delta B_2^*$  to the analytical result  $B_{2,an}^*$  [2]. Right: Reduced virial coefficients  $\tilde{B}_n = B_n/B_2^{n-1}$  of planar dumbbells in dependence on the inverse of the shape parameter  $\alpha^{-1}$  [2].

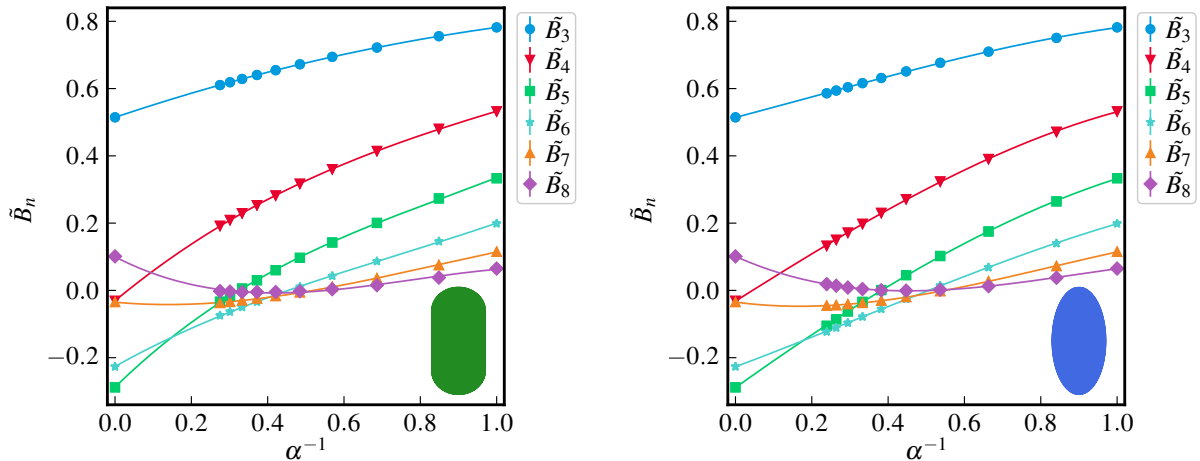


Fig. 12: Reduced virial coefficients  $\tilde{B}_n$  of hard stadia (left) and ellipses (right) in dependence on the inverse of the shape parameter  $\alpha^{-1}$  [3].

For aspect ratios  $\nu \rightarrow 1$ , planar dumbbells, stadia, ellipses, and planar spindles approach hard disks with  $\alpha = 1$  for which virial coefficients up to  $B_{14}^*$  are available [Tabs. A-4 and A-10 (Appendix)]. Rectangles and rhombi result in hard squares with identical  $B_n^*$  instead. While homonuclear dumbbells are by the definition of the geometry restricted to aspect ratios  $1 \leq \nu \leq 2$ , the other investigated geometries approach for  $\nu \rightarrow \infty$  hard needles. These can also be redefined as infinitely thin hard rods of unit length, resulting in the analog geometry of a spherical plate in  $\mathbb{R}^3$  for the two-dimensional Euclidean space. For this geometry, also an analytical expression for  $\tilde{B}_3$  is available in the literature [113] with a slight but significant deviation from the obtained numerical results of this work [3]. The latter still agree with previous numerical results taken from [115], whereas older data reported in [110,112] is already discussed in the literature to be insufficient [113,115].

By considering reduced virial coefficients  $\tilde{B}_n$  in dependence on the inverse of the shape parameter  $\alpha^{-1}$  as shown in Figs. 11 (right) and 12, a qualitatively identical dependence irrespective of the general particle geometry can be observed [3]. Therefore, the data can sufficiently be interpolated by low order polynomials. For planar dumbbells, even a nearly linear dependence can be observed. By that, virial coefficients up to  $B_8^*$  are available for arbitrary aspect ratios for each investigated geometry, covering the limits of isotropic disks up to infinitely thin needles.

### 3.2.4 Anisotropic particles in three-dimensional space

Oppositely to  $\mathbb{R}^2$ , in  $\mathbb{R}^3$  various particle geometries have previously been investigated regarding their virial coefficients [58, 103, 104, 106]. To extend these calculations to unknown virial coefficients of analog geometries in higher-dimensional spaces, already known results are revisited, performing recalculations for selected geometries and aspect ratios. Here, the focus is not to provide virial coefficients for geometries where already respectively high-accurate virial coefficients are available, but to implement and validate overlap-algorithms for arbitrary dimensions of space in an adaptable MSMC simulation. This further allows the calculation of so

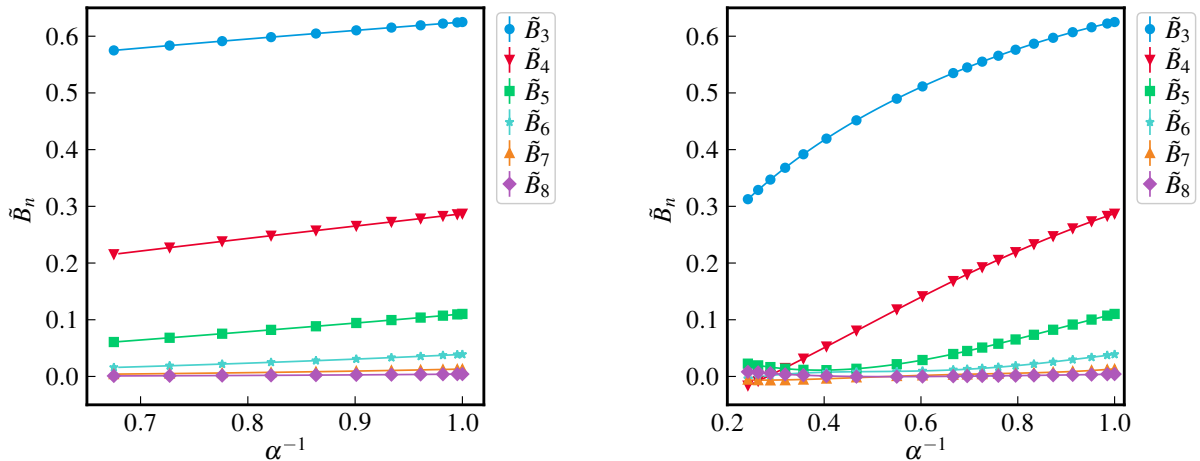


Fig. 13: Reduced virial coefficients  $\tilde{B}_n$  of hard, homonuclear dumbbells (left) and hard spherocylinders (right) in dependence on the inverse of the shape parameter  $\alpha^{-1}$  [2, 104].

far unknown virial coefficients for other geometries with given overlap algorithms in  $\mathbb{R}^3$ , i.e., spindles, cylinders, and doublecones.

In addition to their analog geometries in  $\mathbb{R}^2$  and  $\mathbb{R}^4$ , the virial coefficients of hard, homonuclear dumbbells, spherocylinders, and ellipsoids of revolution are recalculated up to  $B_8^*$ . The results are displayed in Figs. 13 and 14 with numerical data summarized in Tabs. A-18 to A-21 (Appendix C). For comparison, additional data of these and other selected geometries available in the literature are summarized in Tabs. A-18 to A-25, too.

As shown in Figs. 13 (left) and 14 (right), a nearly linear dependence of the reduced virial coefficients  $\tilde{B}_n = B_n/B_2^{n-1}$  on the inverse of the shape parameter  $\alpha^{-1}$  [Eq. (75)] is observed for dumbbells and oblate spheroids [2, 58]. For prolate geometries, i.e., spherocylinders and spheroids with  $\nu > 1$ , a significant non-linearity exist [Figs. 13 (right) and 14 (left)]. However, all data can be interpolated by low order polynomials. While the results agree with previous values provided in the literature [48, 103, 104], the obtained results for prolate spheroids are slightly more accurate compared to the values reported in the literature [103]. Furthermore, new results for  $B_8$  are obtained, providing more reliable values compared to the marginally flawed results from [84] (see [92]). For oblate spheroids with  $\nu = 4/5$ , an erroneous value for  $\tilde{B}_8$  in [58] can be identified. For the remaining geometries, the results from the literature [48, 104] have similar or higher accuracy. For dumbbells and spherocylinders,  $B_9^*$  is reported for various aspect ratios  $\nu$  in [104], too. To accumulate results with smaller uncertainties, the number of steps in each MC simulation could be increased, but since already highly accurate results are available in the literature, this is beyond the scope of this work.

Regarding highly oblate solids of revolution with  $\nu \rightarrow 0$ , spherical plates result with their respective virial coefficients summarized in Tab. A-25 (Appendix C). For these, as generally for highly oblate solids of revolution in  $\mathbb{R}^3$ , positive fourth and negative fifth virial coefficients are obtained [57]. Conversely, highly prolate solids of revolution generally have negative fourth and positive fifth virial coefficients in  $\mathbb{R}^3$ . Comparing this with the corresponding geometries of high anisotropy in  $\mathbb{R}^2$  with positive fourth and negative fifth virial coefficients, the latter

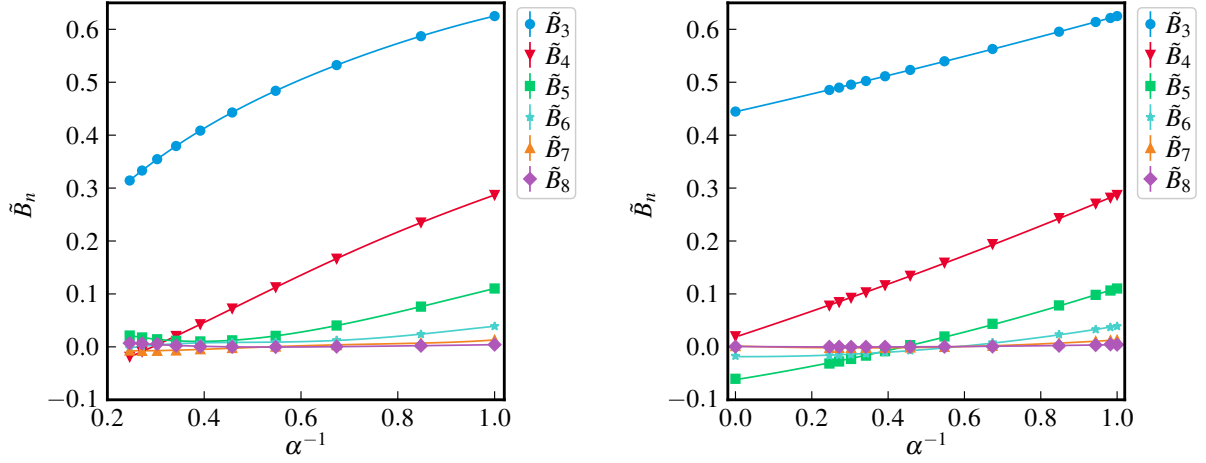


Fig. 14: Reduced virial coefficients  $\tilde{B}_n$  of prolate ellipsoids of revolution (left) and oblate ellipsoids of revolution (right) in dependence on the inverse of the shape parameter  $\alpha^{-1}$ .

behave similarly to oblate solids in  $\mathbb{R}^3$  due to similar orientational degrees of freedom. For virial coefficients with higher orders ( $n > 5$ ), more negative values are obtained for highly oblate solids compared to highly prolate solids in  $\mathbb{R}^3$ .

### 3.2.5 Anisotropic particles in four-dimensional space

As part of this work, for the first time numerical virial coefficients are provided for anisotropic particles in a higher-dimensional space. Therefore, virial coefficients up to the eighth order of hard, homonuclear hyperdumbbells, hyperspherocylinders, and uniaxial hyperellipsoids are calculated with the results summarized in Tabs. A-26 to A-29 (Appendix C) and displayed in Figs. 15 and 16 as reduced virial coefficients  $\tilde{B}_n = B_n/B_2^{n-1}$  in dependence on the inverse of the shape parameter  $\alpha^{-1}$  [Eq. (75)] [1, 2].

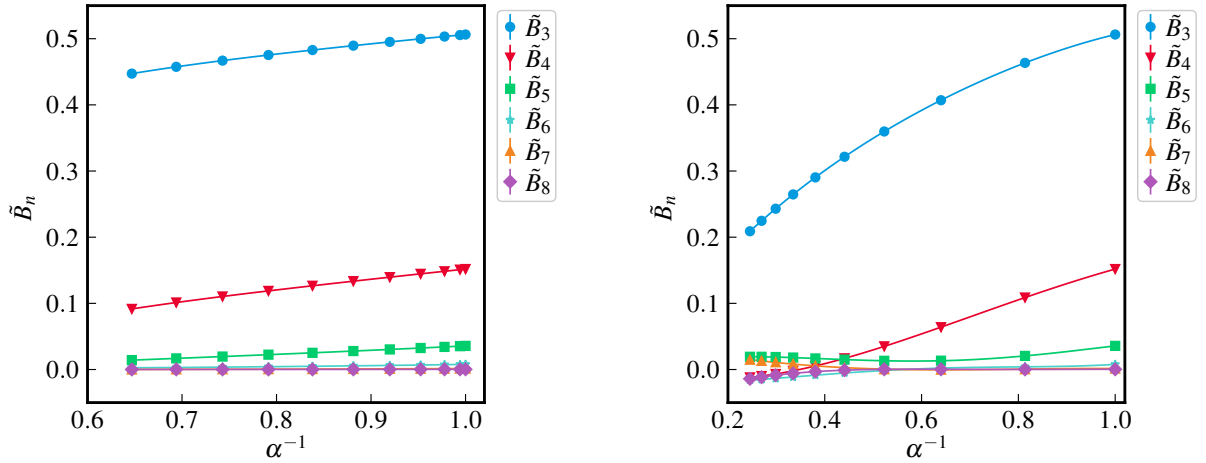


Fig. 15: Reduced virial coefficients  $\tilde{B}_n$  of homonuclear hyperdumbbells (left) and hyperspherocylinders (right) in dependence on the inverse of the shape parameter  $\alpha^{-1}$  [1, 2].

For hyperdumbbells, similar to planar dumbbells in  $\mathbb{R}^2$  and dumbbells in  $\mathbb{R}^3$ , a nearly linear dependence for  $\tilde{B}_n$  on  $\alpha^{-1}$  can be observed [Fig. 15 (left)]. Conversely to the analog geometries

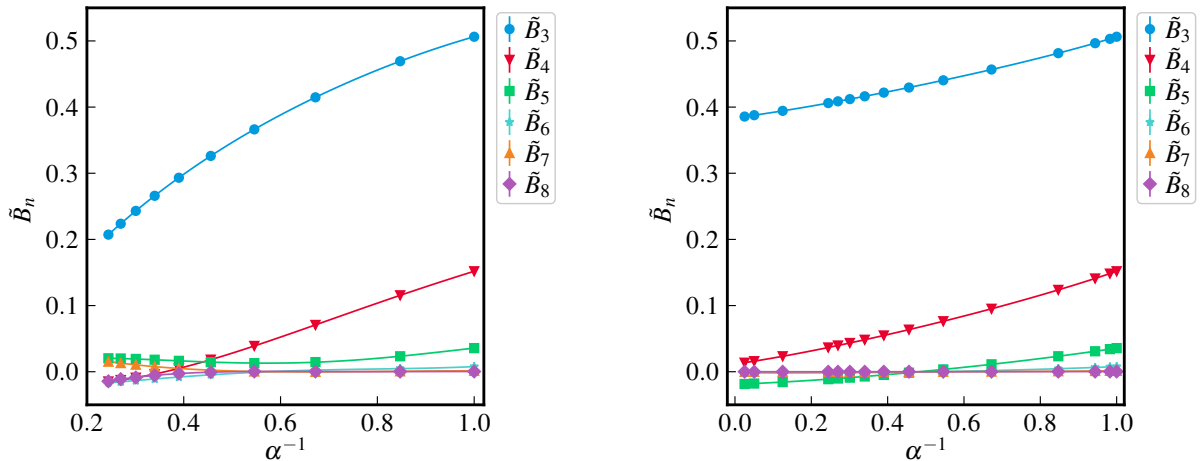


Fig. 16: Reduced virial coefficients  $\tilde{B}_n$  of prolate, uniaxial hyperellipsoids (left) and oblate, uniaxial hyperellipsoids (right) in dependence on the inverse of the shape parameter  $\alpha^{-1}$ .

in  $\mathbb{R}^3$ , for oblate, uniaxial hyperellipsoids a non-linear dependence results in  $\mathbb{R}^4$  [Fig. 16 (right)]. Also, for uniaxial hyperspherocylinders and prolate hyperellipsoids a non-linear dependence can be observed, too. However, all data can still adequately be interpolated by low-order polynomials. Here, for hyperspherocylinders and hyperellipsoids the employed overlap-algorithms are validated by the computation of second virial coefficients with available exact expressions from the Brunn-Minkowski theorem [1, 4], whereas for hyperdumbbells the results for  $B_2^*$  are in agreement with the semi-analytical expressions [2].

For aspect ratios  $\nu \rightarrow 1$ , all of these geometries approach hyperspheres with virial coefficients in accordance to available results [10]. Uniaxial hyperellipsoids with  $\nu \rightarrow 0$  additionally approach spherical hyperplates in the highly anisotropic, oblate limit. For this geometry, no established overlap algorithm is available so far. Thus, no numerical virial coefficients have been provided, leaving only the results of oblate, uniaxial hyperellipsoids with  $\nu \rightarrow 0$  as an indication of the approximate results. With a given efficient algorithm for the overlap detection of spherical hyperplates, the numerical calculation of virial coefficients of hyperlenses would also be straightforward, analogously to lenses in  $\mathbb{R}^3$  [58]. For highly anisotropic, oblate geometries in  $\mathbb{R}^4$ , the fourth virial coefficient is positive while the fifth is negative [Tab. A-29, Appendix C]. This is identical to highly anisotropic, oblate solids of revolution in  $\mathbb{R}^3$  [Tabs. A-21 and A-22, Appendix C]. Oppositely, again identical to analog geometries in  $\mathbb{R}^3$ ,  $B_4^*$  is negative and  $B_5^*$  is positive for uniaxial, prolate geometries with high aspect ratios [Tabs. A-27 and A-28, Appendix C].

For uniaxial, prolate solids with sufficiently high aspect ratios  $\nu \gg 1$  in  $\mathbb{R}^4$ , the provided virial coefficients of odd order are positive and of even order are negative in general. This is similar to the sign of virial coefficients for hyperspheres in high space dimensions [10]. There, the ring diagram with  $n$  nodes dominates the contribution to  $B_n$  with increasing dimension of space [165]. Also, for hyperspheres and anisotropic particles, the absolute value of each reduced virial coefficient  $\tilde{B}_n$  at first decreases with increasing dimension  $D$  and order  $n$  for particles

with analog geometries and aspect ratios [2]. For hyperspheres, reduced virial coefficients  $\tilde{B}_n$  of very high order start to increase again for sufficiently low dimensions of space [10]. Similar to hyperspheres [165], also for anisotropic particles in sufficiently high space dimensions a negligible contribution of high-order virial coefficients to the virial equation of state can be predicted. Vice versa, in  $\mathbb{R}^2$  and  $\mathbb{R}^3$ , higher-ordered virial coefficients significantly contribute to the virial equation of state.

### 3.3 Equation-of-state data and phase behavior

With a finite number of available virial coefficients for a given many-particle system in  $\mathbb{R}^D$ , a truncated virial series [Eq. (3)]

$$Z \approx 1 + \sum_{n=2}^{n_{\max}} B_n^* \eta^{n-1} \quad (76)$$

results for the thermodynamic description of its isotropic phase, considering particle interactions through reduced virial coefficients  $B_n^*$  up to the highest known order  $n_{\max}$ . The accuracy of this equation of state can be evaluated by comparing the results with available numerical data. The obtained compressibility factor  $Z$  in dependence on the volume fraction  $\eta$  is exemplarily shown for ellipses in  $\mathbb{R}^2$  and prolate ellipsoids of revolution in  $\mathbb{R}^3$  in Fig. 17.

With an increasing number of consecutively known, highly accurate virial coefficients the compressibility factor can usually be described more adequately for increasing volume fractions. However, depending on the geometry of the particles, truncation effects of the virial series arise for sufficiently high volume fractions  $\eta < \eta_c$  before an isotropic phase transition at a critical volume fraction  $\eta_c$ . For ellipses and ellipsoids with available phase diagrams [15, 16, 35, 47], similar to other geometries, an isotropic fluid - plastic crystal phase transition is observed for small aspect ratios at higher volume fractions, whereas for moderately and highly anisotropic particles an isotropic-nematic phase transition occurs at smaller volume fractions. Thus, for near-spherical particles more higher-order virial coefficients are required for an adequate thermodynamic description of the isotropic phase at high volume fractions.

For highly anisotropic particles, the isotropic phase is limited to smaller volume fractions instead. Thus, less virial coefficients should be required for an adequate thermodynamic description. However, their obtained virial coefficients are usually less accurate and truncation effects have a bigger impact on the equation-of-state data. Since negative virial coefficients appear at lower orders  $n$  with increasing anisotropy, positive higher-ordered virial coefficients are required to compensate their contributions, otherwise resulting in possibly even nonphysical negative compressibility factors [3, 48]. E.g., for ellipsoids with  $\nu = 10$  (Fig. 17) the negative seventh virial coefficient is overcompensated by a high positive eighth virial coefficient. Here, additional virial coefficients and a reduced uncertainty for the result of  $B_8^*$  are required to decrease these truncation effects on the virial series. For prolate ellipsoids with sufficiently high aspect ratios  $\nu$  in  $\mathbb{R}^3$ ,  $B_9^*$  can be predicted to be negative, similar to spherocylinders [104].

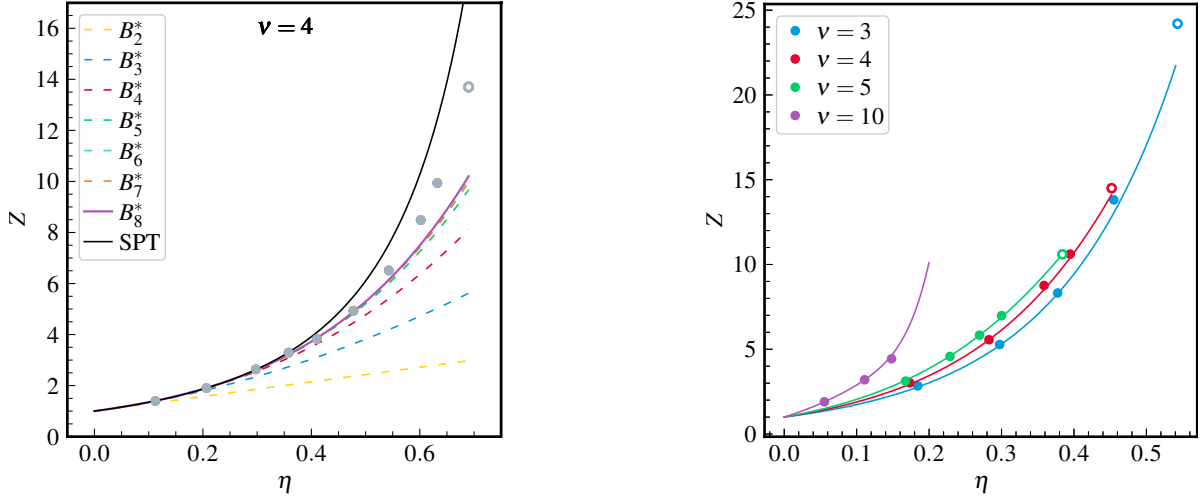


Fig. 17: Isotropic equation-of-state data of ellipses in  $\mathbb{R}^2$  [3] (left) and spheroids in  $\mathbb{R}^3$  (right). The colored lines are from the VEOS [Eq. (76)], considering the sum of virial coefficients up to  $B_n^*$  displayed in the legend (left) and up to  $B_8^*$  (right). The black line results from Eq. (77). Numerical results are taken from [35, 47, 112] and [15, 16, 57] with open circles approximating the point of the isotropic-nematic phase transition.

Furthermore, the virial equation of state can generally also be compared to other provided equations of state. E.g., using scaled particle theory (SPT), Boublík derived

$$Z = \frac{1}{1 - \eta} + \frac{\alpha\eta [1 + \alpha(\eta/7 - \eta^2/14)]}{(1 - \eta)^2} \quad (77)$$

with  $\alpha = B_2^* - 1$  [Eq. (75)] as an approximation for arbitrary convex solids in  $\mathbb{R}^2$  [166]. As seen in Fig. 17 (left), SPT also predicts fairly accurate compressibility factors for small volume fractions, but remains only a useful first order approach in general [115, 151]. Instead, the virial series provides reliable results if enough virial coefficients are known.

To compensate truncation effects, various corrections to the VEOS are available, too [48]. For hyperspheres, unknown virial coefficients of order  $n > n_{\max}$  can be approximated by the Carnahan-Starling method [12], resulting in a closed expression for its equation of state as reported up to  $D = 9$  [167]. For anisotropic particles, a rescaled Carnahan-Starling approach can be used, considering all known virial coefficients and rescaling the remaining to the (approximated) values for hyperspheres [57]. While this is useful for moderately anisotropic particles, a modified Carnahan-Starling equation with correction parameters obtained by least-squares fits of numerical data is more adequate for highly anisotropic particles [48]. If only  $B_2^*$ ,  $B_3^*$ , and  $B_4^*$  are known, the equation of state by Song and Mason for convex solids in arbitrary dimensions of space should be considered, too [168]. For additional data and discussions regarding the equations of state for ellipses and ellipsoids, see [3, 46, 48, 103, 166, 169–171]. In higher-dimensional spaces, the critical volume fraction for an isotropic phase transition, i.e., freezing, starts to decrease, as shown for hyperspheres [172]. Thus, truncation effects of the virial equation of state should have less impact on an adequate description of the isotropic phase in higher dimensions, allowing for the determination of convergence criteria.

## 4 Summary and Outlook

In this work, virial coefficients of various hard, anisometric particles are calculated up to the eighth order in two-, three-, and four-dimensional Euclidean spaces. Previously unknown virial coefficients of planar dumbbells, stadia, ellipses, rectangles, planar spindles (lenses), and rhombi are reported for various aspect ratios in  $\mathbb{R}^2$  [2, 3]. Furthermore, first numerical calculations of virial coefficients for anisotropic particles in Euclidean spaces  $D > 3$ , i.e., uniaxial hyperdumbbells, hyperspherocylinders, and hyperellipsoids are implemented, employing Mayer-sampling Monte Carlo simulations [1, 2]. For the second virial coefficients of arbitrary convex solids, the Brunn-Minkowski theorem employing quermassintegrals provides access to explicit analytical expressions depending on the geometric measures of the particles through excluded volume effects. General and explicit expressions for the quermassintegrals of uniaxial solids of revolution with apical and equatorial singularities in their surface curvature are provided [4], extending the recent variety of anisotropic particle models in arbitrary-dimensional spaces [118]. For higher space dimensions, the influence of the specific particle geometry on the virial coefficients and geometric measures is studied in detail for  $\mathbb{R}^4$ , providing procedures for a straightforward extension to arbitrary higher-dimensional Euclidean spaces. As an extra, for regular, convex polytopes a list of all quermassintegrals for arbitrary-dimensional Euclidean spaces  $\mathbb{R}^D$  is provided, completed by studying the 24-cell, 120-cell, and 600-cell in  $\mathbb{R}^4$ . Also, an expression for the dihedral angles of 4-polytopes in dependence on the Schläfli-symbol  $\{p, q, r\}$  is given. For the study of convex polytopes as an additional part of this work, the mutual scientific exchange with Professor Achill Schürmann and Valentin Dannenberg is especially acknowledged.

For  $D$ -dimensional, uniaxial spherocylinders, a reformulation of the excluded volume by a reduced second virial coefficient  $B_2^*$  depending on at most three geometric measures, volume  $V_P$ , total surface area  $S_P$ , and mean radius of curvature  $\bar{R}_P$ , is obtained and proven for aspect ratios  $\nu \geq 1$ , including the limit of hard needles [Eq. (69)] [4]. Also, the parity  $B_2^*(\nu) = B_2^*(\nu^{-1})$  is proven for uniaxial,  $D$ -dimensional ellipsoids in arbitrary-dimensional Euclidean spaces  $\mathbb{R}^D$  [4]. By additionally studying convex polytopes, the identical parity is obtained for  $D$ -dimensional squared rectangular cuboids, too.

With obtained analytical and semi-analytical expressions for  $B_2^*$  of all investigated particle geometries, higher-order virial coefficients  $B_n^*$  with  $n > 3$  are accessible by Monte Carlo simulations, employing an optimized version of Mayer sampling for hard, anisotropic particles [58]. In addition, algorithms for the contact detection of hard particles in  $\mathbb{R}^D$  can be validated by comparing the numerical and analytical results for  $B_2^*$ . Using reduced virial coefficients  $\tilde{B}_n = B_n/B_2^{n-1}$  and the normalized mutual excess excluded volume per particle  $\alpha$  [Eq. (75)], depending on  $B_2$  for arbitrary dimensions of space [2], a nearly linear dependence of  $\tilde{B}_n$  on the inverse of the shape parameter  $\alpha^{-1}$  is observed for two-, three-, and four-dimensional dumbbells [2]. This is similar to previous results of oblate ellipsoids and lenses in  $\mathbb{R}^3$  [58]. For the remaining geometries, i.e., solids with aspect ratios  $\nu \gg 1$  and uniaxial, oblate hyperellipsoids in  $\mathbb{R}^4$ , a non-linear dependence is observed instead. However, all data can adequately be in-

terpolated heuristically by low-order polynomials [1–3]. Thus, a respectively accurate virial equation of state for sufficiently small volume fractions  $\eta$  results. At high volume fractions in the isotropic phase, truncation effects of the VEOS arise due to a limited number of known virial coefficients and an increasing uncertainty for virial coefficients of higher-order. Therefore, more and accurate higher-order virial coefficients are required for a given particle geometry. Complementarily, the phase behavior should be studied, identifying isotropic phase transitions.

Further insights into the detailed influence of the particle geometry on the virial coefficients can be expected upon studying other shapes, e.g., convex spherical caps [173] or concave particles. For the latter, an interest for self-assembling phenomena and packings of such colloids arose recently [174]. For these systems, generally less virial coefficients are known so far, since their second virial coefficients are not analytically known in general and are thus not available for validating overlap algorithms and Monte Carlo simulations to obtain higher-ordered virial coefficients. Furthermore, virial coefficients of biaxial convex particles could be studied, where a more complex phase behavior is observed, including additional phases [175,176]. Also, in  $\mathbb{R}^4$  beside uniaxial solids of revolution, virial coefficients of other geometries are accessible. Here, hyperellipsoids with axes of different lengths, e.g.,  $r$ ,  $r$ ,  $\nu r$ , and  $\nu r$  can be studied with overlap detection algorithms already being available [154]. Therefore, a uniform random rotation of the particles with multiple orientation vectors is required. In addition, accurate closed expressions for the virial equation of state of anisotropic particles are required, avoiding the approximation of higher-order virial coefficients to values of corresponding hyperspheres, especially for highly anisotropic particles.

Finally, beside the virial equation of state for the thermodynamic description of the isotropic phase, the isotropic-nematic phase transition and the nematic phase can be investigated further for selected particle geometries. Here, nematic virial coefficients of uniaxial solids of revolution, e.g., of ellipsoids [46], provide further insights into the self-organization of anisotropic colloids and can be compared to calculations of the free energy and the chemical potential in dependence on the order parameter.

## 5 Publications

In this section, the four scientific papers [1–4] published as part of this work are shown, all full articles as first-author. For each publication, all authors are listed with their respective contributions according to Contributor Roles Taxonomy (CRediT) and approximated in percent. Additionally, my respective approximated contributions in percent are summarized in Tab. 4.

Tab. 4: Overview of publications resulting as part of this work with own contributions approximated in percent.

No.	Publication	Contribution
I	M. Kulossa, P. Marienhagen, J. Wagner, Virial coefficients of hard hyperspherocylinders in $\mathbb{R}^4$ : Influence of the aspect ratio, <i>Phys. Rev. E</i> <b>105</b> , 064121 (2022).	50 %
II	M. Kulossa, D. Weidig, J. Wagner, Virial coefficients of hard, homonuclear dumbbells in two- to four-dimensional Euclidean spaces, <i>Phys. Rev. E</i> <b>107</b> , 024129 (2023).	50 %
III	M. Kulossa, J. Wagner, Virial coefficients of hard, two-dimensional, convex particles up to the eighth order, <i>Mol. Phys.</i> <b>122</b> , e2289699 (2023).	80 %
IV	M. Kulossa, J. Wagner, Geometric measures of uniaxial solids of revolution in higher-dimensional Euclidean spaces and their relation to the second virial coefficient, <i>Phys. Rev. E</i> <b>111</b> , 024112 (2025).	70 %



## 5.1 Publication I - Virial coefficients of hard hyperspherocylinders in $\mathbb{R}^4$ : Influence of the aspect ratio

M. Kulossa, P. Marienhagen, J. Wagner, *Phys. Rev. E* **105**, 064121 (2022).

DOI: 10.1103/PhysRevE.105.064121

Type: Full article

© 2022 American Physical Society

### Author contributions

**Markus Kulossa:** Conceptualization, Data curation, Formal analysis, Investigation, Methodology, Software, Validation, Visualization, Writing - original draft preparation, Writing - review and editing

Estimated total contribution in percent: 50 %

**Philipp Marienhagen:** Conceptualization, Formal analysis, Investigation, Methodology, Validation, Writing - review and editing

Estimated total contribution in percent: 30 %




**Joachim Wagner:** Conceptualization, Methodology, Project administration, Resources, Supervision, Writing - review and editing

Estimated total contribution in percent: 20 %

Reprinted article with permission from M. Kulossa, P. Marienhagen, J. Wagner, *Phys. Rev. E* **105**, 064121 (2022). Copyright (2022) by the American Physical Society.



## Virial coefficients of hard hyperspherocylinders in $\mathbb{R}^4$ : Influence of the aspect ratio

Markus Kulossa , Philipp Marienhagen , and Joachim Wagner <sup>\*</sup>

*Institut für Chemie, Universität Rostock, 18051 Rostock, Germany*



(Received 25 February 2022; accepted 23 May 2022; published 21 June 2022)

We provide second- to sixth-order virial coefficients of hard hyperspherocylinders in dependence on their aspect ratio  $\nu$ . Virial coefficients of an anisotropic geometry in four dimensions are calculated employing an optimized Mayer-sampling algorithm. As the second virial coefficient of a hard particle is identical to its excluded hypervolume, the numerically obtained second virial coefficients can be compared to analytical relations for the excluded hypervolume based on geometric measures of the respective, convex geometry in dependence on its aspect ratio  $\nu$ .

DOI: [10.1103/PhysRevE.105.064121](https://doi.org/10.1103/PhysRevE.105.064121)

### I. INTRODUCTION

Hard particles have been investigated thoroughly as a model for many-particle systems for more than a century. These studies have significantly contributed to the understanding of self-organization in condensed matter [1]. The virial series introduced by Kamerlingh Onnes [2],

$$p = \rho k_B T (1 + B_2 \rho + B_3 \rho^2 + \dots), \quad (1)$$

where  $p$  denotes the pressure,  $k_B T$  the thermal energy, and  $\rho$  the particle number density, is the first attempt to describe thermodynamic properties of imperfect gases. The coefficients  $B_i$  in the MacLaurin expansion in number density accounting for the nonideal behavior are the virial coefficients. Introducing the volume fraction  $\eta = \rho V_P$  as the product of number density  $\rho$  and particle volume  $V_P$ , with

$$p = \frac{\eta}{V_P} k_B T (1 + B_2^* \eta + B_3^* \eta^2 + \dots), \quad (2)$$

an expansion in terms of the volume fraction  $\eta$  results, where  $B_i^* = B_i/V_P^{i-1}$  are reduced virial coefficients.

The first attempts to calculate virial coefficients use hard spheres as a model system with its geometric constraint of impenetrability [3–6]. The seminal work of Onsager with the analytically treatable model of infinitely thin rods predicted the formation of liquid-crystalline structures beyond a critical volume fraction [7]. Based on the theoretical foundation by means of statistical mechanics [8], with emerging computer performance, virial coefficients of order  $5 \leq i \leq 12$  of hard spheres have been computed [9–15]. These methods have been extended to virial coefficients of anisometric hard bodies with different topology and aspect ratio [16–24].

Virial coefficients of hard discs as two-dimensional analogs of hard spheres have been theoretically [25,26] and numerically [27] calculated. For orders  $i > 5$ , in most cases, these virial coefficients were calculated together with those of hard spheres [10–12,28]. With these data, first insights into the

dimensionality's influence to the nonideal behavior of gases and supercritical fluids with impacts on the maximum packing fraction have been possible [29].

The extension of the hard-sphere model system to Euclidean spaces with dimensionality  $D > 3$ , already published by Ree and Hoover [30], does not only provide useful physical insights [31], but also has implications to information theory [32]. Virial coefficients of hard spheres in higher dimensions interestingly become negative for even orders  $i$  in dimensions  $D \geq 5$  [33]. For hard hyperspheres, selected virial coefficients up to order  $i = 64$  and up to dimension  $D = 100$  are known [28]. Virial coefficients of anisometric, hard objects in dimensions  $D > 3$ , however, are so far unknown.

The aim of this contribution is the calculation of uniaxial, hard hyperspherocylinders' virial coefficients for dimension  $D = 4$  in dependence on their aspect ratio  $\nu$ . Since the second virial coefficient of hard, convex objects equals the mutual excluded volume, its relation to geometric measures is analyzed in dependence on the aspect ratio  $\nu$ . Herewith, expressions for a four-dimensional analog of the Isihara-Hadwiger relation [34–36] can be tested.

### II. THEORETICAL BACKGROUND

Using the Ree-Hoover reformulation, the virial coefficient of order  $i$  can be written as

$$B_i = -\frac{i-1}{i!} \sum_{G \in \mathcal{R}_i^L} c_G S_G, \quad (3)$$

where  $\mathcal{R}_i^L$  is the set of labeled Ree-Hoover graphs  $G$  with  $i$  vertices and weighting factors  $c_G$ , called Ree-Hoover star contents, depending on the graph's topology.  $S_G$  is the configuration integral over interactions represented by the labeled graph  $G$ . Since in the case of hard-body interaction a single Ree-Hoover diagram contributes to the integrand, the calculation based on the Mayer-sampling method [37] can be done employing an optimized algorithm with a bisection search in an ordered list containing all labeled diagrams with their star contents [23]. Mayer sampling as an importance sampling

<sup>\*</sup>joachim.wagner@uni-rostock.de

technique requires the simultaneous calculation of a known reference integral. For the calculation of the second virial coefficients the analytically known second virial coefficient of hard hyperspheres is used as a reference for small aspect ratios  $\nu \leq 5$ . To increase the accuracy for aspect ratios  $\nu \geq 6$ , as a reference, the virial coefficient of hard hyperspherocylinders with aspect ratio  $\nu = 5$  obtained with hard hyperspheres as a reference is used. To minimize the total uncertainties for  $\nu \geq 6$ , this reference value is extensively sampled to reduce the uncertainty of this numerically obtained reference integral. For virial coefficients with order  $i \geq 3$ , however, integrals of highly branched spanning trees containing  $i$  vertices, each with the value  $(-2B_2)^{i-1}$ , are the more efficient choice as an intrinsic reference integral [23].

### A. Geometric measures of hyperspherocylinders in $\mathbb{R}^4$

A hyperspherocylinder is the union of hyperspheres with radius  $r_{\text{eq}}$  the centers of which are located at  $\mathbf{r} = \mathbf{c} + \lambda \hat{\mathbf{u}}$ , where  $\mathbf{c} = (c_w, c_x, c_y, c_z)^T$  is the hyperspherocylinder's center of mass and  $\hat{\mathbf{u}} = (u_w, u_x, u_y, u_z)^T$  its direction indicated by a Cartesian unit vector. The parameter  $-(\nu - 1)r_{\text{eq}} \leq \lambda \leq (\nu - 1)r_{\text{eq}}$  defines the length of the hypercylinder barrel and is related to the hyperspherocylinder's equatorial radius  $r_{\text{eq}}$  and its aspect ratio  $\nu \geq 1$ . The hypervolume  $V$  of a hyperspherocylinder with equatorial radius  $r_{\text{eq}}$  and aspect ratio  $\nu$  reads as

$$V = \frac{16(\nu - 1) + 3\pi}{6} \pi r_{\text{eq}}^4, \quad (4)$$

and its hypersurface  $S$  can be written as

$$S = 2\pi [4(\nu - 1) + \pi] r_{\text{eq}}^3. \quad (5)$$

Its mean radius of curvature  $\tilde{R}$  is accessible as the hypersurface integral of its mean curvature  $\kappa$  [38,39]. Since the latter quantity is  $\kappa = 1/(3r_{\text{eq}}^2)$  in the hypercylindrical part with length  $2(\nu - 1)r_{\text{eq}}$ ,  $1/r_{\text{eq}}^2$  in both hemihyperspheres, and the curvature is continuous at the entire hypersurface, a hyperspherocylinder's mean radius of curvature  $\tilde{R}$  reads as

$$\tilde{R} = \left[ \frac{4(\nu - 1)}{3\pi} + 1 \right] r_{\text{eq}}. \quad (6)$$

### B. Overlap criteria for hyperspherocylinders

Let  $\mathbf{c}_1$  and  $\mathbf{c}_2$  be two hyperspherocylinders' centers of mass,  $\hat{\mathbf{u}}_1$  and  $\hat{\mathbf{u}}_2$  unit vectors describing their orientation,  $r_{\text{eq}}$  their equatorial radius, and  $\nu$  their aspect ratio. The overlap problem of hard hyperspherocylinders in  $\mathbb{R}^4$  can be solved by determination of the minimum distance between the two lines  $\mathbf{r}_1(\lambda) = \mathbf{c}_1 + \lambda \hat{\mathbf{u}}_1$  and  $\mathbf{r}_2(\mu) = \mathbf{c}_2 + \mu \hat{\mathbf{u}}_2$  under the constraints  $|\lambda| \leq (\nu - 1)r_{\text{eq}}$  and  $|\mu| \leq (\nu - 1)r_{\text{eq}}$  in analogy to the overlap problem in  $\mathbb{R}^3$  [40]. If the minimum distance is  $|\mathbf{r}_1(\lambda_{\text{min}}) - \mathbf{r}_2(\mu_{\text{min}})| \leq 2r_{\text{eq}}$ , both hyperspherocylinders overlap, otherwise not. This overlap criterion can easily be extended to arbitrary dimensions  $D$ .

### C. Simulation details

The calculation of the  $i$ th virial coefficient of an uniaxial solid of revolution in  $\mathbb{R}^4$  requires an integration over a  $7(i - 1)$ -dimensional configuration space which can be per-

formed efficiently using a Mayer-sampling algorithm [37] extended to the four-dimensional space. In the case of hard-body systems, the originally proposed acceptance criterion has to be adapted by using a weighted sum of the integrands of both the system of interest and the reference system [23]. The algorithm is based on random translation and rotation attempts of randomly selected particles.

Let  $\boldsymbol{\Omega} = (\vartheta, \chi, \varphi)$  be the angular coordinates of a random unit vector in  $\mathbb{R}^4$  with the probability densities  $p(\vartheta) = 2 \sin^2 \vartheta / \pi$ ,  $p(\chi) = \sin \chi / 2$ , and  $p(\varphi) = 1/(2\pi)$  in  $0 \leq \vartheta \leq \pi$ ,  $0 \leq \chi \leq \pi$ , and  $0 \leq \varphi \leq 2\pi$ . With the abbreviations  $a = \cos \vartheta$ ,  $b = \sin \vartheta \cos \chi$ ,  $c = \sin \vartheta \sin \chi \sin \varphi$ , and  $d = \sin \vartheta \sin \chi \cos \varphi$ , a randomly oriented unit vector  $\hat{\mathbf{u}} = (-d, -c, -b, a)^T$  is generated. A random translation of a particle is achieved by choosing its center-of-mass position  $\mathbf{c}_{N+1}$  at step  $N + 1$  relative to its previous position  $\mathbf{c}_N$ :

$$\mathbf{c}_{N+1} = \mathbf{c}_N + \Delta_{\text{trans}} \xi \hat{\mathbf{u}}, \quad (7)$$

where  $0 \leq \xi \leq 1$  is a uniformly distributed random number. The maximum length of displacement  $\Delta_{\text{trans}}$  is tuned to obtain an acceptance ratio of  $p_{\text{acc}} \approx 1/2$ .

Using again random angular coordinates  $\boldsymbol{\Omega}$ , a left isoclinic rotation matrix in  $\mathbb{R}^4$  can be written as

$$\mathbf{R}(\boldsymbol{\Omega}) = \begin{pmatrix} a & -b & c & -d \\ b & a & -d & -c \\ -c & d & a & -b \\ d & c & b & a \end{pmatrix} \quad (8)$$

based on the Hamilton quaternion [41]. Additionally employing a rotation matrix

$$\begin{aligned} \boldsymbol{\Psi}(\psi) &= \mathbf{R}(\psi, 0, 0) \\ &= \begin{pmatrix} \cos \psi & -\sin \psi & 0 & 0 \\ \sin \psi & \cos \psi & 0 & 0 \\ 0 & 0 & \cos \psi & -\sin \psi \\ 0 & 0 & \sin \psi & \cos \psi \end{pmatrix}, \end{aligned} \quad (9)$$

a randomly rotated unit vector  $\hat{\mathbf{u}}_{N+1}$  can be obtained from the orientation of a given particle  $\hat{\mathbf{u}}_N$  at step  $N$  by

$$\hat{\mathbf{u}}_{N+1} = \mathbf{R}(\boldsymbol{\Omega}) \cdot \boldsymbol{\Psi}(\psi) \cdot \mathbf{R}^T(\boldsymbol{\Omega}) \cdot \hat{\mathbf{u}}_N. \quad (10)$$

Choosing  $\psi$  with  $-\Delta_{\text{rot}} \leq \psi \leq \Delta_{\text{rot}}$  as a random number with probability density  $p(\psi) = 1/(2\Delta_{\text{rot}})$  allows an exploration of the rotational configuration space with uniform density at the unit hypersphere's hypersurface as shown in the Appendix complemented by a detailed description of the rotation. The maximum rotation  $\Delta_{\text{rot}}$  is again chosen to obtain an acceptance probability of  $p_{\text{acc}} \approx 1/2$ .

The calculation of virial coefficients with known overlaps and nonoverlaps is independent of the systems' dimensionality and thus identical to the strategy in  $\mathbb{R}^2$  and  $\mathbb{R}^3$  as described in [23]: After translation and rotation of a selected particle  $i(i - 1)/2$  Mayer  $f$  functions  $f_{jk}$  are calculated based on overlaps and nonoverlaps between particles  $j$  and  $k$  of the obtained configuration, where, in the case of an overlap between particles  $j$  and  $k$ ,  $f_{jk} = -1$  is obtained and otherwise  $f_{jk} = 0$  results. Defining additionally  $e_{jk} = f_{jk} + 1$ , the contribution of the generated configuration to the virial coefficient [Eq. (3)] is a product of  $f$  and  $e$  functions of the single contributing graph  $G$  weighted by its star content  $c_G$  [10].

TABLE I. Reduced virial coefficient  $B_i^*$  of hard, four-dimensional hyperspherocylinders with the aspect ratio  $\nu$ .

$\nu$	$B_2^*$	$B_3^*$	$B_4^*$	$B_5^*$	$B_6^*$
1		32.4061 (19)	77.743 (9)	146.23 (6)	253.2 (8)
	8	32.405759... <sup>a</sup>	77.745183... <sup>a</sup>	146.2451 (5) <sup>a</sup>	253.388 (6) <sup>a</sup>
2	9.6026 (4)	42.7361 (20)	96.325 (14)	174.58 (16)	340 (4)
3	11.9340 (6)	57.9720 (29)	108.70 (4)	270.5 (5)	444 (19)
4	14.3853 (7)	74.454 (9)	104.28 (5)	564.3 (13)	-850 (40)
5	16.87831 (21)	91.606 (11)	81.18 (7)	1213.2 (22)	-7000 (130)
6	19.3904 (11)	109.188 (21)	39.09 (14)	2363 (7)	-23500 (400)
7	21.9132 (13)	127.076 (25)	-21.31 (16)	4161 (12)	-57500 (600)
8	24.4416 (16)	145.19 (4)	-99.59 (24)	6723 (27)	-119000 (1100)
9	26.9744 (11)	163.52 (5)	-194.71 (24)	10180 (40)	-215600 (1900)
10	29.5108 (17)	182.00 (9)	-306.7 (6)	14581 (30)	-360000 (4000)

<sup>a</sup>Value from [28].

For the calculation of virial coefficients of order 2–6 at least 16 independent runs, each with  $5 \times 10^{10}$  Monte Carlo steps, are used. The data provided are averages with confidence intervals given by standard errors.

### III. RESULTS AND DISCUSSION

The calculated virial coefficients of hard hyperspherocylinders with aspect ratios  $1 \leq \nu \leq 10$  from order 2–6 are compiled in Table I. The literature values for hard hyperspheres' virial coefficients are in the limit  $\nu \rightarrow 1^+$  reproduced within their uncertainties for the orders  $3 \leq i \leq 6$ . Since the scope of this paper is an aspect-ratio dependent approach covering orientation averages of anisotropic particles, the numerical effort is drastically increased. The larger uncertainties compared to hard hyperspheres' virial coefficients in [28] are therefore not a principal limitation of the used algorithm, but a consequence of the significantly enlarged computational demands.

#### A. Second virial coefficient and excluded hypervolume

Using the geometric measures of hypersurface  $S$ , mean radius of curvature  $\bar{R}$ , and particle hypervolume  $V_p$ , the relation

$$B_2^* = 1 + \frac{7 S \bar{R}}{4 V_p} \quad (11)$$

was proposed for convex geometries as the excluded hypervolume per particle in  $\mathbb{R}^4$  [38], which is in the case of hard-body interaction identical to the second virial coefficient. While this relation is valid for a hypersphere in the limit  $\nu \rightarrow 1^+$ , for larger aspect ratios severe discrepancies to second virial coefficients calculated by means of Mayer sampling arise (Fig. 1). However, the relation

$$B_2^* = 2 \frac{S \bar{R}}{V_p} = \frac{8 [4(\nu - 1) + 3\pi][4(\nu - 1) + \pi]}{16(\nu - 1) + 3\pi} \quad (12)$$

describes the reduced second virial coefficients for  $1 \leq \nu \leq 10$  with high accuracy.

Recently, the same authors corrected their conjecture (11) using mixed volumes and quermassintegrals [42]. For a convex set  $K$ , the excluded hypervolume per particle  $v_{\text{ex}}$  and thus the second virial coefficient can in the four-dimensional space

be written as

$$B_2 = v_{\text{ex}} = \frac{1}{2\kappa_4} \sum_{i=0}^4 \binom{4}{i} W_i(K) W_{4-i}(K), \quad (13)$$

where  $\kappa_4 = \pi^2/2$  is the hypervolume of the unit hypersphere in  $\mathbb{R}^4$  and  $W_i(K)$  are quermassintegrals of  $K$ . With the latter quantities,  $B_2$  can be written as

$$B_2 = \frac{2}{\pi^2} [W_0(K)W_4(K) + 4W_1(K)W_3(K) + 3W_2^2(K)]. \quad (14)$$

$W_0(K) = V_p^{(D)}(K)$  is the  $D$ -dimensional hypervolume of a convex shape,  $W_1(K) = S^{(D-1)}(K)/D$  its  $(D-1)$ -dimensional hypersurface,  $W_{D-1}(K) = \kappa_D \bar{R}$  its mean radius of curvature  $\bar{R}$  multiplied by the hypervolume  $\kappa_D$  of a  $D$ -dimensional unit

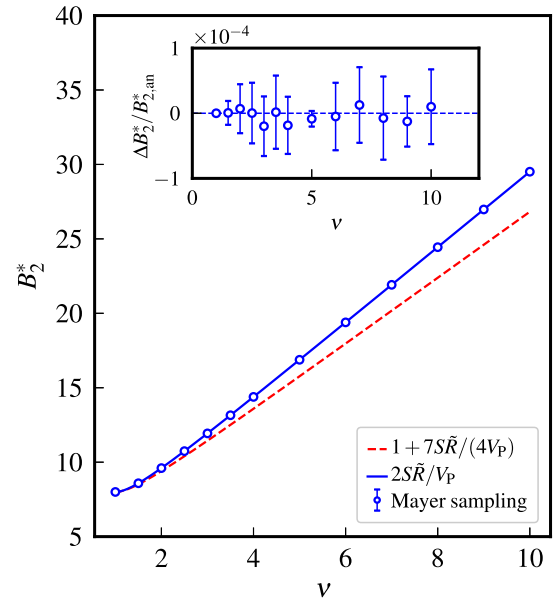


FIG. 1. Reduced second virial coefficients  $B_2^* = B_2/V_p$  for hard, four-dimensional hyperspherocylinders in dependence on the aspect ratio  $\nu$ . The dashed red line represents relation Eq. (11), while the blue solid line represents Eq. (12). The inset displays the relative deviations  $\Delta B_2^* = B_2^* - B_{2,\text{an}}^*$  between numerically calculated, reduced second virial coefficients  $B_2^*$  and analytically calculated  $B_{2,\text{an}}^*$  employing Eq. (12).

hypersphere, and finally  $W_D(\mathbf{K}) = \kappa_D$  the hypervolume of the  $D$ -dimensional unit hypersphere. Using these quantities,  $B_2$  of a convex shape in  $\mathbb{R}^4$  can be expressed as

$$B_2 = V_P^{(4)}(\mathbf{K}) + S^{(3)}(\mathbf{K})\tilde{R}(\mathbf{K}) + \frac{6}{\pi^2}W_2^2(\mathbf{K}) \quad (15)$$

with the missing quermassintegral

$$W_2 = \frac{\pi^2}{2}r_{\text{eq}}^2 + \frac{4\pi}{3}(\nu - 1)r_{\text{eq}}^2 \quad (16)$$

of a hyperspherocylinder in  $\mathbb{R}^4$  [43,44]. As easily can be seen, this leads to  $V_P + 6W_2^2/\pi^2 = S\tilde{R}$  and results in the analytical expression  $B_2 = 2S\tilde{R}$  and therewith  $B_2^* = 2S\tilde{R}/V_P$ . The relation  $V_P + 6W_2^2/\pi^2 = S\tilde{R}$  is to our knowledge unique for hyperspherocylinders in  $\mathbb{R}^4$ .

In the limit of infinitely long hyperspherocylinders, Eq. (12) leads to

$$\lim_{\nu \rightarrow \infty} \frac{B_2^*(\nu)}{\nu} = \frac{8}{\pi} \quad (17)$$

indicating an excluded hypervolume proportional to the aspect ratio  $\nu$ .

In the two-dimensional Euclidean space with the figure's area  $A_F$ , the circumference  $S$ , and the mean radius of curvature  $\tilde{R} = S/(2\pi)$ , the reduced second virial coefficient can be written as  $B_2^* = 1 + S\tilde{R}/(2A_F) = 1 + S^2/(4\pi A_F)$  [45]. In the three-dimensional Euclidean space, the relation  $B_2^* = 1 + S\tilde{R}/V_P$  is obtained with the surface  $S$ , the mean radius of curvature  $\tilde{R}$ , and the particle volume  $V_P$  [34–36].

Despite that the hypervolume in Eq. (12) is not an additive contribution to the excluded hypervolume, the formulation based on quermassintegrals [Eq. (15)] shows that the hypervolume in fact contributes to the mutual excluded hypervolume. In analogy to the excluded volume in the two- and three-dimensional space, also in four- and higher-dimensional Euclidean spaces, the  $D$ -dimensional hypervolumes are additive contributions to the mutual excluded hypervolume.

### B. Higher-order virial coefficients

The excellent agreement of our numerical results for the second virial coefficients with the analytical result [Eq. (12)] proves the correctness of the Mayer-sampling algorithm and the overlap criterion in  $\mathbb{R}^4$ . The third- to sixth-order virial coefficients in Table I are calculated using this analytical result as an exact reference integral. Noticeably, the higher-order virial coefficients exhibit alternating signs between even and odd orders at large aspect ratios: The even-order virial coefficients  $B_4^*$  and  $B_6^*$  are negative and strongly decrease with increasing aspect ratio  $\nu$ , while the odd-order virial coefficients  $B_3^*$  and  $B_5^*$  are positive and notably increase with the aspect ratio  $\nu$ . This behavior is also known for hyperspheres in dimensions  $D \geq 8$  for third- and higher-order virial coefficients [28].

For convex figures in two dimensions and for oblate geometries in three dimensions, a nearly linear dependence of reduced virial coefficients  $\tilde{B}_i = B_i/B_2^{i-1}$  on the inverse excess part of the excluded volume  $\alpha$  appears especially for lower-order virial coefficients [23,46]. Employing Eq. (12), in four dimensions  $\alpha = (B_2 - V_P)/(7V_P) = (2S\tilde{R}/V_P - 1)/7$  results,

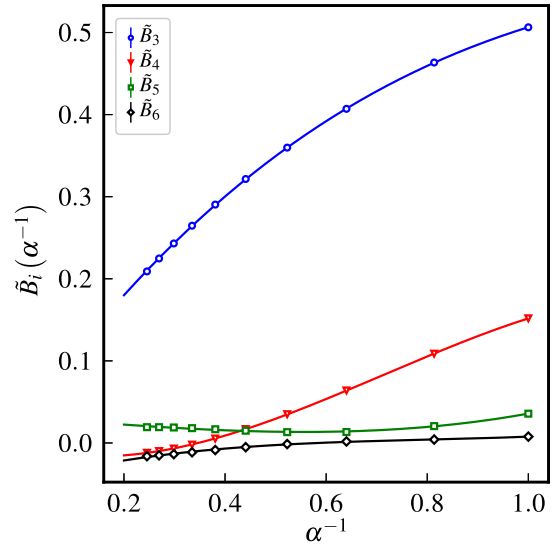


FIG. 2. Reduced virial coefficients  $\tilde{B}_i = B_i/B_2^{i-1}$  in dependence on the inverse of the rescaled, excess part  $\alpha = (2S\tilde{R}/V_P - 1)/7$  of the excluded hypervolume. The solid lines are least-squares fits employing a third-order polynomial as a heuristic approach.

where the scaling factor  $1/7$  guarantees  $\alpha(\nu \rightarrow 1^+) = 1$  in the limit of a hypersphere.

In the case of four-dimensional hyperspherocylinders, consistent with results for three-dimensional spherocylinders [47], already for the third-order reduced virial coefficient  $\tilde{B}_3$ , a significant nonlinearity is observed (Fig. 2). However, the reduced virial coefficients  $\tilde{B}_i$  of order 3–6 can excellently be described using a third-order polynomial in dependence on the aspect ratio  $\nu$  and therewith reliably be interpolated.

## IV. OUTLOOK

With the described approach, for the first time virial coefficients of four-dimensional, anisotropic objects are calculated. Using hard hyperspherocylinders exemplarily as a convex shape with tunable aspect ratio  $\nu$  in  $\mathbb{R}^4$ , the impact of anisometry to the geometric measures of hypervolume, hypersurface, mean radius of curvature, and the quermassintegral  $W_2$  can be analyzed and related to the second virial coefficient.

Our numerical results for  $B_2$  agree with the analytical result employing mixed volumes and quermassintegrals [42]. A remaining task is the calculation of virial coefficients with order  $i > 6$  for four-dimensional hyperspherocylinders and virial coefficients of differently shaped, hard anisotropic objects in  $\mathbb{R}^4$ .

## ACKNOWLEDGMENTS

P.M. gratefully acknowledges financial support by the Universität Rostock within the Ph.D. scholarship program.

## APPENDIX: EXPLORATION OF THE ROTATIONAL CONFIGURATION SPACE

Let  $\Omega_N = (\vartheta_N, \chi_N, \varphi_N)$  be generalized angular coordinates describing the orientation of an uniaxial solid of revolution in

$\mathbb{R}^4$  at step  $N$ . The orientation alternatively can be written as

$$\hat{\mathbf{u}}_N = \begin{pmatrix} \sin \vartheta_N \sin \chi_N \cos \varphi_N \\ \sin \vartheta_N \sin \chi_N \sin \varphi_N \\ \sin \vartheta_N \cos \chi_N \\ \cos \vartheta_N \end{pmatrix} \quad (\text{A1})$$

using the Cartesian unit vector  $\hat{\mathbf{u}}_N$ . A random rotation in  $\mathbb{R}^4$  can be achieved as follows.

(i) Generate a randomly oriented unit vector  $\hat{\mathbf{u}}_r$ . Let  $0 \leq \vartheta_r \leq \pi$  be a random number with probability density  $p(\vartheta_r) = 2 \sin^2 \vartheta_r / \pi$ ,  $0 \leq \chi_r \leq \pi$  a random number with probability density  $p(\chi_r) = \sin \chi_r / 2$ , and  $0 \leq \varphi_r \leq 2\pi$  a random number with probability density  $p(\varphi) = 1/(2\pi)$ .

Using the definitions

$$d = \sin \vartheta_r \sin \chi_r \cos \varphi_r, \quad (\text{A2a})$$

$$c = \sin \vartheta_r \sin \chi_r \sin \varphi_r, \quad (\text{A2b})$$

$$b = \sin \vartheta_r \cos \chi_r, \quad (\text{A2c})$$

$$a = \cos \vartheta_r, \quad (\text{A2d})$$

a left isoclinic rotation matrix in  $\mathbb{R}^4$  [41] can be written as

$$\mathbf{R}(\boldsymbol{\Omega}_r) = \begin{pmatrix} a & -b & c & -d \\ b & a & -d & -c \\ -c & d & a & -b \\ d & c & b & a \end{pmatrix} \quad (\text{A3})$$

with the generalized angular coordinates  $\boldsymbol{\Omega}_r = (\vartheta_r, \chi_r, \varphi_r)$  and the corresponding unit vector  $\hat{\mathbf{u}}_r = (-d, -c, -b, a)^T$ . Using  $\mathbf{R}^T(\boldsymbol{\Omega}_r) \cdot \hat{\mathbf{u}}_r$ , the random unit vector  $\hat{\mathbf{u}}_r$  is rotated, resulting in a unit vector in the positive  $z$  direction  $\hat{\mathbf{u}}_z = (0, 0, 0, 1)^T$ .

(ii) Using an additional rotation matrix

$$\begin{aligned} \boldsymbol{\Psi}(\psi) &= \mathbf{R}(\psi, 0, 0) \\ &= \begin{pmatrix} \cos \psi & -\sin \psi & 0 & 0 \\ \sin \psi & \cos \psi & 0 & 0 \\ 0 & 0 & \cos \psi & -\sin \psi \\ 0 & 0 & \sin \psi & \cos \psi \end{pmatrix}, \end{aligned} \quad (\text{A4})$$

describing a counterclockwise rotation by  $\psi$ , the unit vector  $\hat{\mathbf{u}}_\psi = (0, 0, -\sin \psi, \cos \psi)^T$  results from

$$\hat{\mathbf{u}}_\psi = (0, 0, -\sin \psi, \cos \psi)^T = \boldsymbol{\Psi}(\psi) \cdot \hat{\mathbf{u}}_z. \quad (\text{A5})$$

(iii) Applying

$$\hat{\mathbf{u}}_{\psi, \boldsymbol{\Omega}_r} = \mathbf{R}(\boldsymbol{\Omega}_r) \cdot \hat{\mathbf{u}}_\psi, \quad (\text{A6})$$

the intermediate result  $\hat{\mathbf{u}}_{\psi, \boldsymbol{\Omega}_r}$  is back-transformed to the initial coordinate system. Combining (i)–(iii)

$$\boldsymbol{\Xi}(\boldsymbol{\Omega}_r, \psi) = \mathbf{R}(\boldsymbol{\Omega}_r) \cdot \boldsymbol{\Psi}(\psi) \cdot \mathbf{R}^T(\boldsymbol{\Omega}_r) \quad (\text{A7})$$

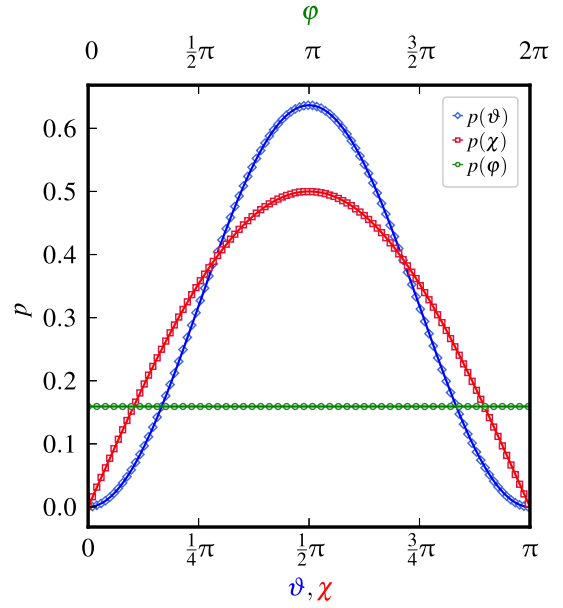


FIG. 3. Probability densities of polar angles  $\vartheta$ ,  $\chi$ , and  $\varphi$  obtained during  $10^{10}$  random rotations according to Eq. (A8) with  $\Delta_{\text{rot}} = 1/2$  starting from the initial orientation  $\hat{\mathbf{u}}_1 = (0, 0, 0, 1)^T$ . The solid lines represent the theoretically expected probability densities.

results, which again is a rotation matrix in  $\mathbb{R}^4$  with the properties  $\boldsymbol{\Xi}^T(\boldsymbol{\Omega}_r, \psi) \cdot \boldsymbol{\Xi}(\boldsymbol{\Omega}_r, \psi) = \mathbf{I}$  and  $\det(\boldsymbol{\Xi}(\boldsymbol{\Omega}_r, \psi)) = 1$ , where  $\mathbf{I}$  denotes the identity. Choosing a random orientation vector  $\boldsymbol{\Omega}_r$  and a random number  $-\Delta_{\text{rot}} \leq \psi \leq \Delta_{\text{rot}}$  with probability density  $p(\psi) = 1/(2\Delta_{\text{rot}})$ , a consecutive application of  $\boldsymbol{\Xi}(\boldsymbol{\Omega}_r, \psi)$

$$\hat{\mathbf{u}}_{N+1} = \boldsymbol{\Xi}(\boldsymbol{\Omega}_r, \psi) \cdot \hat{\mathbf{u}}_N \quad (\text{A8})$$

to a particles' orientation  $\hat{\mathbf{u}}_N$  at step  $N$  leads to a homogeneous exploration of a unit hypersphere's hypersurface as shown in Fig. 3. The probability densities are obtained during  $10^{10}$  random rotations employing Eq. (A8) using  $\Delta_{\text{rot}} = 1/2$  and starting from the initial orientation  $\hat{\mathbf{u}}_1 = (0, 0, 0, 1)^T$ . The solid lines are the theoretical probability densities  $p(\vartheta) = 2 \sin^2 \vartheta / \pi$ ,  $p(\chi) = \sin \chi / 2$ , and  $p(\varphi) = 1/(2\pi)$ . The excellent agreement of the obtained probability densities with the theoretical predictions proves a homogeneous exploration of the rotational configuration space by the described method.

- [1] S. Torquato, *J. Chem. Phys.* **149**, 020901 (2018).  
 [2] H. Kamerlingh Onnes, Proc. K. Ned. Akad. Wet. **4**, 125 (1902).  
 [3] B. Jäger, Sitzungsber. Akad. Wiss. Wien, Math.-Naturwiss. Kl., Abt. 2A **105**, 15 (1896).  
 [4] J. D. van der Waals, Proc. K. Ned. Akad. Wet. **1**, 138 (1899).  
 [5] L. Boltzmann, Sitzungsber. Akad. Wiss. Wien, Math.-Naturwiss. Kl., Abt. 2A **105**, 695 (1896).

- [6] L. Boltzmann, Proc. K. Ned. Akad. Wet. **1**, 398 (1899).  
 [7] L. Onsager, *Ann. NY Acad. Sci.* **51**, 627 (1949).  
 [8] J. E. Mayer and M. G. Mayer, *Statistical Mechanics* (Wiley, New York, 1940).  
 [9] M. N. Rosenbluth and A. W. Rosenbluth, *J. Chem. Phys.* **22**, 881 (1954).  
 [10] F. H. Ree and W. G. Hoover, *J. Chem. Phys.* **40**, 939 (1964).

- [11] F. H. Ree and W. G. Hoover, *J. Chem. Phys.* **46**, 4181 (1967).
- [12] E. J. Janse van Rensburg, *J. Phys. A: Math. Gen.* **26**, 4805 (1993).
- [13] S. Labík, J. Kolafa, and A. Malijevský, *Phys. Rev. E* **71**, 021105 (2005).
- [14] R. J. Wheatley, *Phys. Rev. Lett.* **110**, 200601 (2013).
- [15] A. J. Schultz and D. A. Kofke, *Phys. Rev. E* **90**, 023301 (2014).
- [16] P. A. Monson and M. Rigby, *Mol. Phys.* **35**, 1337 (1978).
- [17] D. Frenkel, *J. Phys. Chem.* **91**, 4912 (1987).
- [18] M. Rigby, *Mol. Phys.* **66**, 1261 (1989).
- [19] W. R. Cooney, S. M. Thompson, and K. E. Gubbins, *Mol. Phys.* **66**, 1269 (1989).
- [20] J. A. C. Veerman and D. Frenkel, *Phys. Rev. A* **45**, 5632 (1992).
- [21] C. Vega, *Mol. Phys.* **92**, 651 (1997).
- [22] A. Y. Vlasov, X.-M. You, and A. J. Masters, *Mol. Phys.* **100**, 3313 (2002).
- [23] P. Marienhagen, R. Hellmann, and J. Wagner, *Phys. Rev. E* **104**, 015308 (2021).
- [24] P. Marienhagen and J. Wagner, *Phys. Rev. E* **105**, 014125 (2022).
- [25] L. Tonks, *Phys. Rev.* **50**, 955 (1936).
- [26] P. C. Hemmer, *J. Chem. Phys.* **42**, 1116 (1965).
- [27] N. Metropolis, A. W. Rosenbluth, M. N. Rosenbluth, A. H. Teller, and E. Teller, *J. Chem. Phys.* **21**, 1087 (1953).
- [28] C. Zhang and B. M. Pettitt, *Mol. Phys.* **112**, 1427 (2014).
- [29] M. Á. G. Maestre, A. Santos, M. Robles, and M. L. de Haro, *J. Chem. Phys.* **134**, 084502 (2011).
- [30] F. H. Ree and W. G. Hoover, *J. Chem. Phys.* **40**, 2048 (1964).
- [31] M. Adda-Bedia, E. Katzav, and D. Vella, *J. Chem. Phys.* **129**, 144506 (2008).
- [32] J. H. Conway and N. J. A. Sloane, *Sphere Packings, Lattices and Groups*, Vol. 290 (Springer, New York, 2013).
- [33] N. Clisby and B. M. McCoy, *J. Stat. Phys.* **122**, 15 (2006).
- [34] A. Isihara, *J. Chem. Phys.* **18**, 1446 (1950).
- [35] A. Isihara and T. Hayashida, *J. Phys. Soc. Jpn.* **6**, 40 (1951).
- [36] H. Hadwiger, *Experientia* **7**, 395 (1951).
- [37] J. K. Singh and D. A. Kofke, *Phys. Rev. Lett.* **92**, 220601 (2004).
- [38] S. Torquato and Y. Jiao, *Phys. Rev. E* **87**, 022111 (2013).
- [39] E. Herold, R. Hellmann, and J. Wagner, *J. Chem. Phys.* **147**, 204102 (2017).
- [40] C. Vega and S. Lago, *Comput. Chem.* **18**, 55 (1994).
- [41] A. Perez-Gracia and F. Thomas, *Adv. Appl. Clifford Algebras* **27**, 523 (2017).
- [42] S. Torquato and Y. Jiao, [arXiv:2203.16764](https://arxiv.org/abs/2203.16764).
- [43] R. Schneider, *Convex Bodies: The Brunn-Minkowski Theory*, Vol. 151 (Cambridge University Press, Cambridge, 2014).
- [44] L. A. Santaló, *Integral Geometry and Geometric Probability* (Cambridge University Press, Cambridge, 2004).
- [45] T. Boublík, *Mol. Phys.* **27**, 1415 (1974).
- [46] M. Rigby, *Mol. Phys.* **78**, 21 (1993).
- [47] M. Francová, J. Kolafa, P. Morávek, S. Labík, and A. Malijevský, *Collect. Czech. Chem. Commun.* **73**, 413 (2008).

## 5.2 Publication II - Virial coefficients of hard, homonuclear dumbbells in two- to four-dimensional Euclidean spaces

M. Kulossa, D. Weidig, J. Wagner, *Phys. Rev. E* **107**, 024129 (2023).

DOI: 10.1103/PhysRevE.107.024129

Type: Full article

© 2023 American Physical Society

### Author contributions

**Markus Kulossa:** Conceptualization, Data curation, Formal analysis, Investigation, Methodology, Software, Validation, Visualization, Writing - original draft preparation, Writing - review and editing

Estimated total contribution in percent: 50 %

**Daniel Weidig:** Conceptualization, Formal analysis, Investigation, Methodology, Software, Writing - review and editing

Estimated total contribution in percent: 30 %

**Joachim Wagner:** Conceptualization, Formal analysis, Investigation, Methodology, Project administration, Resources, Supervision, Writing - review and editing

Estimated total contribution in percent: 20 %

Reprinted article with permission from M. Kulossa, D. Weidig, J. Wagner, *Phys. Rev. E* **107**, 024129 (2023). Copyright (2023) by the American Physical Society.



**Virial coefficients of hard, homonuclear dumbbells in two- to four-dimensional Euclidean spaces**Markus Kulossa , Daniel Weidig , and Joachim Wagner \**Institut für Chemie, Universität Rostock, 18051 Rostock, Germany*

(Received 2 December 2022; accepted 20 January 2023; published 17 February 2023)

We calculated virial coefficients up to the eighth order for hard dumbbells in two-, three-, and four-dimensional Euclidean spaces employing Mayer-sampling Monte Carlo simulations. We improved and extended available data in two dimensions, provide virial coefficients in  $\mathbb{R}^4$  in dependence on their aspect ratio, and recalculated virial coefficients for three-dimensional dumbbells. Highly accurate, semianalytical values for the second virial coefficient of homonuclear, four-dimensional dumbbells are provided. We compare the influence of the aspect ratio and the dimensionality to the virial series for this concave geometry. Lower-order reduced virial coefficients  $\tilde{B}_i = B_i/B_2^{i-1}$  depend in first approximation linearly from the inverse excess part of their mutual excluded volume.

DOI: [10.1103/PhysRevE.107.024129](https://doi.org/10.1103/PhysRevE.107.024129)**I. INTRODUCTION**

Many-particle systems with hard-body interaction are thoroughly investigated model systems for condensed matter since more than a century. These systems essentially contributed to an understanding of the self-organization and structure of matter [1]. Since hard-body systems are purely entropy controlled, less dense systems are supercritical fluids whose departure from the ideal-gas behavior can be expanded in the virial series originally proposed by Kamerlingh Onnes [2]. Employing the virial series

$$\frac{p}{\rho k_B T} = Z = 1 + \sum_{i=2}^{\infty} B_i \rho^{i-1} = 1 + \sum_{i=2}^{\infty} B_i^* \eta^{i-1}, \quad (1)$$

the real gas factor  $Z$  can be written as an expansion in powers of the particle number density  $\rho$ , where  $p$  denotes the pressure and  $k_B T$  the thermal energy. The coefficients  $B_i$  called virial coefficients account for the influence of  $i$ -particle interactions to the imperfect gas behavior. Introducing reduced virial coefficients  $B_i^* = B_i/V_p^{i-1}$ , where  $V_p$  denotes the particle volume, an expansion in powers of the volume fraction  $\eta = \rho V_p$  is obtained.

Virial coefficients of order two to four for hard spheres in three dimensions were already analytically calculated more than 100 years ago [3–7]. With the availability of computers, higher-order virial coefficients were numerically calculated [8–14]. Meanwhile, virial coefficients of three-dimensional hard spheres are known up to order 12 with considerable accuracy [15–17]. Parallel to the virial coefficients of hard spheres in three dimensions, regularly virial coefficients of hard disks are calculated [8,10–14,16]. Ree and Hoover calculated virial coefficients of hard hyperspheres up to the fourth order in Euclidean spaces with dimensionality  $1 \leq D \leq 9$  [18]. Virial coefficients of orders two and three are analytically available for spheres of arbitrary dimensionality [19]. The fourth

virial coefficient is available for arbitrary even-dimensional spaces [20], while for odd-dimensional Euclidean spaces only analytical values up to  $D = 11$  are known [21]. Numerical values for virial coefficients of higher order are calculated in Euclidean spaces of various dimensionalities up to  $D = 100$  [14,16,22,23].

While hard spheres in  $\mathbb{R}^3$  are model systems for atomic systems, inspired by the seminal work of Onsager [24], virial coefficients of various anisometric systems in three dimensions, serving as model systems for liquid-crystalline matter, are calculated [25–29]. Recently, the first virial coefficients for anisometric, hard particles in  $\mathbb{R}^4$  were reported [30]. Mostly, virial coefficients of convex shapes are calculated while only few concave geometries were investigated in three dimensions [31–34] and even less in two dimensions [35,36].

The aim of this contribution is to calculate virial coefficients of second to eighth order of hard, homonuclear dumbbells in dependence on their aspect ratio in  $\mathbb{R}^2$ ,  $\mathbb{R}^3$ , and  $\mathbb{R}^4$ . The three-dimensional dumbbell is a reasonable model system for diatomic molecules. The comparison with two- and four-dimensional analogs might give useful insights for the behavior in three dimensions and thus contribute to the understanding of equation-of-state data and phase behavior of concave, anisometric many-particle systems in three dimensions. The two-dimensional dumbbells are of relevance as a model system for monolayer adsorption with impact on applications such as heterogeneous catalysts.

**II. THEORETICAL BACKGROUND****A. Virial series**

Mayer and Mayer [37,38] have shown that the virial series originally proposed as a heuristic MacLaurin expansion in the number density is connected to the potential energy of interacting many-particle systems, where the virial coefficient of order  $i$  accounts for interactions in  $i$ -particle clusters. In the case of hard-body interaction, the potential energy can in a

\*joachim.wagner@uni-rostock.de

pairwise additive ansatz for an  $N$ -particle system exactly be written as

$$U_N = \sum_j \sum_{k>j} U_{jk}(\mathbf{r}_{jk}, \hat{\mathbf{u}}_j, \hat{\mathbf{u}}_k), \quad (2)$$

where

$$U_{jk} = \begin{cases} \infty & : r_{jk} < \sigma(\hat{\mathbf{r}}_{jk}, \hat{\mathbf{u}}_j, \hat{\mathbf{u}}_k) \\ 0 & : r_{jk} \geq \sigma(\hat{\mathbf{r}}_{jk}, \hat{\mathbf{u}}_j, \hat{\mathbf{u}}_k) \end{cases} \quad (3)$$

is infinite in the case of an overlap and otherwise zero.  $\sigma(\hat{\mathbf{r}}_{jk}, \hat{\mathbf{u}}_j, \hat{\mathbf{u}}_k)$  is the contact distance dependent on the direction of the center-to-center distance expressed as the unit vector  $\hat{\mathbf{r}}_{jk}$  and the particle orientations given by the unit vectors  $\hat{\mathbf{u}}_j$  and  $\hat{\mathbf{u}}_k$ .

The virial coefficient of order  $i$  reads as

$$B_i = -\frac{i-1}{i!} \sum_{G \in \mathbb{M}_i^L} S_G, \quad (4)$$

where  $S_G$  is the integral over products of Mayer  $f$  functions represented by the edges of biconnected graphs  $G$ . The Mayer  $f$  function is

$$f_{jk} = \exp\left[-\frac{U_{jk}}{k_B T}\right] - 1 = \begin{cases} -1 & : r_{jk} < \sigma \\ 0 & : r_{jk} \geq \sigma, \end{cases} \quad (5)$$

in the case of an overlap  $f_{jk} = -1$  and  $f_{jk} = 0$  for a nonoverlap.

$\mathbb{M}_i^L$  is the set of labeled, biconnected graphs with  $i$  vertices, where the Mayer  $f$  functions represent the connections in the graphs. For the second and third virial coefficients, only a single Mayer graph contributes, which reads in the three-dimensional case as

$$B_2 = -\frac{1}{2V} \iint \langle f_{12} \rangle_{\hat{\mathbf{u}}_2} d^3 \mathbf{r}_1 d^3 \mathbf{r}_2 = -\frac{1}{2} \text{---} \bullet \text{---} \quad (6a)$$

$$B_3 = -\frac{1}{3V} \iiint \langle f_{12} f_{13} f_{23} \rangle_{\hat{\mathbf{u}}_2, \hat{\mathbf{u}}_3} d^3 \mathbf{r}_1 d^3 \mathbf{r}_2 d^3 \mathbf{r}_3 = -\frac{1}{3} \triangle \quad (6b)$$

where  $\langle \dots \rangle_{\hat{\mathbf{u}}_2, \dots, \hat{\mathbf{u}}_i}$  indicates the average over the orientations of the second to  $i$ th particle, while the position  $\mathbf{r}_1$  and orientation  $\hat{\mathbf{u}}_1$  of the first particle determine the coordinate system. Since only particle distances  $\mathbf{r}_{jk}$  are relevant for the Mayer  $f$  function, the integration over  $\mathbf{r}_1$  results in the system volume  $V$ . In the  $D$ -dimensional case, for each vertex  $j$ , the volume element has to be replaced by  $d^D \mathbf{r}_j$ .

Since the number of labeled graphs increases dramatically with the order  $i$ , for the calculation of high-order virial coefficients, an optimization is mandatory. Ree and Hoover proposed a reformulation of the Mayer graphs introducing an additional function  $e_{jk} = f_{jk} + 1$  leading to fully connected Ree-Hoover graphs  $\mathbb{G}_i^L$ , connected either by  $f$  bonds or  $e$  bonds [39].

Based on the Ree-Hoover reformulation, the virial coefficient of order  $i$  reads as

$$B_i = -\frac{i-1}{i!} \sum_{G \in \mathbb{G}_i^L} c_G S_G, \quad (7)$$

where  $c_G$  is the Ree-Hoover star content of the graph  $G$  depending on its topology.  $S_G$  is now the integral over products of Mayer  $f$  functions and  $e$  functions represented by edges of the Ree-Hoover graph  $G$ . Since for hard-body interaction  $f_{jk} e_{jk} = 0$ , for a given configuration only a single Ree-Hoover graph contributes to the virial coefficient of order  $i$ . Moreover, the number of graphs with star content  $c_G \neq 0$  reduces to roughly one-third of the Mayer graphs.

## B. Computational details

The second virial coefficients of hard, planar dumbbells and three-dimensional hard dumbbells are analytically known [40,41]. For other orders of virial coefficients and different dimensions, a numerical approach is required.

For the calculation of the second virial coefficient of four-dimensional hyperdumbbells in dependence on their aspect ratio, a Mayer-sampling algorithm [42] with a four-dimensional hypersphere of the same hypervolume as a reference is used. To ensure that the configuration spaces of both, system of interest and reference system are exhaustively sampled also for hard-body systems, the sum of the integrands of system of interest and reference is used as an acceptance criterion [29]. The random translation and rotation in the four-dimensional space is described in [30]. For consistency, the analytically known second virial coefficients of hard homonuclear dumbbells in  $\mathbb{R}^2$  and  $\mathbb{R}^3$  are numerically reproduced using hard disks and hard spheres with the same area and volume, respectively, as a reference (Table I). Analogously, for hyperdumbbells in  $\mathbb{R}^4$  the semianalytical values of  $B_2^*$  (cf. Appendix A) are reproduced by means of Mayer-sampling Monte Carlo integration. For comparison, second virial coefficients for stadia, spherocylinders, and hyperspherocylinders as similar convex shapes with identical aspect ratio are compiled in Table II.

For the calculation of higher-order virial coefficients in any dimension, a Mayer-sampling algorithm optimized for hard-body interaction is used [29]. This algorithm is based on the property of Ree-Hoover diagrams, that in the case of hard-body interaction exactly one diagram contributes to the integrand for a given configuration, which can with the star content  $c_G$  and the number of overlaps  $n$  be written as  $c_G(-1)^n$ . The determination of the star content is realized by a fast method based on a bisection search in an ordered array of Ree-Hoover diagrams represented as ordinal numbers. As a reference, spanning trees with  $i$  vertices, each with the value  $(-2B_2)^{i-1}$ , are used for the virial coefficient of order  $i$ . Here-with, the numerically demanding determination of overlaps and nonoverlaps in a system of different geometry is avoided. At the same time, since either  $B_2$  is analytically known or numerically available with high accuracy and the reference system is identical to the system of interest, the confidence of the obtained virial coefficients is increased compared to other approaches.

For our simulations, we average for a selected virial coefficient and geometry 16 independent simulation runs, where for each run  $5 \times 10^{10}$  configurations are sampled after a tuning phase of  $10^7$  steps. To reduce numerical uncertainties, for the virial coefficients  $B_7$  and  $B_8$  of four-dimensional dumbbells, 16 independent runs each with  $4 \times 10^{11}$  steps were

TABLE I. Reduced second virial coefficients  $B_2^*$  of planar dumbbells, dumbbells, and hyperdumbbells in dependence on their aspect ratio  $\nu$  calculated via Mayer-sampling Monte Carlo simulation (MSMC) and (semi-)analytical equations.

$\nu$	$D = 2$		$D = 3$		$D = 4$	
	$B_2^*$ (MSMC)	$B_2^*$ [Eq. (13)]	$B_2^*$ (MSMC)	$B_2^*$ [Eq. (16)]	$B_2^*$ (MSMC)	$B_2^*$ [Eq. (A21)]
1.1	2.003879 (4)	2.0038787...	4.014341 (13)	4.0143448...	8.041285 (17)	8.041278116 (11)
1.2	2.014986 (9)	2.0149865...	4.055426 (17)	4.0554243...	8.159320 (24)	8.159328006 (2)
1.3	2.032861 (10)	2.0328596...	4.121566 (29)	4.1215709...	8.34919 (4)	8.3491846 (5)
1.4	2.057422 (11)	2.0574229...	4.21253 (4)	4.2125392...	8.60977 (4)	8.609761190 (8)
1.5	2.088985 (13)	2.0889839...	4.32935 (4)	4.3293529...	8.94292 (7)	8.9429226 (4)
1.6	2.128300 (14)	2.1283000...	4.47433 (4)	4.4743249...	9.35272 (4)	9.35274172 (5)
1.7	2.176759 (14)	2.1767625...	4.65123 (7)	4.6512436...	9.84453 (6)	9.84454201 (5)
1.8	2.236848 (15)	2.2368422...	4.86575 (6)	4.8657570...	10.42306 (5)	10.4230371 (9)
1.9	2.313358 (21)	2.3133557...	5.12604 (5)	5.1260408...	11.08794 (7)	11.0879331 (13)
2.0	2.420636 (27)	2.4206379...	5.44393 (7)	5.4439183...	11.82095 (8)	11.8209372 (15)

performed. The maximum translational and rotational displacement is optimized during the tuning phase to obtain an acceptance ratio of  $\approx 0.50$ . The results with uncertainties given by standard errors are compiled in Tables III, IV, and V.

### III. OVERLAP CRITERIA AND GEOMETRIC MEASURES FOR $D$ -DIMENSIONAL DUMBBELLS

A homonuclear  $D$ -dimensional dumbbell is the union of two  $D$ -dimensional spheres with identical radii  $R_0$  whose centers are separated by  $0 \leq L \leq 2R_0$  (Fig. 1), where in the limit  $L \rightarrow 0$  a  $D$ -dimensional sphere and in the limit  $L \rightarrow 2R_0$  two adjacent  $D$ -dimensional spheres result. Its aspect ratio, i.e., the ratio of the long to the short extent, can be written as

$$\nu = \frac{L}{2R_0} + 1 \quad (8)$$

with  $1 \leq \nu \leq 2$ . The overlap criterion of this union of two spheres can be reduced to the simple overlap criterion of spheres: An overlap exists if any of the spheres of the first particle overlaps with any sphere of the second particle and otherwise not. Using the center-of-mass coordinates  $\mathbf{c}_1$  and  $\mathbf{c}_2$  and the orientations given by the unit vectors  $\hat{\mathbf{u}}_1$  and  $\hat{\mathbf{u}}_2$  of

two dumbbells, the centers of the generating  $D$ -dimensional spheres are located at

$$\mathbf{S}_{1,i} = \mathbf{c}_1 \pm (\nu - 1)R_0\hat{\mathbf{u}}_1, \quad (9a)$$

$$\mathbf{S}_{2,j} = \mathbf{c}_2 \pm (\nu - 1)R_0\hat{\mathbf{u}}_2, \quad (9b)$$

where  $\mathbf{r} = \mathbf{c}_2 - \mathbf{c}_1$  is the dumbbells' center-of-mass distance vector. If any of four possible distances

$$d_{ij} = \|\mathbf{S}_{2,j} - \mathbf{S}_{1,i}\| < 2R_0, \quad (10)$$

an overlap occurs and otherwise not.

#### A. Two-dimensional dumbbell

The area or formally the two-dimensional volume  $V_p^{(2)}$  of a homonuclear, planar dumbbell reads as

$$V_p^{(2)} = 2R_0^2 \left[ (2\nu - \nu^2)^{1/2}(\nu - 1) + \arcsin(\nu - 1) + \frac{\pi}{2} \right] \quad (11)$$

in dependence on the radius  $R_0$  of the generating disks and the aspect ratio  $\nu$ . Its circumference or formally one-dimensional surface  $S_p^{(1)}$  can be written as

$$S_p^{(1)} = 4R_0 \left[ \arcsin(\nu - 1) + \frac{\pi}{2} \right]. \quad (12)$$

Rowlinson *et al.* provided the analytical expression

$$B_2^* = \frac{4R_0^2}{V_p^{(2)}} \left\{ \frac{3}{2}\pi + \frac{(\nu - 1)^2}{\pi} - 2 \arccos\left(\frac{\nu - 1}{2}\right) + (\nu - 1) \left[ 1 - \frac{(\nu - 1)^2}{4} \right]^{1/2} \right\} \quad (13)$$

for the reduced second virial coefficient  $B_2^* = B_2/V_p^{(2)}$  [40]. Boublík extended the expression to heteronuclear, planar dumbbells and multimers of fused hard disks [43].

#### B. Three-dimensional dumbbell

For homonuclear dumbbells in the three-dimensional Euclidean space  $\mathbb{R}^3$ , the geometric measures volume  $V_p^{(3)}$  and

 TABLE II. Reduced second virial coefficients  $B_2^*$  of  $D$ -dimensional spherocylinders depending on the aspect ratio  $\nu$ .

$\nu$	$D = 2$	$D = 3$	$D = 4$
	$B_2^*$ (see [44])	$B_2^*$ (see [27])	$B_2^*$ (see [30])
1.0	2	4	8
1.1	2.0035951...	4.0130434...	8.0369564...
1.2	2.0129210...	4.0461538...	8.1290911...
1.3	2.0263938...	4.0931034...	8.2577846...
1.4	2.0429641...	4.15	8.4119480...
1.5	2.0619088...	4.2142857...	8.5845650...
1.6	2.0827138...	4.2842105...	8.7709798...
1.7	2.1050033...	4.3585365...	8.9679811...
1.8	2.1284966...	4.4363636...	9.1732826...
1.9	2.1529792...	4.5170212...	9.3852120...
2.0	2.1782850...	4.6	9.6025180...

TABLE III. Reduced virial coefficients  $B_i^*$  of two-dimensional dumbbells in dependence on their aspect ratio  $\nu$ .

$\nu$	$B_3^*$	$B_4^*$	$B_5^*$	$B_6^*$	$B_7^*$	$B_8^*$
1.0	3.12802 (5)	4.25789 (23)	5.3368 (5)	6.3626 (10)	7.3525 (26)	8.320 (10)
	3.128017... <sup>a</sup>	4.257854... <sup>a</sup>	5.33689664 (64) <sup>a</sup>	6.363026 (11) <sup>a</sup>	7.352080 (29) <sup>a</sup>	8.318669 (65) <sup>a</sup>
1.1	3.13810 (8)	4.27453 (22)	5.35881 (29)	6.3893 (7)	7.3813 (26)	8.347 (10)
1.2	3.16723 (8)	4.32297 (21)	5.4240 (6)	6.4673 (9)	7.4692 (30)	8.447 (9)
1.3	3.21481 (6)	4.40338 (18)	5.5334 (5)	6.5990 (10)	7.6190 (28)	8.607 (13)
	3.22 (4) <sup>b</sup>					
1.4	3.28142 (8)	4.51748 (17)	5.6902 (6)	6.7906 (9)	7.8385 (26)	8.865 (12)
1.5	3.36863 (5)	4.66972 (14)	5.9024 (5)	7.0523 (12)	8.142 (4)	9.190 (18)
	3.370 (7) <sup>c</sup>	4.68 (3) <sup>c</sup>	5.9 (2) <sup>c</sup>			
1.6	3.47997 (7)	4.86783 (21)	6.1823 (5)	7.4011 (8)	8.551 (5)	9.661 (17)
1.7	3.62098 (10)	5.12428 (20)	6.5516 (7)	7.8673 (11)	9.099 (4)	10.276 (21)
	3.62 (4) <sup>b</sup>					
1.8	3.80149 (10)	5.46156 (29)	7.0474 (6)	8.5030 (17)	9.857 (5)	11.17 (4)
1.9	4.04045 (7)	5.92374 (24)	7.7458 (6)	9.4182 (16)	10.967 (6)	12.46 (5)
2.0	4.39398 (9)	6.64200 (30)	8.8815 (8)	10.9668 (29)	12.913 (6)	14.78 (7)
	4.394 (9) <sup>c</sup>	6.64 (4) <sup>c</sup>	8.9 (2) <sup>c</sup>			

<sup>a</sup>Value from [16].<sup>b</sup>Value from [35].<sup>c</sup>Value from [36].surface  $S_p^{(2)}$  can be written as

$$V_p^{(3)} = 2\pi\nu^2 R_0^3 \left(1 - \frac{\nu}{3}\right) \quad (14)$$

and

$$S_p^{(2)} = 4\pi\nu R_0^2. \quad (15)$$

Isihara derived an analytical expression for the second virial coefficient of hard, homonuclear dumbbells in the three-dimensional Euclidean space [41]. The reduced second virial coefficient  $B_2^*$  reads as

$$B_2^* = \frac{\delta}{V_p^{(3)}} R_0^3 \frac{2}{3} \pi \nu [9 - (2\nu - 3)^2] \quad (16)$$

TABLE IV. Reduced virial coefficients  $B_i^*$  of three-dimensional dumbbells in dependence on their aspect ratio  $\nu$ .

$\nu$	$B_3^*$	$B_4^*$	$B_5^*$	$B_6^*$	$B_7^*$	$B_8^*$
1.0	9.9998 (4)	18.3652 (12)	28.225 (6)	39.821 (20)	53.34 (13)	69.0 (17)
	10 <sup>a</sup>	18.36476... <sup>a</sup>	28.22437 (2) <sup>a</sup>	39.8152 (2) <sup>a</sup>	53.3418 (6) <sup>a</sup>	68.526 (4) <sup>a</sup>
1.1	10.0604 (4)	18.4943 (13)	28.422 (7)	40.077 (22)	53.70 (12)	68.8 (17)
	10.060307 (25) <sup>b</sup>	18.49433 (15) <sup>b</sup>	28.42184 (59) <sup>b</sup>	40.0883 (27) <sup>b</sup>	53.659 (15) <sup>b</sup>	68.093 (88) <sup>b</sup>
1.2	10.2345 (4)	18.8709 (11)	28.998 (5)	40.876 (24)	54.77 (17)	69.5 (25)
	10.234601 (25) <sup>b</sup>	18.87081 (15) <sup>b</sup>	28.99836 (65) <sup>b</sup>	40.8812 (30) <sup>b</sup>	54.774 (16) <sup>b</sup>	70.273 (90) <sup>b</sup>
1.3	10.5189 (4)	19.4908 (16)	29.956 (6)	42.209 (24)	56.52 (20)	72.5 (22)
	10.518960 (22) <sup>b</sup>	19.49162 (11) <sup>b</sup>	29.95581 (44) <sup>b</sup>	42.2099 (16) <sup>b</sup>	56.5327 (89) <sup>b</sup>	72.406 (54) <sup>b</sup>
1.4	10.91708 (29)	20.3695 (14)	31.316 (6)	44.09 (4)	59.10 (22)	74.8 (19)
	10.917214 (27) <sup>b</sup>	20.36946 (17) <sup>b</sup>	31.31624 (76) <sup>b</sup>	44.1084 (37) <sup>b</sup>	59.093 (20) <sup>b</sup>	75.23 (12) <sup>b</sup>
1.5	11.4401 (4)	21.5372 (18)	33.130 (6)	46.645 (27)	62.6 (4)	80 (5)
	11.440035 (29) <sup>b</sup>	21.53740 (18) <sup>b</sup>	33.12783 (83) <sup>b</sup>	46.6552 (41) <sup>b</sup>	62.617 (24) <sup>b</sup>	79.95 (15) <sup>b</sup>
1.6	12.1064 (5)	23.0452 (23)	35.473 (8)	49.98 (5)	67.3 (4)	85 (4)
	12.106367 (26) <sup>b</sup>	23.04531 (14) <sup>b</sup>	35.47086 (60) <sup>b</sup>	49.9702 (25) <sup>b</sup>	67.208 (15) <sup>b</sup>	85.52 (10) <sup>b</sup>
1.7	12.9450 (6)	24.9723 (24)	38.459 (11)	54.23 (6)	73.4 (5)	92 (6)
	12.945143 (34) <sup>b</sup>	24.97247 (22) <sup>b</sup>	38.4561 (11) <sup>b</sup>	54.2213 (58) <sup>b</sup>	73.273 (38) <sup>b</sup>	92.50 (26) <sup>b</sup>
1.8	13.9994 (4)	27.4366 (15)	42.251 (9)	59.63 (8)	81.1 (8)	99 (11)
	13.999401 (37) <sup>b</sup>	27.43608 (25) <sup>b</sup>	42.2500 (13) <sup>b</sup>	59.6389 (75) <sup>b</sup>	81.184 (50) <sup>b</sup>	103.47 (37) <sup>b</sup>
1.9	15.3326 (5)	30.6094 (23)	47.095 (14)	66.65 (10)	91.8 (8)	111 (16)
	15.332444 (40) <sup>b</sup>	30.60935 (29) <sup>b</sup>	47.0961 (16) <sup>b</sup>	66.6526 (98) <sup>b</sup>	92.005 (74) <sup>b</sup>	113.51 (54) <sup>b</sup>
2.0	17.0399 (8)	34.763 (4)	53.338 (16)	75.91 (13)	106.6 (19)	140 (40)
	17.039851 (46) <sup>b</sup>	34.76134 (34) <sup>b</sup>	53.3373 (21) <sup>b</sup>	75.797 (13) <sup>b</sup>	106.79 (10) <sup>b</sup>	132.22 (82) <sup>b</sup>

<sup>a</sup>Value from [16].<sup>b</sup>Value from [26].

TABLE V. Reduced virial coefficients  $B_i^*$  of four-dimensional hyperdumbbells in dependence on their aspect ratio  $\nu$ .

$\nu$	$B_3^*$	$B_4^*$	$B_5^*$	$B_6^*$	$B_7^*$	$B_8^*$
1.0	32.4057 (12)	77.747 (6)	146.22 (9)	253.3 (6)	374.7 (28)	610 (80)
	32.405759... <sup>a</sup>	77.745183... <sup>a</sup>	146.2451 (5) <sup>a</sup>	253.388 (6) <sup>a</sup>	375.07 (6) <sup>a</sup>	609.2 (7) <sup>a</sup>
1.1	32.6898 (15)	78.486 (9)	147.59 (11)	256.1 (9)	378.9 (29)	610 (80)
1.2	33.5071 (14)	80.636 (10)	151.46 (7)	263.2 (13)	386 (5)	620 (120)
1.3	34.8407 (14)	84.156 (12)	157.88 (10)	275.7 (11)	398 (6)	680 (160)
1.4	36.7060 (16)	89.070 (15)	166.78 (10)	293.2 (18)	417 (7)	740 (170)
1.5	39.1485 (18)	95.493 (12)	178.48 (10)	317.8 (17)	439 (11)	880 (200)
1.6	42.2394 (19)	103.548 (14)	193.02 (13)	349.5 (19)	461 (15)	900 (400)
1.7	46.0677 (28)	113.371 (13)	210.69 (21)	392 (4)	463 (15)	1000 (500)
1.8	50.7204 (22)	124.972 (20)	231.15 (21)	444 (5)	450 (30)	1900 (800)
1.9	56.2473 (25)	138.046 (30)	253.9 (4)	515 (6)	380 (50)	2400 (1400)
2.0	62.4926 (25)	151.288 (18)	276.4 (5)	594 (11)	220 (80)	2200 (2700)

<sup>a</sup>Value from [16].

with the abbreviations

$$\delta = 2\gamma \left( 1 + \frac{3}{4}x - \frac{1}{16}x^3 \right)^{-1}, \quad (17)$$

$$x = 2(\nu - 1) = \frac{L}{R_0}, \quad (18)$$

$$\begin{aligned} \gamma = \beta - \frac{1}{4\pi} \left\{ \left( 1 - \frac{1}{8}x^2 \right)^{1/2} \left( \frac{2}{5} + \frac{1}{20}x^2 \right) \right. \\ \left. + \left( \frac{64}{5x^2} - 8 + \frac{3}{4}x^2 \right) \arctan \left[ \left( 1 - \frac{1}{8}x^2 \right)^{1/2} \right] \right. \\ \left. + \left( x - \frac{11}{80}x^3 \right) \arctan \left[ \frac{4}{x} \left( 1 - \frac{1}{8}x^2 \right)^{1/2} \right] \right\}, \quad (19) \end{aligned}$$

and

$$\beta = \frac{4}{5x^2} + \frac{x}{2} + \frac{3}{32}x^2 - \frac{x^3}{40}. \quad (20)$$

### C. Four-dimensional hyperdumbbell

The hypervolume  $V_P^{(4)}$  can, using hypercylinder coordinates  $\mathbf{v} = [r(z) \sin \chi \cos \varphi, r(z) \sin \chi \sin \varphi, r(z) \cos \chi, z]^T$  and the meridian curve

$$r(z) = (R_0^2 - z^2)^{1/2}, \quad (21)$$

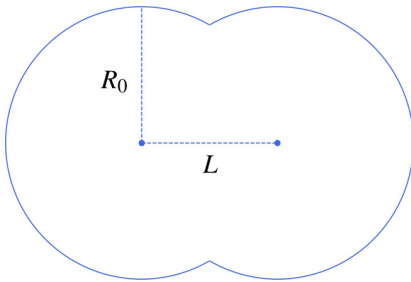


FIG. 1. Two-dimensional section of a dumbbell with dimension  $D \geq 2$  with the radius of the fused  $D$ -dimensional spheres  $R_0$  and the center-to-center distance  $L$ .

be written as

$$V_P^{(4)} = 2 \int_{R_0(1-\nu)}^{R_0} \frac{4}{3} \pi (R_0^2 - z^2)^{3/2} dz \quad (22)$$

resulting in

$$\begin{aligned} V_P^{(4)} = \frac{\pi R_0^4}{6} [6 \arcsin(\nu - 1) + 3\pi \\ + (-4\nu^3 + 12\nu^2 - 2\nu - 6)(2\nu - \nu^2)^{1/2}]. \quad (23) \end{aligned}$$

The hypersurface  $S_P^{(3)}$  reads as

$$\begin{aligned} S_P^{(3)} = 2 \int_{R_0(1-\nu)}^{R_0} 4\pi r^2(z) \left\{ 1 + \left[ \frac{dr(z)}{dz} \right]^2 \right\}^{1/2} dz \\ = 8\pi R_0 \int_{R_0(1-\nu)}^{R_0} (R_0^2 - z^2)^{1/2} dz, \quad (24) \end{aligned}$$

which results in

$$S_P^{(3)} = 4\pi R_0^3 [(\nu - 1)(2\nu - \nu^2)^{1/2} + \pi - \arccos(\nu - 1)] \quad (25)$$

in dependence on the radius  $R_0$  of the generating hyperspheres and the aspect ratio  $\nu$ .

An analytical expression for the second virial coefficient of four-dimensional hyperdumbbells is so far unknown. We provide highly accurate semianalytical values obtained employing an algorithm described in Appendix A (Tables VI and VII).

## IV. RESULTS AND DISCUSSION

Since our Mayer-sampling algorithm uses for the calculation of higher-order virial coefficients spanning trees as reference integrals, which factorize to powers of the second virial coefficient, the uncertainty of higher-order virial coefficients depends on the accuracy of the available second virial coefficients. For two- and three-dimensional, homonuclear dumbbells, analytical values for the second virial coefficients serve as a reference, whereas in the case of four-dimensional hyperdumbbells, highly accurate semianalytical second virial coefficients are used (Table I). Additionally, reproducing known second virial coefficients is a validation

TABLE VI. Reduced second virial coefficients  $B_2^*$  of hard, four-dimensional homonuclear hyperdumbbells with aspect ratio  $1.00 \leq \nu \leq 1.50$ .

$\nu$	$B_2^*$	$\nu$	$B_2^*$
1.00	8	1.26	8.264769125 (19)
1.01	8.000430089 (1)	1.27	8.28481649 (4)
1.02	8.00171175 (8)	1.28	8.30556824 (11)
1.03	8.00383260 (6)	1.29	8.3270242 (7)
1.04	8.006780994 (11)	1.30	8.3491846 (5)
1.05	8.01054591 (6)	1.31	8.3720497 (6)
1.06	8.015117052 (10)	1.32	8.3956203 (8)
1.07	8.02048467 (16)	1.33	8.4198975 (9)
1.08	8.02663965 (26)	1.34	8.4448824 (10)
1.09	8.03357346 (15)	1.35	8.4705767 (9)
1.10	8.041278116 (11)	1.36	8.4969822 (7)
1.11	8.04974618 (6)	1.37	8.5241010 (5)
1.12	8.058970720 (5)	1.38	8.55193526 (27)
1.13	8.068945328 (9)	1.39	8.580487753 (26)
1.14	8.07966407 (6)	1.40	8.609761190 (8)
1.15	8.091121460 (30)	1.41	8.639758633 (19)
1.16	8.1033125 (4)	1.42	8.670483345 (1)
1.17	8.1162326 (6)	1.43	8.70193882 (29)
1.18	8.129877656 (21)	1.44	8.7341287 (6)
1.19	8.144243893 (9)	1.45	8.7670570 (9)
1.20	8.159328006 (2)	1.46	8.8007276 (10)
1.21	8.1751270 (7)	1.47	8.8351450 (11)
1.22	8.19163843 (27)	1.48	8.8703135 (9)
1.23	8.2088600 (4)	1.49	8.9062378 (6)
1.24	8.2267899 (5)	1.50	8.9429226 (4)
1.25	8.24542667 (13)		

TABLE VII. Reduced second virial coefficients  $B_2^*$  of hard, four-dimensional homonuclear hyperdumbbells with aspect ratio  $1.51 \leq \nu \leq 2.00$ .

$\nu$	$B_2^*$	$\nu$	$B_2^*$
1.51	8.9803727 (13)	1.76	10.1810592 (16)
1.52	9.01859360 (20)	1.77	10.2402304 (17)
1.53	9.0575901 (4)	1.78	10.3002848 (5)
1.54	9.09736758 (29)	1.79	10.36122120 (27)
1.55	9.137931510 (2)	1.80	10.4230371 (9)
1.56	9.1792874 (8)	1.81	10.4857288 (13)
1.57	9.2214407 (8)	1.82	10.5492914 (4)
1.58	9.26439705 (19)	1.83	10.61371834 (13)
1.59	9.30816219 (7)	1.84	10.67900131 (16)
1.60	9.35274172 (5)	1.85	10.74513013 (25)
1.61	9.3981413 (9)	1.86	10.8120923 (12)
1.62	9.4443667 (4)	1.87	10.8798731 (9)
1.63	9.491423331 (10)	1.88	10.9484546 (10)
1.64	9.5393168 (9)	1.89	11.0178161 (12)
1.65	9.58805253 (14)	1.90	11.0879331 (13)
1.66	9.6376358 (5)	1.91	11.1587768 (7)
1.67	9.68807154 (26)	1.92	11.2303140 (12)
1.68	9.73936484 (9)	1.93	11.3025056 (16)
1.69	9.791520212 (17)	1.94	11.3753057 (4)
1.70	9.84454201 (5)	1.95	11.4486607 (4)
1.71	9.8984340 (4)	1.96	11.52250680 (12)
1.72	9.9532005 (6)	1.97	11.596767479 (25)
1.73	10.0088438 (8)	1.98	11.67134873 (18)
1.74	10.0653668 (10)	1.99	11.7461298 (7)
1.75	10.1227713 (4)	2.00	11.8209372 (15)

of our algorithm. For this reason, second virial coefficients of homonuclear dumbbells in Euclidean spaces with dimension  $D = 2$  to  $D = 4$  are calculated in dependence on their aspect ratio  $\nu$  by means of Mayer sampling.

### A. Second virial coefficient $B_2$

In Table I, reduced second virial coefficients for hard, homonuclear dumbbells in two- to four-dimensional Euclidean spaces are compiled. Known reference values for two- and three-dimensional dumbbells are included for comparison. The calculated data are in excellent agreement with the analytical values in two and three dimensions as well as the semianalytical values in four dimensions. In Figs. 2–4 the numerically determined, reduced second virial coefficients are displayed as open circles, while the (semi-)analytical values [Eqs. (13), (16), and (A21)] are represented as solid lines. In the inset, relative deviations  $\Delta B_2^*/B_{2,\text{an}}^* = (B_2^* - B_{2,\text{an}}^*)/B_{2,\text{an}}^*$  are analyzed. The deviations are smaller than the estimation of the uncertainty of the numerical data.

Hard spherocylinders in  $\mathbb{R}^3$ , hard stadia in  $\mathbb{R}^2$ , and hard hyperspherocylinders in  $\mathbb{R}^4$  are nearly similar convex, anisometric shapes as the concave homonuclear dumbbell with the same aspect ratio  $1 \leq \nu \leq 2$  in Euclidean spaces with the respective dimensionality, whose second virial coefficients are analytically known [27,30,44]. Despite the similarity of both shapes, beyond the aspect ratio a significant influence of the specific geometry on the reduced second virial coefficients

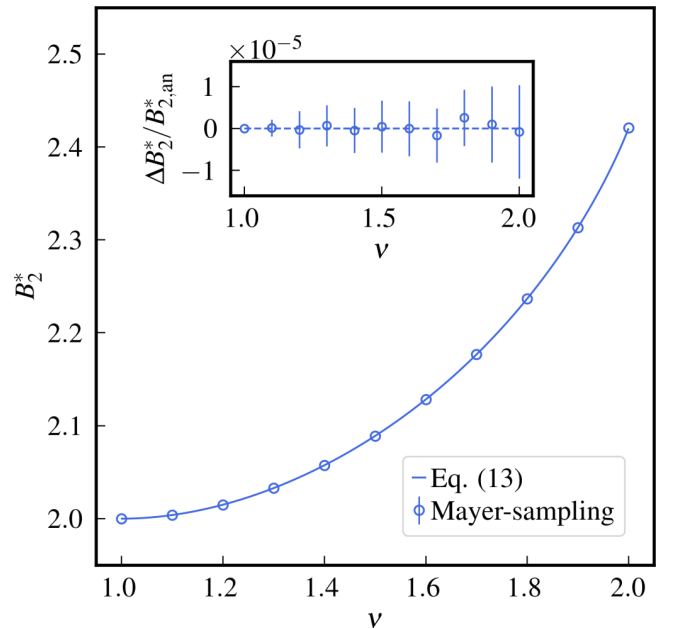


FIG. 2. Reduced second virial coefficients  $B_2^*$  of planar, homonuclear dumbbells in  $\mathbb{R}^2$ . Numerical values obtained by Mayer sampling are displayed as open circles, while the analytical values [Eq. (13)] are displayed as a solid line. In the inset, relative deviations  $\Delta B_2^*/B_{2,\text{an}}^* = (B_2^* - B_{2,\text{an}}^*)/B_{2,\text{an}}^*$  of the numerical values  $B_2^*$  and the analytical values  $B_{2,\text{an}}^*$  are displayed.

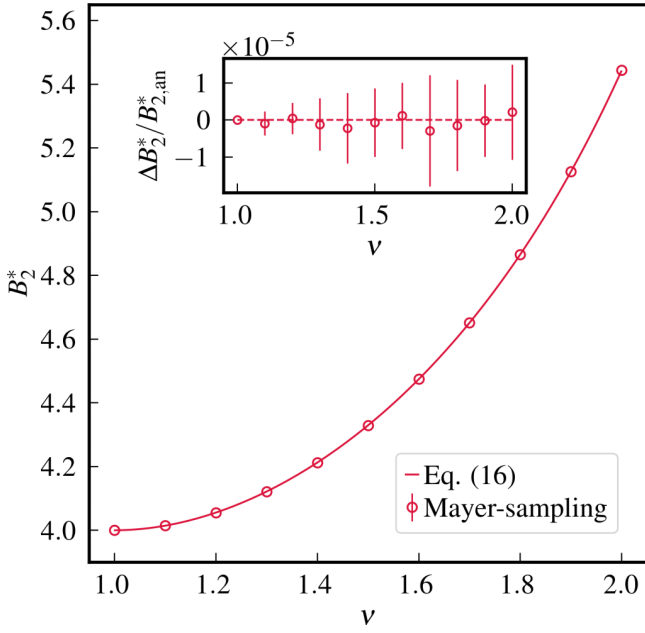


FIG. 3. Reduced second virial coefficients  $B_2^*$  of hard, homonuclear dumbbells in  $\mathbb{R}^3$ . Numerical values obtained by Mayer sampling are displayed as open circles, while the analytical values [Eq. (16)] are displayed as a solid line. In the inset, relative deviations  $\Delta B_2^*/B_{2,an}^* = (B_2^* - B_{2,an}^*)/B_{2,an}^*$  of the numerical values  $B_2^*$  and the analytical values  $B_{2,an}^*$  are displayed.

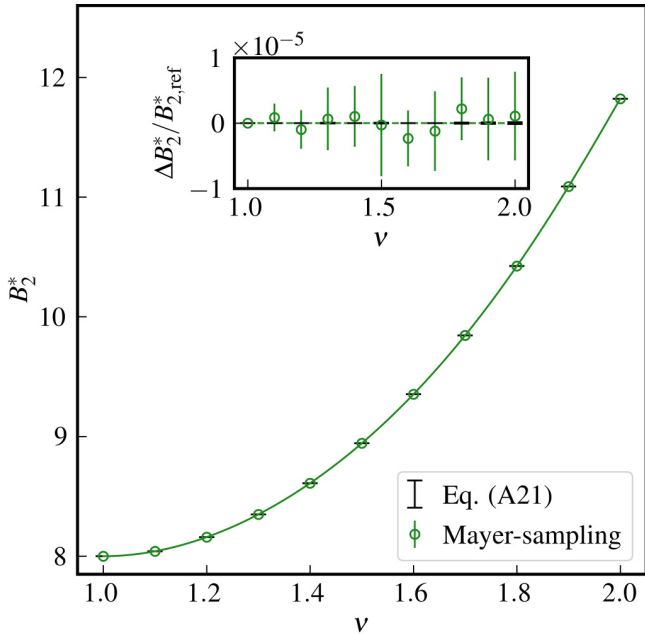


FIG. 4. Reduced second virial coefficients  $B_2^*$  of hard, homonuclear hyperdumbbells in  $\mathbb{R}^4$ . Numerical values obtained by Mayer sampling are displayed as open circles, while the semianalytical values [Eq. (A21)] are displayed as a solid line. In the inset, relative deviations  $\Delta B_2^*/B_{2,ref}^* = (B_2^* - B_{2,ref}^*)/B_{2,ref}^*$  between Mayer-sampling Monte Carlo simulations and the semianalytical reference are displayed. The uncertainties of the semianalytical reference are displayed as black error bars.

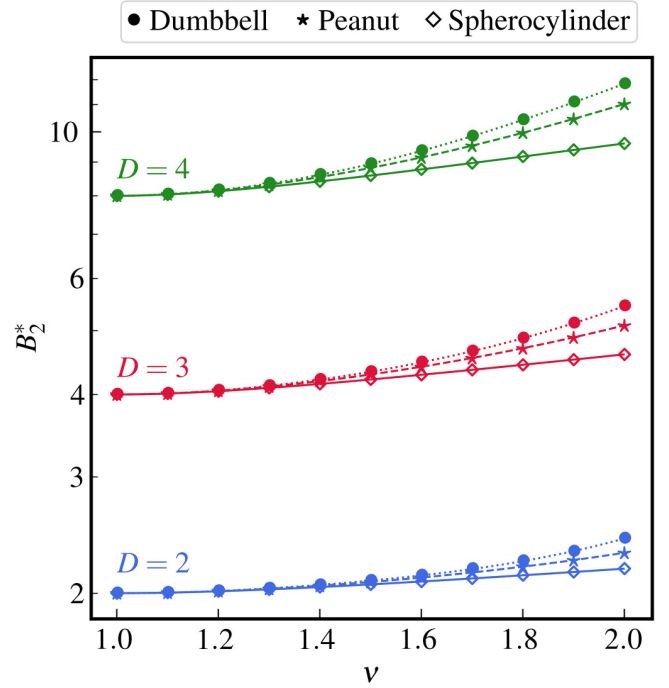


FIG. 5. Reduced second virial coefficients  $B_2^*$  of  $D$ -dimensional, homonuclear dumbbells ( $\bullet$ ) in comparison to  $D$ -dimensional peanuts ( $\star$ ) and  $D$ -dimensional spherocylinders ( $\diamond$ ) in  $\mathbb{R}^2$  (blue),  $\mathbb{R}^3$  (red), and  $\mathbb{R}^4$  (green).

is observed. In Fig. 5, reduced second virial coefficients of hard homonuclear dumbbells and spherocylinders in  $\mathbb{R}^2$ ,  $\mathbb{R}^3$ , and  $\mathbb{R}^4$  are compared: With increasing aspect ratio, the reduced second virial coefficients of homonuclear dumbbells progressively exceed those of the corresponding spherocylinders. Opposite to the convex geometry of a spherocylinder, for dumbbell regions on their surface exist that are inaccessible by a second dumbbell. Filling out the spherical lunes such that a third sphere with radius equal to the dumbbell's generating spheres can completely access the surface, a peanut-shaped particle results. The overlap criterion for these peanut-shaped particles is identical to that of dumbbells for the aspect ratios  $1 \leq v \leq 2$  investigated in this work. As a result, thermodynamic properties such as virial coefficients are identical, despite of a different particle volume  $V_p^{(D)}$ . The meridian curve and particle volumes  $V_p^{(D)}$  of peanut-shaped particles are given in Appendix B. Due to larger  $D$ -dimensional particle volumes  $V_p^{(D)}$ , the reduced virial coefficients  $B_i^* = B_i/V_p^{i-1}$  of hard peanuts are smaller than those of homonuclear dumbbells, but still larger than those of spherocylinders with identical aspect ratio as displayed in Fig. 5.

Analytical values of the reduced second virial coefficients of  $D$ -dimensional spherocylinders for selected aspect ratios are compiled in Table II.

### B. Higher-order virial coefficients $B_3$ – $B_8$

Higher-order virial coefficients of hard, homonuclear dumbbells in  $\mathbb{R}^2$ ,  $\mathbb{R}^3$ , and  $\mathbb{R}^4$  are calculated employing an optimized Mayer-sampling algorithm using spanning trees as an intrinsic reference. In the two- and three-dimensional

spaces, analytical values of the second virial coefficients are used, while in four dimensions, the previously discussed semi-analytical values are used. Since the reference values in  $\mathbb{R}^4$  have uncertainties, these uncertainties have to be included by means of error propagation into the estimation of higher-order virial coefficients' uncertainties. Due to the high accuracy of the reference values for  $B_2^*$  (Table I), this contribution to the total uncertainties of higher-order virial coefficients is mostly negligible compared to the statistical fluctuations of Mayer-sampling runs. The data for the two-dimensional dumbbells are shown in Table III, for three-dimensional dumbbells in Table IV, and for the four-dimensional hyperdumbbells in Table V.

Unlike in the limit of hard disks ( $\nu \rightarrow 1^+$ ), for larger aspect ratios only few virial coefficients of planar, homonuclear dumbbells are reported in the literature so far [35,36]. We reproduced available data, improved its accuracy, and systematically calculated third- to eighth-order virial coefficients in dependence on their aspect ratio. The uncertainties of literature data for hard disks are smaller than our values, which is not a principal limitation of our algorithm: The scope of this contribution is to calculate virial coefficients of anisometric particles in dependence on their aspect ratio rather than improving the reference values for the extensively studied hard-disk fluid. For hard disks, the numerical demanding orientation average can be avoided.

For three-dimensional homonuclear dumbbells, highly accurate virial coefficients up to the ninth order are available [26]. To validate our algorithm, we reproduced these literature data with slightly larger uncertainties; however, up to the eighth order (Table IV). The focus of this paper is the calculation of so far unknown virial coefficients of four-dimensional homonuclear dumbbells, which are compiled in Table V. In the limit  $\nu \rightarrow 1^+$ , our data is in excellent agreement to known virial coefficients of hard hyperspheres in  $\mathbb{R}^4$ .

As earlier reported for oblate, hard ellipsoids of revolution and hard lenses, virial coefficients  $\tilde{B}_i = B_i/B_2^{i-1}$  normalized to powers of the second virial coefficients depend nearly linearly on the inverse excess part  $\alpha^{-1}$  of the mutual excluded volume [29]. Since the orientational average of the mutual excluded volume per particle equals the second virial coefficient in the case of hard-body interaction, its excess part  $\alpha$  can be written as

$$\alpha = \frac{B_2 - V_p^{(D)}}{(2^{D-1} - 1)V_p^{(D)}} = \frac{B_2^* - 1}{2^{D-1} - 1}, \quad (26)$$

where  $B_2^* = 2^{D-1}$  is the reduced second virial coefficient of a  $D$ -dimensional sphere. Hence,  $2^{D-1} - 1$  is the reduced excess part of a  $D$ -dimensional sphere's mutual excluded volume. The normalization leads to

$$\lim_{\nu \rightarrow 1^+} \alpha = 1 \quad (27)$$

in the limit of a spherical particle. As visible in Figs. 6–8, also for homonuclear dumbbells with aspect ratio  $1 \leq \nu \leq 2$ , a nearly linear dependence of reduced virial coefficients  $\tilde{B}_i$  on the rescaled, inverse excess part  $\alpha^{-1}$  of the reduced mutual excluded volume is observed in Euclidean spaces with dimensionality  $2 \leq D \leq 4$ .

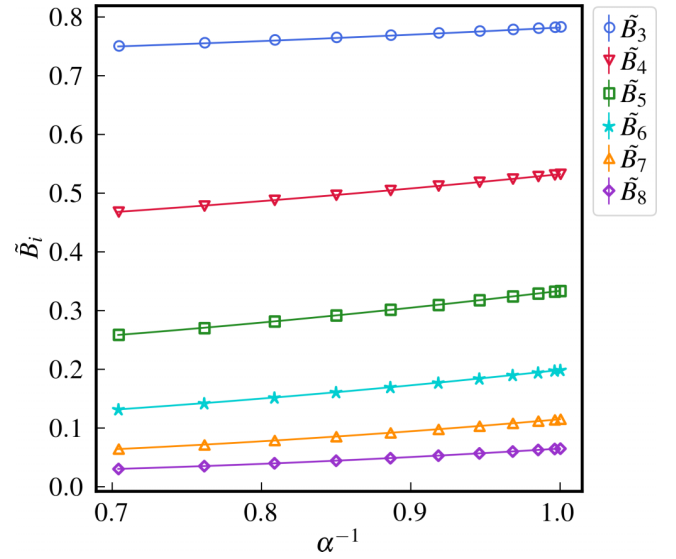


FIG. 6. Reduced virial coefficients  $\tilde{B}_i = B_i/B_2^{i-1}$  of two-dimensional, homonuclear dumbbells in dependence on the inverse excess part  $\alpha^{-1}$  of their rescaled, mutual excluded volume. The solid lines are least-squares fits employing a second-order polynomial as a heuristic approach.

The influence of the dimensionality  $D$  on the reduced virial coefficients  $\tilde{B}_i$  is visible in Figs. 9–11, where exemplarily for the aspect ratios  $\nu = 1$  (sphere),  $\nu = 1.5$ , and  $\nu = 2.0$  reduced virial coefficients from order three to eight in two, three, and four dimensions are compared. For all aspect ratios, reduced virial coefficients  $\tilde{B}_i$  decrease with

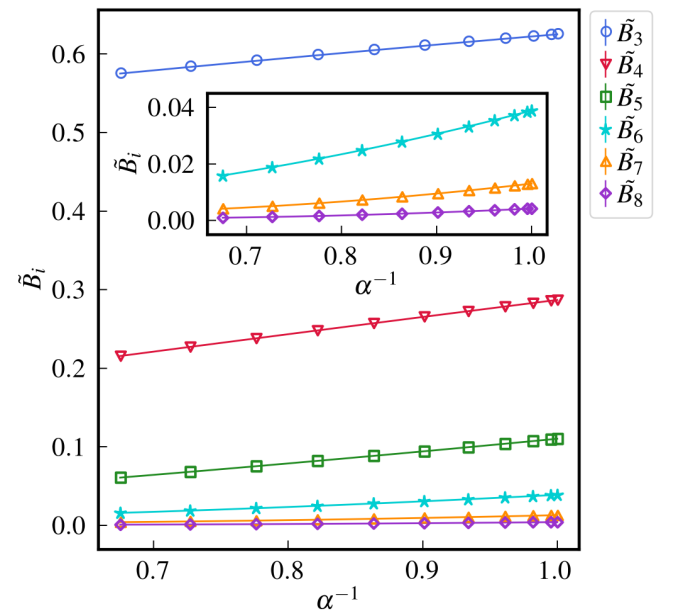


FIG. 7. Reduced virial coefficients  $\tilde{B}_i = B_i/B_2^{i-1}$  of three-dimensional, homonuclear dumbbells in dependence on the inverse excess part  $\alpha^{-1}$  of their rescaled, mutual excluded volume. The solid lines are least-squares fits employing a second-order polynomial as a heuristic approach.

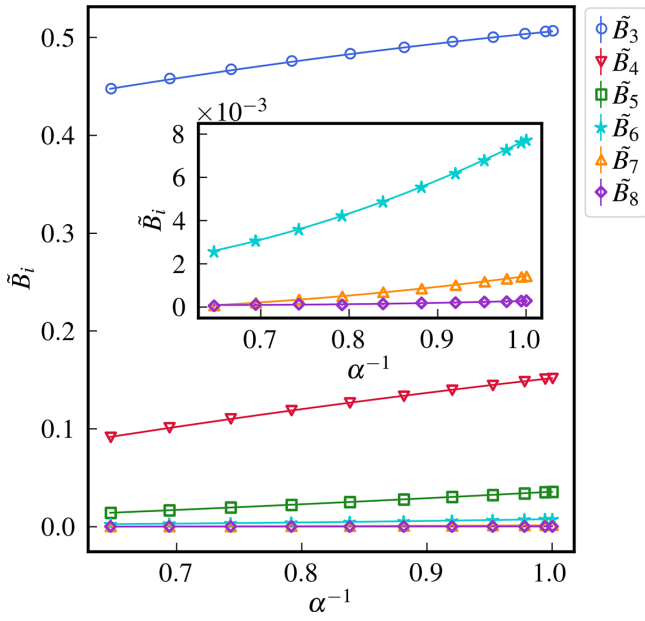


FIG. 8. Reduced virial coefficients  $\tilde{B}_i = B_i/B_2^{i-1}$  of four-dimensional, homonuclear dumbbells in dependence on the inverse excess part  $\alpha^{-1}$  of their rescaled, mutual excluded volume. The solid lines are least-squares fits employing a second-order polynomial as a heuristic approach.

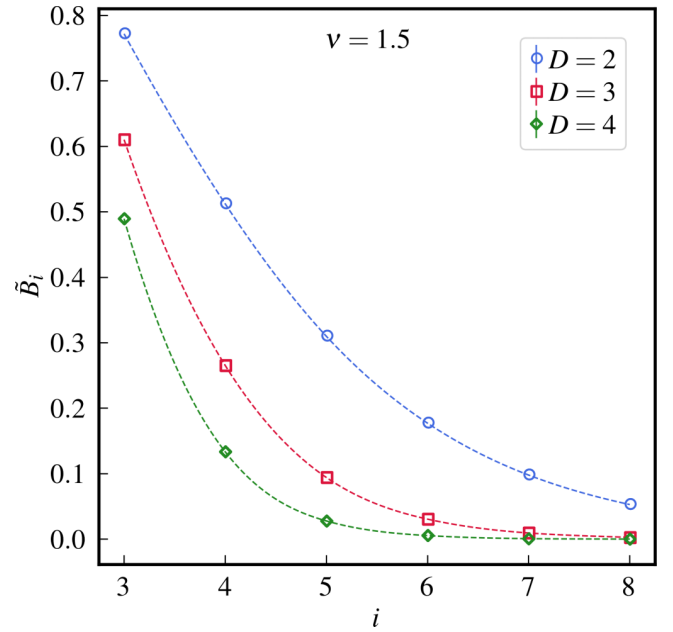


FIG. 10. Reduced virial coefficients  $\tilde{B}_i = B_i/B_2^{i-1}$  of  $D$ -dimensional, homonuclear dumbbells with the aspect ratio  $\nu = 1.5$  in dependence on the order of the virial coefficients  $i$ . The dotted lines are cubic splines as a guide to the eye.

their order  $i$ , where the decay of the virial coefficients is more pronounced with increasing dimensionality. The vanishing importance of higher-order virial coefficients with increasing dimensionality is expectable, since the maximum packing fraction of spheroids, i.e., dumbbells with

$\nu \rightarrow 1^+$ , decreases with the dimensionality: In two dimensions, we have  $\eta_{\max}^{(2)} = \pi/\sqrt{12} = 0.906899\dots$ , in three dimensions  $\eta_{\max}^{(3)} = \pi/\sqrt{18} = 0.740480\dots$ , and in four dimensions  $\eta_{\max}^{(4)} = \pi^2/16 = 0.616850\dots$  [45,46].

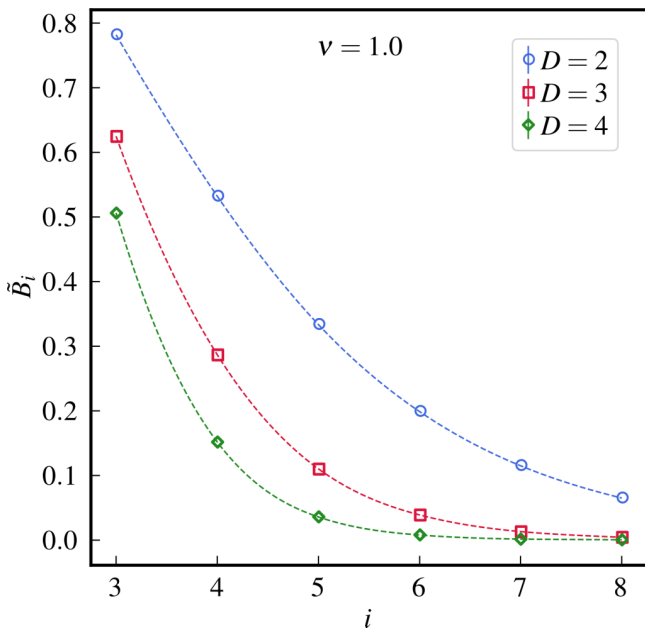


FIG. 9. Reduced virial coefficients  $\tilde{B}_i = B_i/B_2^{i-1}$  of  $D$ -dimensional, homonuclear dumbbells with the aspect ratio  $\nu = 1$  in dependence on the order of the virial coefficients  $i$ . The dotted lines are cubic splines as a guide to the eye.

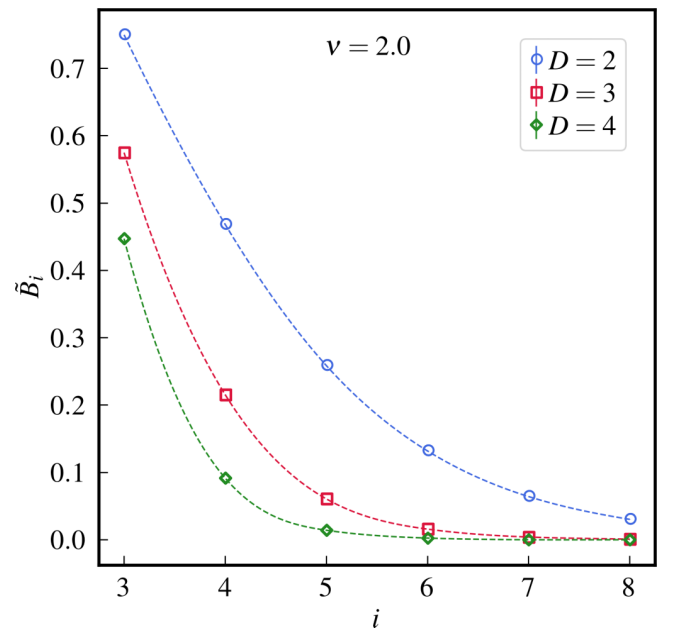


FIG. 11. Reduced virial coefficients  $\tilde{B}_i = B_i/B_2^{i-1}$  of  $D$ -dimensional, homonuclear dumbbells with the aspect ratio  $\nu = 2$  in dependence on the order of the virial coefficients  $i$ . The dotted lines are cubic splines as a guide to the eye.

Comparing the reduced virial coefficients of hard stadia [44,47], hard spherocylinders [26], and hard hyperspherocylinders [30], also for this similar, convex geometry, the vanishing importance of higher-order virial coefficients with increasing dimensionality is observed.

## V. CONCLUSIONS

We calculated virial coefficients of two- to four-dimensional, homonuclear dumbbells up to order eight in Euclidean spaces with the respective dimensionality. For hard, homonuclear dumbbells in  $\mathbb{R}^2$ , we extended and improved the accuracy of available data. We verified available, highly accurate data for homonuclear, three-dimensional dumbbells and provided so-far-unknown virial coefficients of four-dimensional, homonuclear hyperdumbbells up to the eighth order. Herewith, in addition to virial coefficients of hyperspherocylinders as convex, anisotropic solids, also virial coefficients of a concave, anisometric geometry in  $\mathbb{R}^4$  became available.

As already identified in  $\mathbb{R}^3$  for oblate geometries [29], also for homonuclear, hard dumbbells in dimensions two to four, a nearly linear dependence of reduced virial coefficients  $\tilde{B}_i = B_i/B_2^{i-1}$  on the rescaled, inverse excess part of the mutual excluded volume  $\alpha^{-1}$  is observed. The systematic comparison of reduced virial coefficients  $\tilde{B}_i$  at any aspect ratio shows a decreasing importance of higher-order virial coefficients in Euclidean spaces with increasing dimensionality  $D$ . In addition to the calculation of virial coefficients for differently shaped anisometric geometries, the investigation of closest packings consisting of such bodies could improve the understanding of self-organization in condensed matter.

## APPENDIX A: SEMIANALYTICAL RESULTS FOR THE SECOND VIRIAL COEFFICIENT OF FOUR-DIMENSIONAL HOMONUCLEAR HYPERDUMBBELLS

### 1. Overlap criterion for four-dimensional homonuclear hyperdumbbells

Let the unit vector  $\hat{\mathbf{u}}_1$  be the orientation of a homonuclear hyperdumbbell with radius  $R_0$  of the generating hyperspheres at  $\mathbf{c}_1 = \mathbf{0}$ , and the unit vector  $\hat{\mathbf{u}}_2$  the orientation of a second, identical hyperdumbbell centered at  $\mathbf{c}_2 = r\hat{\mathbf{u}}_r$ , where  $r$  denotes the center-to-center distance and the unit vector  $\hat{\mathbf{u}}_r$  its direction.

Without loss of generality, due to the axial symmetry, the orientation  $\hat{\mathbf{u}}_1 = (0, 0, 1)^T$  is chosen to be in the  $z$  direction and the distance vector is with  $\hat{\mathbf{u}}_r = (0, 0, \sin \vartheta_r, \cos \vartheta_r)^T$  chosen to be in the  $(y, z)$  plane. The orientation of the second hyperdumbbell can be written as

$$\hat{\mathbf{u}}_2 = \begin{pmatrix} \sin \vartheta_2 \sin \chi_2 \cos \varphi_2 \\ \sin \vartheta_2 \sin \chi_2 \sin \varphi_2 \\ \sin \vartheta_2 \cos \chi_2 \\ \cos \vartheta_2 \end{pmatrix}. \quad (\text{A1})$$

The hyperdumbbells' generating hyperspheres are located at  $\mathbf{c}_1 \pm L/2\hat{\mathbf{u}}_1$  and  $\mathbf{c}_2 \pm L/2\hat{\mathbf{u}}_2$ , where  $0 \leq L \leq 2R_0$  is the distance between both hyperdumbbells' generating hyperspheres. The aspect ratio of a hyperdumbbell reads as  $\nu = 1 + L/(2R_0)$  [Eq. (8)]. Hence, an overlap occurs if the squared distance between any combination of the generating hyperspheres

$$\left( r\hat{\mathbf{u}}_r \pm \frac{L}{2}\hat{\mathbf{u}}_2 \mp \frac{L}{2}\hat{\mathbf{u}}_1 \right)^2 < 4R_0^2 \quad (\text{A2})$$

is less than its diameter squared. We have

$$d_{aa}^2 = r^2 + \frac{L^2}{2}(1 - \cos \vartheta_2) - rL[\cos \vartheta_r(1 - \cos \vartheta_2) - \sin \vartheta_r \sin \vartheta_2 \cos \chi_2], \quad (\text{A3a})$$

$$d_{ab}^2 = r^2 + \frac{L^2}{2}(1 + \cos \vartheta_2) - rL[\cos \vartheta_r(1 + \cos \vartheta_2) + \sin \vartheta_r \sin \vartheta_2 \cos \chi_2], \quad (\text{A3b})$$

$$d_{ba}^2 = r^2 + \frac{L^2}{2}(1 + \cos \vartheta_2) + rL[\cos \vartheta_r(1 + \cos \vartheta_2) + \sin \vartheta_r \sin \vartheta_2 \cos \chi_2], \quad (\text{A3c})$$

$$d_{bb}^2 = r^2 + \frac{L^2}{2}(1 - \cos \vartheta_2) + rL[\cos \vartheta_r(1 - \cos \vartheta_2) - \sin \vartheta_r \sin \vartheta_2 \cos \chi_2] \quad (\text{A3d})$$

for all possible combinations. Hence, an overlap occurs if  $\min(d_{aa}^2, d_{ab}^2, d_{ba}^2, d_{bb}^2) < 4R_0^2$  and otherwise not. Note that  $d_{ij}^2$  does not depend on the azimuth  $\varphi_2$ . As symmetry relations, the parities

$$d_{aa}^2(\vartheta_r, \vartheta_2, \chi_2) = d_{ab}^2(\vartheta_r, \pi - \vartheta_2, \pi - \chi_2), \quad (\text{A4a})$$

$$d_{aa}^2(\vartheta_r, \vartheta_2, \chi_2) = d_{ba}^2(\pi - \vartheta_r, \pi - \vartheta_2, \chi_2), \quad (\text{A4b})$$

$$d_{aa}^2(\vartheta_r, \vartheta_2, \chi_2) = d_{bb}^2(\pi - \vartheta_r, \vartheta_2, \pi - \chi_2), \quad (\text{A4c})$$

$$d_{ab}^2(\vartheta_r, \vartheta_2, \chi_2) = d_{ba}^2(\pi - \vartheta_r, \vartheta_2, \pi - \chi_2), \quad (\text{A4d})$$

$$d_{ab}^2(\vartheta_r, \vartheta_2, \chi_2) = d_{bb}^2(\pi - \vartheta_r, \pi - \vartheta_2, \chi_2), \quad (\text{A4e})$$

$$d_{ba}^2(\vartheta_r, \vartheta_2, \chi_2) = d_{bb}^2(\vartheta_r, \pi - \vartheta_2, \pi - \chi_2) \quad (\text{A4f})$$

exist.

### 2. Calculation of the second virial coefficient of four-dimensional homonuclear hyperdumbbells

Let  $f(r, \vartheta_r, \vartheta_2, \chi_2)$  be the four-dimensional hyperdumbbell's contact function with

$$f(r, \vartheta_r, \vartheta_2, \chi_2) = \begin{cases} 1 : r < \sigma(\vartheta_r, \vartheta_2, \chi_2) \\ 0 : r \geq \sigma(\vartheta_r, \vartheta_2, \chi_2), \end{cases} \quad (\text{A5})$$

where  $\sigma$  denotes the contact distance depending on the angular coordinates  $\Omega_r = (\vartheta_r)$  of the distance vector and the orientation  $\Omega_2 = (\vartheta_2, \chi_2)$  of the second hyperdumbbell.

The second virial coefficient of a homonuclear hyperdumbbell with radius  $R_0$  of the generating hyperspheres can be written as

$$B_2 = \frac{1}{2} \int_0^{2\nu R_0} 2\pi^2 r^3 \langle f(r, \vartheta_r, \vartheta_2, \chi_2) \rangle_{\vartheta_r, \vartheta_2, \chi_2} dr, \quad (\text{A6})$$

with

$$\langle f(r, \vartheta_r, \vartheta_2, \chi_2) \rangle_{\vartheta_r, \vartheta_2, \chi_2} = \frac{2}{\pi^2} \int_0^\pi \int_0^\pi \int_0^\pi f(r, \vartheta_r, \vartheta_2, \chi_2) \sin^2 \vartheta_r \sin^2 \vartheta_2 \sin \chi_2 d\chi_2 d\vartheta_2 d\vartheta_r. \quad (\text{A7})$$

An analytical result for the integration over  $\chi_2$  can be obtained as follows: Let us formally calculate the critical cosines  $\alpha_{ij} = \cos \chi_{2,\text{crit}}$  at the contact distances  $d_{ij}^2 = 4R_0^2$ . We obtain

$$\alpha_{aa} = -\frac{\frac{1}{L}(r - \frac{4R_0^2}{r}) + (1 - \cos \vartheta_2)(\frac{L}{2r} - \cos \vartheta_r)}{\sin \vartheta_r \sin \vartheta_2}, \quad (\text{A8a})$$

$$\alpha_{ab} = \frac{\frac{1}{L}(r - \frac{4R_0^2}{r}) + (1 + \cos \vartheta_2)(\frac{L}{2r} - \cos \vartheta_r)}{\sin \vartheta_r \sin \vartheta_2}, \quad (\text{A8b})$$

$$\alpha_{ba} = -\frac{\frac{1}{L}(r - \frac{4R_0^2}{r}) + (1 + \cos \vartheta_2)(\frac{L}{2r} + \cos \vartheta_r)}{\sin \vartheta_r \sin \vartheta_2}, \quad (\text{A8c})$$

$$\alpha_{bb} = \frac{\frac{1}{L}(r - \frac{4R_0^2}{r}) + (1 - \cos \vartheta_2)(\frac{L}{2r} + \cos \vartheta_r)}{\sin \vartheta_r \sin \vartheta_2}. \quad (\text{A8d})$$

Looking further at the slopes of  $\partial d_{ij}^2 / \partial \chi_2$  in  $0 \leq \chi_2 \leq \pi$ ,

$$\frac{\partial d_{aa}^2}{\partial \chi_2} < 0 \quad \forall \quad 0 \leq \chi_2 \leq \pi, \quad (\text{A9a})$$

$$\frac{\partial d_{ab}^2}{\partial \chi_2} > 0 \quad \forall \quad 0 \leq \chi_2 \leq \pi, \quad (\text{A9b})$$

$$\frac{\partial d_{ba}^2}{\partial \chi_2} < 0 \quad \forall \quad 0 \leq \chi_2 \leq \pi, \quad (\text{A9c})$$

$$\frac{\partial d_{bb}^2}{\partial \chi_2} > 0 \quad \forall \quad 0 \leq \chi_2 \leq \pi, \quad (\text{A9d})$$

we obtain choosing  $R_0 = 1$  the conditions

$$\alpha_{aa} = \begin{cases} < -1 & : d_{aa}^2 > 4 \quad \forall \quad 0 \leq \chi_2 \leq \pi \\ -1 \leq \alpha_{aa} \leq 1 & : d_{aa}^2 < 4 \quad \forall \quad \chi_2 > \arccos(\alpha_{aa}) \\ > 1 & : d_{aa}^2 < 4 \quad \forall \quad 0 \leq \chi_2 \leq \pi, \end{cases} \quad (\text{A10a})$$

$$\alpha_{ab} = \begin{cases} < -1 & : d_{ab}^2 < 4 \quad \forall \quad 0 \leq \chi_2 \leq \pi \\ -1 \leq \alpha_{ab} \leq 1 & : d_{ab}^2 < 4 \quad \forall \quad \chi_2 < \arccos(\alpha_{ab}) \\ > 1 & : d_{ab}^2 > 4 \quad \forall \quad 0 \leq \chi_2 \leq \pi, \end{cases} \quad (\text{A10b})$$

$$\alpha_{ba} = \begin{cases} < -1 & : d_{ba}^2 > 4 \quad \forall \quad 0 \leq \chi_2 \leq \pi \\ -1 \leq \alpha_{ba} \leq 1 & : d_{ba}^2 < 4 \quad \forall \quad \chi_2 > \arccos(\alpha_{ba}) \\ > 1 & : d_{ba}^2 < 4 \quad \forall \quad 0 \leq \chi_2 \leq \pi, \end{cases} \quad (\text{A10c})$$

$$\alpha_{bb} = \begin{cases} < -1 & : d_{bb}^2 < 4 \quad \forall \quad 0 \leq \chi_2 \leq \pi \\ -1 \leq \alpha_{bb} \leq 1 & : d_{bb}^2 < 4 \quad \forall \quad \chi_2 < \arccos(\alpha_{bb}) \\ > 1 & : d_{bb}^2 > 4 \quad \forall \quad 0 \leq \chi_2 \leq \pi \end{cases} \quad (\text{A10d})$$

for an overlap. Combining Eqs. (A10), the analytical expression

$$\int_0^\pi f(r, \vartheta_r, \vartheta_2, \chi_2) \sin \chi_2 d\chi_2 = 2 + \min \{ \max [ \max (\alpha_{aa}, -1), \max (\alpha_{ba}, -1) ] - \min [ \min (\alpha_{ab}, 1), \min (\alpha_{bb}, 1) ], 0 \} \quad (\text{A11})$$

for the integral over  $\chi_2$  is obtained. Using the parities Eqs. (A4) leading to

$$\begin{aligned} f(r, \vartheta_r, \vartheta_2, \chi_2) &= f(r, \vartheta_r, \pi - \vartheta_2, \pi - \chi_2) \\ &= f(r, \pi - \vartheta_r, \vartheta_2, \pi - \chi_2), \end{aligned} \quad (\text{A12})$$

the relation

$$\begin{aligned} &\int_0^{\pi/2} f(r, \vartheta_r, \pi - \vartheta_2, \chi_2) \sin \chi_2 d\chi_2 \\ &= \int_{\pi/2}^{\pi} f(r, \vartheta_r, \pi - \vartheta_2, \chi_2) \sin \chi_2 d\chi_2 \end{aligned} \quad (\text{A13})$$

results. Hence,

$$\begin{aligned} &\int_0^{\pi} f(r, \vartheta_r, \vartheta_2, \chi_2) \sin \chi_2 d\chi_2 \\ &= \int_0^{\pi} f(r, \vartheta_r, \pi - \vartheta_2, \chi_2) \sin \chi_2 d\chi_2 \end{aligned} \quad (\text{A14})$$

is obtained. Analogously, the parity

$$\begin{aligned} &\int_0^{\pi} f(r, \vartheta_r, \vartheta_2, \chi_2) \sin \chi_2 d\chi_2 \\ &= \int_0^{\pi} f(r, \pi - \vartheta_r, \vartheta_2, \chi_2) \sin \chi_2 d\chi_2 \end{aligned} \quad (\text{A15})$$

results. Using these symmetry relations, we can express the orientational average in Eq. (A7) as

$$\begin{aligned} &\langle f(r, \vartheta_r, \vartheta_2, \chi_2) \rangle_{\vartheta_r, \vartheta_2, \chi_2} \\ &= \frac{8}{\pi^2} \int_0^{\pi/2} \int_0^{\pi/2} \int_0^{\pi} f(r, \vartheta_r, \vartheta_2, \chi_2) \sin \chi_2 d\chi_2 \\ &\quad \times \sin^2 \vartheta_2 d\vartheta_2 \sin^2 \vartheta_r d\vartheta_r. \end{aligned} \quad (\text{A16})$$

The closest nonoverlap distance occurs at  $\vartheta_r = \vartheta_2 = \chi_2 = \pi/2$ , where

$$d_{aa}^2 = d_{ab}^2 = d_{ba}^2 = d_{bb}^2 = \sigma^2 + \frac{L^2}{2} = 4R_0^2. \quad (\text{A17})$$

Using

$$L = 2R_0(\nu - 1) \quad (\text{A18})$$

we obtain

$$\sigma = R_0(2 + 4\nu - 2\nu^2)^{1/2}. \quad (\text{A19})$$

Since for any angular configuration at  $r < \sigma$  an overlap occurs,

$$B_2^{(c)} = \frac{1}{2} \int_0^{\sigma} 2\pi^2 r^3 dr = \frac{\pi^2}{4} (2 + 4\nu - 2\nu^2)^2 R_0^4 \quad (\text{A20})$$

is the core contribution to the second virial coefficient. Here-with, we can reformulate the second virial coefficient of a homonuclear hyperdumbbell as

$$B_2 = \frac{\pi^2}{4} \sigma^4 + \frac{1}{2} \int_{\sigma}^{2\nu R_0} 2\pi^2 r^3 \langle f(r, \vartheta_r, \vartheta_2, \chi_2) \rangle_{\vartheta_r, \vartheta_2, \chi_2} dr. \quad (\text{A21})$$

Using the analytical expressions, Eq. (A20), for the core contribution  $B_2^{(c)}$ , the integration over  $\chi_2$  [Eq. (A11)], and

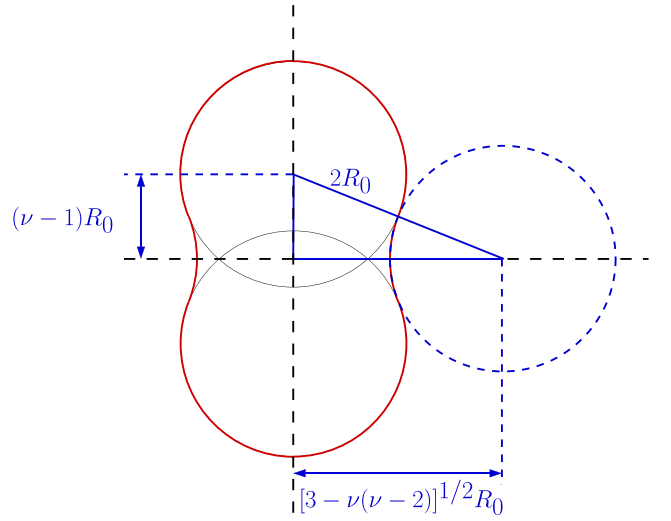


FIG. 12. Configuration of peanut-shaped particles in comparison with homonuclear dumbbells with the same aspect ratio. The minimum distance for a nonoverlap is for both geometries the same, as well as the overlap function.

performing the remaining integrations numerically employing adaptive Gauss-Kronrod algorithms, highly accurate values for the second virial coefficients are calculated. The results with uncertainties are compiled in Tables VI and VII.

## APPENDIX B: COMPARISON OF HARD DUMBBELLS WITH PEANUT-SHAPED PARTICLES

Filling out the surface of a homonuclear dumbbell at its spherical lunes inaccessible for a sphere with radius  $R_0$  identical to the dumbbell's generating spheres, a peanut-shaped particle results. The meridian curve of a peanut-shaped particle with overlap criterion identical to that of a dumbbell and maximum particle volume  $V_p^{(D)}$  reads as

$$r(z) = \begin{cases} [R_0^2 - (z - \frac{L}{2})^2]^{1/2} & : \frac{L}{4} < z \leq \nu R_0 \\ r_{\text{off}} - (R_0^2 - z^2)^{1/2} & : -\frac{L}{4} \leq z \leq \frac{L}{4} \\ [R_0^2 - (z + \frac{L}{2})^2]^{1/2} & : -\nu R_0 \leq z < -\frac{L}{4}, \end{cases} \quad (\text{B1})$$

where

$$L = 2R_0(\nu - 1) \quad (\text{B2})$$

is the center-to-center distance [Eq. (8)] and

$$r_{\text{off}} = [3 - \nu(\nu - 2)]^{1/2} R_0 \quad (\text{B3})$$

the minimum nonoverlap distance to a third sphere with radius  $R_0$  with respect to the dumbbell's center of mass (Fig. 12).

The volume  $V_p^{(D)}$  of a  $D$ -dimensional peanut-shaped particle reads as

$$V_p^{(D)} = 2 \int_0^{\nu R_0} \kappa^{(D-1)} r(z)^{D-1} dz \quad (\text{B4})$$

with

$$\kappa^{(D)} = \frac{\pi^{D/2}}{\Gamma(1 + D/2)} \quad (\text{B5})$$

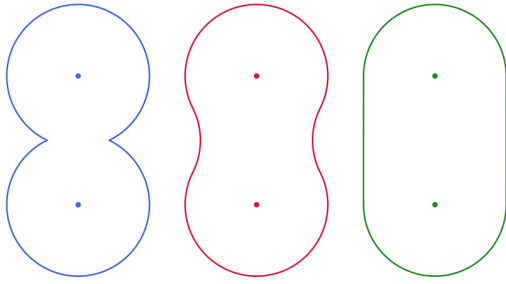


FIG. 13. Two-dimensional sections of  $D$ -dimensional dumbbells (blue), peanuts (red), and spherocylinders (green) with the aspect ratio  $\nu = 1.9$ .

being the volume of a  $D$ -dimensional unit sphere. For dimensions  $2 \leq D \leq 4$ ,

$$\begin{aligned} V_P^{(2)} &= [2(\nu - 1)(3 + 2\nu - \nu^2)^{1/2} + \pi]R_0^2 \\ &= \pi R_0^2 + L r_{\text{off}}, \end{aligned} \quad (\text{B6})$$

$$\begin{aligned} V_P^{(3)} &= \frac{2\pi}{3} \left[ 3\nu(1 + \nu) - 3 - \nu^3 - 3(3 + 2\nu - \nu^2)^{1/2} \right. \\ &\quad \left. \times \arcsin\left(\frac{\nu - 1}{2}\right) \right] R_0^3, \end{aligned} \quad (\text{B7})$$

and

$$\begin{aligned} V_P^{(4)} &= \frac{\pi}{2} \left[ \pi + (8\nu^2 - 16\nu - 24) \arcsin\left(\frac{\nu - 1}{2}\right) \right. \\ &\quad \left. - \frac{4}{3}(\nu - 1)(\nu^2 - 2\nu - 7)(3 + 2\nu - \nu^2)^{1/2} \right] R_0^4 \end{aligned} \quad (\text{B8})$$

results. The volume of  $D$ -dimensional peanut-shaped particles is in between those of dumbbells and spherocylinders with the same aspect ratio  $\nu$ , radius  $R_0$ , and dimension  $D$  (Fig. 13).

While the virial coefficients  $B_i(\nu)$  and reduced virial coefficients  $\tilde{B}_i(\nu) = B_i(\nu)/B_2^{i-1}(\nu)$  are identical for dumbbells and peanut-shaped particles, the reduced virial coefficients  $B_i^*(\nu) = B_i(\nu)/V_P^{i-1}(\nu)$  can be obtained as

$$B_{i,\text{PS}}^* = B_{i,\text{DB}}^* \left( \frac{V_{\text{P,DB}}}{V_{\text{P,PS}}} \right)^{i-1} \quad (\text{B9})$$

with  $V_{\text{P,PS}}$  denoting the volume of a peanut-shaped particle,  $V_{\text{P,DB}}$  that of a homonuclear dumbbell, and  $B_{i,\text{DB}}^*$  the provided data for reduced virial coefficients of homonuclear dumbbells in the respective dimension. The excess part  $\alpha$  of the mutual excluded volume per particle differs for peanut-shaped particles from that of dumbbells and can be obtained using Eq. (26) accordingly.

- 
- [1] S. Torquato, *J. Chem. Phys.* **149**, 020901 (2018).  
 [2] H. Kamerlingh Onnes, *Proc. K. Ned. Akad. Wet.* **4**, 125 (1902).  
 [3] B. Jäger, *Sitzungsber. Akad. Wiss. Wien, Math.-Naturwiss. Kl., Abt. 2A* **105**, 15 (1896).  
 [4] L. Boltzmann, *Sitzungsber. Akad. Wiss. Wien, Math.-Naturwiss. Kl., Abt. 2A* **105**, 695 (1896).  
 [5] L. Boltzmann, *Proc. K. Ned. Akad. Wet.* **1**, 398 (1899).  
 [6] J. D. van der Waals, *Proc. K. Ned. Akad. Wet.* **1**, 138 (1899).  
 [7] J. J. van Laar, *Amsterdam Akad. Versl.* **7**, 350 (1899).  
 [8] N. Metropolis, A. W. Rosenbluth, M. N. Rosenbluth, A. H. Teller, and E. Teller, *J. Chem. Phys.* **21**, 1087 (1953).  
 [9] M. N. Rosenbluth and A. W. Rosenbluth, *J. Chem. Phys.* **22**, 881 (1954).  
 [10] F. H. Ree and W. G. Hoover, *J. Chem. Phys.* **40**, 939 (1964).  
 [11] F. H. Ree and W. G. Hoover, *J. Chem. Phys.* **46**, 4181 (1967).  
 [12] E. J. Janse van Rensburg, *J. Phys. A: Math. Gen.* **26**, 4805 (1993).  
 [13] S. Labík, J. Kolafa, and A. Malijevský, *Phys. Rev. E* **71**, 021105 (2005).  
 [14] N. Clisby and B. M. McCoy, *J. Stat. Phys.* **122**, 15 (2006).  
 [15] R. J. Wheatley, *Phys. Rev. Lett.* **110**, 200601 (2013).  
 [16] C. Zhang and B. M. Pettitt, *Mol. Phys.* **112**, 1427 (2014).  
 [17] A. J. Schultz and D. A. Kofke, *Phys. Rev. E* **90**, 023301 (2014).  
 [18] F. H. Ree and W. G. Hoover, *J. Chem. Phys.* **40**, 2048 (1964).  
 [19] M. Luban and A. Baram, *J. Chem. Phys.* **76**, 3233 (1982).  
 [20] I. Urrutia, *J. Stat. Phys.* **187**, 29 (2022).  
 [21] I. Lyberg, *J. Stat. Phys.* **119**, 747 (2005).  
 [22] B. C. Freasier and D. J. Isbister, *Mol. Phys.* **42**, 927 (1981).  
 [23] M. Bishop, A. Masters, and J. H. Clarke, *J. Chem. Phys.* **110**, 11449 (1999).  
 [24] L. Onsager, *Ann. NY Acad. Sci.* **51**, 627 (1949).  
 [25] C. Vega, *Mol. Phys.* **92**, 651 (1997).  
 [26] M. Francová, J. Kolafa, P. Morávek, S. Labík, and A. Malijevský, *Collect. Czech. Chem. Commun.* **73**, 413 (2008).  
 [27] E. Herold, R. Hellmann, and J. Wagner, *J. Chem. Phys.* **147**, 204102 (2017).  
 [28] M. E. Irrgang, M. Engel, A. J. Schultz, D. A. Kofke, and S. C. Glotzer, *Langmuir* **33**, 11788 (2017).  
 [29] P. Marienhagen, R. Hellmann, and J. Wagner, *Phys. Rev. E* **104**, 015308 (2021).  
 [30] M. Kulossa, P. Marienhagen, and J. Wagner, *Phys. Rev. E* **105**, 064121 (2022).  
 [31] D. Jolly, B. C. Freasier, and R. J. Bearman, *Chem. Phys. Lett.* **46**, 75 (1977).  
 [32] I. Nezbeda, B. Tříška, and A. Malijevský, *Czech. J. Phys.* **38**, 1234 (1988).  
 [33] C. Vega, S. Lago, and B. Garzón, *Mol. Phys.* **82**, 1233 (1994).  
 [34] T. Boublík, *J. Chem. Phys.* **119**, 7512 (2003).  
 [35] J. Talbot and D. J. Tildesley, *J. Chem. Phys.* **83**, 6419 (1985).  
 [36] C. W. Goulding and M. Rigby, *Mol. Phys.* **75**, 623 (1992).  
 [37] J. E. Mayer, *J. Chem. Phys.* **5**, 67 (1937).  
 [38] J. E. Mayer and M. G. Mayer, *Statistical Mechanics* (Wiley, New York, 1940).  
 [39] F. H. Ree and W. G. Hoover, *J. Chem. Phys.* **41**, 1635 (1964).  
 [40] J. S. Rowlinson, J. Talbot, and D. J. Tildesley, *Mol. Phys.* **54**, 1065 (1985).  
 [41] A. Ishihara, *J. Chem. Phys.* **19**, 397 (1951).

- [42] J. K. Singh and D. A. Kofke, *Phys. Rev. Lett.* **92**, 220601 (2004).
- [43] T. Boublík, *Mol. Phys.* **57**, 287 (1986).
- [44] G. Tarjus, P. Viot, S. M. Ricci, and J. Talbot, *Mol. Phys.* **73**, 773 (1991).
- [45] M. Skoge, A. Donev, F. H. Stillinger, and S. Torquato, *Phys. Rev. E* **74**, 041127 (2006).
- [46] S. Torquato and F. H. Stillinger, *Rev. Mod. Phys.* **82**, 2633 (2010).
- [47] M. Rigby, *Mol. Phys.* **78**, 21 (1993).

### 5.3 Publication III - Virial coefficients of hard, two-dimensional, convex particles up to the eighth order

M. Kulossa, J. Wagner, *Mol. Phys.* **122**, e2289699 (2023).

DOI: 10.1080/00268976.2023.2289699

Type: Full article

© 2023 Taylor & Francis

#### Author contributions

**Markus Kulossa:** Conceptualization, Data curation, Formal analysis, Investigation, Methodology, Software, Validation, Visualization, Writing - original draft preparation, Writing - review and editing

Estimated total contribution in percent: 80 %

**Joachim Wagner:** Conceptualization, Formal analysis, Investigation, Methodology, Project administration, Resources, Supervision, Writing - review and editing

Estimated total contribution in percent: 20 %

Reprinted from M. Kulossa, J. Wagner, *Mol. Phys.* **122**, e2289699 (2023) with the permission of Taylor & Francis.



# Virial coefficients of hard, two-dimensional, convex particles up to the eighth order

Markus Kulossa  and Joachim Wagner 

Institut für Chemie, Universität Rostock, Rostock, Germany

## ABSTRACT

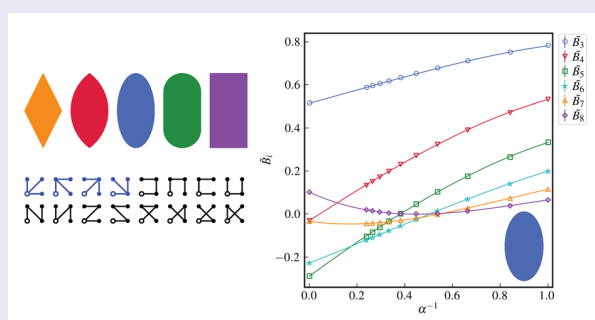
We calculated virial coefficients for hard ellipses, stadia, rectangles, planar lenses and rhombi up to the eighth order employing Mayer-sampling Monte Carlo simulations. We improved and extended available data for ellipses, stadia, and rectangles and provide virial coefficients for planar lenses and rhombi. The influence of the aspect ratio  $\nu$  on the virial coefficients is discussed, including hard discs as the limit of ellipses, stadia, and planar lenses and hard squares as the limit of rectangles and rhombi with aspect ratio  $\nu \rightarrow 1$ . In two dimensions, both in the limit  $\nu \rightarrow 0$  and  $\nu \rightarrow \infty$ , anisotropic figures approach hard needles. The dependence of reduced virial coefficients  $\tilde{B}_i = B_i/B_2^{i-1}$  on the shape parameter  $\alpha = B_2^\nu - 1$ , with  $B_2^\nu = B_2/V_P$  and  $V_P$  the particle area is analysed. The reduced virial coefficients  $\tilde{B}_i(\alpha)$  are approximated as functions of the shape parameter employing third-order polynomials, enabling an interpolation for all aspect ratios  $\nu$ .

## ARTICLE HISTORY

Received 10 July 2023  
Accepted 7 November 2023

## KEYWORDS

Virial coefficients; hard body interaction; convex particles; Mayer-sampling Monte Carlo simulation



## 1. Introduction

The compressibility factor  $Z$  as a quantitative parameter describing the equation of state for gaseous and supercritical fluids can, with the pressure  $p$  and thermal energy  $k_B T$ , be written as


$$Z = \frac{p}{\rho k_B T} = 1 + \sum_{i=2}^{\infty} B_i \rho^{i-1}, \quad (1)$$

a power series in the particle number density  $\rho$ . This power series, originally proposed by Kamerlingh Onnes [1] as a heuristic approach for the equation of state, is known as virial series with the virial coefficients  $B_i$ . Later on, Mayer and Mayer [2,3] derived the virial series employing the grand canonical partition function

and have shown that the virial coefficient of order  $i$  is related to interactions in an  $i$ -particle cluster. Since the free energy of a multi-particle system is related to its equation of state, virial coefficients are also relevant in classical density-functional theory [4–7] and computational chemistry [8].

The first virial coefficients of order two to four have been calculated for hard spheres as a well established model system for condensed matter [9–13]. More than thirty years later, for hard discs as a two-dimensional analogue, these lower-order virial coefficients have been calculated for the first system in an even-dimensional Euclidean space [14–16]. Virial coefficients of hard spheres and discs with order  $i \geq 5$  are so far not analytically accessible. These quantities became available with

**CONTACT** Joachim Wagner  joachim.wagner@uni-rostock.de  Institut für Chemie, Universität Rostock, 18051 Rostock, Germany

 Supplemental data for this article can be accessed online at <https://doi.org/10.1080/00268976.2023.2289699>.

emerging computer performance by the pioneering work of Metropolis *et al.* [17,18] and Ree and Hoover [19,20] up to order  $i=7$ . Nowadays, virial coefficients for hard spheres are available up to order  $i=12$  and for hard discs up to order  $i=14$  [21,22]. The first virial coefficients of hyperspheres in Euclidean spaces with dimension  $D > 3$  have been calculated by Ree and Hoover [23].

Due to their relevance as model systems for liquid-crystalline matter, virial coefficients of non-spherical, hard particles became into the focus of scientific interest. Starting point is the seminal work of Onsager [24] predicting an isotropic-nematic phase transition of infinitely thin, hard rods in the three-dimensional Euclidean space. Since in the case of hard-particle interaction the second virial coefficient is identical to the mutual excluded volume per particle,  $B_2$  for convex shapes is accessible by Minkowski functionals or quermassintegrals as geometric measures of the respective geometry in arbitrary dimension  $D$  [25–27].

With advancing computer simulations, also higher-order virial coefficients for differently shaped, hard particles such as ellipsoids [28–32], spherocylinders [30,31,33,34], lenses [32] in dependence on their aspect ratio, and polytopes [35] became available. Also virial coefficients of concave geometries such as homonuclear dumbbells in the three-dimensional Euclidean space have been reported [34]. Recently, virial coefficients up to order  $i=8$  of planar, homonuclear dumbbells as two-dimensional analogues have been published [36]. In the case of hard, convex particles in the two-dimensional Euclidean space, only virial coefficients of ellipses and stadia up to order  $i=5$  and rectangles up to order  $i=4$  are known for selected aspect ratios [37,38].

The aim of this work is to provide highly accurate virial coefficients up to the eighth order for multiple convex geometries (ellipses, stadia, rectangles, planar lenses, and rhombi) in dependence on their aspect ratio  $\nu$ . Additionally, virial coefficients of hard needles as highly anisotropic limit for both  $\nu \rightarrow \infty$  and  $\nu \rightarrow 0$  are calculated as well as discs and squares for  $\nu \rightarrow 1$  in the case of ellipses, planar lenses and stadia, and rectangles and rhombi, respectively. We systematically investigate the influence of both, the detailed particle shape and aspect ratio on equation-of-state data of anisometric figures in the two-dimensional Euclidean space with impact on self-organisation of monolayers at planar surfaces.

## 2. Theoretical background

### 2.1. Virial theory

As already shown by Langmuir [39], the two-dimensional analogue of the pressure  $p$  is formally a

surface tension  $\gamma$  which can, by the virial series, be expanded in a series

$$\frac{\gamma}{\rho k_B T} = 1 + \sum_{i=2}^{\infty} B_i \rho^{i-1} = 1 + \sum_{i=2}^{\infty} B_i^* \eta^{i-1} \quad (2)$$

of the particle number per area  $\rho = N/A$ . Introducing reduced virial coefficients  $B_i^* = B_i/V_p^{i-1}$  normalised to the  $(i-1)$ th power of the particle area  $V_p$ , an expansion in powers of the area fraction  $\eta = \rho V_p$  is obtained.

For arbitrary dimension  $D$  of an Euclidean space, starting from the grand canonical partition function  $\Xi$ , the virial coefficient of order  $i$  can be written as

$$B_i = -\frac{i-1}{i!} \sum_{G \in \mathbb{M}_i^{\perp}} S_G, \quad (3)$$

where  $S_G$  is the configuration integral of an  $i$ -particle cluster whose interactions are represented by the edges of a biconnected graph  $G$  with  $i$  vertices, called Mayer graph [2,3].  $\mathbb{M}_i^{\perp}$  is the set of labelled Mayer graphs with  $i$  vertices.

Defining the edges  $(j, k)$  connecting vertices  $j$  and  $k$  of a graph as Mayer  $f$ -function

$$f_{jk} = \exp \left[ -\frac{U_{jk}}{k_B T} \right] - 1, \quad (4)$$

the second virial coefficient reads as

$$\begin{aligned} B_2 &= -\frac{1}{2V} \iint \langle f_{12} \rangle_{\hat{\mathbf{u}}_2} d^2 \mathbf{r}_1 d^2 \mathbf{r}_{12} \\ &= -\frac{1}{2} \bullet \text{---} \bullet, \end{aligned} \quad (5)$$

with  $V$  denoting the two-dimensional system volume (area),  $\mathbf{r}_1$  the position of the centre of the first particle,  $\mathbf{r}_{12}$  the centre-to-centre distance vector, and  $U_{jk}$  the pair interaction between particles  $j=1$  and  $k=2$ . Performing the integration over  $\mathbf{r}_1$  results in the two-dimensional system volume  $V$ . In the case of anisotropic particles, the orientational average  $\langle \dots \rangle_{\hat{\mathbf{u}}_2, \dots, \hat{\mathbf{u}}_i}$  over all particle orientations  $\hat{\mathbf{u}}_2, \dots, \hat{\mathbf{u}}_i$  except the first particle defining the coordinate system has to be used as the integrand.

In the case of hard-body interactions, the pair potential reads as

$$U_{12} = \begin{cases} \infty & : r_{12} < \sigma(\hat{\mathbf{r}}_{12}, \hat{\mathbf{u}}_1, \hat{\mathbf{u}}_2) \\ 0 & : r_{12} \geq \sigma(\hat{\mathbf{r}}_{12}, \hat{\mathbf{u}}_1, \hat{\mathbf{u}}_2) \end{cases}, \quad (6)$$

with the unit vector  $\hat{\mathbf{r}}_{12}$  denoting the direction of the distance vector of length  $r_{12}$  between the centres of both particles, the unit vectors  $\hat{\mathbf{u}}_1$  and  $\hat{\mathbf{u}}_2$  their orientations, and  $\sigma(\hat{\mathbf{r}}_{12}, \hat{\mathbf{u}}_1, \hat{\mathbf{u}}_2)$  the contact distance of the given configuration. In the case  $r_{12} < \sigma$ , the particles overlap with

$U_{12} = \infty$  and otherwise,  $r_{12} \geq \sigma$ , they do not overlap with  $U_{12} = 0$ . Hence, the Mayer  $f$ -function is

$$f_{jk} = \begin{cases} -1 & : r_{ij} < \sigma(\hat{\mathbf{r}}_{jk}, \hat{\mathbf{u}}_j, \hat{\mathbf{u}}_k) \\ 0 & : r_{ij} \geq \sigma(\hat{\mathbf{r}}_{jk}, \hat{\mathbf{u}}_j, \hat{\mathbf{u}}_k) \end{cases} \quad (7)$$

Furthermore, for hard body systems the pairwise additive representation of the potential energy

$$U = \sum_j \sum_{k>j} U_{jk}(\mathbf{r}_{jk}, \hat{\mathbf{u}}_j, \hat{\mathbf{u}}_k) \quad (8)$$

for many-particle systems is exact.

This leads to the expression

$$\begin{aligned} B_3 &= -\frac{1}{3V} \iiint \langle f_{12} f_{13} f_{23} \rangle_{\hat{\mathbf{u}}_2, \hat{\mathbf{u}}_3} d^2\mathbf{r}_1 d^2\mathbf{r}_{12} d^2\mathbf{r}_{13} \\ &= -\frac{1}{3} \triangle \end{aligned} \quad (9)$$

for the third virial coefficient with a product of three Mayer  $f$ -functions as integrand. While for the second and third virial coefficients only a single biconnected graph exists, the number of labelled Mayer graphs dramatically increases with the order of virial coefficients [40]. Introducing an additional function  $e_{jk} = f_{jk} + 1$ , Ree and Hoover could reduce for virial coefficients of order  $i > 3$  the number of labelled graphs to be considered to roughly one third of the Mayer graphs [41]. Using these fully, either with  $f$ - or  $e$ -bonds connected graphs, the virial coefficient of order  $i$  reads as

$$B_i = -\frac{i-1}{i!} \sum_{G \in \mathbb{G}_i^L} c_G S_G \quad (10)$$

with  $G$  denoting a labelled Ree-Hoover graph in the set  $\mathbb{G}_i^L$ . The weighting factor  $c_G$  is the Ree-Hoover star content of the graph  $G$  resulting from the reformulation. In the case of hard-body interaction, with  $e_{jk} = 0$  for an overlap and  $e_{jk} = 1$  for a non-overlap, resulting in  $f_{jk} e_{jk} = 0$ , only a single Ree-Hoover graph contributes for a given configuration with overlaps and non-overlaps to the virial coefficient.

## 2.2. Computational details

In the two-dimensional Euclidean space, for the computation of the virial coefficient of order  $i$ , a  $3(i-1)$ -dimensional integration in the configurational space is required. This problem can efficiently be solved employing the Mayer-sampling Monte Carlo method originally proposed by Singh and Kofke [42]. This variant of an umbrella sampling method samples the configurational space exhaustively in regions, where the modulus of the integrand is large. Since the configurational space is

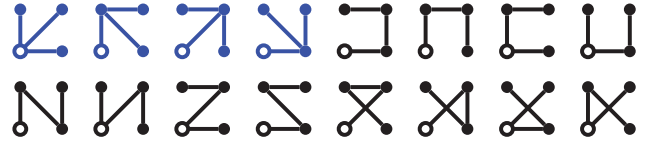


**Figure 1.** Spanning trees with four vertices. The 16 existing spanning trees can be subdivided in two topological classes with one vertex of order 3 and three vertices of order 1 and two vertices of order 2 and 2 vertices of order 1.

inhomogeneously sampled, the parallel computation of an already known reference integral at the same points of the configurational space is required. The statistical fluctuations of this method are minimised and thus its accuracy is increased if the system of interest and the reference system are as similar as possible: For moderately anisotropic particles, the virial coefficient of hard discs of the same order is a suitable reference, whereas for highly anisotropic systems a similar anisotropic shape leads to higher accuracy. As recently shown, for virial coefficients of order  $i \geq 3$  the accuracy can be increased and the computational effort reduced by approximately 50 % by using spanning trees as reference integrals [32]. A spanning tree connecting  $i$  vertices by  $i-1$  Mayer  $f$ -bonds has the value  $(-2B_2)^{i-1}$ . Despite  $i^{i-2}$  spanning trees with  $i$  vertices exists, it is sufficient to use only the topological class of  $i$  spanning trees with one vertex of order  $i-1$  and  $i-1$  vertices of order 1. Exemplarily, in Figure 1 spanning trees with four vertices belonging to two topological classes are displayed. Since the second virial coefficients of convex geometries are analytically known (Section 3.1), the reference integral of a spanning tree is exactly known and does not contribute to the uncertainty of the calculated virial coefficient.

In this work, each virial coefficient is calculated by averaging 16 independent simulation runs with  $5 \times 10^{10}$  configurations sampled in each run. The uncertainty of the result is estimated by the standard deviation between these runs. Before each run, the translational and rotational displacement is adjusted in a tuning phase with  $10^7$  steps to achieve an acceptance rate of  $\approx 0.50$ .

## 3. Geometric measures of two-dimensional convex solids

We calculate virial coefficients of ellipses, stadia, rectangles, planar lenses and rhombi as anisometric, convex geometries. The anisometry is quantified by the aspect ratio  $\nu$ , which is the ratio of height  $h = 2\nu r_{\text{eq}}$  to width  $w = 2r_{\text{eq}}$ . Let us, without loss of generality, restrict  $h \geq w$ , with  $\nu \geq 1$  for all investigated geometries. In the limit  $\nu \rightarrow 1$  ellipses, stadia, and planar lenses approach discs,

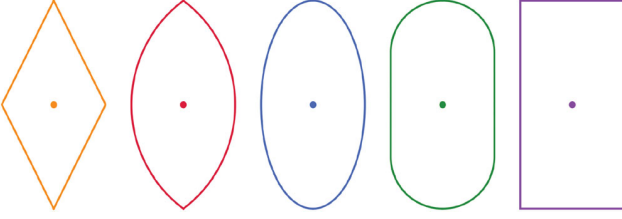


**Figure 2.** Characteristic shapes of a rhombus, planar lens, ellipse, stadium, and rectangle with the aspect ratio  $\nu = 2$  (from left to right).

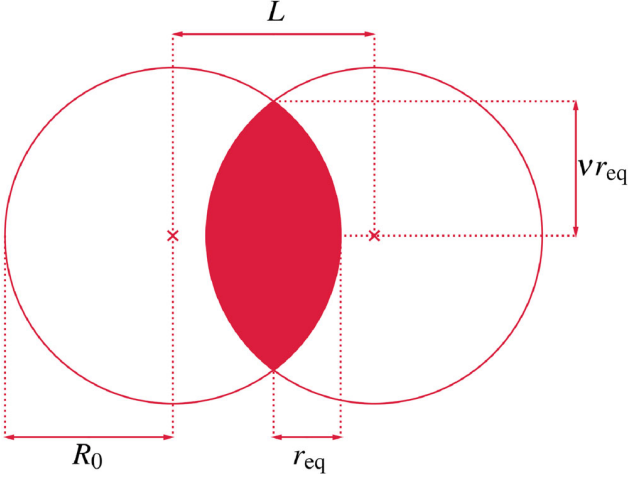


**Figure 3.** Construction of a planar lens with radius  $r_{\text{eq}}$  and aspect ratio  $\nu = 2$  by two circles with radius  $R_0$  and centre-to-centre distance  $L$ .

while rectangles and rhombi become squares. The investigated shapes with  $\nu = 2$  are displayed in Figure 2. In the limit  $\nu \rightarrow \infty$ , all considered geometries approach infinitely thin needles with a characteristic length.

A stadium is the union of a rectangle with height  $h' = 2(\nu - 1)r_{\text{eq}}$  and width  $w = 2r_{\text{eq}}$  capped with two semi-circles with radius  $r_{\text{eq}}$ . The planar lens is the section of two circles with the radius

$$R_0 = \frac{\nu^2 + 1}{2} r_{\text{eq}}, \quad (11)$$

separated by the distance

$$L = 2(R_0 - r_{\text{eq}}) = (\nu^2 - 1)r_{\text{eq}} \quad (12)$$

with  $0 \leq L < 2R_0$  as shown in Figure 3.

The geometric measures area  $V_P$  and perimeter  $S_P$  for the investigated geometries are provided in Table 1.

The circumference of an ellipse can with the complete elliptic integral of the second kind  $E(\lambda)$

$$E(\lambda) = \int_0^{\pi/2} [1 - \lambda^2 \sin^2(t)]^{1/2} dt \quad (13)$$

**Table 1.** Area  $V_P$  and perimeter  $S_P$  for selected geometries in dependence on the height  $h = 2\nu r_{\text{eq}}$  and width  $w = 2r_{\text{eq}}$  of the particles.

	$V_P$	$S_P$
Ellipse	$\pi \nu r_{\text{eq}}^2$	$4\nu r_{\text{eq}} E(\lambda)$
Stadion	$\pi r_{\text{eq}}^2 + 4r_{\text{eq}}^2(\nu - 1)$	$2\pi r_{\text{eq}} + 4r_{\text{eq}}(\nu - 1)$
Rectangle	$4\nu r_{\text{eq}}^2$	$4r_{\text{eq}}(\nu + 1)$
Planar lens	$\frac{1}{4} r_{\text{eq}} (\nu^2 + 1) S_P$ $- r_{\text{eq}}^2 \nu (\nu^2 - 1)$	$2r_{\text{eq}}(\nu^2 + 1) \arccos$ $[1 - 2(\nu^2 + 1)^{-1}]$
Rhombus	$2\nu r_{\text{eq}}^2$	$4r_{\text{eq}}(\nu^2 + 1)^{1/2}$

and

$$\lambda^2 = 1 - \nu^{-2} \quad (14)$$

be written as  $S_P = 4\nu r_{\text{eq}} E(\lambda)$ .

### 3.1. Excluded volume and quermassintegrals

The excluded volume of two convex bodies  $K$  and  $L$  can be written as

$$V_{\text{ex}}(K, L) = \frac{1}{\kappa_D} \sum_{j=0}^D \binom{D}{j} W_{D-j}(K) W_j(L) \quad (15)$$

with

$$\kappa_D = \frac{\pi^{D/2}}{\Gamma(1 + D/2)} \quad (16)$$

being the volume of a  $D$ -dimensional unit sphere [26]. For  $D = 2$ , this leads for identical shapes  $K = L$  to

$$V_{\text{ex}}(K) = \frac{1}{\pi} [2W_0(K)W_2(K) + 2W_1(K)^2], \quad (17)$$

where  $W_j$  are the quermassintegrals of the body  $K$ , which are also referred as Minkowski functionals or intrinsic volumes. For the calculation of the quermassintegrals some special cases occur as shown, e.g. by Torquato and Jiao [26], which can be formulated as

$$W_0(K) = V_P(K), \quad (18a)$$

$$W_1(K) = \frac{1}{D} S_P(K), \quad (18b)$$

$$W_{D-1}(K) = \kappa_D \tilde{R}_P(K), \quad (18c)$$

and

$$W_D(K) = \kappa_D, \quad (18d)$$

where  $V_P$  is the volume,  $S_P$  the surface area and  $\tilde{R}_P$  the mean radius of curvature of the convex particle  $K$ .

In the two-dimensional Euclidean space  $\mathbb{R}^2$ , the particle Volume  $V_P$  is often simply referred as area and the

surface area  $S_p$  as perimeter. In  $\mathbb{R}^2$ , the mean radius of curvature  $\tilde{R}_p$  directly relates to the perimeter as

$$\tilde{R}_p = \frac{S_p}{2\pi} \quad (19)$$

[Equations (18b) and (18c)]. Using Equations (17) and (18), the excluded volume  $V_{\text{ex}}$  can be reformulated as

$$V_{\text{ex}} = 2V_p + S_p \tilde{R}_p = 2V_p + \frac{S_p^2}{4\pi} \quad (20)$$

for arbitrary, two-dimensional convex bodies  $K$ .

Since in the case of hard bodies the second virial coefficient is the excluded volume per particle ( $B_2 = V_{\text{ex}}/2$ ),

$$B_2 = V_p + \frac{S_p^2}{4\pi} \quad (21)$$

is obtained as the second virial coefficient, which is identical to the expression provided by Boublík [37,43].

For the analytical calculation of the second virial coefficients for arbitrary, two-dimensional, convex geometries only the geometric measures  $V_p$  and  $S_p$  need to be calculated. For the selected shapes these are compiled in Table 1 in dependence on the aspect ratio  $\nu$  and radius  $r_{\text{eq}}$ .

### 3.2. Overlap criteria

For the calculation of virial coefficients with order  $i \geq 3$ , the contact function  $\sigma(\hat{\mathbf{r}}_{12}, \hat{\mathbf{u}}_1, \hat{\mathbf{u}}_2)$  [Equation (6)] for the given geometry is required which depends on the direction  $\hat{\mathbf{r}}_{12}$  of the distance vector  $\mathbf{r}_{12} = \mathbf{c}_2 - \mathbf{c}_1$  between the centres  $\mathbf{c}_1$  and  $\mathbf{c}_2$  of the particles and their orientations denoted by the unit vectors  $\hat{\mathbf{u}}_1$  and  $\hat{\mathbf{u}}_2$ . In the following, the overlap criteria for the investigated geometries are discussed.

#### 3.2.1. Stadia and needles

The overlap criterion of two hard stadia with centres  $\mathbf{c}_1$ ,  $\mathbf{c}_2$  and orientations  $\hat{\mathbf{u}}_1$ ,  $\hat{\mathbf{u}}_2$  can be reduced to the determination of the minimum distance  $d_{\text{min}}$  between two hard rods described by

$$\mathbf{r}_1(\lambda) = \mathbf{c}_1 + \lambda \hat{\mathbf{u}}_1 \quad (22)$$

and

$$\mathbf{r}_2(\mu) = \mathbf{c}_2 + \mu \hat{\mathbf{u}}_2 \quad (23)$$

under the constraints  $|\lambda| \leq (\nu - 1)r_{\text{eq}}$  and  $|\mu| \leq (\nu - 1)r_{\text{eq}}$ . The minimum squared distance

$$d^2(\lambda, \mu) = [\mathbf{r}_2(\mu) - \mathbf{r}_1(\lambda)]^2 \quad (24)$$

occurs at the roots of the derivatives  $\partial d^2(\lambda, \mu)/\partial \lambda$  and  $\partial d^2(\lambda, \mu)/\partial \mu$  as analogously described by Vega and Lago [44] in  $\mathbb{R}^3$ . This criterion can be adapted for Euclidean spaces with arbitrary dimension  $\mathbb{R}^D$  [27]. If  $d_{\text{min}} < 2r_{\text{eq}}$ , two stadia overlap and otherwise not.

The limiting case of hard needles with  $\nu \rightarrow \infty$  can formally be described as stadia with  $r_{\text{eq}} \rightarrow 0$  and length  $l = 1$  leading to the constraints  $|\lambda| \leq l/2$  and  $|\mu| \leq l/2$ . An overlap of needles occurs when  $d_{\text{min}} = 0$  while at  $d_{\text{min}} > 0$  needles do not overlap.

#### 3.2.2. Ellipses

For the overlap criterion of hard ellipses, the well established Perram-Wertheim algorithm for hard ellipsoids [45] can be employed, restricting centres  $\mathbf{c}_1$ ,  $\mathbf{c}_2$ , and orientations  $\hat{\mathbf{u}}_1$ ,  $\hat{\mathbf{u}}_2$  of the ellipsoids to a fixed plane. However, due to higher numerical stability, in this work, the overlap algorithm proposed by Gilitschenski and Hanebeck for arbitrary  $D$ -dimensional hyperellipsoids [46] is used instead. We summarise their algorithm as follows.

An ellipse with centre at  $\mathbf{c}$  and orientation  $\hat{\mathbf{u}}^T = [-b, a]$  can be written as

$$(\mathbf{r} - \mathbf{c})^T \underline{\mathbf{R}}^T \underline{\mathbf{A}}_0 \underline{\mathbf{R}} (\mathbf{r} - \mathbf{c}) \leq 1 \quad (25)$$

with the rotation matrix

$$\underline{\mathbf{R}} = \begin{bmatrix} a & b \\ -b & a \end{bmatrix} \quad (26)$$

and the shape matrix

$$\underline{\mathbf{A}}_0 = \begin{bmatrix} \frac{1}{r_{\text{eq}}^2} & 0 \\ 0 & \frac{1}{r_{\text{eq}}^2 \nu^2} \end{bmatrix} \quad (27)$$

of an ellipse with the half axes  $r_{\text{eq}}$  and  $\nu r_{\text{eq}}$ . The rotation matrix  $\underline{\mathbf{R}}$  fulfils the conditions  $\underline{\mathbf{R}}^T \underline{\mathbf{R}} = \underline{\mathbf{I}}$  with  $\underline{\mathbf{I}}$  denoting matrix identity and  $\det(\underline{\mathbf{R}}) = 1$ .

With

$$\underline{\mathbf{A}}_j = \underline{\mathbf{R}}^T \underline{\mathbf{A}}_0 \underline{\mathbf{R}}, \quad (28)$$

the polynomial function  $K(\lambda)$  for a configuration of two ellipses can be written as

$$K(\lambda) = 1 - \lambda \mathbf{c}_1^T \underline{\mathbf{A}}_1 \mathbf{c}_1 - (1 - \lambda) \mathbf{c}_2^T \underline{\mathbf{A}}_2 \mathbf{c}_2 + \mathbf{m}^T \underline{\mathbf{E}}_\lambda \mathbf{m} \quad (29)$$

with  $\lambda \in \mathbb{R}$  and  $0 \leq \lambda \leq 1$ .

To obtain

$$\mathbf{m}^T \underline{\mathbf{E}}_\lambda \mathbf{m} = [\lambda \underline{\mathbf{A}}_1 \mathbf{c}_1 + (1 - \lambda) \underline{\mathbf{A}}_2 \mathbf{c}_2]^T \underline{\mathbf{E}}_\lambda^{-1} \cdot [\lambda \underline{\mathbf{A}}_1 \mathbf{c}_1 + (1 - \lambda) \underline{\mathbf{A}}_2 \mathbf{c}_2], \quad (30)$$

the inverse of

$$\underline{\mathbf{E}}_\lambda = \lambda \underline{\mathbf{A}}_1 + (1 - \lambda) \underline{\mathbf{A}}_2 \quad (31)$$

is required. Using  $\underline{\mathbf{M}} = \underline{\mathbf{A}}_1 - \underline{\mathbf{A}}_2$  and  $\underline{\mathbf{X}} = -\underline{\mathbf{A}}_2$ , the inverse  $\underline{\mathbf{E}}_\lambda^{-1}$  can be rewritten as

$$\underline{\mathbf{E}}_\lambda^{-1} = [\lambda (\underline{\mathbf{A}}_1 - \underline{\mathbf{A}}_2) + \underline{\mathbf{A}}_2]^{-1} = (\lambda \underline{\mathbf{M}} - \underline{\mathbf{X}})^{-1} \quad (32)$$

which analytically can be inverted by Leverrier's algorithm [47] (see Appendix). If  $\exists \lambda : K(\lambda) < 0$ , two ellipses do not overlap, otherwise they overlap.

### 3.2.3. Rectangles and rhombi

For all  $D$ -dimensional, convex polytopes, a possible overlap can be determined using a  $(D - 1)$ -dimensional plane of separation. For rectangles and rhombi in  $\mathbb{R}^2$ , a line of separation is the criterion for an overlap or non-overlap. If all polygonal faces of the first  $D$ -dimensional convex polytope are located at one side of a  $(D - 1)$ -dimensional plane of separation and all polygonal faces of the second convex polytope are at the opposite side of that plane, these polytopes do not overlap. If a plane of separation does not exist, both polytopes overlap.

If at least one polygonal face of a polytope is in a plane of separation, both polytopes do not overlap. Opposite, if none of the polygonal faces is in a separation plane, an overlap exists.

If a plane defined by a polytope's face is a plane of separation, all vertices not contained in that face have to be separated by that plane from all vertices of the second polytope. In  $\mathbb{R}^2$ , a face is the edge of a polygon.

Both, rectangles and rhombi are convex quadrilaterals. Let  $\mathbf{e}_{12} = (x_2 - x_1, y_2 - y_1)$  be the edge between the vertices  $(x_1, y_1)$  and  $(x_2, y_2)$ . Two points  $\mathbf{r}_i = (x_i, y_i)$  and  $\mathbf{r}_j = (x_j, y_j)$  are located at the same side of the edge, if  $t_i$  and  $t_j$  with

$$\begin{aligned} t_i &= (y_i - y_1)(x_2 - x_1) - (y_2 - y_1)(x_i - x_1) \\ t_j &= (y_j - y_1)(x_2 - x_1) - (y_2 - y_1)(x_j - x_1) \end{aligned} \quad (33)$$

have the same sign. The positions of the four vertices of a rectangle are

$$\begin{aligned} \mathbf{A}_j &= \mathbf{c}_j - r_{\text{eq}}(1 + \nu^2)^{1/2} \\ &\times \begin{bmatrix} \nu(1 + \nu^2)^{-1/2} & -(1 + \nu^2)^{-1/2} \\ (1 + \nu^2)^{-1/2} & \nu(1 + \nu^2)^{-1/2} \end{bmatrix} \cdot \hat{\mathbf{u}}_j \end{aligned} \quad (34a)$$

$$\begin{aligned} \mathbf{B}_j &= \mathbf{c}_j + r_{\text{eq}}(1 + \nu^2)^{1/2} \\ &\times \begin{bmatrix} \nu(1 + \nu^2)^{-1/2} & (1 + \nu^2)^{-1/2} \\ -(1 + \nu^2)^{-1/2} & \nu(1 + \nu^2)^{-1/2} \end{bmatrix} \cdot \hat{\mathbf{u}}_j \end{aligned} \quad (34b)$$

$$\begin{aligned} \mathbf{C}_j &= \mathbf{c}_j + r_{\text{eq}}(1 + \nu^2)^{1/2} \\ &\times \begin{bmatrix} \nu(1 + \nu^2)^{-1/2} & -(1 + \nu^2)^{-1/2} \\ (1 + \nu^2)^{-1/2} & \nu(1 + \nu^2)^{-1/2} \end{bmatrix} \cdot \hat{\mathbf{u}}_j \end{aligned} \quad (34c)$$

$$\begin{aligned} \mathbf{D}_j &= \mathbf{c}_j - r_{\text{eq}}(1 + \nu^2)^{1/2} \\ &\times \begin{bmatrix} \nu(1 + \nu^2)^{-1/2} & (1 + \nu^2)^{-1/2} \\ -(1 + \nu^2)^{-1/2} & \nu(1 + \nu^2)^{-1/2} \end{bmatrix} \cdot \hat{\mathbf{u}}_j \end{aligned} \quad (34d)$$

with the centre  $\mathbf{c}_j$  and the orientation  $\hat{\mathbf{u}}_j$ . For rhombi, the vertices are

$$\mathbf{A}_j = \mathbf{c}_j + r_{\text{eq}} \begin{bmatrix} 0 & 1 \\ -1 & 0 \end{bmatrix} \cdot \hat{\mathbf{u}}_j \quad (35a)$$

$$\mathbf{B}_j = \mathbf{c}_j + \nu r_{\text{eq}} \hat{\mathbf{u}}_j \quad (35b)$$

$$\mathbf{C}_j = \mathbf{c}_j - r_{\text{eq}} \begin{bmatrix} 0 & 1 \\ -1 & 0 \end{bmatrix} \cdot \hat{\mathbf{u}}_j \quad (35c)$$

$$\mathbf{D}_j = \mathbf{c}_j - \nu r_{\text{eq}} \hat{\mathbf{u}}_j. \quad (35d)$$

### 3.2.4. Planar lenses

As described earlier, a planar lens with aspect ratio  $\nu$  and radius  $r_{\text{eq}}$  consists of two intersecting circles with radius

$$R_0 = \frac{\nu^2 + 1}{2} r_{\text{eq}}$$

[see Equation (11)], separated by the centre-to-centre distance

$$L = 2(R_0 - r_{\text{eq}}) = (\nu^2 - 1)r_{\text{eq}}$$

[see Equation (12)]. The generating circles of a planar lens with centre  $\mathbf{r}_i$  and orientation  $\hat{\mathbf{u}}_i$  are at

$$\mathbf{c}_{i\pm} = \mathbf{r}_i \pm \zeta \underline{\mathbf{R}} \cdot \hat{\mathbf{u}}_i \quad (36)$$

with  $\zeta = R_0 - r_{\text{eq}}$  and the rotation matrix

$$\underline{\mathbf{R}} = \begin{bmatrix} 0 & -1 \\ 1 & 0 \end{bmatrix}. \quad (37)$$

Let

$$d_{\text{max}} = \|\mathbf{r}_2 - \mathbf{r}_1 \pm \zeta \underline{\mathbf{R}} \cdot \hat{\mathbf{u}}_2 \mp \zeta \underline{\mathbf{R}} \cdot \hat{\mathbf{u}}_1\| \quad (38)$$

be the maximum distance between the four generating circles. If  $d_{\text{max}} \geq 2R_0$ , an overlap is impossible. Otherwise,

$$\mathbf{P}_1 = \begin{bmatrix} -\frac{p}{2} + \left(\frac{p^2}{4} - q\right)^{1/2} \\ a + \frac{bp}{2} - b\left(\frac{p^2}{4} - q\right)^{1/2} \end{bmatrix} \quad (39)$$

and

$$\mathbf{P}_2 = \begin{bmatrix} -\frac{p}{2} - \left(\frac{p^2}{4} - q\right)^{1/2} \\ a + \frac{bp}{2} + b\left(\frac{p^2}{4} - q\right)^{1/2} \end{bmatrix} \quad (40)$$

with

$$a = \frac{c_{2x}^2 + c_{2y}^2 - c_{1x}^2 - c_{1y}^2}{2(c_{2y} - c_{1y})}, \quad (41a)$$

$$b = \frac{c_{2x} - c_{1x}}{c_{2y} - c_{1y}}, \quad (41b)$$

$$p = \frac{2bc_{1y} - 2c_{1x} - 2ab}{b^2 + 1}, \quad (41c)$$

$$q = \frac{c_{1x}^2 + c_{1y}^2 - 2ac_{1y} + a^2 - R_0^2}{b^2 + 1} \quad (41d)$$

are the sections of both generating circles with distance  $d_{\max}$ . If  $c_{1y} = c_{2y}$ , the circles are parallelly aligned to the  $x$ -axis and

$$\mathbf{P}_1 = \begin{bmatrix} \frac{1}{2}(c_{1x} + c_{2x}) \\ c_{1y} + \nu r_{\text{eq}} \end{bmatrix}, \quad (42a)$$

$$\mathbf{P}_2 = \begin{bmatrix} \frac{1}{2}(c_{1x} + c_{2x}) \\ c_{1y} - \nu r_{\text{eq}} \end{bmatrix} \quad (42b)$$

result.

If at least one point of  $\mathbf{P}_1$  and  $\mathbf{P}_2$  is inside both planar lenses, they overlap. This is fulfilled when  $(\|\mathbf{P}_1 - \mathbf{c}_1\| < \nu r_{\text{eq}} \wedge \|\mathbf{P}_1 - \mathbf{c}_2\| < \nu r_{\text{eq}}) \vee (\|\mathbf{P}_2 - \mathbf{c}_1\| < \nu r_{\text{eq}} \wedge \|\mathbf{P}_2 - \mathbf{c}_2\| < \nu r_{\text{eq}})$  and otherwise not. In Figure 4, a configuration with  $d_{\max} < 2R_0$  is shown where planar lenses do not overlap.

## 4. Results and discussion

### 4.1. Second virial coefficient

The reduced, second virial coefficients

$$B_2^* = \frac{B_2}{V_p} = 1 + \frac{1}{4\pi} \frac{S_p^2}{V_p} \quad (43)$$

of hard, two-dimensional, convex particles are analytically available from the area  $V_p$  and perimeter  $S_p$  as geometric measures of the respective geometry employing Equation (21). The analytically obtained, reduced second virial coefficients of ellipses, stadia, rectangles, planar lenses, and rhombi for selected aspect ratios are compiled in Table 2. These analytical data are compared to the results obtained by means of Mayer-sampling Monte Carlo simulations. The excellent agreement of analytical

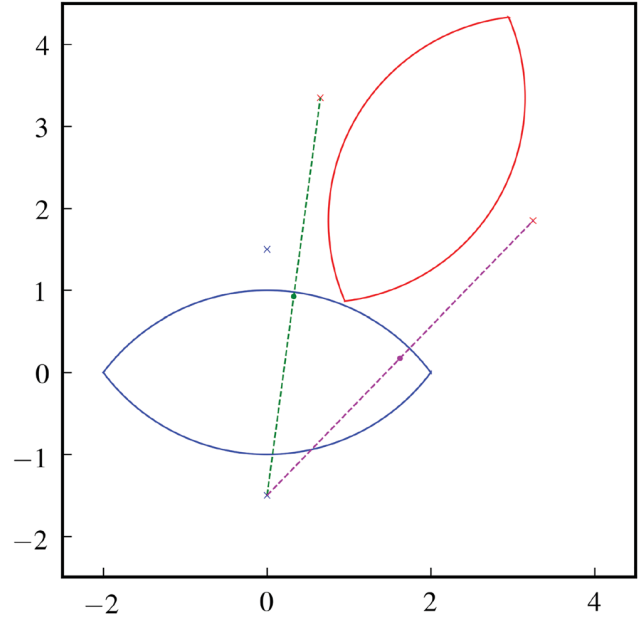


**Figure 4.** Configuration of two planar lenses with  $\nu = 2$ ,  $r_{\text{eq}} = 1$ ,  $\mathbf{r}_{12} = (1.95, 2.6)$ ,  $\hat{\mathbf{u}}_1 = (1, 0)$ , and  $\hat{\mathbf{u}}_2 = (\frac{1}{2}, \frac{\sqrt{3}}{2})$ . The centres of the planar lens' generating circles are indicated by crosses. The dotted lines whose central points are marked by dots indicate distances between these centres.

and numerical data is a validation of both, the overlap criterion, and the algorithm used. In Figure 5, the reduced virial coefficients for these geometries with an aspect ratio  $\nu \leq 10$  are shown. Due to the normalisation to the particle area  $V_p$ , the influence of the detailed geometry is visible: The reduced excluded area of rhombi exceeds those of all other shapes investigated. Despite the similar shape of ellipses and planar lenses, with increasing aspect ratio, the reduced virial coefficients of planar lenses exceed those of ellipses since  $S_p^2/V_p$  increases faster with increasing aspect ratio for planar lenses than for ellipses. In the limit  $\nu \rightarrow 1^+$ , both geometries as well as stadia approach to discs with  $B_{2,\text{disc}}^* = 2$ . However, rectangles and rhombi approach squares in the limit  $\nu \rightarrow 1$  with  $B_{2,\text{square}}^* = 1 + 4/\pi$ . Opposite, in the limit  $\nu \rightarrow \infty$ , all geometries approach hard, infinitely thin needles of length  $l$  with  $B_2 = l^2/\pi$ . Hard needles as one-dimensional objects can in  $\mathbb{R}^2$  be treated like stadia with a modified overlap criterion (Section 3.2.1).

For sufficiently large aspect ratios, the reduced second virial coefficients  $B_2^*(\nu) \propto \nu$  are proportional to the aspect ratio with

$$\lim_{\nu \rightarrow \infty} \frac{B_2^{*,(\text{stad})}(\nu)}{\nu} = \frac{1}{\pi}, \quad (44a)$$

$$\lim_{\nu \rightarrow \infty} \frac{B_2^{*,(\text{rect})}(\nu)}{\nu} = \frac{1}{\pi}, \quad (44b)$$

**Table 2.** Reduced second virial coefficients  $B_2^* = B_2/V_P$  of ellipses, stadia, rectangles, planar lenses, and rhombi in dependence on their aspect ratio  $\nu$ .

$\nu$	$B_2^*$				
	Ellipse	Stadion	Rectangle	Planar lens	Rhombus
1	2	2	2.2732395... 2.273240 (11)	2	2.2732395... 2.273236 (16)
2	2.1888271... 2.188825 (13)	2.1782850... 2.178284 (14)	2.4323944... 2.432392 (20)	2.2238322... 2.223831 (14)	2.5915494... 2.591541 (24)
3	2.5081689... 2.508172 (25)	2.4571122... 2.457123 (20)	2.6976527... 2.697659 (24)	2.6123451... 2.612358 (19)	3.1220659... 3.12207 (5)
4	2.8640392... 2.864049 (21)	2.7567999... 2.75681 (4)	2.9894367... 2.989428 (30)	3.0449732... 3.044973 (26)	3.7056340... 3.70564 (7)
5	3.2362698... 3.23626 (12)	3.0642705... 3.06427 (5)	3.2918311... 3.29185 (4)	3.4954664... 3.49547 (5)	4.3104228... 4.31040 (7)
6	3.6175228... 3.61753 (15)	3.3754882... 3.37549 (5)	3.5995307... 3.59952 (5)	3.9549296... 3.95492 (8)	4.9258219... 4.92583 (7)
7	4.0043790... 4.00437 (16)	3.6887963... 3.68882 (6)	3.9102618... 3.91028 (6)	4.4195283... 4.41951 (6)	5.5472840... 5.54729 (8)
8	4.3949948... 4.39506 (14)	4.0033894... 4.00339 (5)	4.2228875... 4.22288 (6)	4.8873400... 4.88731 (9)	6.1725356... 6.17254 (9)
9	4.7882751... 4.78832 (20)	4.3188286... 4.31882 (8)	4.5367765... 4.53679 (8)	5.3572950... 5.35731 (9)	6.8003134... 6.80035 (11)
10	5.1835228... 5.18350 (23)	4.6348545... 4.63489 (7)	4.8515496... 4.85159 (7)	5.8287510... 5.82876 (14)	7.4298597... 7.42986 (14)

Note: For each aspect ratio the values in the first row display the analytical results from Equation (43) and the second row the numerical results from Mayer-sampling Monte Carlo simulations.

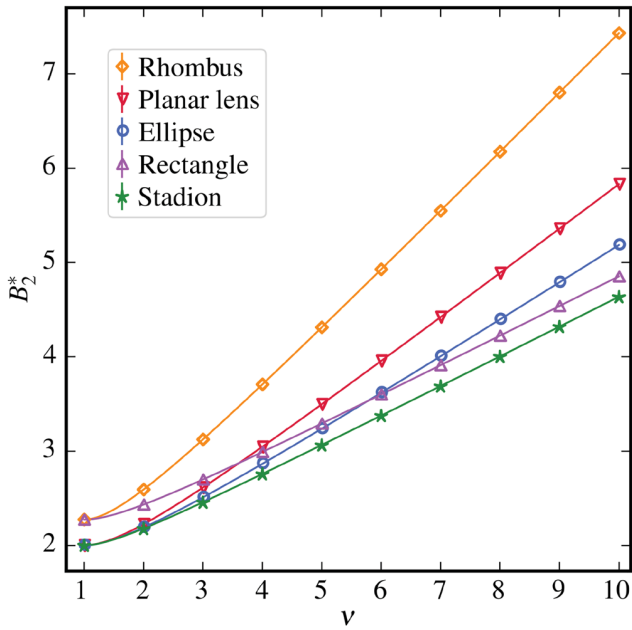


**Figure 5.** Reduced second virial coefficients  $B_2^* = B_2/V_P$  of hard rhombi, planar lenses, ellipses, rectangles and stadia for selected aspect ratios  $\nu$ . Analytical values [Equation (43)] are shown as solid lines and numerical values obtained by Mayer-sampling Monte Carlo simulations as open symbols. The deviations are compiled in Table 2.

$$\lim_{\nu \rightarrow \infty} \frac{B_2^{*,(\text{ell})}(\nu)}{\nu} = \frac{4}{\pi^2}, \quad (44c)$$

$$\lim_{\nu \rightarrow \infty} \frac{B_2^{*,(\text{pl})}(\nu)}{\nu} = \frac{3}{2\pi}, \quad (44d)$$

and

$$\lim_{\nu \rightarrow \infty} \frac{B_2^{*,(\text{rhomb})}(\nu)}{\nu} = \frac{2}{\pi}. \quad (44e)$$

As expected, in the limit  $\nu \rightarrow \infty$ , the reduced second virial coefficients of stadia are identical to those of rectangles since the contribution of the capping semicircles can be neglected for sufficiently long stadia.

#### 4.2. Higher-order virial coefficients

Reduced, higher-order virial coefficients  $B_i^* = B_i/V_P^{i-1}$  of ellipses, planar lenses, stadia, rectangles, and rhombi are compiled in Tables 3–7. For hard needles as the limit of all investigated geometries in this work with  $\nu \rightarrow \infty$ , reduced virial coefficients  $\tilde{B}_i = B_i/B_2^{i-1}$  are provided in Table 8. For all shapes, the data of this work excellently agrees with known literature data [37,38], however with significantly improved accuracy. So far unknown, higher-order virial coefficients are systematically calculated up to the eighth order in dependence on the aspect ratio  $\nu$ . Despite the numerical data in our work for hard needles agree with previously reported numerical results [38], discrepancies to the analytical result [37] within the confidence of our numerical data exist.

In analogy to three- and four-dimensional Euclidean spaces, at large aspect ratios negative higher-order virial coefficients appear [27,31,32,34]. The critical aspect ratio  $\nu_{\text{crit}}$  leading to negative virial coefficients increases from rhombi, planar lenses, and ellipses to rectangles and stadia related to increasing curvature at the elongated axis.

**Table 3.** Reduced virial coefficients  $B_i^* = B_i/V_p^{i-1}$  of hard ellipses in dependence on their aspect ratio  $\nu$ .

$\nu$	$B_3^*$	$B_4^*$	$B_5^*$	$B_6^*$	$B_7^*$	$B_8^*$
1	3.12799 (6)	4.25777 (23)	5.3370 (4)	6.3625 (8)	7.3520 (21)	8.321 (9)
2	3.128017... <sup>a</sup>	4.257854... <sup>a</sup>	5.33689664 (64) <sup>a</sup>	6.363026 (11) <sup>a</sup>	7.352080 (28) <sup>a</sup>	8.318668 (62) <sup>a</sup>
3	3.59622 (10)	4.94310 (24)	6.0753 (5)	7.0261 (9)	7.946 (5)	9.01 (4)
4	3.5961 (15) <sup>b</sup>	4.950 (11) <sup>b</sup>	6.06 (5) <sup>b</sup>			
5	3.593 (5) <sup>c</sup>	4.939 (21) <sup>c</sup>				
6	4.46471 (10)	6.1635 (6)	6.9348 (9)	6.787 (5)	6.668 (20)	7.89 (15)
7	4.4647 (19) <sup>b</sup>	6.169 (16) <sup>b</sup>	6.97 (8) <sup>b</sup>			
8	5.54971 (17)	7.6062 (6)	6.8812 (19)	2.735 (9)	-1.22 (7)	3.1 (6)
9	5.5475 (25) <sup>b</sup>	7.588 (24) <sup>b</sup>	6.86 (14) <sup>b</sup>			
10	5.553 (9) <sup>c</sup>	7.59 (5) <sup>c</sup>				
11	6.81920 (30)	9.1990 (10)	4.988 (5)	-9.108 (24)	-22.73 (20)	-2.5 (21)
12	6.817 (4) <sup>b</sup>	9.19 (4) <sup>b</sup>	4.94 (22) <sup>b</sup>			
13	6.818 (11) <sup>c</sup>	9.22 (7) <sup>c</sup>				
14	8.26395 (28)	10.9071 (9)	0.181 (8)	-34.32 (5)	-68.4 (5)	3 (5)
15	8.264 (4) <sup>b</sup>	10.89 (5) <sup>b</sup>	0.2 (4) <sup>b</sup>			
16	8.258 (14) <sup>c</sup>	10.89 (10) <sup>c</sup>				
17	9.8800 (4)	12.7066 (16)	-8.790 (12)	-80.67 (9)	-153.7 (10)	67 (17)
18	11.6664 (5)	14.5789 (27)	-23.359 (11)	-157.95 (15)	-298.6 (19)	270 (50)
19	11.642 (6) <sup>b</sup>	14.43 (9) <sup>b</sup>	-23.9 (8) <sup>b</sup>			
20	13.6219 (5)	16.5092 (19)	-45.157 (26)	-278.94 (25)	-530 (5)	810 (90)
21	15.7462 (8)	18.478 (4)	-76.00 (5)	-458.9 (4)	-884 (6)	1880 (190)
22	15.748 (9) <sup>b</sup>	18.4 (2) <sup>b</sup>	-75.8 (15) <sup>b</sup>			

<sup>a</sup>Value from [40]<sup>b</sup>Value from [38]<sup>c</sup>Value from [37]**Table 4.** Reduced virial coefficients  $B_i^* = B_i/V_p^{i-1}$  of planar lenses in dependence on their aspect ratio  $\nu$ .

$\nu$	$B_3^*$	$B_4^*$	$B_5^*$	$B_6^*$	$B_7^*$	$B_8^*$
1	3.12804 (8)	4.25781 (25)	5.3368 (5)	6.3633 (10)	7.3518 (16)	8.318 (10)
2	3.128017... <sup>a</sup>	4.257854... <sup>a</sup>	5.33689664 (64) <sup>a</sup>	6.363026 (11) <sup>a</sup>	7.352080 (28) <sup>a</sup>	8.318668 (62) <sup>a</sup>
3	3.70315 (8)	5.1400 (4)	6.3479 (7)	7.3334 (19)	8.240 (5)	9.21 (4)
4	4.79564 (11)	6.7005 (5)	7.3796 (12)	6.761 (7)	6.330 (17)	8.52 (24)
5	6.17692 (21)	8.4973 (5)	6.5653 (26)	-1.036 (13)	-7.13 (8)	6.7 (8)
6	7.81020 (27)	10.4278 (14)	2.078 (8)	-24.495 (23)	-46.42 (23)	23 (5)
7	9.6857 (4)	12.4518 (17)	-8.162 (9)	-75.81 (7)	-132.9 (7)	132 (13)
8	11.8001 (5)	14.5403 (27)	-26.594 (19)	-171.73 (17)	-298.7 (15)	490 (110)
9	14.1516 (7)	16.6740 (27)	-55.978 (30)	-334.08 (29)	-592 (4)	1440 (120)
10	16.7395 (9)	18.829 (4)	-99.44 (4)	-591.0 (4)	-1070 (5)	3540 (170)
11	19.5631 (9)	20.987 (4)	-160.55 (6)	-976.2 (7)	-1811 (13)	7700 (600)

<sup>a</sup>Value from [40]**Table 5.** Reduced virial coefficients  $B_i^* = B_i/V_p^{i-1}$  of hard stadia in dependence on their aspect ratio  $\nu$ .

$\nu$	$B_3^*$	$B_4^*$	$B_5^*$	$B_6^*$	$B_7^*$	$B_8^*$
1	3.12803 (6)	4.25781 (23)	5.3367 (5)	6.3630 (11)	7.3526 (19)	8.315 (11)
2	3.128017... <sup>a</sup>	4.257854... <sup>a</sup>	5.33689664 (64) <sup>a</sup>	6.363026 (11) <sup>a</sup>	7.352080 (28) <sup>a</sup>	8.318668 (62) <sup>a</sup>
3	3.58548 (9)	4.96478 (20)	6.1581 (4)	7.1502 (15)	8.022 (4)	8.86 (4)
4	3.5843 (15) <sup>b</sup>	4.961 (11) <sup>b</sup>	6.15 (5) <sup>b</sup>			
5	3.587 (5) <sup>c</sup>	4.930 (21) <sup>c</sup>				
6	4.35851 (11)	6.1491 (4)	7.3115 (11)	7.7567 (26)	7.911 (15)	8.35 (12)
7	4.3566 (19) <sup>b</sup>	6.142 (15) <sup>b</sup>	7.29 (8) <sup>b</sup>			
8	5.27623 (15)	7.5506 (5)	8.2301 (18)	6.829 (7)	4.689 (27)	4.4 (4)
9	5.2766 (23) <sup>b</sup>	7.543 (21) <sup>b</sup>	8.20 (12) <sup>b</sup>			
10	5.236 (8) <sup>c</sup>	7.56 (5) <sup>c</sup>				
11	6.31242 (20)	9.1236 (8)	8.537 (4)	2.833 (11)	-4.75 (9)	-5.9 (13)
12	6.3071 (29) <sup>b</sup>	9.121 (29) <sup>b</sup>	8.64 (18) <sup>b</sup>			
13	6.310 (10) <sup>c</sup>	9.15 (6) <sup>c</sup>				
14	7.45958 (20)	10.8501 (10)	7.824 (4)	-6.292 (24)	-24.97 (20)	-24 (4)
15	7.456 (4) <sup>b</sup>	10.81 (4) <sup>b</sup>	7.79 (26) <sup>b</sup>			
16	7.463 (12) <sup>c</sup>	10.88 (8) <sup>c</sup>				
17	8.71429 (23)	12.7211 (12)	5.630 (6)	-23.21 (5)	-62.0 (5)	-46 (11)
18	10.0755 (5)	14.7273 (21)	1.411 (12)	-51.39 (6)	-124.4 (7)	-80 (14)
19	10.076 (5) <sup>b</sup>	14.69 (7) <sup>b</sup>	1.0 (6) <sup>b</sup>			
20	11.5423 (6)	16.8625 (18)	-5.428 (11)	-95.13 (10)	-222.9 (10)	-99 (26)
21	13.1142 (6)	19.1200 (21)	-15.582 (14)	-159.37 (13)	-370.8 (21)	-100 (50)
22	13.119 (7) <sup>b</sup>	19.12 (10) <sup>b</sup>	-15.7 (10) <sup>b</sup>			

<sup>a</sup>Value from [40]<sup>b</sup>Value from [38]<sup>c</sup>Value from [37]

**Table 6.** Reduced virial coefficients  $B_i^* = B_i/V_p^{i-1}$  of hard rectangles in dependence on their aspect ratio  $\nu$ .

$\nu$	$B_3^*$	$B_4^*$	$B_5^*$	$B_6^*$	$B_7^*$	$B_8^*$
1	3.98333 (10) 3.98 (2) <sup>a</sup>	5.94843 (25) 5.94 (8) <sup>a</sup>	7.9507 (6)	9.7521 (15)	11.103 (5)	11.766 (22)
2	4.43409 (14) 4.44 (2) <sup>a</sup>	6.6993 (4) 6.72 (8) <sup>a</sup>	8.8470 (8)	10.542 (4)	11.543 (7)	11.64 (6)
3	5.24381 (13)	8.0503 (4)	10.2095 (10)	10.994 (6)	10.231 (18)	7.97 (17)
4	6.21777 (22) 6.22 (3) <sup>a</sup>	9.6715 (7) 9.7 (5) <sup>a</sup>	11.3221 (19)	9.343 (12)	3.75 (6)	-2.98 (30)
5	7.31910 (19) 7.31 (4) <sup>a</sup>	11.4963 (7) 11.4 (8) <sup>a</sup>	11.756 (5)	3.743 (15)	-12.26 (16)	-27.6 (15)
6	8.53585 (21) 8.53 (6) <sup>a</sup>	13.4993 (9) 14 (2) <sup>a</sup>	11.067 (5)	-8.22 (4)	-43.74 (30)	-71 (5)
7	9.8632 (4)	15.6678 (16)	8.765 (7)	-29.59 (6)	-98.9 (6)	-136 (9)
8	11.2984 (4)	17.9906 (19)	4.283 (9)	-64.30 (8)	-188.8 (11)	-222 (13)
9	12.8406 (5)	20.4600 (21)	-3.021 (19)	-117.06 (14)	-326.4 (18)	-321 (25)
10	14.4890 (5)	23.0705 (21)	-13.814 (20)	-193.51 (23)	-529.8 (29)	-440 (60)

<sup>a</sup>Value from [37]**Table 7.** Reduced virial coefficients  $B_i^* = B_i/V_p^{i-1}$  of hard rhombi in dependence on their aspect ratio  $\nu$ .

$\nu$	$B_3^*$	$B_4^*$	$B_5^*$	$B_6^*$	$B_7^*$	$B_8^*$
1	3.98335 (11) 3.98 (2) <sup>a</sup>	5.94841 (21) 5.94 (8) <sup>a</sup>	7.9505 (6)	9.7530 (17)	11.104 (4)	11.776 (19)
2	4.90794 (16)	7.4813 (4)	9.6767 (13)	11.048 (5)	11.507 (17)	11.12 (15)
3	6.64549 (21)	10.1098 (7)	10.397 (4)	5.477 (12)	0.02 (9)	8.1 (7)
4	8.86529 (29)	13.0689 (11)	5.109 (7)	-26.741 (24)	-57.39 (27)	36 (6)
5	11.5232 (7)	16.2044 (14)	-11.408 (14)	-116.26 (10)	-217.1 (9)	300 (21)
6	14.6075 (5)	19.441 (4)	-45.40 (4)	-309.06 (20)	-571.9 (30)	1330 (90)
7	18.1136 (7)	22.722 (5)	-104.20 (5)	-669.1 (4)	-1262 (8)	4480 (170)
8	22.0399 (8)	26.000 (5)	-196.29 (6)	-1281.3 (10)	-2486 (16)	11700 (1000)
9	26.3854 (11)	29.214 (9)	-331.29 (13)	-2255.0 (14)	-4530 (40)	27300 (1600)
10	31.1492 (15)	32.330 (16)	-519.81 (14)	-3725.0 (23)	-7790 (70)	57900 (2400)

<sup>a</sup>Value from [37]**Table 8.** Reduced virial coefficients  $\tilde{B}_i = B_i/B_2^{i-1}$  of hard needles.

$i$	$\tilde{B}_i$
3	0.514547 (19) 0.5142024... <sup>a</sup> 0.5145 (3) <sup>b</sup>
4	-0.031027 (19) -0.031 (1) <sup>b</sup>
5	-0.28816 (5) -0.288 (2) <sup>b</sup>
6	-0.22659 (9)
7	-0.03464 (25)
8	0.1012 (8)

<sup>a</sup>Value from [37]<sup>b</sup>Value from [38]

In Figures 6 and 7, reduced virial coefficients  $\tilde{B}_i = B_i/B_2^{i-1}$  are displayed in dependence on the shape parameter

$$\alpha = \frac{B_2 - V_P}{V_P} = B_2^* - 1 \quad (45)$$

as the reduced excess contribution of the mutual excluded volume per particle [36,38]. For its inverse, the relation  $0 \leq \alpha^{-1} \leq 1$  holds with the limiting cases of  $\alpha^{-1} = 1$  for a hard disc and  $\alpha^{-1} = 0$  for a hard needle. As known from reduced virial coefficients of prolate shapes in  $\mathbb{R}^3$ , a non-linear dependence on  $\alpha^{-1}$  appears which, however,

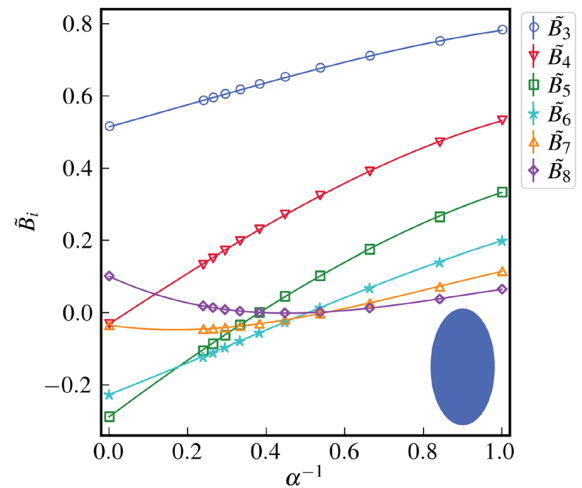


**Figure 6.** Reduced virial coefficients  $\tilde{B}_i = B_i/B_2^{i-1}$  of ellipses in dependence on the inverse of the shape parameter  $\alpha^{-1}$ . The solid curves are least-squares fits employing a third-order polynomial as a heuristic approach. The polynomial coefficients are provided in the supplemental material.

excellently can be described by lower-order polynomials allowing an interpolation for arbitrary aspect ratios  $\nu$  [32,34,36]. For rectangles and rhombi, with the limiting case of squares for  $\nu \rightarrow 1^+$ , the inverse of the excess

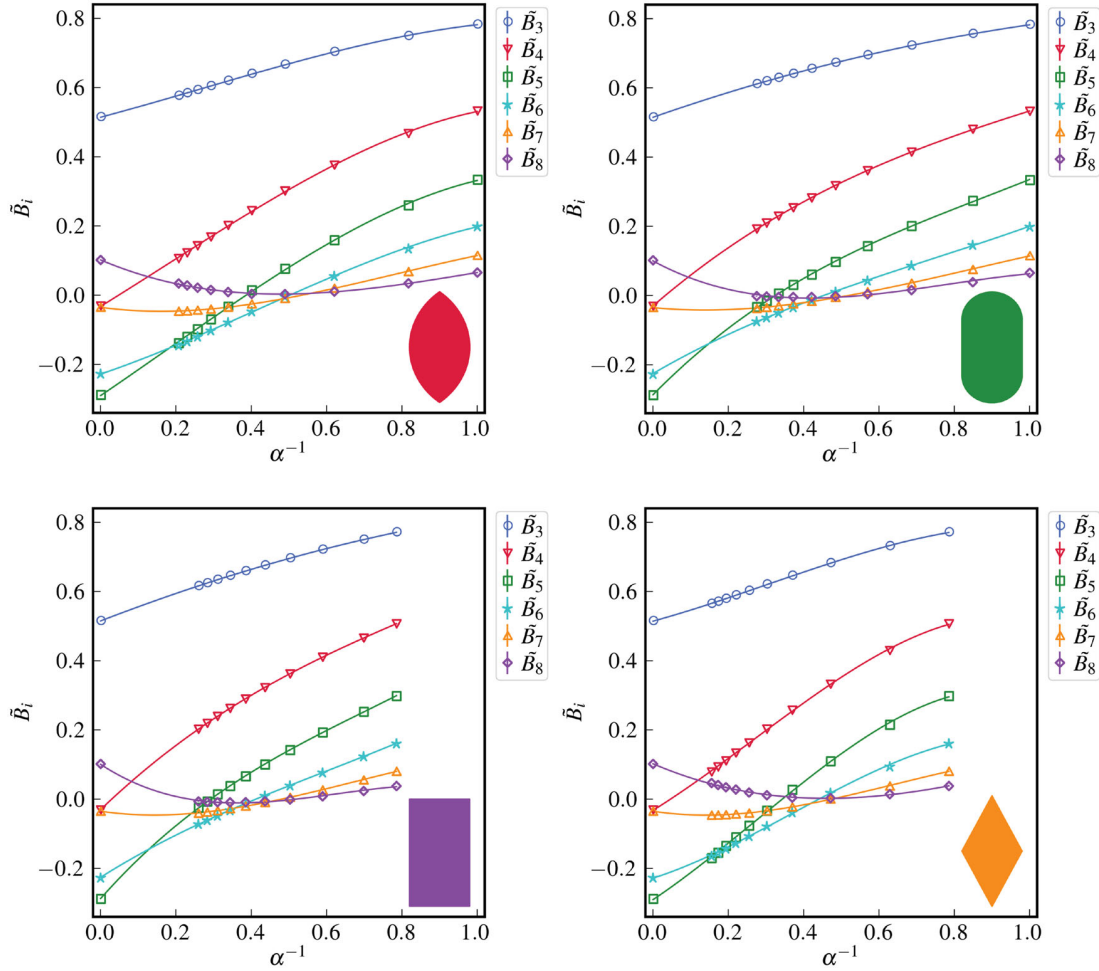


**Figure 7.** Reduced virial coefficients  $\tilde{B}_i = B_i/B_2^{i-1}$  of planar lenses (upper left), stadia (upper right), rectangles (lower left), and rhombi (lower right) in dependence on the inverse of the shape parameter  $\alpha^{-1}$ . The solid curves are least-squares fits employing a third-order polynomial as a heuristic approach. The polynomial coefficients are provided in the supplemental material.

excluded volume per particle is limited to  $0 \leq \alpha^{-1} \leq \pi/4$ .

### 4.3. Equation-of-state data and phase behaviour

Employing Equation (2), the compressibility factor  $Z$  can be written as

$$Z = \frac{\gamma}{\rho k_B T} = 1 + \sum_{i=2}^{\infty} B_i^* \eta^{i-1} \quad (46)$$

with the reduced virial coefficients  $B_i^*$  of order  $i$  and the area fraction  $\eta$ . Using scaled particle theory, Boublík suggested

$$Z = \frac{1}{(1-\eta)} + \frac{\alpha\eta(1+\alpha\eta/8)}{(1-\eta)^2} \quad (47)$$

as a generalised equation of state for arbitrary convex, two-dimensional shapes [43,48,49]. Here again, the shape

parameter  $\alpha = B_2^* - 1 = S_p^2/(4\pi V_p)$  is the excess part of the mutual excluded area per particle.

We compare in Figure 8 the virial equation of state [Equation (46)] to the scaled particle equation of state [Equation (47)] exemplarily for ellipses with various aspect ratios  $\nu$  in dependence on the area fraction  $\eta$  within the phase boundaries of the isotropic phase. For small area fractions, with increasing number of virial coefficients, independent of the aspect ratio, both equations of state result in identical compressibility factors. For small aspect ratios, even at moderate area fractions deviations between both equations of state vanish with increasing number of virial coefficients considered (Figure 8). With emerging negative virial coefficients at higher aspect ratios, for higher and even moderate area fractions, the virial equation of states predicts significantly smaller compressibility factors than Equation (47). At  $\nu = 9$ , even non-physical, negative compressibility factors appear using virial coefficients up to order eight.

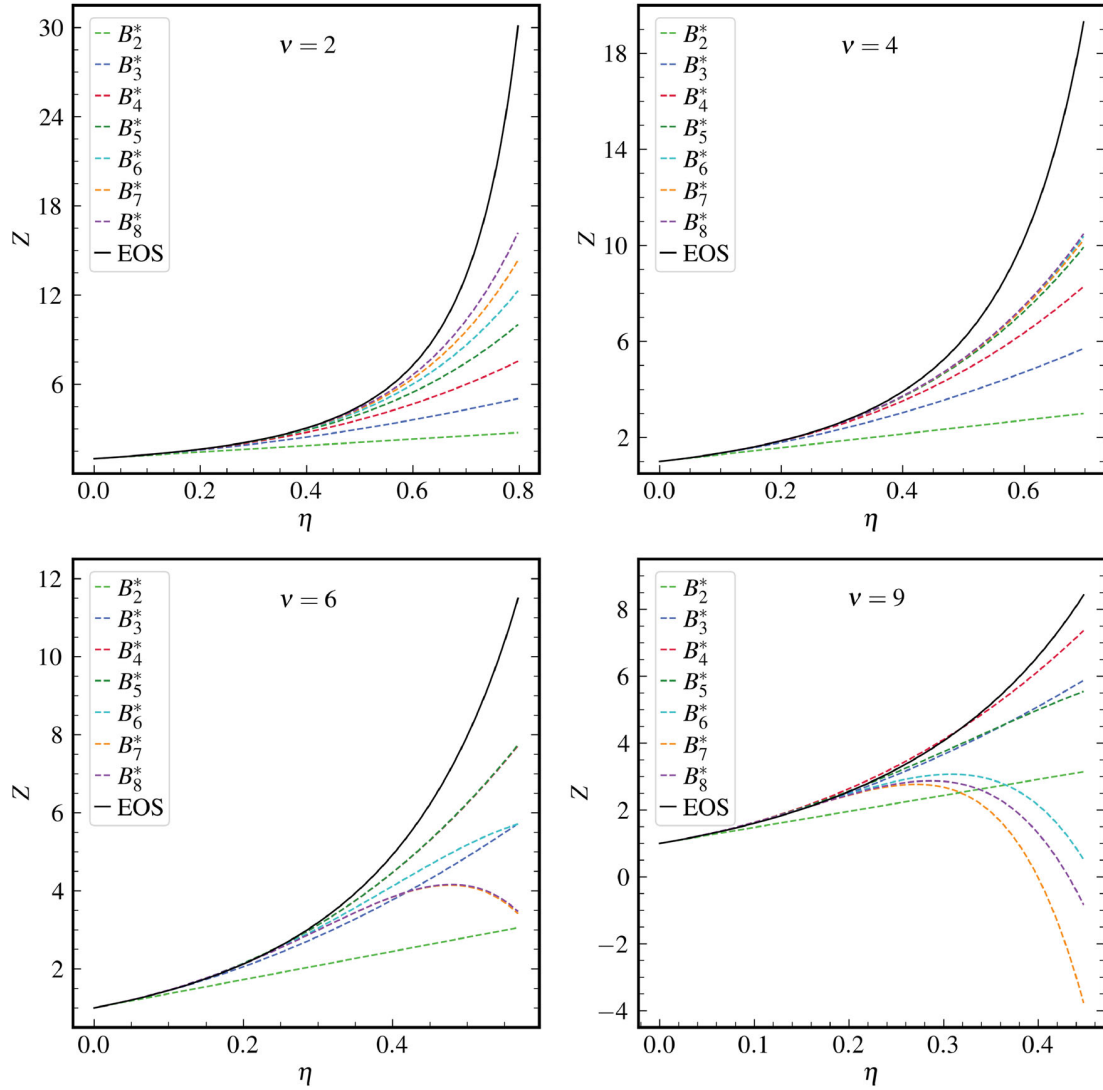


**Figure 8.** Equations of state for ellipses with  $\nu = 2, 4, 6,$  and  $9$ . The dotted lines are from Equation (46), considering the sum of virial coefficients up to the order displayed in the legends. The solid lines represent Equation (47) using scaled particle theory.

At high aspect ratios, long-range orientational correlations appear, leading to an isotropic-nematic phase transition at a critical area fraction  $\eta_{\text{crit}}$  decreasing with the aspect ratio  $\nu$  [50,51]. The critical area fractions  $\eta_{\text{crit}}$  for the transition from the isotropic to a crystalline or liquid-crystalline phase are compiled in Table 9. Even for the isotropic phase, long-range orientational correlations with correlation lengths exceeding the size of clusters up to eight particles contributing to virial coefficients up to order eight are reported [50,51]. To overcompensate the negative virial coefficients, even higher-order, again positive virial coefficients are required. In the case of ellipses, planar lenses, and rhombi, already the eighth virial coefficient is again positive for large aspect ratios as well as for hard needles. Interestingly, opposite to other shapes, the maximum packing fraction of two-dimensional

**Table 9.** Upper bound for the critical area fraction  $\eta_{\text{crit}}$  of an isotropic phase transition of hard ellipses with aspect ratio  $\nu$  reported by Xu *et al.* [51].

$\nu$	$\eta_{\text{crit}}$	Phase transition
2	$> 0.80$	$I \rightarrow S$
3	$\approx 0.75$	$I \rightarrow N$
4	$\approx 0.69$	$I \rightarrow N$
5	$\approx 0.63$	$I \rightarrow N$
6	$\approx 0.57$	$I \rightarrow N$
7	$\approx 0.53$	$I \rightarrow N$
8	$\approx 0.47$	$I \rightarrow N$
9	$\approx 0.45$	$I \rightarrow N$
10	$\approx 0.42$	$I \rightarrow N$

ellipses

$$\eta_{\text{max}} = \rho_{\text{max}} V_{\text{P}} = \frac{\pi}{2\sqrt{3}} = 0.906899\dots \quad (48)$$

is independent of the aspect ratio  $\nu$  as already reported by Vieillard-Baron [52]. Since stretching preserves the packing fraction, and applying a stretching transformation to discs yields an ellipse, ellipses have the same packing fraction as discs ( $\nu = 1$ ).

## 5. Conclusion

We provide virial coefficients for the anisometric shapes of ellipses, planar lenses, stadia, rectangles, and rhombi in  $\mathbb{R}^2$  in dependence on their aspect ratio  $\nu$ . Using Mayer-sampling Monte Carlo simulations as an efficient method to explore the configuration space, the accuracy of available virial coefficients could significantly be improved and so far unknown virial coefficients are systematically calculated. The comparison with analytically obtained second virial coefficients employing the Isihara-Hadwiger theorem is used to validate both, the Mayer-sampling algorithm used, and the overlap criteria for the investigated shapes. The dependence of reduced, higher-order virial coefficients  $\tilde{B}_i = B_i/B_2^{i-1}$  on the inverse excess part of the mutual excluded volume per particle  $\alpha$  as a universal shape parameter can accurately be described by lower-order polynomials as a heuristic approach. Hereby, a reliable interpolation of virial coefficients can be achieved.

Exemplarily for ellipses, compressibility factors from the virial series up to the eighth order are compared to an equation of state resulting from scaled particle theory. With emerging negative, higher-order virial coefficients, truncation effects of the virial series are evident: For highly anisometric shapes, angular correlations with correlation lengths exceeding the size of simulated clusters arise. To include these effects in the virial series, even higher-order, positive virial coefficients are required. A change of sign from negative to positive eighth-order virial coefficients is observed for sufficiently anisometric shapes. A remaining task is to calculate even higher-order virial coefficients for these objects.

## Acknowledgements

The authors thank Philipp Marienhagen for fruitful discussions.

## Disclosure statement

No potential conflict of interest was reported by the author(s).

## ORCID

Markus Kulossa  <http://orcid.org/0000-0002-9064-2685>

Joachim Wagner  <http://orcid.org/0000-0001-6570-8710>

## References

- [1] H. Kamerlingh Onnes, Proc. K. Ned. Akad. Wet. **4**, 125–147 (1902).
- [2] J.E. Mayer, J. Chem. Phys. **5**, 67–73 (1937). doi:10.1063/1.1749933
- [3] J.E. Mayer and M.G. Mayer, *Statistical Mechanics* (Wiley, New York, 1940).
- [4] R. Hołyst and A. Poniewierski, Phys. Rev. A **39**, 2742–2744 (1989). doi:10.1103/PhysRevA.39.2742
- [5] A. Poniewierski and R. Hołyst, Phys. Rev. Lett. **61**, 2461–2464 (1988). doi:10.1103/PhysRevLett.61.2461
- [6] H. Löwen, J. Phys.: Condens. Matter **14**, 11897 (2002). doi:10.1088/0953-8984/14/46/301.
- [7] M. te Vrugt, H. Löwen and R. Wittkowski, Adv. Phys. **69**, 121–247 (2020). doi:10.1080/00018732.2020.1854965
- [8] A.J. Schultz and D.A. Kofke, J. Chem. Phys. **157**, 190901 (2022). doi:10.1063/5.0113730
- [9] G. Jäger, Sitzungsber. Akad. Wiss. Wien, Math.-Naturwiss. Kl., Abt. 2A **105**, 15–21 (1896).
- [10] L. Boltzmann, Sitzungsber. Akad. Wiss. Wien, Math.-Naturwiss. Kl., Abt. 2A **105**, 695–706 (1896).
- [11] L. Boltzmann, Proc. K. Ned. Akad. Wet. **1**, 398–404 (1899).
- [12] J.D. van der Waals, Proc. K. Ned. Akad. Wet. **1**, 138–143 (1899).
- [13] J.J. van Laar, Amst. Akad. Versl. **7**, 350–364 (1899).
- [14] L. Tonks, Phys. Rev. **50**, 955–963 (1936). doi:10.1103/PhysRev.50.955
- [15] J.S. Rowlinson, Mol. Phys. **7**, 593–594 (1964). doi:10.1080/00268976300101421
- [16] P.C. Hemmer, J. Chem. Phys. **42**, 1116–1118 (1965). doi:10.1063/1.1696049
- [17] N. Metropolis, A.W. Rosenbluth, M.N. Rosenbluth, A.H. Teller and E. Teller, J. Chem. Phys. **21**, 1087–1092 (1953). doi:10.1063/1.1699114
- [18] M.N. Rosenbluth and A.W. Rosenbluth, J. Chem. Phys. **22**, 881–884 (1954). doi:10.1063/1.1740207
- [19] F.H. Ree and W.G. Hoover, J. Chem. Phys. **40**, 939–950 (1964). doi:10.1063/1.1725286
- [20] F.H. Ree and W.G. Hoover, J. Chem. Phys. **46**, 4181–4197 (1967). doi:10.1063/1.1840521
- [21] A.J. Schultz and D.A. Kofke, Phys. Rev. E **90**, 023301 (2014). doi:10.1103/PhysRevE.90.023301
- [22] C. Zhang and B.M. Pettitt, Mol. Phys. **112**, 1427–1447 (2014). doi:10.1080/00268976.2014.904945
- [23] F.H. Ree and W.G. Hoover, J. Chem. Phys. **40**, 2048–2049 (1964). doi:10.1063/1.1725456
- [24] L. Onsager, Ann. NY Acad. Sci. **51**, 627–659 (1949). doi:10.1111/j.1749-6632.1949.tb27296.x
- [25] E. Herold, R. Hellmann and J. Wagner, J. Chem. Phys. **147**, 204102 (2017). doi:10.1063/1.5004687
- [26] S. Torquato and Y. Jiao, J. Stat. Mech.: Theory Exp. **2022**, 093404 (2022). doi:10.1088/1742-5468/ac8c8b
- [27] M. Kulossa, P. Marienhagen and J. Wagner, Phys. Rev. E **105**, 064121 (2022). doi:10.1103/PhysRevE.105.064121
- [28] B. Freasier and R. Bearman, Mol. Phys. **32**, 551–554 (1976). doi:10.1080/00268977600103281
- [29] M. Rigby, Mol. Phys. **66**, 1261–1268 (1989). doi:10.1080/00268978900100851
- [30] A.Y. Vlasov, X.M. You and A.J. Masters, Mol. Phys. **100**, 3313–3324 (2002). doi:10.1080/00268970210153754

- [31] X.M. You, A.Y. Vlasov and A.J. Masters, *J. Chem. Phys.* **123**, 034510 (2005). doi:10.1063/1.1992471
- [32] P. Marienhagen, R. Hellmann and J. Wagner, *Phys. Rev. E* **104**, 015308 (2021). doi:10.1103/PhysRevE.104.015308
- [33] M. Rigby, *J. Chem. Phys.* **53**, 1021–1023 (1970). doi:10.1063/1.1674089
- [34] M. Francová, J. Kolafa, P. Morávek, S. Labík and A. Malijevský, *Collect. Czech. Chem. Commun.* **73**, 413–423 (2008). doi:10.1135/cccc20080413
- [35] M.E. Irrgang, M. Engel, A.J. Schultz, D.A. Kofke and S.C. Glotzer, *Langmuir* **33**, 11788–11796 (2017). doi:10.1021/acs.langmuir.7b02384
- [36] M. Kulossa, D. Weidig and J. Wagner, *Phys. Rev. E* **107**, 024129 (2023). doi:10.1103/PhysRevE.107.024129
- [37] G. Tarjus, P. Viot, S.M. Ricci and J. Talbot, *Mol. Phys.* **73**, 773–787 (1991). doi:10.1080/00268979100101541
- [38] M. Rigby, *Mol. Phys.* **78**, 21–27 (1993). doi:10.1080/00268979300100031
- [39] I. Langmuir, *J. Am. Chem. Soc.* **54**, 2798–2832 (1932). doi:10.1021/ja01346a022
- [40] S. Labík, J. Kolafa and A. Malijevský, *Phys. Rev. E* **71**, 021105 (2005). doi:10.1103/PhysRevE.71.021105
- [41] F.H. Ree and W.G. Hoover, *J. Chem. Phys.* **41**, 1635–1645 (1964). doi:10.1063/1.1726136
- [42] J.K. Singh and D.A. Kofke, *Phys. Rev. Lett.* **92**, 220601 (2004). doi:10.1103/PhysRevLett.92.220601
- [43] T. Boublík, *Mol. Phys.* **29**, 421–428 (1975). doi:10.1080/00268977500100361
- [44] C. Vega and S. Lago, *Comput. Chem.* **18**, 55–59 (1994). doi:10.1016/0097-8485(94)80023-5
- [45] J.W. Perram and M.S. Wertheim, *J. Comput. Phys.* **58**, 409–416 (1985). doi:10.1016/0021-9991(85)90171-8
- [46] I. Gilitschenski and U.D. Hanebeck, in *2014 Sensor Data Fusion: Trends, Solutions, Applications (SDF)* (IEEE, Bonn, Germany, 2014), pp. 1–6.
- [47] B. Mertzios, *IEEE Trans. Autom. Control* **29**, 652–653 (1984). doi:10.1109/TAC.1984.1103602
- [48] T. Boublík, *Mol. Phys.* **63**, 685–690 (1988). doi:10.1080/00268978800100491
- [49] T. Boublík, *Mol. Phys.* **109**, 1575–1580 (2011). doi:10.1080/00268976.2011.573508
- [50] G. Bautista-Carbajal and G. Odriozola, *J. Chem. Phys.* **140**, 204502 (2014). doi:10.1063/1.4878411
- [51] W.S. Xu, Y.W. Li, Z.Y. Sun and L.J. An, *J. Chem. Phys.* **139**, 024501 (2013). doi:10.1063/1.4812361
- [52] J. Vieillard-Baron, *J. Chem. Phys.* **56**, 4729–4744 (1972). doi:10.1063/1.1676946

## Appendix. Leverrier's algorithm

Leverrier's algorithm can be used to calculate the resolvent

$$\underline{\mathbf{S}} = (\lambda \underline{\mathbf{I}} - \underline{\mathbf{X}})^{-1} = -(\underline{\mathbf{X}} - \lambda \underline{\mathbf{I}})^{-1} \quad (\text{A1})$$

of a matrix  $\underline{\mathbf{X}} \in \mathbb{R}^{D \times D}$  with  $\lambda \in \mathbb{R}$  and the identity matrix  $\underline{\mathbf{I}} \in \mathbb{R}^{D \times D}$  [46]. For the computation of the inverse of a matrix  $\underline{\mathbf{E}}_\lambda$

with

$$\underline{\mathbf{E}}_\lambda^{-1} = (\lambda \underline{\mathbf{M}} - \underline{\mathbf{X}})^{-1}, \quad (\text{A2})$$

the algorithm needs to be generalised since  $\underline{\mathbf{M}}$  can be singular [47]. Leverrier's algorithm inverts a matrix analytically, which increases especially for matrices with elements close to zero the computational stability and accuracy compared to numerical inversion algorithms. The inverse of a matrix  $\underline{\mathbf{E}}_\lambda$  with

$$\underline{\mathbf{E}}_\lambda^{-1} = \frac{\text{adj}(\underline{\mathbf{E}}_\lambda)}{\det(\underline{\mathbf{E}}_\lambda)} \quad (\text{A3})$$

is the quotient of the adjugate and the determinant of the matrix  $\underline{\mathbf{E}}_\lambda$ . Defining

$$\underline{\mathbf{R}}(\lambda) = \text{adj}(\underline{\mathbf{E}}_\lambda) = \text{adj}(\lambda \underline{\mathbf{M}} - \underline{\mathbf{X}}) \quad (\text{A4})$$

and

$$q(\lambda) = \det(\underline{\mathbf{E}}_\lambda) = \det(\lambda \underline{\mathbf{M}} - \underline{\mathbf{X}}), \quad (\text{A5})$$

the recursive relations

$$\underline{\mathbf{R}}(\lambda) = \sum_{k=0}^{D-1} \underline{\mathbf{R}}_{D-1,k} \lambda^k \quad (\text{A6})$$

and

$$q(\lambda) = \sum_{k=0}^D q_{D,k} \lambda^k \quad (\text{A7})$$

with

$$\underline{\mathbf{R}}_{j+1,k} = \begin{cases} -\underline{\mathbf{M}} \underline{\mathbf{R}}_{j,k-1} + q_{j+1,k} \underline{\mathbf{I}} & : k = j + 1 \\ \underline{\mathbf{X}} \underline{\mathbf{R}}_{j,k} - \underline{\mathbf{M}} \underline{\mathbf{R}}_{j,k-1} + q_{j+1,k} \underline{\mathbf{I}} & : k = 1, \dots, j \\ \underline{\mathbf{X}} \underline{\mathbf{R}}_{j,k} + q_{j+1,k} \underline{\mathbf{I}} & : k = 0 \end{cases} \quad (\text{A8})$$

and

$$q_{j+1,k} = \begin{cases} \frac{1}{j+1} \text{tr}(\underline{\mathbf{M}} \underline{\mathbf{R}}_{j,k-1}) & : k = j + 1 \\ -\frac{1}{j+1} \text{tr}(\underline{\mathbf{X}} \underline{\mathbf{R}}_{j,k} - \underline{\mathbf{M}} \underline{\mathbf{R}}_{j,k-1}) & : k = 1, \dots, j \\ -\frac{1}{j+1} \text{tr}(\underline{\mathbf{X}} \underline{\mathbf{R}}_{j,k}) & : k = 0 \end{cases} \quad (\text{A9})$$

result [47]. Here,  $\text{tr}(\underline{\mathbf{Z}})$  is the trace of matrix  $\underline{\mathbf{Z}} \in \mathbb{R}^{D \times D}$ , i.e. the sum of their main diagonal elements and  $\underline{\mathbf{R}}_{0,0} = \underline{\mathbf{I}}$  is the matrix identity.

## Supplemental Material

### Virial coefficients of hard, two-dimensional, convex particles up to the eighth order

Markus Kulossa and Joachim Wagner

Institut für Chemie, Universität Rostock, 18051 Rostock, Germany

#### S-I. Interpolation of reduced virial coefficients $\tilde{B}_i$

The dependence of reduced virial coefficients  $\tilde{B}_i = B_i/B_2^{i-1}$  on the shape parameter  $\alpha^{-1}$  can for each investigated geometry heuristically be described using a third order polynomial

$$\tilde{B}_i \approx a\alpha^{-3} + b\alpha^{-2} + c\alpha^{-1} + d \quad (\text{S-1})$$

with the coefficients  $a$ ,  $b$ ,  $c$ , and  $d$ . Their optimum values determined by least-squares fits are compiled in Tab. S-1.

**Table S-1.** Coefficients  $a$ ,  $b$ ,  $c$ , and  $d$  of third-order polynomials [Eq. (S-1)] as an heuristic approach for the dependence of reduced virial coefficients  $\tilde{B}_i$  on the shape parameter  $\alpha^{-1}$ .

	$i$	$a$	$b$	$c$	$d$
Stadion	3	0.0044 (18)	-0.1189 (26)	0.3820 (11)	0.51450 (14)
	4	0.156 (11)	-0.534 (15)	0.942 (6)	-0.0307 (8)
	5	0.294 (27)	-0.78 (4)	1.104 (16)	-0.2874 (21)
	6	0.172 (20)	-0.382 (29)	0.636 (12)	-0.2260 (15)
	7	-0.162 (15)	0.418 (21)	-0.106 (9)	-0.0350 (11)
	8	-0.41 (5)	0.96 (7)	-0.588 (27)	0.100 (4)
Rectangle	3	0.000 (5)	-0.121 (5)	0.4213 (15)	0.51451 (15)
	4	0.233 (10)	-0.646 (11)	1.048 (4)	-0.0309 (4)
	5	0.46 (4)	-0.97 (4)	1.229 (12)	-0.2879 (11)
	6	0.247 (23)	-0.443 (27)	0.689 (9)	-0.2264 (9)
	7	-0.318 (21)	0.645 (24)	-0.165 (8)	-0.0348 (8)
	8	-0.73 (6)	1.38 (7)	-0.711 (22)	0.1007 (22)
Ellipse	3	-0.077 (13)	0.045 (18)	0.300 (8)	0.5141 (10)
	4	-0.105 (25)	-0.05 (4)	0.717 (15)	-0.0320 (20)
	5	-0.069 (24)	-0.12 (4)	0.812 (14)	-0.2890 (19)
	6	-0.093 (13)	0.093 (19)	0.425 (8)	-0.2271 (10)
	7	-0.202 (7)	0.503 (10)	-0.152 (5)	-0.0349 (6)
	8	-0.277 (9)	0.750 (13)	-0.509 (6)	0.1011 (7)
Planar lens	3	-0.119 (15)	0.096 (22)	0.291 (9)	0.5138 (12)
	4	-0.23 (4)	0.12 (6)	0.672 (24)	-0.033 (4)
	5	-0.25 (5)	0.13 (8)	0.74 (4)	-0.291 (4)
	6	-0.23 (4)	0.29 (6)	0.367 (22)	-0.2283 (28)
	7	-0.223 (9)	0.524 (14)	-0.151 (6)	-0.0350 (7)
	8	-0.207 (17)	0.632 (25)	-0.462 (11)	0.1019 (14)
Rhombus	3	-0.271 (27)	0.25 (3)	0.299 (11)	0.5139 (11)
	4	-0.62 (8)	0.49 (10)	0.677 (30)	-0.0330 (30)
	5	-0.73 (12)	0.60 (13)	0.73 (5)	-0.291 (5)
	6	-0.59 (9)	0.65 (10)	0.35 (4)	-0.229 (4)
	7	-0.350 (17)	0.677 (20)	-0.169 (7)	-0.0349 (7)
	8	-0.16 (5)	0.62 (6)	-0.469 (18)	0.1024 (18)

## 5.4 Publication IV - Geometric measures of uniaxial solids of revolution in higher-dimensional Euclidean spaces and their relation to the second virial coefficient

M. Kulossa, J. Wagner, *Phys. Rev. E* **111**, 024112 (2025).

DOI: 10.1103/PhysRevE.111.024112

Type: Full article

© 2025 American Physical Society

### Author contributions

**Markus Kulossa:** Conceptualization, Data curation, Formal analysis, Investigation, Methodology, Software, Validation, Visualization, Writing - original draft preparation, Writing - review and editing

Estimated total contribution in percent: 70 %



**Joachim Wagner:** Conceptualization, Formal analysis, Investigation, Methodology, Project administration, Resources, Supervision, Writing - review and editing

Estimated total contribution in percent: 30 %

Reprinted article with permission from M. Kulossa, J. Wagner, *Phys. Rev. E* **111**, 024112 (2025). Copyright (2025) by the American Physical Society.



## Geometric measures of uniaxial solids of revolution in higher-dimensional Euclidean spaces and their relation to the second virial coefficient

Markus Kulossa  and Joachim Wagner \*

*Institut für Chemie, Universität Rostock, 18051 Rostock, Germany*



(Received 29 November 2024; accepted 28 January 2025; published 12 February 2025)

We provide analytical expressions for the second virial coefficients of various hard, convex, monoaxial solids of revolution in higher-dimensional Euclidean spaces. Therefore, the rotation-averaged mutual excluded volume per particle is calculated employing the Brunn-Minkowski theorem using quermassintegrals of the respective shape. In addition to geometries without singularities in their surface curvature, so far unknown quermassintegrals for geometries with singularities in their surface curvature, such as hyperlenses and hypercones, are calculated. Studying the influence of the detailed particle shape, the second virial coefficients are analyzed in four dimensions depending on the aspect ratio  $\nu$ . These analytical expressions are extended to arbitrary-dimensional Euclidean spaces. The resulting virial coefficients are compared to available data for analogs in two and three dimensions. For hard hyperspheroids, the universal parity  $B_2^*(\nu) = B_2^*(\nu^{-1})$  of the reduced second virial coefficient with respect to the aspect ratio  $\nu$  is proven. Unlike other geometric shapes, the excluded volume of hyperspherocylinders in any dimension solely depends on at most three quermassintegrals.

DOI: [10.1103/PhysRevE.111.024112](https://doi.org/10.1103/PhysRevE.111.024112)

### I. INTRODUCTION

The geometric description of particle shapes is of crucial importance for predicting physical and chemical properties of many-particle systems with hard-body interaction serving as model systems for colloids, liquid crystals, and granular matter [1–4]. Most experimentally investigated nonspherical particle shapes are modeled either as polytopes [5,6] or solids of revolution [7–9]. Sufficiently anisotropic solids of revolution, both as prolate and oblate shapes, lead to a complex phase behavior, including liquid-crystalline nematic [10–14] and smectic phases [15,16].

Classical density functional theory (DFT) is a commonly used approach to predict the phase behavior of many-particle systems consisting of hard, anisotropic solids connected to the free energy of these systems [17–19]. The real gas factor  $Z = p/(\rho k_B T)$ , where  $p$  denotes the pressure,  $\rho$  the particle number density, and  $k_B T$  the thermal energy, reads, using virial theory as

$$Z = 1 + \sum_{i=2}^{\infty} B_i \rho^{i-1} = 1 + \sum_{i=2}^{\infty} B_i^* \eta^{i-1}, \quad (1)$$

an expansion in powers of the number density  $\rho$  or the volume fraction  $\eta$ , respectively, and provides an access to closed expressions for the free energy. The coefficients  $B_i$  are virial coefficients of order  $i$  and  $B_i^* = B_i/V_p^{i-1}$  reduced virial coefficients, with  $V_p$  denoting the volume of a single particle. Since commonly only few orders of virial coefficients are known, contributions of so far unknown, higher-order virial coefficients are approximated via the Carnahan-Starling series

[20]. In many cases, DFT studies employ expressions for the free energy solely based on the second virial coefficient of the respective, anisometric particle shape [21,22].

For hard, convex particles, the second virial coefficient corresponding to half of the orientationally averaged mutual excluded volume can analytically be expressed employing the Brunn-Minkowski theorem [23] based on quermassintegrals as geometric measures of the respective shape. In three dimensions, only volume  $V_p$ , surface area  $S_p$ , and mean radius of curvature  $\bar{R}_p$  as geometric measures are required to obtain the second virial coefficient  $B_2 = V_p + S_p \bar{R}_p$  of a convex particle. This relation is also known as Isihara-Hadwiger theorem [24–26]. In two dimensions, even two geometric measures are sufficient to calculate the second virial coefficient  $B_2 = V_p + S_p^2/(4\pi)$  of a convex shape, with  $V_p$  denoting the two-dimensional particle volume or area and  $S_p$  the two-dimensional surface area or perimeter [27,28].

In the two- [29] and three-dimensional space [30–32], analytical expressions for the second virial coefficients of various hard convex solids are available. Also second virial coefficients of four-dimensional particles have been provided [33,34], and the Brunn-Minkowski theorem [35,36] has been applied to calculate second virial coefficients of various convex particles in higher-dimensional spaces [23]. Furthermore, accurate values for second virial coefficients, serving both as a reference and validation of Monte Carlo simulation techniques, are relevant for the numerical calculation of higher-order virial coefficients [37,38].

In this work we provide so far unknown expressions for virial coefficients of uniaxial solids of revolution in  $\mathbb{R}^4$  and compare the results with analog geometries in lower- and higher-dimensional spaces. We investigate the influence of removable singularities in the surface curvature giving access to the second virial coefficients of hard,  $D$ -dimensional

\*Contact author: [joachim.wagner@uni-rostock.de](mailto:joachim.wagner@uni-rostock.de)

spindles, lenses, cones, doublecones, truncated cones, and spherical caps. Beyond contributing to equation-of-state data and phase behavior in higher dimensions, the availability of second virial coefficients for various shapes in dependence on the aspect ratio can provide insights into close packings in higher-dimensional spaces [30,39–42].

This paper is organized as follows: After introducing virial theory, emphasizing the second virial coefficient related to the excluded volume of hard bodies, we introduce the Brunn-Minkowski theorem. The required quermassintegrals of uniaxial, four-dimensional solids of revolution are calculated as surface integrals over generalized principal curvatures, starting with shapes with continuous surface curvature. Possible contributions of singularities in the surface curvature, where for uniaxial solids of revolution in  $\mathbb{R}^4$  only zero- and two-dimensional singularities exist, are analyzed. Extending the calculation of contributions of singularities in the surface curvature of uniaxial solids of revolution in Euclidean spaces with arbitrary dimension is straightforward. We provide quermassintegrals for several solids of revolution in  $\mathbb{R}^4$  needed to calculate their second virial coefficients. Finally, we analyze the influence of detailed shape and aspect ratio in  $\mathbb{R}^4$  and compare the results to analogs with identical meridian curves in other dimensions.

## II. THEORETICAL BACKGROUND

### A. Virial theory

Mayer and Mayer have shown by means of statistical mechanics, starting from the grand-canonical partition function, that the virial coefficient of order  $i$  depends on interactions in an  $i$ -particle cluster [43,44]. The second virial coefficient, describing the initial departure from the ideal-gas behavior in the low-density limit, reads as

$$B_2 = -\frac{1}{2} \int \left\{ \exp \left[ -\frac{U(\mathbf{r}_{12})}{k_B T} \right] - 1 \right\} d^D \mathbf{r}_{12}, \quad (2)$$

with  $U(\mathbf{r}_{12})$  denoting the potential energy of two particles with centers located at  $\mathbf{r}_1$  and  $\mathbf{r}_2$  with distance vector  $\mathbf{r}_{12} = \mathbf{r}_2 - \mathbf{r}_1$ . The integrand in Eq. (2) is the Mayer  $f$  function  $f_{12}$ , depending on the interaction of both particles. For hard-body interaction, the potential reads as

$$U(\mathbf{r}_{12}) = \begin{cases} \infty & : r_{12} < \sigma \\ 0 & : r_{12} \geq \sigma, \end{cases} \quad (3)$$

with  $\sigma$  denoting the contact distance, which in the case of uniaxial, anisometric shapes depends on the unit vectors  $\hat{\mathbf{u}}_1$ ,  $\hat{\mathbf{u}}_2$  denoting their orientations and the direction of the distance vector  $\hat{\mathbf{r}}_{12} = \mathbf{r}_{12}/r_{12}$ . Hence, irrespective of the thermal energy  $k_B T$ ,  $f_{12} = -1$  results for overlap configurations while the integrand vanishes for nonoverlap configurations.

For  $D$ -dimensional spheres with radius  $r_0$  the contact distance is, independent of the orientation,  $\sigma = 2r_0$ , leading to

$$B_2 = \frac{1}{2} \beta_D \int_0^\sigma r^{D-1} dr = \frac{1}{2} \kappa_D (2r_0)^D, \quad (4)$$

with

$$\beta_D = \frac{2\pi^{D/2}}{\Gamma(D/2)} \quad (5)$$

denoting the surface area and

$$\kappa_D = \frac{\beta_D}{D} = \frac{\pi^{D/2}}{\Gamma(1 + D/2)} \quad (6)$$

the volume of the  $D$ -dimensional unit sphere.

Since in the case of uniaxial, anisometric shapes the contact distance depends on the orientations  $\hat{\mathbf{u}}_1$ ,  $\hat{\mathbf{u}}_2$ , and  $\hat{\mathbf{r}}_{12}$ , the orientation-averaged Mayer  $f$  function has to be used as integrand, leading to

$$B_2 = -\frac{1}{2} \int \langle f_{12} \rangle_{\hat{\mathbf{u}}_2} d^D \mathbf{r}_{12}, \quad (7)$$

where the direction  $\hat{\mathbf{u}}_1$  defines the orientation of the coordinate system. For hard-body interaction, the second virial coefficient

$$B_2 = \frac{1}{2} V_{\text{ex}} \quad (8)$$

is half the orientation-averaged mutual excluded volume between two identical particles and is thus solely related to geometric properties of the considered shape.

### B. Excluded volumes of convex solids

Let  $K, L \in \mathbb{R}^D$  be two convex bodies. The rotation-averaged excluded volume  $V_{\text{ex}}(K, L)$  is

$$V_{\text{ex}}(K, L) = \frac{1}{\kappa_D} \sum_{i=0}^D \binom{D}{i} W_i(K) W_{D-i}(L), \quad (9)$$

known as the Brunn-Minkowski theorem [23,35,36]. Employing this expression, not only second virial coefficients of identical convex solids with  $K = L$  but also cross virial coefficients of different convex shapes are accessible. The latter quantities are of interest for thermodynamics of mixtures leading to the second virial coefficient,

$$B_2^{\text{mix}} = \sum_{i=1}^m \sum_{j=1}^m x_i x_j B_2(i, j), \quad (10)$$

of an  $m$ -component system with number fractions  $x_i$ .

The quantity  $W_i(K)$  is the mixed volume of  $(D - i)$  convex bodies  $K$  and  $i$   $D$ -dimensional unit spheres denoted as the  $i$ th quermassintegral of  $K$ , which relates to the intrinsic volume  $v_i$  as

$$v_i(K) = \binom{D}{i} \frac{W_{D-i}(K)}{\kappa_{D-i}} \quad (11)$$

for a convex set. If  $L$  is a  $D$ -dimensional sphere with radius  $\varepsilon$ , Eq. (9) reads as

$$V_{\text{ex}}(K, \varepsilon) = \sum_{i=0}^D \binom{D}{i} W_i(K) \varepsilon^i, \quad (12)$$

also known as the Steiner formula [45].

Focusing on identical convex bodies  $K = L$ , the Brunn-Minkowski theorem provides an analytical expression for the second virial coefficient of a convex particle, since due to the rotational invariance of quermassintegrals directly the orientation average is obtained. Quermassintegrals  $W_i$  of orders

$i = \{0, 1\}$  and  $i = \{D - 1, D\}$  are related to common geometric measures as

$$W_0(K) = V_P(K), \quad (13a)$$

$$W_1(K) = \frac{1}{D} S_P(K), \quad (13b)$$

$$W_{D-1}(K) = \tilde{R}_P(K) \kappa_D, \quad (13c)$$

$$W_D(K) = \kappa_D, \quad (13d)$$

where  $V_P$  denotes the volume of  $K$ ,  $S_P$  its total surface area, and  $\tilde{R}_P$  its mean radius of curvature [23,30].

Using these common measures, in the two- and three-dimensional Euclidean space second virial coefficients for arbitrary convex solids  $K$  can be calculated. In  $\mathbb{R}^4$ , the second virial coefficient reads as

$$B_2(K) = V_P(K) + S_P(K) \tilde{R}_P(K) + \frac{6}{\pi^2} W_2^2(K). \quad (14)$$

To calculate  $W_2(K)$ , the surface integral over the continuous surface curvature,

$$W_2(K) = \frac{1}{D} \oint H_P(K) d^{D-1}S, \quad (15)$$

is required, where  $H_P$  is the mean curvature

$$H_P(K) = \frac{1}{D-1} \sum_{i=1}^{D-1} \frac{1}{R_i(K)}, \quad (16)$$

depending on the principal radii of curvature  $R_i$  of a convex solid [31,46].

### III. GEOMETRIC MEASURES OF UNIAXIAL SOLIDS OF REVOLUTION WITH CONTINUOUS SURFACE CURVATURE

Let  $K$  be a convex particle in  $\mathbb{R}^4$ . Its second virial coefficient  $B_2(K)$  can analytically be calculated with Eq. (14) using its geometric measures volume  $V_P(K)$ , surface area  $S_P(K)$ , second quermassintegral  $W_2(K)$ , and mean radius of curvature  $\tilde{R}_P(K)$ . Uniaxial solids of revolution with meridian curve  $r(z)$  can be parameterized conveniently in hypercylindrical coordinates,

$$\Psi = \begin{pmatrix} w \\ x \\ y \\ z \end{pmatrix} = \begin{pmatrix} r \sin \vartheta \sin \chi \cos \varphi \\ r \sin \vartheta \sin \chi \sin \varphi \\ r \sin \vartheta \cos \chi \\ r \cos \vartheta \end{pmatrix} = \begin{pmatrix} r(z) \sin \chi \cos \varphi \\ r(z) \sin \chi \sin \varphi \\ r(z) \cos \chi \\ z \end{pmatrix}, \quad (17)$$

related to Cartesian or polar coordinates. Since the volume of a uniaxial solid of revolution in  $\mathbb{R}^D$  is simply

$$V_P(K) = \kappa_{D-1} \int r^{D-1}(z) dz, \quad (18)$$

using hypercylindrical coordinates, the expression

$$V_P(K) = \frac{4}{3} \pi \int_{z_{\min}}^{z_{\max}} r^3(z) dz \quad (19)$$

results in  $\mathbb{R}^4$  for a particle with height  $h = z_{\max} - z_{\min}$ . If  $r(z_{\min}) = r(z_{\max}) = 0$ , its total surface area equals its lateral

surface area and can be written as

$$S_P(K) = \beta_{D-1} \int r^{D-2}(z) \left\{ 1 + \left[ \frac{dr(z)}{dz} \right]^2 \right\}^{1/2} dz \quad (20)$$

in  $\mathbb{R}^D$ , with

$$ds = \{[dr(z)]^2 + [dz]^2\}^{1/2} = \left\{ 1 + \left[ \frac{dr(z)}{dz} \right]^2 \right\}^{1/2} dz \quad (21)$$

being the infinitesimal arc length element of the meridian curve with the result

$$S_P(K) = 4\pi \int_{z_{\min}}^{z_{\max}} r^2(z) [1 + \dot{r}^2(z)]^{1/2} dz \quad (22)$$

in  $\mathbb{R}^4$  [31,34].

The second quermassintegral  $W_2(K)$  depends on the principal radii of curvature  $R_i$  of the convex solid [Eqs. (15) and (16)], accessible as reciprocal eigenvalues of the Weingarten map:

$$\mathcal{W} = \mathbf{I}^{-1} \mathbf{II}. \quad (23)$$

The Weingarten map  $\mathcal{W}$  is also known as shape operator, where  $\mathbf{I}$  and  $\mathbf{II}$  denote the first and second fundamental form of the solid's surface  $\Psi$ . In  $\mathbb{R}^4$ , both fundamental forms can be written as

$$\mathbf{I} = \begin{bmatrix} \left( \frac{\partial \Psi}{\partial \varphi} \right) \cdot \left( \frac{\partial \Psi}{\partial \varphi} \right) & \left( \frac{\partial \Psi}{\partial \varphi} \right) \cdot \left( \frac{\partial \Psi}{\partial \chi} \right) & \left( \frac{\partial \Psi}{\partial \varphi} \right) \cdot \left( \frac{\partial \Psi}{\partial z} \right) \\ \left( \frac{\partial \Psi}{\partial \chi} \right) \cdot \left( \frac{\partial \Psi}{\partial \varphi} \right) & \left( \frac{\partial \Psi}{\partial \chi} \right) \cdot \left( \frac{\partial \Psi}{\partial \chi} \right) & \left( \frac{\partial \Psi}{\partial \chi} \right) \cdot \left( \frac{\partial \Psi}{\partial z} \right) \\ \left( \frac{\partial \Psi}{\partial z} \right) \cdot \left( \frac{\partial \Psi}{\partial \varphi} \right) & \left( \frac{\partial \Psi}{\partial z} \right) \cdot \left( \frac{\partial \Psi}{\partial \chi} \right) & \left( \frac{\partial \Psi}{\partial z} \right) \cdot \left( \frac{\partial \Psi}{\partial z} \right) \end{bmatrix} \quad (24)$$

and

$$\mathbf{II} = \begin{bmatrix} \hat{\mathbf{n}} \cdot \frac{\partial^2 \Psi}{\partial \varphi^2} & \hat{\mathbf{n}} \cdot \frac{\partial^2 \Psi}{\partial \varphi \partial \chi} & \hat{\mathbf{n}} \cdot \frac{\partial^2 \Psi}{\partial \varphi \partial z} \\ \hat{\mathbf{n}} \cdot \frac{\partial^2 \Psi}{\partial \chi \partial \varphi} & \hat{\mathbf{n}} \cdot \frac{\partial^2 \Psi}{\partial \chi^2} & \hat{\mathbf{n}} \cdot \frac{\partial^2 \Psi}{\partial \chi \partial z} \\ \hat{\mathbf{n}} \cdot \frac{\partial^2 \Psi}{\partial z \partial \varphi} & \hat{\mathbf{n}} \cdot \frac{\partial^2 \Psi}{\partial z \partial \chi} & \hat{\mathbf{n}} \cdot \frac{\partial^2 \Psi}{\partial z^2} \end{bmatrix}, \quad (25)$$

with the normal field  $\hat{\mathbf{n}} \equiv \hat{\mathbf{n}}(\varphi, \chi, z)$  of the solid's surface, which reads with  $\mathbf{a} = \partial \Psi / \partial \varphi$ ,  $\mathbf{b} = \partial \Psi / \partial \chi$ , and  $\mathbf{c} = \partial \Psi / \partial z$ , as

$$\mathbf{n}(\mathbf{a}, \mathbf{b}, \mathbf{c}) = \det \begin{pmatrix} e_w & a_w & b_w & c_w \\ e_x & a_x & b_x & c_x \\ e_y & a_y & b_y & c_y \\ e_z & a_z & b_z & c_z \end{pmatrix}, \quad (26)$$

using the canonical basis  $(e_w, e_x, e_y, e_z)$  with

$$\mathbf{n}(\mathbf{a}, \mathbf{b}, \mathbf{c}) = -\mathbf{n}(\mathbf{b}, \mathbf{a}, \mathbf{c}) = \mathbf{n}(\mathbf{c}, \mathbf{a}, \mathbf{b}) = -\mathbf{n}(\mathbf{c}, \mathbf{b}, \mathbf{a}) \quad (27)$$

as parities. This results in

$$\hat{\mathbf{n}} = \frac{\mathbf{n}}{\|\mathbf{n}\|} = \frac{1}{[1 + \dot{r}^2(z)]^{1/2}} \begin{bmatrix} -\sin \chi \cos \varphi \\ -\sin \chi \sin \varphi \\ -\cos \chi \\ \dot{r}(z) \end{bmatrix}, \quad (28)$$

and, finally, the Weingarten map

$$\underline{\mathcal{W}} = \begin{bmatrix} \frac{1}{r(z)[1+\dot{r}^2(z)]^{1/2}} & 0 & 0 \\ 0 & \frac{1}{r(z)[1+\dot{r}^2(z)]^{1/2}} & 0 \\ 0 & 0 & -\frac{\ddot{r}(z)}{[1+\dot{r}^2(z)]^{3/2}} \end{bmatrix} \quad (29)$$

is obtained as a main diagonal matrix. Hence, its eigenvalues are directly accessible from the diagonal elements indicating the principal curvatures. The mean curvature thus can be written with the trace of the Weingarten map as

$$H_P = \frac{1}{D-1} \text{Tr}(\underline{\mathcal{W}}). \quad (30)$$

Hence, for a uniaxial solid of revolution in  $\mathbb{R}^4$ , three principal radii of curvature,

$$R_1(z) = R_2(z) = r(z)[1 + \dot{r}^2(z)]^{1/2} \quad (31)$$

$$R_3(z) = -\frac{1}{\ddot{r}(z)}[1 + \dot{r}^2(z)]^{3/2}, \quad (32)$$

result as inverses of the principal curvatures, where two of them are identical. Using the surface element  $d^3S = r^2(z) \sin \chi \, d\varphi \, d\chi \, dz$ , the second quermassintegral in  $\mathbb{R}^4$  with Eqs. (15) and (21), performing the integration over the angular coordinates  $\varphi$  and  $\chi$ , finally reads as

$$W_2(K) = \frac{\pi}{3} \int_{z_{\min}}^{z_{\max}} r^2(z) \left[ \frac{1}{R_1(z)} + \frac{1}{R_2(z)} + \frac{1}{R_3(z)} \right] \times [1 + \dot{r}^2(z)]^{1/2} dz \quad (33)$$

for convex solids with continuous surface curvatures.

The mean radius of curvature of a convex solid with continuous surface curvature can, in general, be calculated from its principal radii of curvature as

$$\tilde{R}_P = \frac{1}{\beta_D} \oint \frac{1}{D-1} \left[ \sum_{i=1}^{D-1} R_i(\phi_0, \dots, \phi_{D-2}) \right] \prod_{j=0}^{D-2} \sin^j(\phi_j) \, d\phi_j, \quad (34)$$

normalized to the surface area of a  $D$ -dimensional unit sphere. Employing the surface element

$$d^3S = R_1 R_2 R_3 \sin^2 \vartheta \sin \chi \, d\varphi \, d\chi \, d\vartheta \\ = r^2(z) \sin \chi [1 + \dot{r}^2(z)]^{1/2} \, d\varphi \, d\chi \, dz, \quad (35)$$

the angular integral can be written as a surface integral,

$$\tilde{R}_P(K) = \frac{2}{3\pi} \int_{z_{\min}}^{z_{\max}} r^2(z) \left[ \frac{1}{R_2(z)R_3(z)} + \frac{1}{R_1(z)R_3(z)} + \frac{1}{R_1(z)R_2(z)} \right] [1 + \dot{r}^2(z)]^{1/2} dz, \quad (36)$$

where again the integration over the angular coordinates  $\varphi$  and  $\chi$  results in a factor  $4\pi$ .

Using the relations to the other quermassintegrals in Eq. (13), analytical expressions for them can be summarized as

$$W_0(K) = V_P, \quad (37a)$$

$$W_1(K) = \frac{1}{4} \oint d^3S = \frac{1}{4} S_P, \quad (37b)$$

$$W_2(K) = \frac{1}{4} \oint \frac{1}{3} \left[ \frac{1}{R_1} + \frac{1}{R_2} + \frac{1}{R_3} \right] d^3S, \quad (37c)$$

$$W_3(K) = \frac{1}{4} \oint \frac{1}{3} \left[ \frac{1}{R_1 R_2} + \frac{1}{R_1 R_3} + \frac{1}{R_2 R_3} \right] d^3S = \tilde{R}_P \kappa_4, \quad (37d)$$

$$W_4(K) = \frac{1}{4} \oint \frac{1}{R_1 R_2 R_3} d^3S = \kappa_4, \quad (37e)$$

for convex solids with continuous surface curvature in  $\mathbb{R}^4$ .

For arbitrary-dimensional Euclidean spaces  $\mathbb{R}^D$ , this can generally be written as

$$W_i(K) = \begin{cases} V_P & : i = 0 \\ \frac{1}{D} \oint d^{D-1}S & : i = 1 \\ \frac{1}{D} \oint \frac{1}{\binom{D-1}{i}} \left[ \sum_{j=1}^{D-i+1} a_{D-i+1,j} \right] d^{D-1}S & : 2 \leq i \leq D \end{cases} \quad (38)$$

with

$$a_{ij} = \begin{cases} \frac{1}{R_j} & : i = D-1 \\ \frac{1}{R_j} \sum_{k=j+1}^{i+1} a_{i+1,k} & : i \leq D-2 \end{cases} \quad (39)$$

and

$$d^D S = \left[ \prod_{i=1}^D R_i \right] \left[ \prod_{j=0}^{D-1} \sin^j(\phi_j) \, d\phi_j \right] \quad (40)$$

for the surface element. For uniaxial solids of revolution in  $\mathbb{R}^D$ , their principal radii of curvature can directly be obtained by

$$R_i = \begin{cases} \pm r(z) [1 + \dot{r}^2(z)]^{1/2} & : 1 \leq i \leq D-2 \\ \mp \frac{1}{\ddot{r}(z)} [1 + \dot{r}^2(z)]^{3/2} & : i = D-1, \end{cases} \quad (41)$$

in dependence on their meridian curve  $r(z)$  with the sign defined by the direction of the normal field. For convex solids with discontinuities in their surface curvature, additional contributions to quermassintegrals  $W_i(K)$  need to be considered: Additional contributions to  $W_1(K)$  exist for uniaxial solids of revolution in  $\mathbb{R}^4$  if  $r(z_{\min}) \neq 0$  or  $r(z_{\max}) \neq 0$ . One- and two-dimensional singularities of the surface curvature, where in the case of uniaxial solids of revolution in  $\mathbb{R}^4$  only two-dimensional singularities can exist, cause additional contributions to  $W_2(K)$  and  $W_3(K)$ . Zero-dimensional singularities, which can for uniaxial solids of revolution only exist at  $r(z) = 0$ , do not cause additional contributions to  $W_i$  for  $0 \leq i \leq D$ . In the following we provide quermassintegrals for various uniaxial solids of revolution in  $\mathbb{R}^4$ , including shapes with discontinuities in their surface curvature.

#### IV. SPECIFIC GEOMETRIC MEASURES FOR SELECTED SOLIDS OF REVOLUTION

A uniaxial solid of revolution in  $\mathbb{R}^D$  can solely be defined by its meridian curve  $r(z)$ , with  $z$  being the invariant axis. Using the aspect ratio  $\nu$  as the ratio of height  $h$  and maximum diameter  $2r_i$ , the meridian curves of the geometries investigated in this work can be conveniently summarized as shown

TABLE I. Meridian curves  $r(z)$  of  $D$ -dimensional uniaxial solids of revolution defined in range  $z_{\min} \leq z \leq z_{\max}$ .

Geometry	$r(z)$		
Sphere	$(r_0^2 - z^2)^{\frac{1}{2}}$	:	$-r_0 \leq z \leq r_0$
Ellipsoid	$[r_{\text{eq}}^2 - (\frac{z}{\nu})^2]^{\frac{1}{2}}$	:	$-\nu r_{\text{eq}} \leq z \leq \nu r_{\text{eq}}$
Spherocylinder	$\{r_{\text{eq}}^2 - [z - (\nu - 1)r_{\text{eq}}]^2\}^{\frac{1}{2}}$	:	$(\nu - 1)r_{\text{eq}} \leq z \leq \nu r_{\text{eq}}$
	$r_{\text{eq}}$	:	$(1 - \nu)r_{\text{eq}} \leq z \leq (\nu - 1)r_{\text{eq}}$
Cylinder	$\{r_{\text{eq}}^2 - [z + (\nu - 1)r_{\text{eq}}]^2\}^{\frac{1}{2}}$	:	$-\nu r_{\text{eq}} \leq z \leq (1 - \nu)r_{\text{eq}}$
	$r_{\text{eq}}$	:	$-\nu r_{\text{eq}} \leq z \leq \nu r_{\text{eq}}$
Spindle	$(\frac{1-\nu^2}{2})r_{\text{eq}} + \frac{1}{2}[(\nu^2 + 1)^2 r_{\text{eq}}^2 - 4z^2]^{\frac{1}{2}}$	:	$-\nu r_{\text{eq}} \leq z \leq \nu r_{\text{eq}}$
Lens	$[\frac{ z r_{\text{eq}}(\nu^2 - 1)}{\nu} + (r_{\text{eq}}^2 - z^2)]^{\frac{1}{2}}$	:	$-\nu r_{\text{eq}} \leq z \leq \nu r_{\text{eq}}$
Spherical cap	$(r_0^2 - z^2)^{\frac{1}{2}}$	:	$r_0 - h \leq z \leq r_0$
Doublecone	$r_{\text{eq}} - \frac{ z }{\nu}$	:	$-\nu r_{\text{eq}} \leq z \leq \nu r_{\text{eq}}$
Cone	$r_0 - \frac{z}{\nu}$	:	$0 \leq z \leq \nu r_0$
Truncated cone	$r_0 - \frac{r_0 - r_1}{h} z$	:	$0 \leq z \leq h$

in Table I. Two-dimensional sections of these geometries are displayed in Fig. 1.

Let, in general,

$$W_i = W_i' + W_i'' + W_i''' \quad (42)$$

be the quermassintegral of a convex uniaxial solid of revolution, with  $W_i'$  being the contribution of the continuous surface curvature,  $W_i''$  the total contribution of all  $(D - 2)$ -dimensional singularities in the surface curvature of the solid, and  $W_i'''$  the total contribution of all zero-dimensional singularities in the surface curvature. For four-dimensional uniaxial solids of revolution,  $W_i'$  can with the meridian curve  $r(z)$  defined in Table I be obtained by Eqs. (19), (22), (33), and (36) or for arbitrary dimensions by Eq. (38) in general.

Therefore, the principal radii of curvature have to be calculated by Eqs. (31) and (32) in  $\mathbb{R}^4$  or by Eq. (41) in general.

If a solid has discontinuities in its surface curvature, their contributions to the quermassintegrals have separately to be considered in addition to the contribution of the continuous parts  $W_i'$ .

For geometries with a  $(D - 2)$ -dimensional singularity, e.g., the equator of a hyperlens, the meridian curve  $r(z)$  can in the vicinity of the singularity continuously be replaced by a toroidal hypercylinder with height  $2\varepsilon$  and meridian curve

$$r^\sharp(z) = \xi + (r_1^2 - z^2)^{1/2}, \quad (43)$$

with  $r^\sharp(\varepsilon) = r(\varepsilon)$  and  $\dot{r}^\sharp(\varepsilon) = \dot{r}(\varepsilon)$  as shown for a hyperlens in Fig. 2.

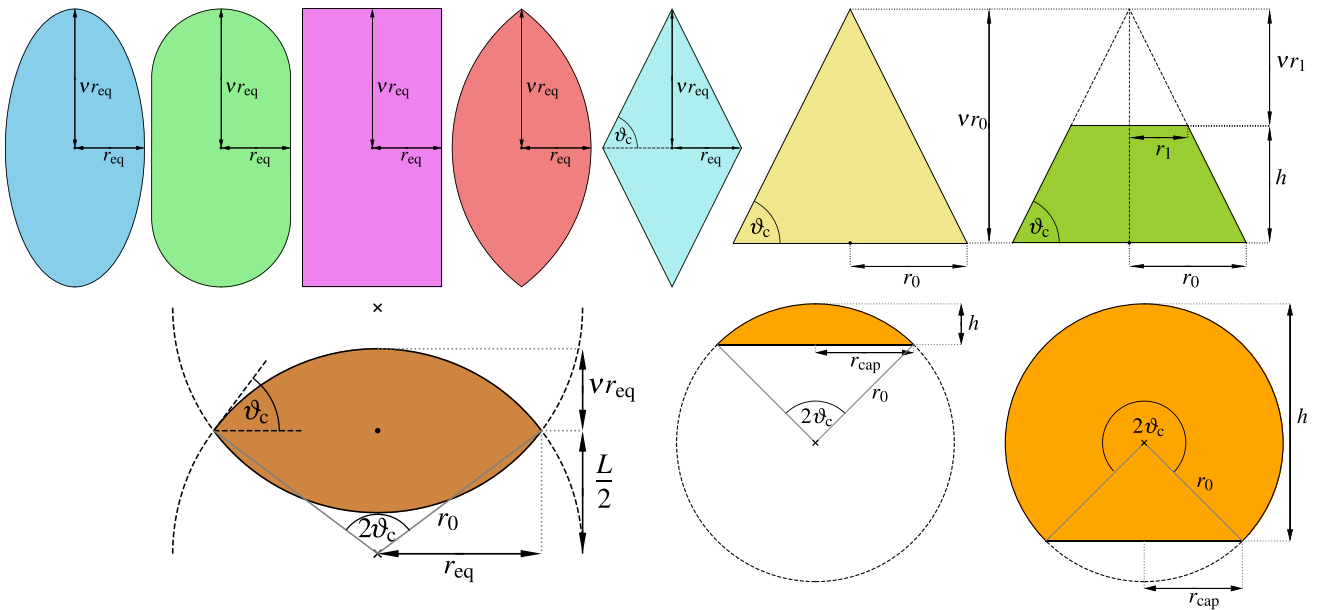


FIG. 1. Two-dimensional sections of uniaxial solids of revolution. FLTR: Hyperellipsoid, hyperspherocylinder, hypercylinder, hyperspindle, hyperdoublecone, hypercone, truncated hypercone, hyperlens, hyperspherical cap ( $h < r_0$  and  $h > r_0$ ).

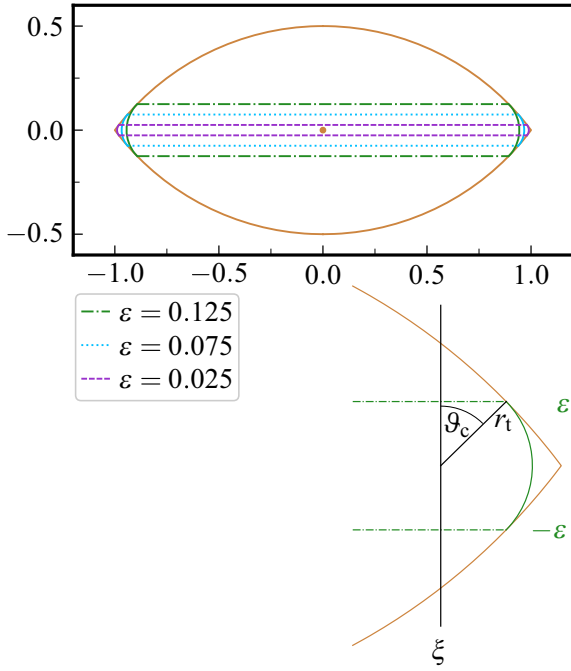


FIG. 2. Continuous completion of a hyperlens with radius  $r_{\text{eq}} = 1$  and aspect ratio  $\nu = 1/2$  by a hypertorus of height  $2\varepsilon$  with meridian radius  $r_t$  and distance  $\xi$  between the center of the torus and the center of the meridian arc.

In Eq. (43),  $r_t$  is the meridian radius of the hypertorus and  $\xi$  the distance between the center of the hypertorus and the center of the meridian arc. In the limit  $\varepsilon \rightarrow 0$ , the contribution of the equatorial singularity to the quermassintegrals,

$$W_i'' = \kappa_{D-1} \frac{i-1}{D} r_{\text{eq}}^{D-i} \int_{\vartheta_c}^{\pi-\vartheta_c} \sin^{i-2}(\vartheta) d\vartheta, \quad (44)$$

results for  $1 \leq i \leq D-1$ , in dependence on the critical angle  $\vartheta_c$  of the singularity. To the quermassintegrals of order  $i \in \{0, 1, D\}$ , the singularity does not contribute. Expressions for these angles  $\vartheta_c$  are compiled for the investigated geometries in Table II. In the case of hyperspherical caps, hypercones, and truncated hypercones, half of the respective contributions  $W_i''$  of Eq. (44) need to be considered, in addition to half the contribution of a  $(D-1)$ -dimensional spherical hyperplate  $W_i''$  for each singularity.

TABLE II. Critical angles  $\vartheta_c$  of  $D$ -dimensional uniaxial solids of revolution with equatorial singularities.

Geometry	$\vartheta_c$
Cylinder	$\frac{\pi}{2}$
Lens	$\arccos\left(\frac{1-\nu^2}{1+\nu^2}\right)$
Spherical cap	$\arccos\left(1 - \frac{h}{r_0}\right)$
Doublecone	$\arccos\left(\frac{1}{\sqrt{1+\nu^2}}\right)$
Cone	$\arccos\left(\frac{1}{\sqrt{1+\nu^2}}\right)$
Truncated cone	$\arccos\left(\frac{r_0-r_1}{\sqrt{h^2+(r_0-r_1)^2}}\right)$

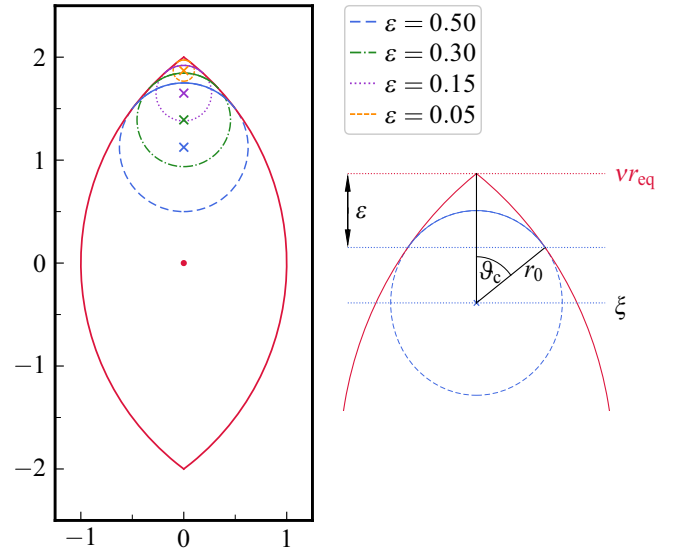


FIG. 3. Continuous completion of a hyperspindle with radius  $r_{\text{eq}} = 1$  and aspect ratio  $\nu = 2$  by hypersphere segments with radius  $r_0$  and the vicinity to the apex  $\varepsilon$ . The crosses indicate the centers of the hyperspheres with  $z = \xi$ .

To determine the contribution of a zero-dimensional singularity to the quermassintegrals of a convex uniaxial solid of revolution, its meridian curve  $r(z)$  can in the vicinity of the singularity continuously be replaced by the meridian curve of a hypersphere, as visualized in Fig. 3 for a hyperspindle. Here  $\xi$  is the  $z$  position of the hypersphere's center and  $r_0$  its radius. Performing the integration over the critical angle  $\vartheta_c(\varepsilon)$  results in the limit  $\varepsilon \rightarrow 0$  in a vanishing contribution

$$W_i''' = 0 \quad (45)$$

to the quermassintegrals.

For few uniaxial solids of revolution, their quermassintegrals are already reported in the literature for arbitrary-dimensional Euclidean spaces  $\mathbb{R}^D$  [23,35,36]. Their expressions are summarized in Table III. For  $D$ -dimensional ellipsoids of revolution, the Gauss hypergeometric function  ${}_2F_1(a, b, c; z)$  can be used in general, which is directly related to the complete elliptic integrals of first and second kind. To study the influence of the detailed particle shape, further

TABLE III. Known quermassintegrals  $W_i$  of  $D$ -dimensional, uniaxial solids of revolution in the literature [23].

Sphere	$W_i = \kappa_D r_0^{D-i}$
Ellipsoid	$W_i = \kappa_D \nu^{i+1} r_{\text{eq}}^{D-i} {}_2F_1\left(\frac{D+1}{2}, \frac{i}{2}, \frac{D}{2}; 1 - \nu^2\right)$
Spherocylinder	$W_i = [\kappa_D + 2(\nu-1) \frac{D-i}{D} \kappa_{D-1}] r_{\text{eq}}^{D-i}$
Cylinder	$W_i = \begin{cases} 2\kappa_{D-1} \nu r_{\text{eq}}^D & : i = 0 \\ \frac{2}{D} \kappa_{D-1} [(D-i)\nu + \frac{\beta_i}{2\kappa_{i-1}}] r_{\text{eq}}^{D-i} & : i \geq 1 \end{cases}$
Spherical plate	$W_i = \begin{cases} 0 & : i = 0 \\ \frac{\kappa_{D-1}}{D} \frac{\beta_i}{\kappa_{i-1}} r_0^{D-i} & : i \geq 1 \end{cases}$

TABLE IV. Geometric measures of four-dimensional hyperspheres, hyperellipsoids of revolution, hyperspherocylinders, hypercylinders, and spherical hyperplates.

Hypersphere	$V_P = \frac{1}{2}\pi^2 r_0^4$ $S_P = 2\pi^2 r_0^3$ $W_2 = \frac{1}{2}\pi^2 r_0^2$ $\tilde{R}_P = r_0$
Hyperellipsoid	$V_P = \frac{1}{2}\pi^2 \nu r_{\text{eq}}^4$ $S_P = 2\pi^2 \nu^2 r_{\text{eq}}^3 {}_2\mathcal{F}_1\left(\frac{5}{2}, \frac{1}{2}; 2; 1 - \nu^2\right)$ $W_2 = \frac{1}{3}\pi^2 r_{\text{eq}}^2 \left(\frac{1-\nu^2}{1-\nu^2}\right)$ $\tilde{R}_P = \nu^4 r_{\text{eq}} {}_2\mathcal{F}_1\left(\frac{5}{2}, \frac{3}{2}; 2; 1 - \nu^2\right)$
Hyperspherocylinder	$V_P = \left[\frac{1}{2}\pi^2 + \frac{8}{3}(\nu - 1)\pi\right]r_{\text{eq}}^4$ $S_P = [2\pi^2 + 8(\nu - 1)\pi]r_{\text{eq}}^3$ $W_2 = \left[\frac{1}{2}\pi^2 + \frac{4}{3}(\nu - 1)\pi\right]r_{\text{eq}}^2$ $\tilde{R}_P = \left[1 + \frac{4}{3\pi}(\nu - 1)\right]r_{\text{eq}}$
Hypercylinder	$V_P = \frac{8}{3}\pi \nu r_{\text{eq}}^4$ $S_P = \frac{8}{3}\pi(3\nu + 1)r_{\text{eq}}^3$ $W_2 = \frac{1}{3}\pi(4\nu + \pi)r_{\text{eq}}^2$ $\tilde{R}_P = \frac{4}{3\pi}(\nu + 2)r_{\text{eq}}$
Spherical hyperplate	$V_P = 0$ $S_P = \frac{8}{3}\pi r_0^3$ $W_2 = \frac{1}{3}\pi^2 r_0^2$ $\tilde{R}_P = \frac{8}{3\pi}r_0$

geometries with singularities in their surface curvature are investigated in  $\mathbb{R}^4$  in the following, which can straightforwardly

TABLE V. Geometric measures of four-dimensional hyperspindles, hyperlenses, hyperspherical caps, hyperdoublecones, hypercones, and truncated hypercones.

Hyperspindle	$V_P = \frac{5\pi}{16}r_{\text{eq}}^4 \left[ (v^4 - \frac{6}{5}v^2 + 1)(v^2 + 1)^2 \arcsin\left(\frac{2v}{v^2+1}\right) - 2v^7 - \frac{14}{15}v^5 + \frac{14}{15}v^3 + 2v \right]$ $S_P = \frac{1}{2}\pi r_{\text{eq}}^3 \left[ (3v^6 + v^4 + v^2 + 3) \arcsin\left(\frac{2v}{v^2+1}\right) - 6v^5 + 6v \right]$ $W_2 = \frac{5\pi}{12}r_{\text{eq}}^2 \left[ (v^4 + \frac{2}{5}v^2 + 1) \arcsin\left(\frac{2v}{v^2+1}\right) - 2v^3 + 2v \right]$ $\tilde{R}_P = \frac{r_{\text{eq}}}{\pi} \left[ (v^2 + 1) \arcsin\left(\frac{2v}{v^2+1}\right) - \frac{2}{3}v \frac{v^2-1}{v^2+1} \right]$
Hyperlens	$V_P = \frac{\pi r_{\text{eq}}^4}{32\nu^4} \left\{ (1 + v^2)^4 \left[ \pi - 2 \arcsin\left(\frac{1-v^2}{1+v^2}\right) \right] - 4\nu \left[ 1 - v^6 + \frac{11}{3}v^2(1 - v^2) \right] \right\}$ $S_P = \frac{\pi(1+v^2)r_{\text{eq}}^3}{4\nu^3} \left\{ (1 + v^2)^2 \left[ \pi - 2 \arcsin\left(\frac{1-v^2}{1+v^2}\right) \right] - 4\nu(1 - v^2) \right\}$ $W_2 = \frac{\pi r_{\text{eq}}^2}{8\nu^2} \left[ (1 + v^2)^2 \pi - 2(v^4 - \frac{2}{3}v^2 + 1) \arcsin\left(\frac{1-v^2}{1+v^2}\right) - 4\nu(1 - v^2) \right]$ $\tilde{R}_P = \frac{r_{\text{eq}}}{2\pi\nu} \left\{ (1 + v^2) \left[ \pi - 2 \arcsin\left(\frac{1-v^2}{1+v^2}\right) \right] + \frac{4\nu}{3} \frac{1-v^2}{1+v^2} \right\}$
Hyperspherical cap	$V_P = \frac{\pi^2}{4}r_0^4 \left[ 1 - \frac{2}{\pi} \arctan\left(\frac{r_0-h}{r_{\text{cap}}}\right) - \frac{2r_{\text{cap}}}{3\pi r_0^2} (r_0 - h)(3r_0^2 + 2r_{\text{cap}}^2) \right]$ $S_P = \pi^2 r_0^3 \left[ 1 - \frac{2}{\pi} \arctan\left(\frac{r_0-h}{r_{\text{cap}}}\right) - \frac{2r_{\text{cap}}}{\pi r_0^2} (r_0 - h) \right] + \frac{4}{3}\pi r_{\text{cap}}^3$ $W_2 = \frac{\pi^2}{4}r_0^2 \left[ 1 - \frac{2}{\pi} \arctan\left(\frac{r_0-h}{r_{\text{cap}}}\right) - \frac{2r_{\text{cap}}}{\pi r_0^2} (r_0 - h) \right] + \frac{\pi}{3}r_{\text{cap}}^2 \left[ \frac{\pi}{2} + \arcsin\left(1 - \frac{h}{r_0}\right) \right]$ $\tilde{R}_P = \frac{r_0}{2} \left[ 1 - \frac{2}{\pi} \arctan\left(\frac{r_0-h}{r_{\text{cap}}}\right) - \frac{2r_{\text{cap}}}{\pi r_0^2} (r_0 - h) \right] + \frac{4}{3\pi}r_{\text{cap}} \left( 2 - \frac{h}{r_0} \right)$
Hyperdoublecone	$V_P = \frac{2}{3}\pi \nu r_{\text{eq}}^4$ $S_P = \frac{8}{3}\pi r_{\text{eq}}^3 \sqrt{1 + \nu^2}$ $W_2 = \frac{2}{3}\pi r_{\text{eq}}^2 \left[ \nu + \arcsin\left(\frac{1}{\sqrt{1+\nu^2}}\right) \right]$ $\tilde{R}_P = \frac{4}{3\pi}r_{\text{eq}} \frac{\nu^2+2}{\sqrt{1+\nu^2}}$
Hypercone	$V_P = \frac{1}{3}\pi \nu r_0^4$ $S_P = \frac{4}{3}\pi r_0^3 (\sqrt{1 + \nu^2} + 1)$ $W_2 = \frac{1}{6}\pi r_0^2 \left[ 2\nu + \pi + 2 \arcsin\left(\frac{1}{\sqrt{1+\nu^2}}\right) \right]$ $\tilde{R}_P = \frac{2}{3\pi}r_0 \left( 2 + \frac{\nu^2+2}{\sqrt{1+\nu^2}} \right)$
Truncated hypercone	$V_P = \frac{h}{3}\pi (r_0^3 + r_0^2 r_1 + r_0 r_1^2 + r_1^3)$ $S_P = \frac{4}{3}\pi [r_0^3 + r_1^3 + (r_0^2 + r_0 r_1 + r_1^2) \sqrt{h^2 + (r_0 - r_1)^2}]$ $W_2 = \frac{1}{3}\pi (r_0 + r_1) \left\{ h + (r_0 - r_1) \arcsin\left[\frac{r_0-r_1}{\sqrt{h^2+(r_0-r_1)^2}}\right] \right\} + \frac{1}{6}\pi^2 (r_0^2 + r_1^2)$ $\tilde{R}_P = \frac{2}{3\pi} \left[ 2(r_0 + r_1) + \frac{h^2+2(r_0-r_1)^2}{\sqrt{h^2+(r_0-r_1)^2}} \right]$

be extended to arbitrary higher-dimensional uniaxial solids of revolution.

## V. RESULTS

The excluded volume per particle of four-dimensional, convex solids of revolution, derived from the geometric measures volume  $V_P$ , total surface area  $S_P$ , second quermass-integral  $W_2$ , and mean radius of curvature  $\tilde{R}_P$  provided in Sec. IV, is obtained using Eq. (14). These geometric measures are summarized in Tables IV and V. To investigate, independent of the particle volume  $V_P$ , the influence of the specific particle shape in dependence on the aspect ratio  $\nu$ , reduced second virial coefficients

$$B_2^* = \frac{B_2}{V_P} = 1 + \frac{S_P \tilde{R}_P}{V_P} + \frac{6}{\pi^2} \frac{W_2^2}{V_P} \quad (46)$$

are compared.

### A. Solids with inversion symmetry

In Fig. 4, second virial coefficients  $B_2$  of hyperellipsoids, hyperspherocylinders, hyperspindles, hypercylinders, hyperdoublecones, and hyperlenses as four-dimensional, uniaxial solids of revolution with inversion symmetry are shown. While hyperspherocylinders and hyperspindles are strictly prolate geometries with  $\nu \geq 1$ , hyperlenses are strictly oblate geometries with  $0 \leq \nu \leq 1$ . Hyperellipsoids, hyper-

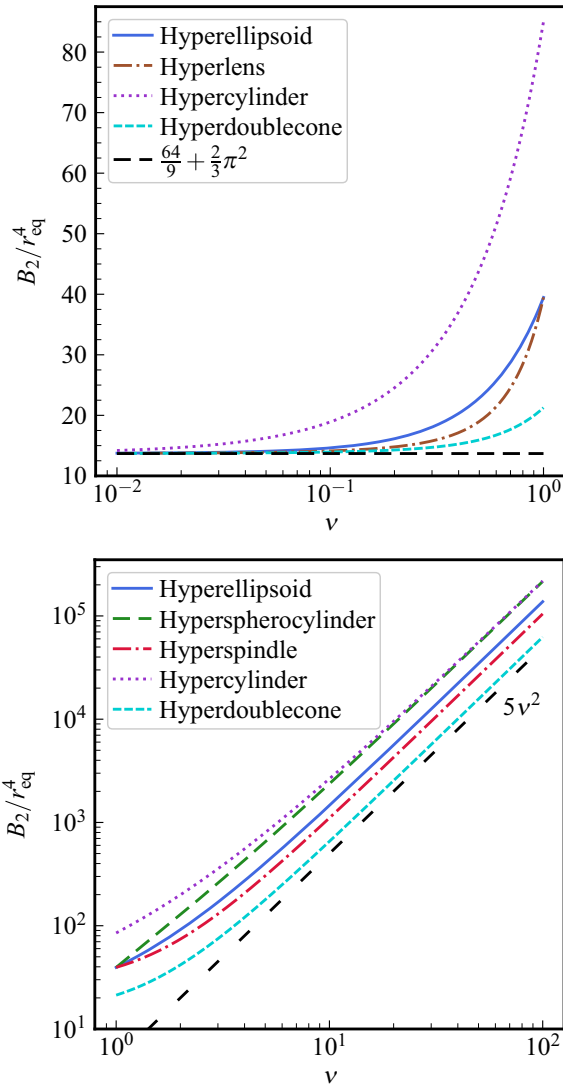


FIG. 4. Second virial coefficient  $B_2/r_{\text{eq}}^4$  of oblate (top) and prolate (bottom) uniaxial solids of revolution with inversion symmetry in dependence on the aspect ratio  $\nu$ . For  $\nu \rightarrow 0$ , the common limit  $B_2/r_{\text{eq}}^4 = 64/9 + 2\pi^2/3$  of a spherical hyperplate is approached as visualized by the horizontal line. To indicate the common slope at infinite aspect ratio,  $5\nu^2$  is depicted as a guide to the eye.

cylinders, and hyperdoublecones can be prolate or oblate with  $0 \leq \nu < \infty$ .

As visible in Fig. 4, hyperellipsoids, hyperspherocylinders, hyperspindles, and hyperlenses approach in the limit  $\nu \rightarrow 1$  hyperspheres with radius  $r_{\text{eq}}$  and  $B_2^{(\text{hsph})} = 4\pi^2 r_{\text{eq}}^4$  as their second virial coefficient. For oblate geometries, with decreasing aspect ratio all geometries approach the limit

$$\lim_{\nu \rightarrow 0} \frac{B_2}{r_{\text{eq}}^4} = \frac{64}{9} + \frac{2}{3}\pi^2 \quad (47)$$

for spherical hyperplates with radius  $r_{\text{eq}}$ .

In the limit  $\nu \rightarrow \infty$ , hard hyperneedles result, where hyperspherocylinders approach hypercylinders since the contribution of the capping hyperspheres becomes negligible. For sufficiently large aspect ratios, the proportionality

$B_2(\nu \gg 1) \propto \nu^2$  is observed as indicated by the black line  $5\nu^2$ . The limits

$$\lim_{\nu \rightarrow \infty} \frac{B_2^{(\text{hcyl})}}{\nu^2 r_{\text{eq}}^4} = \lim_{\nu \rightarrow \infty} \frac{B_2^{(\text{hscy})}}{\nu^2 r_{\text{eq}}^4} = \frac{64}{3}, \quad (48a)$$

$$\lim_{\nu \rightarrow \infty} \frac{B_2^{(\text{hell})}}{\nu^2 r_{\text{eq}}^4} = \frac{64}{9} + \frac{2}{3}\pi^2, \quad (48b)$$

$$\lim_{\nu \rightarrow \infty} \frac{B_2^{(\text{hspl})}}{\nu^2 r_{\text{eq}}^4} = \frac{1408}{135}, \quad (48c)$$

$$\lim_{\nu \rightarrow \infty} \frac{B_2^{(\text{hdcn})}}{\nu^2 r_{\text{eq}}^4} = \frac{56}{9} \quad (48d)$$

decrease from hypercylinders (hcyl) and hyperspherocylinders (hscy) with identical value over hyperellipsoids (hell) and hyperspindles (hspl) to hyperdoublecones (hdcn). This sequence is in accordance to the relation

$$K^{(\text{hdcn})} \subset K^{(\text{hspl})} \subset K^{(\text{hell})} \subset K^{(\text{hscy})} \subset K^{(\text{hcyl})} \quad (49)$$

for convex sets  $K \equiv K(\nu, r_{\text{eq}})$  of hyperdoublecones, hyperspindles, hyperellipsoids, hyperspherocylinders, and hypercylinders with identical aspect ratio  $\nu$  and equatorial radius  $r_{\text{eq}}$ . This behavior is identical to their three-dimensional analogs [31].

### 1. Prolate geometries

To analyze the influence of the detailed particle geometry, reduced virial coefficients  $B_2^*$  are compared in Fig. 5 (top) in dependence on their aspect ratio  $\nu$ . For a better display of relative deviances, the ratios of reduced second virial coefficients  $B_2^*(\nu)$  to the reduced second virial coefficient  $B_2^{*(\text{hell})}(\nu)$  of hyperellipsoids are shown in Fig. 5 (bottom). In the limit  $\nu \rightarrow 1$ , hyperellipsoids, hyperspherocylinders, and hyperspindles approach hyperspheres with a reduced second virial coefficient of  $B_2^{*(\text{hsph})} = 8$  in accordance to the general result

$$B_2^{*(\text{hsph})} = 2^{D-1} \quad (50)$$

for  $D$ -dimensional spheres [47].

With increasing aspect ratio  $\nu$ , the general proportionality  $B_2^*(\nu \gg 1) \propto \nu$  is observed with the limits

$$\lim_{\nu \rightarrow \infty} \frac{B_2^{*(\text{hcyl})}}{\nu} = \lim_{\nu \rightarrow \infty} \frac{B_2^{*(\text{hscy})}}{\nu} = \frac{8}{\pi}, \quad (51a)$$

$$\lim_{\nu \rightarrow \infty} \frac{B_2^{*(\text{hspl})}}{\nu} = \frac{77}{9\pi}, \quad (51b)$$

$$\lim_{\nu \rightarrow \infty} \frac{B_2^{*(\text{hell})}}{\nu} = \frac{4}{3} + \frac{128}{9\pi^2}, \quad (51c)$$

$$\lim_{\nu \rightarrow \infty} \frac{B_2^{*(\text{hdcn})}}{\nu} = \frac{28}{3\pi}, \quad (51d)$$

in increasing order [Fig. 5 (bottom)]. Again, for large aspect ratios hyperspherocylinders approach hypercylinders with a negligible contribution of the capping hyperspheres. The limit for four-dimensional hyperspherocylinders is already reported in a previous work [33].

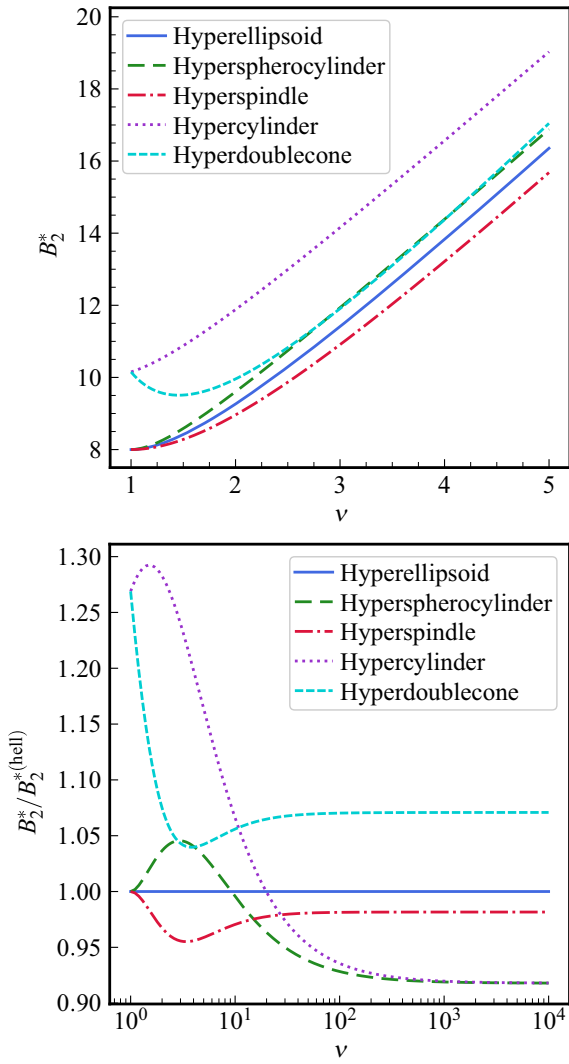


FIG. 5. Reduced second virial coefficients  $B_2^*$  of prolate solids of revolution with inversion symmetry in dependence on the aspect ratio  $\nu$  (top) and these coefficients normalized to the reduced second virial coefficients of hyperellipsoids  $B_2^{*(hell)}$  at an extended scale of aspect ratios  $\nu$  (bottom).

Interestingly, in  $\mathbb{R}^4$ , unlike  $\mathbb{R}^3$  [31], the reduced second virial coefficients

$$[B_2^{*(hycl)}(\nu = 1)] = [B_2^{*(hdcn)}(\nu = 1)] = 3 + \frac{20}{\pi} + \frac{\pi}{4} \quad (52)$$

of hypercylinders and hyperdoublecones with aspect ratio  $\nu = 1$  are identical. In  $\mathbb{R}^2$ , both analog geometries are hard squares for  $\nu = 1$  with trivially identical reduced virial coefficients  $B_2^* = 1 + 4/\pi$  [29]. Results for dimensions  $D > 4$  are shown in Sec. V D.

Comparing Fig. 5 (bottom) with the analog three-dimensional results (Fig. 7 in [31]), significant differences are observed between  $\mathbb{R}^3$  and  $\mathbb{R}^4$ : For large aspect ratios  $\nu \gg 1$ , the ratios of the reduced second virial coefficients  $B_2^*/B_2^{*(hell)}$  are more similar in  $\mathbb{R}^4$  than in  $\mathbb{R}^3$  due to the additional symmetry of the solid. The reduced second virial coefficients of hyperspherocylinders and hypercylinders in  $\mathbb{R}^4$  normalized to those of hyperellipsoids similarly depend on

the aspect ratio  $\nu$  as the reduced second virial coefficients of spherocylinders and cylinders normalized to ellipsoids in  $\mathbb{R}^3$ . However, for solids with apical singularities, deviations are observed. Opposite to spindles in  $\mathbb{R}^3$ , for hyperspindles in  $\mathbb{R}^4$  the ratio  $[B_2^*(\nu)/B_2^{*(hell)}(\nu)] < 1$  results for  $\nu \rightarrow \infty$ . Also for hyperdoublecones with increasing aspect ratio  $\nu$ , the ratio  $B_2^*(\nu)/B_2^{*(hell)}(\nu)$  is significantly smaller than for doublecones in  $\mathbb{R}^3$ . Especially, the reduced second virial coefficients of geometries with apical singularities differ much less in  $\mathbb{R}^4$  at large aspect ratios  $\nu \gg 1$  from those without apical singularities than in  $\mathbb{R}^3$ .

## 2. Oblate geometries

While hyperellipsoids of revolution, hypercylinders, and hyperdoublecones exist in addition to prolate aspect ratios  $\nu \geq 1$  also as oblate solids of revolution with  $0 \leq \nu \leq 1$ , hyperlenses are restricted to oblate aspect ratios. In Fig. 6 (top), reduced second virial coefficients  $B_2^*$  of oblate geometries are shown in dependence on their inverse aspect ratio  $\nu^{-1}$ .

In the limit  $\nu^{-1} \rightarrow 1$ , hyperlenses and hyperellipsoids approach hyperspheres with  $B_2^* = 8$ . With decreasing aspect ratio  $\nu$ , the proportionality  $B_2^*(\nu \ll 1) \propto \nu^{-1}$  is observed with the limits

$$\lim_{\nu \rightarrow 0} [\nu B_2^{*(hycl)}] = \frac{\pi}{4} + \frac{8}{3\pi}, \quad (53a)$$

$$\lim_{\nu \rightarrow 0} [\nu B_2^{*(hell)}] = \frac{4}{3} + \frac{128}{9\pi^2}, \quad (53b)$$

$$\lim_{\nu \rightarrow 0} [\nu B_2^{*(hlen)}] = \frac{5}{8}\pi + \frac{20}{3\pi}, \quad (53c)$$

$$\lim_{\nu \rightarrow 0} [\nu B_2^{*(hdcn)}] = \pi + \frac{32}{3\pi}, \quad (53d)$$

in increasing order. Note that for hyperellipsoids of revolution the relation

$$\lim_{\nu \rightarrow 0} [\nu B_2^*(\nu)] = \lim_{\nu \rightarrow \infty} \frac{B_2^*(\nu)}{\nu} \quad (54)$$

is fulfilled [Eqs. (51c) and (53b)]. Despite that hyperlenses and oblate hyperellipsoids are similar particle shapes, the reduced second virial coefficients of hyperlenses exceed those of the corresponding hyperellipsoids of revolution for all aspect ratios  $\nu < 1$ , indicating the influence of the detailed particle shape beyond size and aspect ratio. In  $\mathbb{R}^4$ , for small aspect ratios  $0 < \nu \ll 1$ , larger differences between the reduced second virial coefficients of these geometries are observed than between their analogs in  $\mathbb{R}^3$  [Fig. 11 in [31] and Fig. 6 (bottom)], which is opposite to the comparison of prolate geometries between  $\mathbb{R}^3$  and  $\mathbb{R}^4$ .

## 3. Comparison of shapes existing both as prolate and oblate solids of revolution

Hyperellipsoids, hypercylinders, and hyperdoublecones exist both as prolate and oblate solids of revolution with aspect ratios  $0 \leq \nu < \infty$ . Since in addition to the former geometries with inversion symmetry also hypercones (discussed later in Sec. V B 2) exist as prolate and oblate solids of revolution, they are for completeness included in this comparison. In

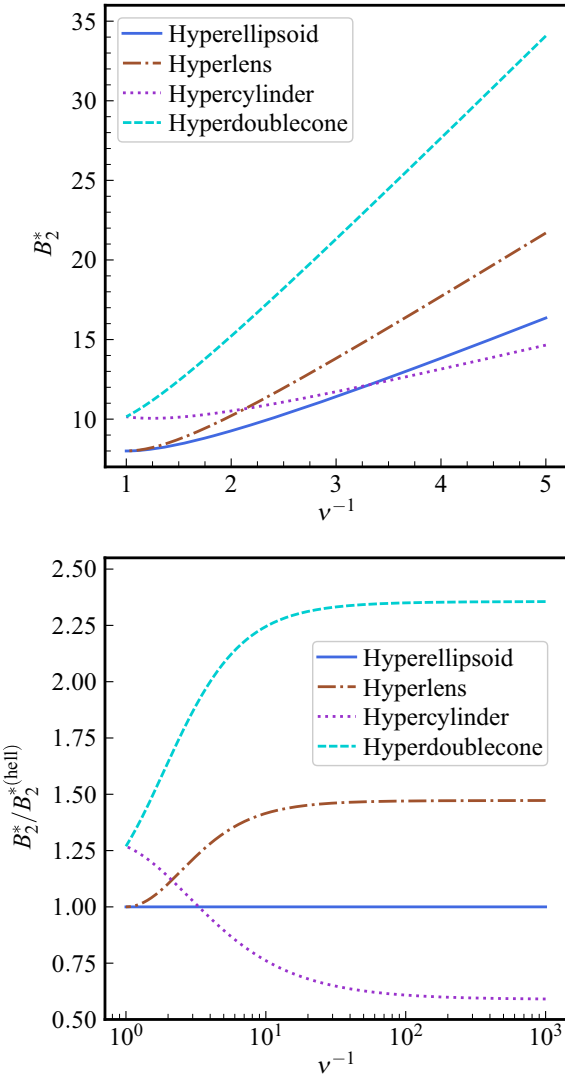


FIG. 6. Reduced second virial coefficients  $B_2^*$  of oblate solids of revolution with inversion symmetry in dependence on the inverse aspect ratio  $\nu^{-1}$  (top) and these coefficients normalized to the reduced second virial coefficients of hyperellipsoids  $B_2^{*(\text{hell})}$  at an extended scale of inverse aspect ratios  $\nu^{-1}$  (bottom).

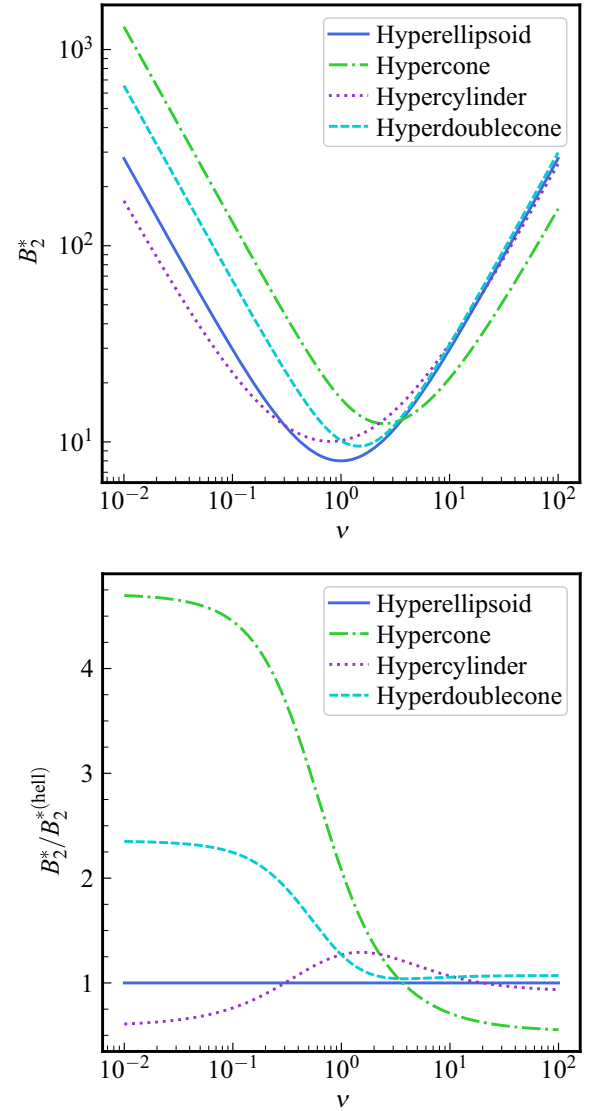


FIG. 7. Reduced second virial coefficients  $B_2^*$  for shapes existing as prolate and oblate solids of revolution (top) and their reduced second virial coefficients normalized to those of hyperellipsoids  $B_2^*/B_2^{*(\text{hell})}$  (bottom) in dependence on the aspect ratio  $\nu$ .

Fig. 7, reduced second virial coefficients  $B_2^*$  of these geometries are displayed as well as reduced second virial coefficients normalized to those of hyperellipsoids of revolution in dependence of their aspect ratio  $\nu$ . The reduced second virial coefficient  $B_2^*$  for each geometry traverses a minimum  $B_{2,\min}^*$  at  $\nu_{\min}$  as summarized in Table VI.

TABLE VI. Minima of reduced second virial coefficients  $B_{2,\min}^*$  and corresponding aspect ratios  $\nu_{\min}$  in  $\mathbb{R}^4$ .

Geometry	$\nu_{\min}$	$B_{2,\min}^*(\nu_{\min})$
Hyperellipsoid	1	8
Hyperdoublecone	1.456 428 ...	9.506 809 ...
Hypercylinder	0.801 098 ...	10.050 852 ...
Hypercone	2.502 640 ...	12.394 541 ...

As expected, hyperellipsoids approach for  $\nu \rightarrow 1$  a hypersphere with the smallest  $B_2^*$  possible for a convex solid, while for different geometries the minima are located at  $\nu_{\min} \neq 1$ . In addition to the symmetry relation for reduced second virial coefficients of hyperellipsoids of revolution, in the limits  $\nu \rightarrow 0$  and  $\nu \rightarrow \infty$  [Eq. (54)], a general symmetry relation

$$B_2^{*(\text{hell})}(\nu) = B_2^{*(\text{hell})}(\nu^{-1}) \quad (55)$$

can be identified in  $\mathbb{R}^4$ , which also exists for ellipsoids of revolution in  $\mathbb{R}^3$  [31]. This parity is universal for arbitrary-dimensional, uniaxial ellipsoids of revolution as proven in Appendix A.

### B. Solids without inversion symmetry

Hyperspherical caps, hypercones, and truncated hypercones are convex, uniaxial solids of revolution without

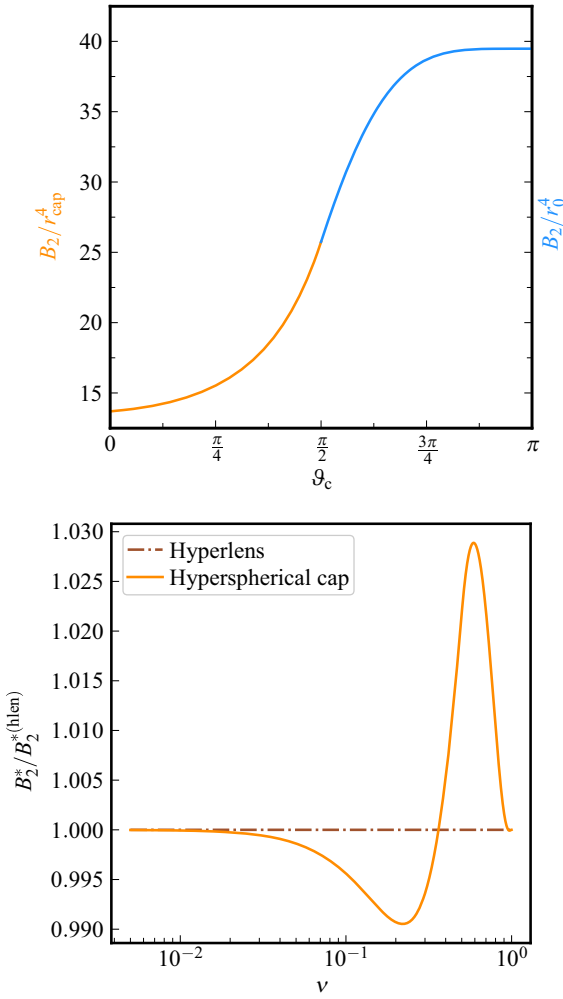


FIG. 8. Second virial coefficient  $B_2$  of hyperspherical caps with radius of the generating hypersphere  $r_0$  and radius of the spherical singularity  $r_{\text{cap}}$  in dependence on the critical angle  $\vartheta_c$  (top) and reduced second virial coefficients  $B_2^*(\nu)/B_2^{*(\text{hlen})}(\nu)$  normalized to those of hyperlenses in dependence on their aspect ratio  $\nu$  (bottom).

inversion symmetry whose second virial coefficients are compared in the following.

### 1. Hyperspherical caps

The second virial coefficients of hyperspherical caps can either be expressed in dependence on the critical angle  $\vartheta_c$  or the aspect ratio  $\nu$ . The latter quantities are related by

$$\nu = \begin{cases} \frac{h}{2r_{\text{cap}}} = [1 - \cos(\vartheta_c)][2 \sin(\vartheta_c)]^{-1} & : h \leq r_0 \\ \frac{h}{2r_0} = \frac{1}{2}[1 - \cos(\vartheta_c)] & : h \geq r_0 \end{cases} \quad (56)$$

with  $\vartheta_c \in [0, \pi]$ .

In Fig. 8 (top), the second virial coefficients  $B_2$  of hyperspherical caps are shown in dependence on the critical angle  $\vartheta_c$ . For critical angles  $\vartheta_c \rightarrow 0$ , a spherical hyperplate with radius  $r_{\text{cap}}$  and second virial coefficient  $B_2 = (\frac{64}{9} + \frac{2}{3}\pi^2)r_{\text{cap}}^4$  results, while for  $\vartheta_c \rightarrow \pi$  a hypersphere with radius  $r_0$  and second virial coefficient  $B_2 = 4\pi^2 r_0^4$  is obtained. For  $\vartheta_c =$

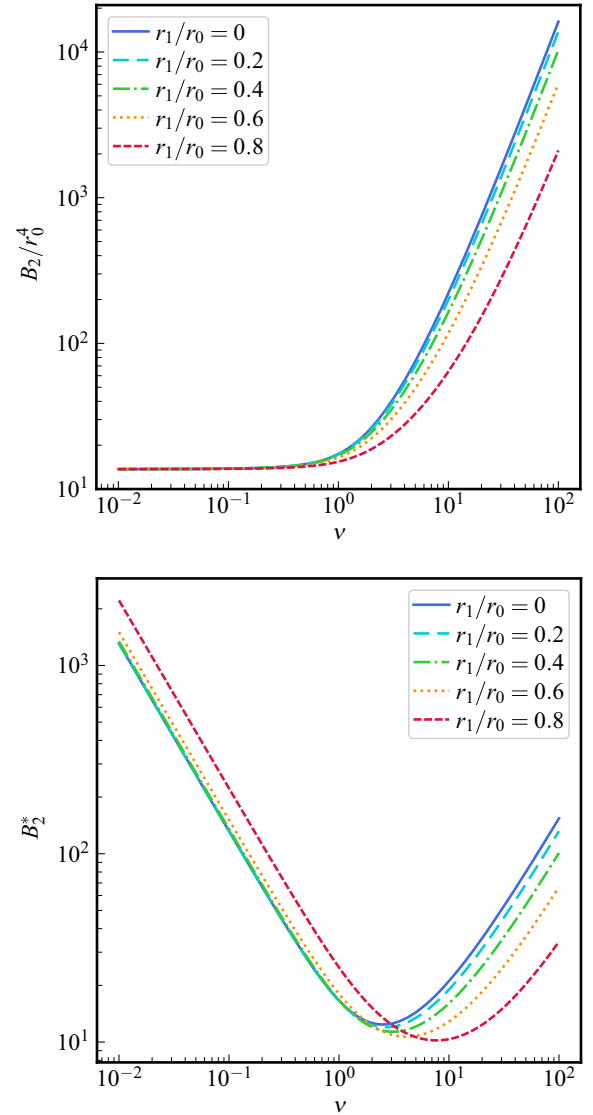


FIG. 9. Second virial coefficient  $B_2$  (top) and reduced second virial coefficient  $B_2^*$  (bottom) of truncated hypercones in dependence on the aspect ratio  $\nu$  for selected ratios of radii  $r_1/r_0$ . In the limit  $r_1/r_0 \rightarrow 0$ , a hypercone results.

$\pi/2$ , with  $r_{\text{cap}} = r_0 = h$ , the second virial coefficient  $B_2 = (\frac{43}{24}\pi^2 + 2\pi + \frac{16}{9})r_0^4$  is obtained.

The ratio of reduced second virial coefficients of hyperspherical caps and hyperlenses  $B_2^*(\nu)/B_2^{*(\text{hlen})}(\nu)$  is displayed in Fig. 8 (bottom) in dependence on the aspect ratio  $\nu$ . The reduced second virial coefficients are nearly identical in the whole range of aspect ratios with a maximum at  $\nu \approx 0.59$ , a minimum at  $\nu \approx 0.22$ , and a second, less pronounced minimum at  $\nu \approx 0.95$ . In the limit  $\nu \rightarrow 0$ , both geometries approach a spherical hyperplate.

### 2. Hypercones and truncated hypercones

The second virial coefficients  $B_2$  and reduced second virial coefficients  $B_2^*$  of truncated hypercones are depicted in Fig. 9, in dependence on the aspect ratio  $\nu$  for selected ratios  $r_1/r_0$ . In the limit  $r_1/r_0 \rightarrow 0$ , truncated hypercones approach hyper-

cones. For the second virial coefficient  $B_2^{(\text{hcon})}$  of hypercones, in the limit

$$\lim_{\nu \rightarrow \infty} \frac{B_2^{(\text{hcon})}}{\nu^2 r_0^4} = \frac{14}{9} \quad (57)$$

the proportionality  $B_2(\nu \gg 1) \propto \nu^2$  is observed, while for the reduced second virial coefficient,

$$\lim_{\nu \rightarrow \infty} \frac{B_2^{*(\text{hcon})}}{\nu} = \frac{14}{3\pi}, \quad (58)$$

the proportionality  $B_2^*(\nu \gg 1) \propto \nu$  results. The second virial coefficients of both hypercones and truncated hypercones approach in the limit  $\nu \rightarrow 0$  the expected value of a spherical hyperplate. In the limit  $r_1/r_0 \rightarrow 0$ , approaching hypercones with the reduced second virial coefficient  $B_2^{*(\text{hcon})}$ , in the limit

$$\lim_{\nu \rightarrow 0} [\nu B_2^{*(\text{hcon})}] = 2\pi + \frac{64}{3\pi}, \quad (59)$$

the proportionality  $B_2^{*(\text{hcon})}(\nu \ll 1) \propto \nu^{-1}$  is observed for vanishing aspect ratios  $\nu$ . With increasing aspect ratio  $\nu$ , the second virial coefficient  $B_2$  of the truncated hypercones decreases with increasing ratio of radii  $r_1/r_0$ . The minima of reduced second virial coefficients  $B_2^*$  in dependence on the aspect ratio  $\nu$  decrease with rising ratio of radii  $r_1/r_0$  and shift to larger  $\nu$ .

### C. Excluded volume of hyperspherocylinders

Using the general expression for quermassintegrals of  $D$ -dimensional, uniaxial spherocylinders in Euclidean spaces  $\mathbb{R}^D$ ,

$$W_i = \left[ \kappa_D + 2(\nu - 1) \frac{D-i}{D} \kappa_{D-1} \right] r_{\text{eq}}^{D-i} \quad (60)$$

[23,33], and the Brunn-Minkowski theorem [Eq. (9)], the excluded volume of two identical hyperspherocylinders can be written as

$$V_{\text{ex}}^{(\text{scyl})} = 2^D V_P + 2^{D-2} (S_P \tilde{R}_P - D V_P) \quad (61)$$

in  $\mathbb{R}^D$ , depending only on quermassintegrals of orders  $i \in \{0, 1, D-1\}$ , as proven in Appendix B.

As a unique feature of four-dimensional spherocylinders, their excluded volume  $V_{\text{ex}}^{(\text{hscy})}$  [Eq. (61)] does not depend on the particle volume  $V_P$  [33]. Using Eq. (46), the reduced second virial coefficient of  $D$ -dimensional, uniaxial spherocylinders reads as

$$B_2^{*(\text{scyl})} = 2^{D-1} + 2^{D-3} \left( \frac{S_P \tilde{R}_P}{V_P} - D \right). \quad (62)$$

The influence of the aspect ratio  $\nu$  is visible from the reformulation

$$B_2^{*(\text{scyl})} = 2^{D-1} \left[ 1 + \frac{D-1}{D} \frac{\kappa_{D-1}}{\kappa_D} \frac{(\nu-1)^2}{2(\nu-1) + \kappa_D \kappa_{D-1}^{-1}} \right] \quad (63)$$

with the limit

$$\lim_{\nu \rightarrow 1} B_2^{*(\text{scyl})}(D, \nu) = 2^{D-1}$$

TABLE VII. Reduced second virial coefficients  $B_2^*$  for  $D$ -dimensional spherocylinders and cylinders with aspect ratio  $\nu$  in the limit  $\nu \rightarrow \infty$  [Eq. (64)].

$D$	$\lim_{\nu \rightarrow \infty} \frac{B_2^*(D, \nu)}{\nu}$	$D$	$\lim_{\nu \rightarrow \infty} \frac{B_2^*(D, \nu)}{\nu}$
1	0	2	$\frac{1}{\pi}$
3	1	4	$\frac{2^3}{\pi}$
5	6	6	$\frac{2^7}{3\pi}$
7	30	8	$\frac{2^{11}}{10\pi}$
9	140	10	$\frac{2^{15}}{35\pi}$
11	630	12	$\frac{2^{19}}{126\pi}$

for a  $D$ -dimensional sphere [Eq. (50)], and

$$\lim_{\nu \rightarrow \infty} \frac{B_2^{*(\text{scyl})}(D, \nu)}{\nu} = 2^D \frac{D-1}{8\sqrt{\pi}} \frac{\Gamma(D/2)}{\Gamma[(D+1)/2]} \quad (64)$$

for an infinitely long,  $D$ -dimensional spherocylinder. In the latter limit, the proportionality  $B_2^* \propto \nu$  is obtained in accordance to the results in dimensions  $2 \leq D \leq 4$  reported in the literature [29,31,33]. Since in the limit  $\nu \rightarrow \infty$  the contributions of the capping  $D$ -dimensional hemispheres are negligible (see Sec. V A 1), the limits are identical for  $D$ -dimensional spherocylinders and cylinders. In Table VII the results for these limits are provided for Euclidean spaces  $\mathbb{R}^D$  with  $D \leq 12$ .

Instead of an infinitely long  $D$ -dimensional spherocylinder with radius  $r_{\text{eq}}$ , a rod with length  $l$  and radius  $r_{\text{eq}} = 0$  is an alternative description of a hard needle in  $\mathbb{R}^D$  [29]. The quermassintegrals  $W_i$  read as

$$W_i = \begin{cases} 0 & : i \leq D-2 \\ \frac{\kappa_{D-1}}{D} l & : i = D-1 \\ \kappa_D & : i = D \end{cases} \quad (65)$$

for such line segments [23,36]. With Eq. (9), in  $\mathbb{R}^1$  the excluded volume  $V_{\text{ex}} = 2l$  and in  $\mathbb{R}^2$  the rotation-averaged excluded volume  $V_{\text{ex}} = 2l^2/\pi$  of hard rods are obtained. In Euclidean spaces  $\mathbb{R}^D$  with  $D \geq 3$ , the rotation-averaged excluded volume  $V_{\text{ex}} = 0$  of infinitely thin rods with length  $l$  vanishes [23].

### D. Geometric measures of hyperdoublecones

The results for quermassintegrals of convex solids of revolution in  $\mathbb{R}^4$  can straightforwardly be extended to higher-dimensional Euclidean spaces  $\mathbb{R}^D$  as exemplarily shown for hyperdoublecones in the following. Using Eq. (18), with the defined meridian curves,

$$V_P^{(\text{cyl})}(\nu, r_{\text{eq}}) = D V_P^{(\text{dcn})}(\nu, r_{\text{eq}}) = 2\kappa_{D-1} \nu r_{\text{eq}}^D, \quad (66)$$

is obtained for the volumes of hypercylinders and hyperdoublecones. For hyperdoublecones, also the lateral surface area equals the total surface area, which can directly be obtained using Eq. (22). For the remaining quermassintegrals  $W_i$  with  $i \in \{2, D-1\}$ , the contributions of the continuous part  $W_i'$  can be obtained by Eq. (38) and of the equatorial singularity

TABLE VIII. Quermassintegrals  $W_i$  of  $D$ -dimensional, uniaxial solids of revolution. For spherical caps with  $h \leq r_0$ ,  $W_0$  and  $W_1$  are reported by Li [48], with  $\mathcal{I}_x(a, b)$  being the regularized incomplete beta function.

Spherical cap $0 \leq h \leq r_0$ :	$W_0 = \frac{\kappa_D}{2} r_0^D \mathcal{I}_{r_{\text{cap}}^2/r_0^2}(\frac{D+1}{2}, \frac{1}{2})$
	$W_1 = \frac{\kappa_D}{2} r_0^{D-1} \mathcal{I}_{r_{\text{cap}}^2/r_0^2}(\frac{D-1}{2}, \frac{1}{2}) + \frac{\kappa_{D-1}}{D} r_{\text{cap}}^{D-1}$
$r_0 \leq h \leq 2r_0$ :	$W_0 = \frac{\kappa_D}{2} r_0^D [2 - \mathcal{I}_{r_{\text{cap}}^2/r_0^2}(\frac{D+1}{2}, \frac{1}{2})]$
	$W_1 = \frac{\kappa_D}{2} r_0^{D-1} [2 - \mathcal{I}_{r_{\text{cap}}^2/r_0^2}(\frac{D-1}{2}, \frac{1}{2})] + \frac{\kappa_{D-1}}{D} r_{\text{cap}}^{D-1}$
Doublecone $1 \leq i \leq D-1$ :	$W_0 = \frac{2}{D} \kappa_{D-1} \nu r_{\text{eq}}^D$
	$W_i = W_i' + W_i''$
	$W_i' = \frac{2}{D} \kappa_{D-1} \nu^{i-1} (1 + \nu^2)^{(2-i)/2} r_{\text{eq}}^{D-i}$
	$W_i'' = \kappa_{D-1} \frac{i-1}{D} r_{\text{eq}}^{D-i} \int_{\vartheta_c}^{\pi-\vartheta_c} \sin^{i-2}(\vartheta) d\vartheta$
Cone $1 \leq i \leq D-1$ :	$W_0 = \frac{1}{D} \kappa_{D-1} \nu r_0^D$
	$W_i = W_i' + W_i''$
	$W_i' = \frac{\kappa_{D-1}}{D} \nu^{i-1} (1 + \nu^2)^{(2-i)/2} r_0^{D-i}$
	$W_i'' = \frac{\kappa_{D-1}}{D} r_0^{D-i} [\frac{\beta_i}{2\kappa_{i-1}} + (i-1) \int_{\vartheta_c}^{\pi/2} \sin^{i-2}(\vartheta) d\vartheta]$
Truncated cone	$W_0 = \frac{\kappa_{D-1}}{D} h \frac{r_1^D - r_0^D}{r_1 - r_0}$
	$W_1 = \frac{\kappa_{D-1}}{D} [r_0^{D-1} + r_1^{D-1} + \frac{r_1^{D-1} - r_0^{D-1}}{r_1 - r_0} \sqrt{h^2 + (r_0 - r_1)^2}]$

$W_i''$  by Eq. (44), resulting in the expressions summarized in Table VIII.

Using these general expressions for the quermassintegrals  $W_i$ , the reduced second virial coefficients of  $D$ -dimensional doublecones and cylinders can be compared. For solids with aspect ratio  $\nu = 1$ , this is shown in Fig. 10 up to  $D = 12$ . Remarkably, for  $D = 2$  and  $D = 4$  the values are identical. While in  $\mathbb{R}^3$  the reduced second virial coefficient of a doublecone is

smaller than of a cylinder, in higher dimensions ( $D > 4$ ) the opposite is observed for the analogs.

General expressions for quermassintegrals of further uniaxial solids of revolution in arbitrary dimension can be obtained using Eqs. (38) and (44) with the critical angles from Table II. For solids of revolution whose total surface area exceeds their lateral surface area, only half the contribution of Eq. (44) and half the contribution of a spherical hyperplate [cf. Table III] need to be considered.

## VI. SUMMARY AND OUTLOOK

In this work, analytical expressions for the geometric measures volume  $V_P$ , surface area  $S_P$ , second quermassintegrals  $W_2$ , and mean radius of curvature  $\bar{R}_P$  are derived for selected convex solids of revolution in  $\mathbb{R}^4$ . The results are summarized in Tables IV and V. Using Eqs. (13), analytical expressions for so far unknown quermassintegrals  $W_i$  are obtained. Employing these quantities, with Eq. (11) the intrinsic volumes  $v_i$  of these convex solids of revolution are analytically accessible, too.

In addition to hyperspheres, hyperellipsoids of revolution, hyperspherocylinders, hypercylinders, and spherical hyperplates with already known quermassintegrals (Table III), analytical expressions for so far unknown quermassintegrals of hyperspindles, hyperlenses, hyperspherical caps, hyperdoublecones, hypercones, and truncated hypercones are provided. The latter geometries possess removable singularities in their surface curvature. While apical, zero-dimensional singularities do not contribute to quermassintegrals, higher-dimensional singularities contribute to quermassintegrals  $W_i$  with  $0 < i < D$ , as exemplarily shown for hyperlenses. This contribution, in general, depends on the critical angle enclosed within the  $\varepsilon$  vicinity of the respective singularity. For uniaxial solids of revolution with infinitely large aspect ratios in  $\mathbb{R}^4$ ,

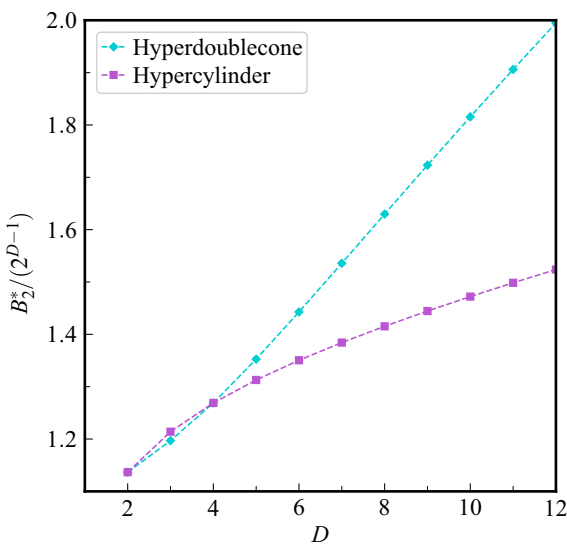


FIG. 10. Reduced second virial coefficients  $B_2^*$  of  $D$ -dimensional doublecones and cylinders with aspect ratio  $\nu = 1$ . The dashed lines serve as a guide to the eye.

a general proportionality  $B_2^* \propto \nu$  of reduced second virial coefficients to the aspect ratio arises, whereas for infinitely thin oblate geometries, the general proportionality  $B_2^* \propto \nu^{-1}$  results.

With known principal radii of curvature, the quermassintegrals are accessible for arbitrary convex solids in  $\mathbb{R}^4$  [Eqs. (37)]. The generalization to dimensions  $D > 4$  for geometries with continuous surfaces curvature [Eq. (38)] is straightforward. Possible contributions of singularities can be determined analogously as demonstrated in  $\mathbb{R}^3$  [31] and  $\mathbb{R}^4$  (this work). For selected geometries with discontinuities in their surface curvature, general expressions for their quermassintegrals are compiled in Table VIII. Using such general expressions, the parity  $B_2^*(\nu) = B_2^*(\nu^{-1})$  for uniaxial,  $D$ -dimensional ellipsoids of revolution is proven. Additionally, for  $D$ -dimensional, uniaxial spherocylinders, the dependence of the reduced second virial coefficient  $B_2^*$  on at most three quermassintegrals  $W_0$ ,  $W_1$ , and  $W_{D-1}$  is proven, too.

#### APPENDIX A: PROOF OF THE PARITY $B_2^*(\nu) = B_2^*(\nu^{-1})$ FOR UNIAXIAL HYPERELLIPSOIDS

*Theorem A1.* For  $D$ -dimensional, uniaxial ellipsoids of revolution with aspect ratio  $\nu$  the parity

$$B_2^{*(\text{ell})}(D, \nu) = B_2^{*(\text{ell})}(D, \nu^{-1}) \quad (\text{A1})$$

is fulfilled for the reduced second virial coefficient  $B_2^{*(\text{ell})}$  in arbitrary-dimensional Euclidean spaces  $\mathbb{R}^D$ .

*Proof.* Starting from the Brunn-Minkowski theorem for the rotation-averaged excluded volume of two identical convex particles  $K$ ,

$$V_{\text{ex}}(K) = \frac{1}{\kappa_D} \sum_{i=0}^D \binom{D}{i} W_i(K) W_{D-i}(K)$$

[Eq. (9)], the reduced second virial coefficient of  $D$ -dimensional spheroids can be written as

$$\begin{aligned} B_2^{*(\text{ell})}(D, \nu) &= \frac{1}{2\kappa_D^2 \nu r_{\text{eq}}^D} \sum_{i=0}^D \left[ \binom{D}{i} \kappa_D^2 \nu^{D+2} r_{\text{eq}}^D \right. \\ &\quad \times {}_2\mathcal{F}_1\left(\frac{D+1}{2}, \frac{i}{2}, \frac{D}{2}; 1 - \nu^2\right) \\ &\quad \left. \times {}_2\mathcal{F}_1\left(\frac{D+1}{2}, \frac{D-i}{2}, \frac{D}{2}; 1 - \nu^2\right) \right], \quad (\text{A2}) \end{aligned}$$

using the general expression

$$W_i = \kappa_D \nu^{i+1} r_{\text{eq}}^{D-i} {}_2\mathcal{F}_1\left(\frac{D+1}{2}, \frac{i}{2}, \frac{D}{2}; 1 - \nu^2\right) \quad (\text{A3})$$

for the quermassintegrals of this geometry [23] and  $B_2^*(K) = V_{\text{ex}}(K)/[2W_0(K)]$ . Equation (A2) can be simplified to

$$\begin{aligned} B_2^{*(\text{ell})}(D, \nu) &= \frac{1}{2} \nu^{D+1} \sum_{i=0}^D \left[ \binom{D}{i} {}_2\mathcal{F}_1\left(\frac{D+1}{2}, \frac{i}{2}, \frac{D}{2}; 1 - \nu^2\right) \right. \\ &\quad \left. \times {}_2\mathcal{F}_1\left(\frac{D+1}{2}, \frac{D-i}{2}, \frac{D}{2}; 1 - \nu^2\right) \right], \quad (\text{A4}) \end{aligned}$$

and analogously for aspect ratios  $\nu^{-1}$ ,

$$\begin{aligned} B_2^{*(\text{ell})}(D, \nu^{-1}) &= \frac{1}{2} \nu^{-(D+1)} \sum_{i=0}^D \left[ \binom{D}{i} \right. \\ &\quad \times {}_2\mathcal{F}_1\left(\frac{D+1}{2}, \frac{i}{2}, \frac{D}{2}; 1 - \frac{1}{\nu^2}\right) \\ &\quad \left. \times {}_2\mathcal{F}_1\left(\frac{D+1}{2}, \frac{D-i}{2}, \frac{D}{2}; 1 - \frac{1}{\nu^2}\right) \right] \quad (\text{A5}) \end{aligned}$$

is obtained. Using the Pfaff transformation [49],

$${}_2\mathcal{F}_1(a, b, c; z) = (1-z)^{-a} {}_2\mathcal{F}_1\left(a, c-b, c; \frac{z}{z-1}\right) \quad (\text{A6a})$$

$$= (1-z)^{-b} {}_2\mathcal{F}_1\left(c-a, b, c; \frac{z}{z-1}\right), \quad (\text{A6b})$$

the relations

$$\begin{aligned} &{}_2\mathcal{F}_1\left(\frac{D+1}{2}, \frac{i}{2}, \frac{D}{2}; 1 - \nu^2\right) \\ &= \nu^{-(D+1)} {}_2\mathcal{F}_1\left(\frac{D+1}{2}, \frac{D-i}{2}, \frac{D}{2}; 1 - \frac{1}{\nu^2}\right) \quad (\text{A7}) \end{aligned}$$

and

$$\begin{aligned} &{}_2\mathcal{F}_1\left(\frac{D+1}{2}, \frac{D-i}{2}, \frac{D}{2}; 1 - \nu^2\right) \\ &= \nu^{-(D+1)} {}_2\mathcal{F}_1\left(\frac{D+1}{2}, \frac{i}{2}, \frac{D}{2}; 1 - \frac{1}{\nu^2}\right) \quad (\text{A8}) \end{aligned}$$

result. Using Eqs. (A7) and (A8), Eq. (A5) can be transformed into Eq. (A4). Hence, Eq. (A1) results. This completes the proof. ■

#### APPENDIX B: ON THE EXCLUDED VOLUME OF UNIAXIAL HYPERSPHEROCYLINDERS

*Theorem B1.* For identical, uniaxial  $D$ -dimensional spherocylinders with aspect ratio  $\nu$  and radius  $r_{\text{eq}}$ , the rotation-averaged excluded volume  $V_{\text{ex}}^{(\text{scyl})}$  can be written as

$$V_{\text{ex}}^{(\text{scyl})} = 2^D V_P + 2^{D-2} (S_P \tilde{R}_P - D V_P) \quad (\text{B1a})$$

$$\begin{aligned} &= (2r_{\text{eq}})^D \left[ \kappa_D + 2(\nu-1)\kappa_{D-1} \right. \\ &\quad \left. + (\nu-1)^2 \frac{D-1}{D} \frac{\kappa_{D-1}^2}{\kappa_D} \right] \quad (\text{B1b}) \end{aligned}$$

in Euclidean spaces  $\mathbb{R}^D$  with arbitrary dimension  $D$ .

*Proof.* Starting from the Brunn-Minkowski theorem [Eq. (9)] for the rotation-averaged excluded volume between any two identical convex solids  $K$ , the expression

$$\begin{aligned} V_{\text{ex}}^{(\text{scyl})} &= \frac{1}{\kappa_D} \sum_{i=0}^D \binom{D}{i} \left\{ \left[ \kappa_D r_{\text{eq}}^{D-i} + 2(\nu-1) \frac{D-i}{D} \kappa_{D-1} r_{\text{eq}}^{D-i} \right] \right. \\ &\quad \left. \times \left[ \kappa_D r_{\text{eq}}^i + 2(\nu-1) \frac{i}{D} \kappa_{D-1} r_{\text{eq}}^i \right] \right\} \quad (\text{B2}) \end{aligned}$$

results for  $D$ -dimensional spherocylinders using Eq. (60). This can be rewritten as

$$V_{\text{ex}}^{(\text{scyl})} = \sum_{i=0}^D \binom{D}{i} \kappa_D r_{\text{eq}}^D + \sum_{i=0}^D \binom{D}{i} 2(\nu - 1) \kappa_{D-1} r_{\text{eq}}^D + \sum_{i=0}^D \binom{D}{i} 4(\nu - 1)^2 \frac{(D-i)i}{D^2} \frac{\kappa_{D-1}^2}{\kappa_D} r_{\text{eq}}^D. \quad (\text{B3})$$

Using the binomial theorem,

$$V_{\text{ex}}^{(\text{scyl})} = (2r_{\text{eq}})^D [\kappa_D + 2(\nu - 1)\kappa_{D-1}] + \frac{(\nu - 1)^2}{D} \frac{\kappa_{D-1}^2}{\kappa_D} r_{\text{eq}}^D \sum_{i=0}^D \binom{D}{i} 4 \frac{(D-i)i}{D} \quad (\text{B4})$$

is obtained. With

$$\sum_{i=0}^D \binom{D}{i} 4 \frac{(D-i)i}{D} = 2^D (D-1), \quad (\text{B5})$$

immediately Eq. (B1b) results. Using the representation of geometric measures  $V_P$ ,  $S_P$ , and  $\tilde{R}_P$  via quermassintegrals

$$V_P = \kappa_D r_{\text{eq}}^D + 2(\nu - 1) \kappa_{D-1} r_{\text{eq}}^D, \quad (\text{B6a})$$

$$S_P = D \kappa_D r_{\text{eq}}^{D-1} + 2(\nu - 1)(D-1) \kappa_{D-1} r_{\text{eq}}^{D-1}, \quad (\text{B6b})$$

$$\tilde{R}_P = r_{\text{eq}} + 2(\nu - 1) \frac{1}{D} \frac{\kappa_{D-1}}{\kappa_D} r_{\text{eq}}, \quad (\text{B6c})$$

the relation

$$S_P \tilde{R}_P - D V_P = 4(\nu - 1)^2 \frac{D-1}{D} \frac{\kappa_{D-1}^2}{\kappa_D} r_{\text{eq}}^D \quad (\text{B7})$$

is obtained for  $D$ -dimensional spherocylinders [Eqs. (13) and (60)]. With Eqs. (B6a) and (B7), the excluded volume with Eq. (B1b) can be rewritten as Eq. (B1a). This completes the proof. ■

- 
- [1] M. J. Stephen and J. P. Straley, *Rev. Mod. Phys.* **46**, 617 (1974).  
 [2] S. Torquato and F. H. Stillinger, *Rev. Mod. Phys.* **82**, 2633 (2010).  
 [3] V. R. Dugyala, S. V. Daware, and M. G. Basavaraj, *Soft Matter* **9**, 6711 (2013).  
 [4] J. Zhao, S. Zhao, and S. Luding, *Nat. Rev. Phys.* **5**, 505 (2023).  
 [5] T. K. Sau and A. L. Rogach, *Adv. Mater.* **22**, 1781 (2010).  
 [6] H. Zhang, M. Jin, and Y. Xia, *Angew. Chem. Int. Ed.* **51**, 7656 (2012).  
 [7] M. Ozaki, S. Kratochvil, and E. Matijević, *J. Colloid Interface Sci.* **102**, 146 (1984).  
 [8] M. Ocaña, M. P. Morales, and C. J. Serna, *J. Colloid Interface Sci.* **212**, 317 (1999).  
 [9] J. Roller, J. D. Geiger, M. Vöggrenreiter, J.-M. Meijer, and A. Zumbusch, *Soft Matter* **16**, 1021 (2020).  
 [10] G. Odriozola, *J. Chem. Phys.* **136**, 134505 (2012).  
 [11] G. Bautista-Carbajal, A. Moncho-Jordá, and G. Odriozola, *J. Chem. Phys.* **138**, 064501 (2013).  
 [12] P. Marienhagen and J. Wagner, *Phys. Rev. E* **105**, 014125 (2022).  
 [13] G. Cinacchi and S. Torquato, *J. Chem. Phys.* **143**, 224506 (2015).  
 [14] P. Marienhagen and J. Wagner, *Phys. Rev. E* **106**, 014101 (2022).  
 [15] M. Esposito and G. T. Evans, *Mol. Phys.* **83**, 835 (1994).  
 [16] D. Costa, F. Micali, F. Saija, and P. V. Giaquinta, *J. Phys. Chem. B* **106**, 12297 (2002).  
 [17] A. Poniewierski and R. Hořst, *Phys. Rev. Lett.* **61**, 2461 (1988).  
 [18] R. Hořst and A. Poniewierski, *Phys. Rev. A* **39**, 2742 (1989).  
 [19] H. Graf and H. Löwen, *Phys. Rev. E* **59**, 1932 (1999).  
 [20] N. F. Carnahan and K. E. Starling, *J. Chem. Phys.* **51**, 635 (1969).  
 [21] H. Hansen-Goos and K. Mecke, *Phys. Rev. Lett.* **102**, 018302 (2009).  
 [22] H. Hansen-Goos and K. Mecke, *J. Phys.: Condens. Matter* **22**, 364107 (2010).  
 [23] S. Torquato and Y. Jiao, *J. Stat. Mech.* (2022) 093404.  
 [24] A. Ishihara, *J. Chem. Phys.* **18**, 1446 (1950).  
 [25] A. Ishihara and T. Hayashida, *J. Phys. Soc. Jpn.* **6**, 40 (1951).  
 [26] H. Hadwiger, *Experientia* **7**, 395 (1951).  
 [27] T. Boublík, *Mol. Phys.* **29**, 421 (1975).  
 [28] G. Tarjus, P. Viot, S. M. Ricci, and J. Talbot, *Mol. Phys.* **73**, 773 (1991).  
 [29] M. Kulossa and J. Wagner, *Mol. Phys.* **122**, e2289699 (2024).  
 [30] S. Torquato and Y. Jiao, *Phys. Rev. E* **87**, 022111 (2013).  
 [31] E. Herold, R. Hellmann, and J. Wagner, *J. Chem. Phys.* **147**, 204102 (2017).  
 [32] M. E. Irrgang, M. Engel, A. J. Schultz, D. A. Kofke, and S. C. Glotzer, *Langmuir* **33**, 11788 (2017).  
 [33] M. Kulossa, P. Marienhagen, and J. Wagner, *Phys. Rev. E* **105**, 064121 (2022).  
 [34] M. Kulossa, D. Weidig, and J. Wagner, *Phys. Rev. E* **107**, 024129 (2023).  
 [35] R. Schneider, *Convex Bodies: The Brunn–Minkowski Theory* (Cambridge University Press, Cambridge, England, 2013).  
 [36] L. A. Santaló, *Integral Geometry and Geometric Probability* (Cambridge University Press, Cambridge, England, 2004).  
 [37] J. K. Singh and D. A. Kofke, *Phys. Rev. Lett.* **92**, 220601 (2004).  
 [38] P. Marienhagen, R. Hellmann, and J. Wagner, *Phys. Rev. E* **104**, 015308 (2021).  
 [39] S. Torquato, *J. Chem. Phys.* **149**, 020901 (2018).  
 [40] A. J. Schultz and D. A. Kofke, *J. Chem. Phys.* **157**, 190901 (2022).

- [41] P. W. A. Schönhöfer, K. Sun, X. Mao, and S. C. Glotzer, *Phys. Rev. Lett.* **131**, 258201 (2023).
- [42] I. Nezbeda and J. Škvára, *Mol. Phys.* **122**, e2304648 (2024).
- [43] J. E. Mayer, *J. Chem. Phys.* **5**, 67 (1937).
- [44] J. E. Mayer and M. G. Mayer, *Statistical Mechanics* (Wiley, New York, 1940).
- [45] J.-M. Morvan, in *Generalized Curvatures* (Springer, Berlin Heidelberg, 2008), pp. 153–164.
- [46] H. Groemer, *Math. Ann.* **198**, 23 (1972).
- [47] I. Urrutia, *J. Stat. Phys.* **187**, 29 (2022).
- [48] S. Li, *Asian J. Math. Stat.* **4**, 66 (2010).
- [49] F. W. J. Olver, A. B. Olde Daalhuis, D. W. Lozier, B. I. Schneider, R. F. Boisvert, C. W. Clark, B. R. Miller, B. V. Saunders, H. S. Cohl, M. A. McClain *et al.*, NIST digital library of mathematical functions, <https://dlmf.nist.gov>, Release 1.1.11 of 2023-09-15 (2023).

## List of Figures

1	Examples for cyclic graphs with three nodes. . . . .	7
2	The 64 undirected simple graphs with four nodes. Color-highlighted are the empty graph (red), the 16 spanning trees with three or two leaves (orange or blue), and the complete graph (violet). Isomorphic graphs are bounded by a dashed green box. . . . .	8
3	Two-dimensional sections of selected uniaxial solids or revolution in this work, FLTR: Ellipsoid, spherocylinder, cylinder, spindle, doublecone, cone, truncated cone, lens, spherical segment ( $\vartheta_c < \pi/2$ ), spherical segment ( $\vartheta_c > \pi/2$ ), homonuclear dumbbell, peanut [2, 4]. . . . .	14
4	The five Platonic solids tetrahedron {3,3}, cube {4,3}, octahedron {3,4}, dodecahedron {5,3}, and icosahedron {3,5}. . . . .	16
5	Excluded area for parallel-oriented (green) and anti-parallel-oriented (orange) hexagons as the area inside the solid lines with the orientation-averaged excluded area $V_{\text{ex}}$ as the area inside the dashed line. . . . .	18
6	Left: Continuous completion of a hyperlens by a hypertorus at the vicinity of the equator [4]. Right: Continuous completion of a hyperspindle by a hypersphere segment at the vicinity of the upper apex [4]. . . . .	23
7	Left: Reduced second virial coefficients $B_2^*$ for anisotropic solids with aspect ratios $\nu$ in $\mathbb{R}^2$ [3]. Right: Reduced second virial coefficients $B_2^*$ of prolate, uniaxial solids of revolution with inversion symmetry and aspect ratios $\nu$ in $\mathbb{R}^4$ [4].	25
8	Left: Reduced second virial coefficients $B_2^*$ of prolate, uniaxial solids of revolution with aspect ratios $\nu \geq 1$ in $\mathbb{R}^4$ , normalized to corresponding values of uniaxial hyperellipsoids $B_2^{*(\text{hell})}$ [4]. Right: Reduced second virial coefficients $B_2^*$ of uniaxial solids of revolution defined for prolate and oblate aspect ratios $\nu$ in $\mathbb{R}^4$ [4]. . . . .	26
9	Left: Reduced second virial coefficients $B_2^*$ of $D$ -dimensional doublecones and cylinders with aspect ratio $\nu = 1$ in $\mathbb{R}^D$ [4]. The dashed lines serve as a guide to the eye. Right: Reduced second virial coefficients $B_2^*$ of $D$ -dimensional homonuclear dumbbells, peanut-shaped particles and spherocylinders with aspect ratio $\nu$ in $\mathbb{R}^D$ [2]. . . . .	27
10	Reduced second virial coefficients $B_2^*$ of hyperspheres and the three regular, convex polytopes in arbitrary-dimensional Euclidean spaces $\mathbb{R}^D$ for $D \leq 11$ . The solid lines serve as guide to the eye. . . . .	29
11	Left: Reduced second virial coefficients $B_2^*$ of planar dumbbells in dependence on the aspect ratio $\nu$ with deviations $\Delta B_2^*$ to the analytical result $B_{2,\text{an}}^*$ [2]. Right: Reduced virial coefficients $\tilde{B}_n = B_n/B_2^{n-1}$ of planar dumbbells in dependence on the inverse of the shape parameter $\alpha^{-1}$ [2]. . . . .	32
12	Reduced virial coefficients $\tilde{B}_n$ of hard stadia (left) and ellipses (right) in dependence on the inverse of the shape parameter $\alpha^{-1}$ [3]. . . . .	33

13	Reduced virial coefficients $\tilde{B}_n$ of hard, homonuclear dumbbells (left) and hard spherocylinders (right) in dependence on the inverse of the shape parameter $\alpha^{-1}$ [2, 104]. . . . .	34
14	Reduced virial coefficients $\tilde{B}_n$ of prolate ellipsoids of revolution (left) and oblate ellipsoids of revolution (right) in dependence on the inverse of the shape parameter $\alpha^{-1}$ . . . . .	35
15	Reduced virial coefficients $\tilde{B}_n$ of homonuclear hyperdumbbells (left) and hyperspherocylinders (right) in dependence on the inverse of the shape parameter $\alpha^{-1}$ [1, 2]. . . . .	35
16	Reduced virial coefficients $\tilde{B}_n$ of prolate, uniaxial hyperellipsoids (left) and oblate, uniaxial hyperellipsoids (right) in dependence on the inverse of the shape parameter $\alpha^{-1}$ . . . . .	36
17	Isotropic equation-of-state data of ellipses in $\mathbb{R}^2$ [3] (left) and spheroids in $\mathbb{R}^3$ (right). The colored lines are from the VEOS [Eq. (76)], considering the sum of virial coefficients up to $B_n^*$ displayed in the legend (left) and up to $B_8^*$ (right). The black line results from Eq. (77). Numerical results are taken from [35, 47, 112] and [15, 16, 57] with open circles approximating the point of the isotropic-nematic phase transition. . . . .	38

## List of Tables

1	Cardinality of the sets of labeled and unlabeled Mayer graphs ( $\mathcal{M}_i^L, \mathcal{M}_i^U$ ) and respectively Ree-Hoover graphs ( $\mathcal{R}_i^L, \mathcal{R}_i^U$ ) with $i$ nodes [11, 92, 93]. . . . .	9
2	Schläfli symbol $\{p_1, \dots, p_{D-1}\}$ , number of $k$ -faces $N_k$ , and dihedral angle $\delta_P$ for the three regular, convex $D$ -polytopes in arbitrary-dimensional Euclidean spaces $\mathbb{R}^D$ [143]. . . . .	17
3	Critical angles $\vartheta_c$ of $D$ -dimensional, uniaxial solids of revolution with singularities in their surface curvatures contributing to $W_i$ . . . . .	22
4	Overview of publications resulting as part of this work with own contributions approximated in percent. . . . .	41
A-1	Meridian curves $r(z)$ of $D$ -dimensional, uniaxial solids of revolution defined in range $z_{\min} \leq z \leq z_{\max}$ with (equatorial) radii $r_{\text{eq}}, r_0, r_1$ , height $h$ , and aspect ratio $\nu$ [2, 4]. . . . .	115
A-2	Quermassintegrals $W_i$ of selected $D$ -dimensional, convex solids in $\mathbb{R}^D$ with $W_D = \kappa_D$ [4, 118]. . . . .	116
A-3	Quermassintegrals $W_i$ of selected convex solids in $\mathbb{R}^4$ with $W_4 = \pi^2/2$ [4]. . . . .	117
A-4	Virial coefficients of $D$ -dimensional spheres and $(D - 1)$ -dimensional spherical plates with radius $r_0$ in $\mathbb{R}^D$ [69, 113, 118]. . . . .	118
A-5	Reduced, analytical second virial coefficients $B_2^*$ of planar dumbbells in $\mathbb{R}^2$ and dumbbells in $\mathbb{R}^3$ and reduced, semi-analytical second virial coefficients $B_2^*$ of hyperdumbbells in $\mathbb{R}^4$ with aspect ratio $\nu$ [2]. . . . .	118
A-6	Reduced second virial coefficients $B_2^*$ of convex solids with aspect ratio $\nu$ in $\mathbb{R}^2$ [3].	119
A-7	Reduced second virial coefficients $B_2^*$ of convex solids of revolution with aspect ratio $\nu$ in $\mathbb{R}^3$ [58, 73]. . . . .	119
A-8	Reduced second virial coefficients $B_2^*$ of convex, uniaxial solids of revolution with aspect ratio $\nu$ in $\mathbb{R}^4$ [4]. . . . .	120
A-9	Reduced second virial coefficients $B_2^*$ of regular, convex polytopes in $\mathbb{R}^2, \mathbb{R}^3$ , and $\mathbb{R}^4$ , including the quasiregular polytopes in $\mathbb{R}^3$ with their dual geometries and limiting the number of side for polygons up to eleven [117, 118, 142]. . . . .	120
A-10	Reduced virial coefficients $B_n^*$ of $D$ -dimensional spheres in $\mathbb{R}^D$ . Values from [10, 92].	121
A-11	Reduced virial coefficients $B_n^*$ of planar dumbbells with aspect ratio $\nu$ . First row: This work [2], second row: Values from [111, 114]. . . . .	121
A-12	Reduced virial coefficients $B_n^*$ of stadia with aspect ratio $\nu$ . First row: This work [3], second row: Values from [115]. . . . .	122
A-13	Reduced virial coefficients $B_n^*$ of ellipses with aspect ratio $\nu$ . First row: This work [3], second row: Values from [115]. . . . .	122
A-14	Reduced virial coefficients $B_n^*$ of planar spindles (lenses) with aspect ratio $\nu$ [3].	123
A-15	Reduced virial coefficients $B_n^*$ of rectangles with aspect ratio $\nu$ . First row: This work [3], second row: Values from [113]. . . . .	123

A-16	Reduced virial coefficients $B_n^*$ of rhombi with aspect ratio $\nu$ . First row: This work [3], second row: Values from [113]. . . . .	124
A-17	Reduced virial coefficients $\tilde{B}_n$ of infinitesimal thin needles. First row: This work [3], second row: Values from [113], third row: Values from [115]. . . . .	124
A-18	Reduced virial coefficients $B_n^*$ of dumbbells with aspect ratio $\nu$ . First row: This work [2], second row: Values from [104]. . . . .	125
A-19	Reduced virial coefficients $B_n^*$ of prolate spherocylinders with aspect ratio $\nu$ . First row: This work, second row: Values from [104]. . . . .	126
A-20	Reduced virial coefficients $B_n^*$ of prolate ellipsoids of revolution with aspect ratio $\nu$ . First row: This work, second row: Values from [100,103]. . . . .	126
A-21	Reduced virial coefficients $B_n^*$ of oblate ellipsoids of revolution with aspect ratio $\nu$ . First row: This work, second row: Values from [58]. . . . .	127
A-22	Reduced virial coefficients $B_n^*$ of lenses with aspect ratio $\nu$ . Values from [58]. . . . .	127
A-23	Reduced virial coefficients $B_n^*$ of cylinders with aspect ratio $\nu$ . Values from [57]. . . . .	128
A-24	Reduced virial coefficients $B_n^*$ of regular polyhedra. Values from [105,106]. . . . .	128
A-25	Reduced virial coefficients $\tilde{B}_n$ of spherical plates. First row: This work, second row: Values from [103]. . . . .	128
A-26	Reduced virial coefficients $B_n^*$ of hyperdumbbells with aspect ratio $\nu$ [2]. . . . .	129
A-27	Reduced virial coefficients $B_n^*$ of hyperspherocylinders with aspect ratio $\nu$ [1]. . . . .	129
A-28	Reduced virial coefficients $B_n^*$ of prolate, uniaxial hyperellipsoids of revolution with aspect ratio $\nu$ . . . . .	130
A-29	Reduced virial coefficients $B_n^*$ of oblate, uniaxial hyperellipsoids of revolution with aspect ratio $\nu$ . . . . .	130

## References

- [1] M. Kulossa, P. Marienhagen and J. Wagner, *Phys. Rev. E* **105**, 064121 (2022).
- [2] M. Kulossa, D. Weidig and J. Wagner, *Phys. Rev. E* **107**, 024129 (2023).
- [3] M. Kulossa and J. Wagner, *Mol. Phys.* **122**, e2289699 (2023).
- [4] M. Kulossa and J. Wagner, *Phys. Rev. E* **111**, 024112 (2025).
- [5] C.P. Royall, P. Charbonneau, M. Dijkstra, J. Russo, F. Smallenburg, T. Speck and C. Valeriani, *Rev. Mod. Phys.* **96**, 045003 (2024).
- [6] P.N. Pusey, E. Zaccarelli, C. Valeriani, E. Sanz, W.C.K. Poon and M.E. Cates, *Philos. Trans.: Math., Phys. Eng. Sci.* **367**, 4993–5011 (2009).
- [7] R. Roth, *J. Phys.: Condens. Matter* **22**, 063102 (2010).
- [8] A.J. Schultz and D.A. Kofke, *J. Chem. Phys.* **157**, 190901 (2022).
- [9] R.J. Wheatley, *Phys. Rev. Lett.* **110**, 200601 (2013).
- [10] C. Zhang and B.M. Pettitt, *Mol. Phys.* **112**, 1427–1447 (2014).
- [11] A.J. Schultz and D.A. Kofke, *Phys. Rev. E* **90**, 023301 (2014).
- [12] N.F. Carnahan and K.E. Starling, *J. Chem. Phys.* **51**, 635–636 (1969).
- [13] L. Onsager, *Ann. N. Y. Acad. Sci.* **51**, 627–659 (1949).
- [14] M. Dijkstra, *Adv. Chem. Phys.* **156**, 35–71 (2014).
- [15] G. Odriozola, *J. Chem. Phys.* **136**, 134505 (2012).
- [16] G. Bautista-Carbajal, A. Moncho-Jordá and G. Odriozola, *J. Chem. Phys.* **138**, 064501 (2013).
- [17] S.C. McGrother, D.C. Williamson and G. Jackson, *J. Chem. Phys.* **104**, 6755–6771 (1996).
- [18] P. Bolhuis and D. Frenkel, *J. Chem. Phys.* **106**, 666–687 (1997).
- [19] J.T. Lopes, F. Romano, E. Grelet, L.F.M. Franco and A. Giacometti, *J. Chem. Phys.* **154**, 104902 (2021).
- [20] G. Cinacchi and S. Torquato, *J. Chem. Phys.* **143**, 224506 (2015).
- [21] G. Cinacchi and S. Torquato, *Soft Matter* **14**, 8205–8218 (2018).
- [22] G. Cinacchi and S. Torquato, *Phys. Rev. E* **100**, 062902 (2019).
- [23] U. Agarwal and F.A. Escobedo, *Nat. Mater.* **10**, 230–235 (2011).

- [24] P.F. Damasceno, M. Engel and S.C. Glotzer, *Science* **337**, 453–457 (2012).
- [25] P. Gandhi and A. Kuhnhold, *Soft Matter* **20**, 5351–5358 (2024).
- [26] C. Vega, E.P.A. Paras and P.A. Monson, *J. Chem. Phys.* **96**, 9060–9072 (1992).
- [27] C. Vega, E.P.A. Paras and P.A. Monson, *J. Chem. Phys.* **97**, 8543–8548 (1992).
- [28] K. Milinković, M. Dennison and M. Dijkstra, *Phys. Rev. E* **87**, 032128 (2013).
- [29] M. Marechal, R.J. Kortschot, A.F. Demirörs, A. Imhof and M. Dijkstra, *Nano Lett.* **10**, 1907–1911 (2010).
- [30] M. Marechal and M. Dijkstra, *Phys. Rev. E* **82**, 031405 (2010).
- [31] G. Cinacchi and J.S. van Duijneveldt, *J. Phys. Chem. Lett.* **1**, 787–791 (2010).
- [32] G. Cinacchi, *J. Chem. Phys.* **139**, 124908 (2013).
- [33] G. Cinacchi and A. Tani, *J. Chem. Phys.* **141**, 154901 (2014).
- [34] J.P. Ramírez González and G. Cinacchi, *J. Chem. Phys.* **159**, 044903 (2023).
- [35] G. Bautista-Carbajal and G. Odriozola, *J. Chem. Phys.* **140**, 204502 (2014).
- [36] M.A. Bates and D. Frenkel, *J. Chem. Phys.* **112**, 10034–10041 (2000).
- [37] Y. Martínez-Ratón, E. Velasco and L. Mederos, *J. Chem. Phys.* **122**, 064903 (2005).
- [38] A. Donev, J. Burton, F.H. Stillinger and S. Torquato, *Phys. Rev. B* **73**, 054109 (2006).
- [39] D. Dertli and T. Speck, *Phys. Rev. Res.* **7**, L012034 (2025).
- [40] J.P. Ramírez González and G. Cinacchi, *Phys. Rev. E* **102**, 042903 (2020).
- [41] J.P. Ramírez González and G. Cinacchi, *Phys. Rev. E* **104**, 054604 (2021).
- [42] J. Colt, L. Nelson, S. Cargile, T. Brzinski and S.V. Franklin, *Phys. Rev. E* **109**, 024901 (2024).
- [43] J.P. Ramírez González and G. Cinacchi, *Phys. Rev. E* **110**, 044701 (2024).
- [44] J. Roller, J.D. Geiger, M. Voggenreiter, J.M. Meijer and A. Zumbusch, *Soft Matter* **16**, 1021–1028 (2020).
- [45] M. Voggenreiter, J. Roller, J. Geiger, L. Ebner, A. Zumbusch and J.M. Meijer, *Langmuir* **36**, 13087–13095 (2020).
- [46] M. Dennison and A.J. Masters, *Phys. Rev. E* **84**, 021709 (2011).
- [47] W.S. Xu, Y.W. Li, Z.Y. Sun and L.J. An, *J. Chem. Phys.* **139**, 024501 (2013).

- [48] P. Marienhagen and J. Wagner, Phys. Rev. E **105**, 014125 (2022).
- [49] P. Marienhagen and J. Wagner, Phys. Rev. E **106**, 014101 (2022).
- [50] H. Hansen-Goos and K. Mecke, Phys. Rev. Lett. **102**, 018302 (2009).
- [51] H. Hansen-Goos and K. Mecke, J. Phys.: Condens. Matter **22**, 364107 (2010).
- [52] G. Cinacchi and F. Schmid, J. Phys.: Condens. Matter **14**, 12223 (2002).
- [53] P.W.A. Schönhöfer, G.E. Schröder-Turk and M. Marechal, J. Chem. Phys. **148**, 124104 (2018).
- [54] A. Poniewierski and R. Hołyst, Phys. Rev. Lett. **61**, 2461–2464 (1988).
- [55] R. Hołyst and A. Poniewierski, Phys. Rev. A **39**, 2742–2744 (1989).
- [56] J.D. Parsons, Phys. Rev. A **19**, 1225–1230 (1979).
- [57] C. Vega, Mol. Phys. **92**, 651–666 (1997).
- [58] P. Marienhagen, R. Hellmann and J. Wagner, Phys. Rev. E **104**, 015308 (2021).
- [59] S. Torquato and F.H. Stillinger, Rev. Mod. Phys. **82**, 2633–2672 (2010).
- [60] J. de Graaf, R. van Roij and M. Dijkstra, Phys. Rev. Lett. **107**, 155501 (2011).
- [61] S. Torquato and Y. Jiao, Phys. Rev. E **86**, 011102 (2012).
- [62] S. Torquato, J. Chem. Phys. **149**, 020901 (2018).
- [63] J. Zhao, S. Zhao and S. Luding, Nat. Rev. Phys. **5**, 505–525 (2023).
- [64] G. Jäger, Sitzungsber. Akad. Wiss. Wien, Math.-Naturwiss. Kl., Abt. 2A **105**, 15–21 (1896).
- [65] L. Boltzmann, Sitzungsber. Akad. Wiss. Wien, Math.-Naturwiss. Kl., Abt. 2A **105**, 695–706 (1896).
- [66] L. Boltzmann, Proc. K. Ned. Akad. Wet. **1**, 398–404 (1899).
- [67] J.D. van der Waals, Proc. K. Ned. Akad. Wet. **1**, 138–143 (1899).
- [68] I. Urrutia, J. Stat. Phys. **187**, 29 (2022).
- [69] I. Lyberg, J. Stat. Phys. **119**, 747–764 (2005).
- [70] A. Isihara, J. Chem. Phys. **18**, 1446–1449 (1950).
- [71] A. Isihara and T. Hayashida, J. Phys. Soc. Jpn. **6**, 40–45 (1951).
- [72] H. Hadwiger, Experientia **7**, 395–398 (1951).

- [73] E. Herold, R. Hellmann and J. Wagner, *J. Chem. Phys.* **147**, 204102 (2017).
- [74] J.S. Rowlinson, J. Talbot and D.J. Tildesley, *Mol. Phys.* **54**, 1065–1071 (1985).
- [75] T. Boublík, *Mol. Phys.* **57**, 287–293 (1986).
- [76] A. Isihara, *J. Chem. Phys.* **19**, 397–403 (1951).
- [77] K. Kornick, T. Brzinski and S.V. Franklin, *Phys. Rev. E* **104**, 034904 (2021).
- [78] N. Metropolis, A.W. Rosenbluth, M.N. Rosenbluth, A.H. Teller and E. Teller, *J. Chem. Phys.* **21**, 1087–1092 (1953).
- [79] M.N. Rosenbluth and A.W. Rosenbluth, *J. Chem. Phys.* **22**, 881–884 (1954).
- [80] F.H. Ree and W.G. Hoover, *J. Chem. Phys.* **40**, 939–950 (1964).
- [81] F.H. Ree and W.G. Hoover, *J. Chem. Phys.* **46**, 4181–4197 (1967).
- [82] K.W. Kratky, *Phys. A (Amsterdam, Neth.)* **87**, 584–600 (1977).
- [83] E.J. Janse van Rensburg, *J. Phys. A: Math. Gen.* **26**, 4805 (1993).
- [84] A.Y. Vlasov, X.M. You and A.J. Masters, *Mol. Phys.* **100**, 3313–3324 (2002).
- [85] F.H. Ree and W.G. Hoover, *J. Chem. Phys.* **40**, 2048–2049 (1964).
- [86] B.C. Freasier and D.J. Isbister, *Mol. Phys.* **42**, 927–936 (1981).
- [87] M. Bishop, A. Masters and J.H.R. Clarke, *J. Chem. Phys.* **110**, 11449–11453 (1999).
- [88] M. Bishop, A. Masters and A.Y. Vlasov, *J. Chem. Phys.* **121**, 6884–6886 (2004).
- [89] M. Bishop, A. Masters and A.Y. Vlasov, *J. Chem. Phys.* **122**, 154502 (2005).
- [90] L. Babai, P. Erdős and S.M. Selkow, *SIAM J. Comput.* **9**, 628–635 (1980).
- [91] B.D. McKay, *Congr. Numer.* **30**, 45–87 (1981).
- [92] S. Labík, J. Kolafa and A. Malijevský, *Phys. Rev. E* **71**, 021105 (2005).
- [93] N. Clisby and B.M. McCoy, *J. Stat. Phys.* **122**, 15–57 (2006).
- [94] Y. Chen and W.A. Steele, *J. Chem. Phys.* **52**, 5284–5286 (1970).
- [95] M. Rigby, *J. Chem. Phys.* **53**, 1021–1023 (1970).
- [96] B. Freasier and R. Bearman, *Mol. Phys.* **32**, 551–554 (1976).
- [97] I. Nezbeda, W.R. Smith and T. Boublík, *Mol. Phys.* **37**, 985–989 (1979).
- [98] R. Eppenga and D. Frenkel, *Mol. Phys.* **52**, 1303–1334 (1984).

- [99] I. Nezbeda, Czech. J. Phys. **35**, 752–767 (1985).
- [100] M. Rigby, Mol. Phys. **66**, 1261–1268 (1989).
- [101] J.A.C. Veerman and D. Frenkel, Phys. Rev. A **45**, 5632–5648 (1992).
- [102] C. Vega, S. Lago and B. Garzón, Mol. Phys. **82**, 1233–1247 (1994).
- [103] X.M. You, A.Y. Vlasov and A.J. Masters, J. Chem. Phys. **123**, 034510 (2005).
- [104] M. Francová, J. Kolafa, P. Morávek, S. Labík and A. Malijevský, Collect. Czech. Chem. Commun. **73**, 413–423 (2008).
- [105] J. Kolafa and S. Labík, Mol. Phys. **113**, 1119–1123 (2015).
- [106] M.E. Irrgang, M. Engel, A.J. Schultz, D.A. Kofke and S.C. Glotzer, Langmuir **33**, 11788–11796 (2017).
- [107] J.K. Singh and D.A. Kofke, Phys. Rev. Lett. **92**, 220601 (2004).
- [108] K.M. Benjamin, A.J. Schultz and D.A. Kofke, Ind. Eng. Chem. Res. **45**, 5566–5573 (2006).
- [109] A.J. Schultz and D.A. Kofke, J. Chem. Phys. **161**, 154108 (2024).
- [110] D. Frenkel and R. Eppenga, Phys. Rev. A **31**, 1776–1787 (1985).
- [111] J. Talbot and D.J. Tildesley, J. Chem. Phys. **83**, 6419–6424 (1985).
- [112] J.A. Cuesta and D. Frenkel, Phys. Rev. A **42**, 2126–2136 (1990).
- [113] G. Tarjus, P. Viot, S.M. Ricci and J. Talbot, Mol. Phys. **73**, 773–787 (1991).
- [114] C.W. Goulding and M. Rigby, Mol. Phys. **75**, 623–631 (1992).
- [115] M. Rigby, Mol. Phys. **78**, 21–27 (1993).
- [116] T. Boublík, Mol. Phys. **29**, 421–428 (1975).
- [117] S. Torquato and Y. Jiao, Phys. Rev. E **87**, 022111 (2013).
- [118] S. Torquato and Y. Jiao, J. Stat. Mech.: Theory Exp. **2022**, 093404 (2022).
- [119] H. Kamerlingh Onnes, Proc. K. Ned. Akad. Wet. **4**, 125–147 (1902).
- [120] T. Kihara, Rev. Mod. Phys. **25**, 831–843 (1953).
- [121] T. Kihara, Rev. Mod. Phys. **27**, 412–423 (1955).
- [122] J.E. Mayer, J. Chem. Phys. **5**, 67–73 (1937).
- [123] J.E. Mayer and M. Goeppert Mayer, *Statistical Mechanics* (Wiley, New York, 1940).

- [124] M. Born, *Physica* **4**, 1034–1044 (1937).
- [125] W.G. Hoover and A.G. De Rocco, *J. Chem. Phys.* **36**, 3141–3162 (1962).
- [126] M. Born, K. Fuchs and E.T. Whittaker, *Proc. R. Soc. London, Ser. A* **166**, 391–414 (1938).
- [127] C.H.J. Johnson and T.H. Spurling, *Aust. J. Chem.* **27**, 241–247 (1974).
- [128] K.M. Benjamin, A.J. Schultz and D.A. Kofke, *J. Phys. Chem. B* **113**, 7810–7815 (2009).
- [129] K.M. Benjamin, A.J. Schultz and D.A. Kofke, *J. Phys. Chem. B* **114**, 4388–4388 (2010).
- [130] B. Jäger, R. Hellmann, E. Bich and E. Vogel, *J. Chem. Phys.* **135**, 084308 (2011).
- [131] A. Cayley, *Q. J. Math.* **23**, 376–378 (1889).
- [132] B.D. McKay and A. Piperno, *J. Symb. Comput.* **60**, 94–112 (2014).
- [133] L. Babai, *Proc. Int. Congr. Math.* **4**, 3337–3354 (2018).
- [134] F.H. Ree and W.G. Hoover, *J. Chem. Phys.* **41**, 1635–1645 (1964).
- [135] M. Luban and A. Baram, *J. Chem. Phys.* **76**, 3233–3241 (1982).
- [136] N. Clisby and B.M. McCoy, *J. Stat. Phys.* **114**, 1343–1361 (2004).
- [137] M.S. Wertheim, *J. Chem. Phys.* **78**, 4625–4631 (1983).
- [138] N. Clisby and B.M. McCoy, *Pramana* **64**, 775–783 (2005).
- [139] A. Perez-Gracia and F. Thomas, *Adv. Appl. Clifford Algebras* **27**, 523–538 (2017).
- [140] A. Aguilera and R. Pérez-Aguila, *General n-dimensional rotations* (UNION Agency, Pilsen, 2004).
- [141] M. Henk, J. Richter-Gebert and G.M. Ziegler, in *Handbook of Discrete and Computational Geometry*, edited by C.D. Toth, J. O’Rourke and J.E. Goodman, 3rd ed. (Chapman and Hall/CRC, New York, 2017), pp. 383–413.
- [142] R. Schneider, *Convex Bodies: The Brunn–Minkowski Theory* (Cambridge University Press, Cambridge, 2013).
- [143] H.S.M. Coxeter, *Regular polytopes* (Dover Publications, New York, 1973).
- [144] L.A. Santaló, *Integral Geometry and Geometric Probability* (Cambridge University Press, Cambridge, 2004).
- [145] H. Groemer, *Math. Ann.* **198**, 23–56 (1972).
- [146] J.F. Robinson, R. Roth and C.P. Royall, *Philos. Mag.* **100**, 2614–2635 (2020).

- [147] C. Tsonopoulos, *AIChE J.* **20**, 263–272 (1974).
- [148] S. Li, *Asian J. Math. Stat.* **4**, 66–70 (2011).
- [149] U. Betke and M. Henk, *Monatsh. Math.* **115**, 27–33 (1993).
- [150] H. Hadwiger, *Math. Ann.* **239**, 271–288 (1979).
- [151] I. Nezbeda and T. Boublík, *Mol. Phys.* **51**, 1443–1447 (1984).
- [152] C. Vega and S. Lago, *Comput. Chem. (Oxford, U. K.)* **18**, 55–59 (1994).
- [153] J.W. Perram and M.S. Wertheim, *J. Comput. Phys.* **58**, 409–416 (1985).
- [154] I. Gilitschenski and U.D. Hanebeck, in *2014 Sensor Data Fusion: Trends, Solutions, Applications (SDF)* (IEEE, Bonn, Germany, 2014), pp. 1–6.
- [155] B. Mertzios, *IEEE Trans. Autom. Control* **29**, 652–653 (1984).
- [156] A. Ostaszewski, *Advanced Mathematical Methods* (Cambridge University Press, Cambridge, 1991).
- [157] J. de Graaf, L. Filion, M. Marechal, R. van Roij and M. Dijkstra, *J. Chem. Phys.* **137**, 214101 (2012).
- [158] M. He and P. Siders, *J. Phys. Chem.* **94**, 7280–7288 (1990).
- [159] D. Vranek, *J. Graph. Tools* **7**, 23–31 (2002).
- [160] N. Ibarra-Avalos, A. Gil-Villegas and A. Martinez Richa, *Mol. Simul.* **33**, 505–515 (2007).
- [161] C. Wellmann, C. Lillie and P. Wriggers, *Eng. Comput.* **25**, 432–442 (2008).
- [162] S. Zhao, N. Zhang, X. Zhou and L. Zhang, *Powder Technol.* **310**, 175–186 (2017).
- [163] R.D. Batten, F.H. Stillinger and S. Torquato, *Phys. Rev. E* **81**, 061105 (2010).
- [164] T. Boublík, *Mol. Phys.* **27**, 1415–1427 (1974).
- [165] H.L. Frisch and J.K. Percus, *Phys. Rev. E* **60**, 2942–2948 (1999).
- [166] T. Boublík, *Mol. Phys.* **109**, 1575–1580 (2011).
- [167] J. Amorós and S. Ravi, *Phys. Lett. A* **377**, 2089–2092 (2013).
- [168] Y. Song and E.A. Mason, *Phys. Rev. A* **41**, 3121–3124 (1990).
- [169] D. Frenkel and B.M. Mulder, *Mol. Phys.* **55**, 1171–1192 (1985).
- [170] M.P. Allen, G.T. Evans, D. Frenkel and B.M. Mulder, *Adv. Chem. Phys.* **86**, 1–166 (1993).

- [171] A. Samborski, G.T. Evans, C.P. Mason and M.P. Allen, *Mol. Phys.* **81**, 263–276 (1994).
- [172] M. Skoge, A. Donev, F.H. Stillinger and S. Torquato, *Phys. Rev. E* **74**, 041127 (2006).
- [173] J.M. McBride and C. Avendaño, *Soft Matter* **13**, 2085–2098 (2017).
- [174] C. Avendaño and F.A. Escobedo, *Curr. Opin. Colloid Interface Sci.* **30**, 62–69 (2017).
- [175] S. Dussi and M. Dijkstra, *Nat. Commun.* **7**, 11175 (2016).
- [176] M. Chiappini, T. Drwenski, R. van Roij and M. Dijkstra, *Phys. Rev. Lett.* **123**, 068001 (2019).

## A Geometric measures for selected particle geometries

Tab. A-1: Meridian curves  $r(z)$  of  $D$ -dimensional, uniaxial solids of revolution defined in range  $z_{\min} \leq z \leq z_{\max}$  with (equatorial) radii  $r_{\text{eq}}, r_0, r_1$ , height  $h$ , and aspect ratio  $\nu$  [2, 4].

Geometry	$r(z)$	$z_{\min}$	$z_{\max}$
Sphere	$(r_0^2 - z^2)^{1/2}$	$-r_0$	$r_0$
Homonuclear	$\left\{ r_0^2 - [z - (\nu - 1)r_0]^2 \right\}^{1/2}$	0	$\nu r_0$
dumbbell	$\left\{ r_0^2 - [z + (\nu - 1)r_0]^2 \right\}^{1/2}$	$-\nu r_0$	0
Peanut	$\left\{ r_0^2 - [z - (\nu - 1)r_0]^2 \right\}^{1/2}$	$(\nu - 1)r_0/2$	$\nu r_0$
	$[3 - \nu(\nu - 2)]^{1/2} r_0 - (r_0^2 - z^2)^{1/2}$ $\left\{ r_0^2 - [z + (\nu - 1)r_0]^2 \right\}^{1/2}$	$-(\nu - 1)r_0/2$	$(\nu - 1)r_0/2$
Ellipsoid	$\left[ r_{\text{eq}}^2 - \left( \frac{z}{\nu} \right)^2 \right]^{1/2}$	$-\nu r_{\text{eq}}$	$\nu r_{\text{eq}}$
Spherocylinder	$\left\{ r_{\text{eq}}^2 - [z - (\nu - 1)r_{\text{eq}}]^2 \right\}^{1/2}$	$(\nu - 1)r_{\text{eq}}$	$\nu r_{\text{eq}}$
	$r_{\text{eq}}$ $\left\{ r_{\text{eq}}^2 - [z + (\nu - 1)r_{\text{eq}}]^2 \right\}^{1/2}$	$-(\nu - 1)r_{\text{eq}}$	$(\nu - 1)r_{\text{eq}}$
Cylinder	$r_{\text{eq}}$	$-\nu r_{\text{eq}}$	$\nu r_{\text{eq}}$
Spindle	$\left( \frac{1 - \nu^2}{2} \right) r_{\text{eq}} + \frac{1}{2} \left[ (\nu^2 + 1)^2 r_{\text{eq}}^2 - 4z^2 \right]^{1/2}$	$-\nu r_{\text{eq}}$	$\nu r_{\text{eq}}$
Lens	$\left[ \frac{ z r_{\text{eq}}(\nu^2 - 1) + \nu(r_{\text{eq}}^2 - z^2)}{\nu} \right]^{1/2}$	$-\nu r_{\text{eq}}$	$\nu r_{\text{eq}}$
Spherical segment	$(r_0^2 - z^2)^{1/2}$	$r_0 - h$	$r_0$
Doublecone	$r_{\text{eq}} - \frac{ z }{\nu}$	$-\nu r_{\text{eq}}$	$\nu r_{\text{eq}}$
Cone	$r_0 - \frac{z}{\nu}$	0	$\nu r_0$
Truncated cone	$r_0 - \frac{r_0 - r_1}{h} z$	0	$h$

Tab. A-2: Quermassintegrals  $W_i$  of selected  $D$ -dimensional, convex solids in  $\mathbb{R}^D$  with  $W_D = \kappa_D$  [4, 118].

Geometry	$W_i$
Sphere	$\kappa_D r_0^{D-i}$
Ellipsoid	$\kappa_D \nu^{i+1} r_{\text{eq}}^{D-i} {}_2F_1\left(\frac{D+1}{2}, \frac{i}{2}, \frac{D}{2}; 1 - \nu^2\right) = \kappa_D \nu r_{\text{eq}}^{D-i} {}_2F_1\left(-\frac{1}{2}, \frac{i}{2}, \frac{D}{2}; 1 - \frac{1}{\nu^2}\right)$
Spherocylinder	$[\kappa_D + 2(\nu - 1)\frac{D-i}{D}\kappa_{D-1}] r_{\text{eq}}^{D-i}$
Cylinder	$\begin{cases} 2\kappa_{D-1}\nu r_{\text{eq}}^D & : i = 0 \\ \frac{2}{D}\kappa_{D-1}\left[(D-i)\nu + \frac{\beta_i}{2\kappa_{i-1}}\right] r_{\text{eq}}^{D-i} & : i \geq 1 \end{cases}$
Doublecone	$\begin{cases} \frac{2}{D}\kappa_{D-1}\nu r_{\text{eq}}^D & : i = 0 \\ \frac{\kappa_{D-1}}{D} r_{\text{eq}}^{D-i} \left[ 2\nu^{i-1}(1+\nu^2)^{\frac{2-i}{2}} + (i-1) \int_{\vartheta_c}^{\pi-\vartheta_c} \sin^{i-2} \vartheta d\vartheta \right] & : 0 < i < D \end{cases}$
Cone	$\begin{cases} \frac{\kappa_{D-1}}{D} \nu r_0^D & : i = 0 \\ \frac{\kappa_{D-1}}{D} r_0^{D-i} \left[ \nu^{i-1}(1+\nu^2)^{\frac{2-i}{2}} + \frac{\beta_i}{2\kappa_{i-1}} + (i-1) \int_{\vartheta_c}^{\frac{\pi}{2}} \sin^{i-2} \vartheta d\vartheta \right] & : 0 < i < D \end{cases}$
Spherical plate	$\begin{cases} 0 & : i = 0 \\ \frac{\kappa_{D-1}}{\kappa_{i-1}} \frac{i}{D} \kappa_i r_0^{D-i} & : i \geq 1 \end{cases}$
Quadratic plate	$\frac{i}{D} \kappa_i a^{D-i}$
Cube	$\kappa_i a^{D-i}$
Quadratic pillar	$\kappa_i \left[ \nu + (1-\nu)\frac{i}{D} \right] a^{D-i}$
Simplex	$\left(\frac{a}{\sqrt{2}}\right)^{D-i} \frac{\kappa_i}{\sqrt{\pi}} \frac{D+1}{\Gamma(D-i+1)} \int_{-\infty}^{\infty} e^{-(D-i+1)x^2} \left(\frac{1}{\sqrt{x}} \int_{-\infty}^x e^{-y^2} dy\right)^i dx$
Cross-polytope	$\begin{cases} \frac{2^D}{D!} \left(\frac{a}{\sqrt{2}}\right)^D & : i = 0 \\ \left(\frac{a}{\sqrt{2}}\right)^{D-i} \frac{2^D i \kappa_i}{\Gamma(D-i+1)\sqrt{\pi}} \int_0^{\infty} e^{-(D-i+1)x^2} \left(\frac{1}{\sqrt{\pi}} \int_0^x e^{-y^2} dy\right)^{i-1} dx & : i \geq 1 \end{cases}$
Line segment	$\begin{cases} 0 & : i < D-1 \\ \frac{\kappa_{D-1}}{D} a & : i = D-1 \end{cases}$

Tab. A-3: Quermassintegrals  $W_i$  of selected convex solids in  $\mathbb{R}^4$  with  $W_4 = \pi^2/2$  [4].

Geometry	$W_i$
Hyperspindle	$W_0 = \frac{5\pi}{16} r_{\text{eq}}^4 \left[ (\nu^4 - \frac{6}{5}\nu^2 + 1) (\nu^2 + 1)^2 \arcsin\left(\frac{2\nu}{\nu^2+1}\right) - 2\nu^7 - \frac{14}{15}\nu^5 + \frac{14}{15}\nu^3 + 2\nu \right]$ $W_1 = \frac{\pi}{8} r_{\text{eq}}^3 \left[ (3\nu^6 + \nu^4 + \nu^2 + 3) \arcsin\left(\frac{2\nu}{\nu^2+1}\right) - 6\nu^5 + 6\nu \right]$ $W_2 = \frac{5\pi}{12} r_{\text{eq}}^2 \left[ (\nu^4 + \frac{2}{5}\nu^2 + 1) \arcsin\left(\frac{2\nu}{\nu^2+1}\right) - 2\nu^3 + 2\nu \right]$ $W_3 = \frac{\pi}{2} r_{\text{eq}} \left[ (\nu^2 + 1) \arcsin\left(\frac{2\nu}{\nu^2+1}\right) - \frac{2}{3}\nu \frac{\nu^2-1}{\nu^2+1} \right]$
Hyperlens	$W_0 = \frac{\pi r_{\text{eq}}^4}{32\nu^4} \left\{ (1 + \nu^2)^4 \left[ \pi - 2 \arcsin\left(\frac{1-\nu^2}{1+\nu^2}\right) \right] - 4\nu + 4\nu^7 - \frac{44}{3}\nu^3 (1 - \nu^2) \right\}$ $W_1 = \frac{\pi(1+\nu^2)r_{\text{eq}}^3}{16\nu^3} \left\{ (1 + \nu^2)^2 \left[ \pi - 2 \arcsin\left(\frac{1-\nu^2}{1+\nu^2}\right) \right] - 4\nu (1 - \nu^2) \right\}$ $W_2 = \frac{\pi^2 r_{\text{eq}}^2}{8\nu^2} \left[ (1 + \nu^2)^2 - \frac{2}{\pi} (\nu^4 - \frac{2}{3}\nu^2 + 1) \arcsin\left(\frac{1-\nu^2}{1+\nu^2}\right) - \frac{4\nu}{\pi} (1 - \nu^2) \right]$ $W_3 = \frac{\pi r_{\text{eq}}}{4\nu} \left\{ (1 + \nu^2) \left[ \pi - 2 \arcsin\left(\frac{1-\nu^2}{1+\nu^2}\right) \right] + \frac{4\nu}{3} \frac{1-\nu^2}{1+\nu^2} \right\}$
Hyperspherical segment	$W_0 = \frac{\pi^2}{4} r_0^4 \left[ 1 - \frac{2}{\pi} \arctan\left(\frac{r_0-h}{r_{\text{cap}}}\right) - \frac{2r_{\text{cap}}}{3\pi r_0^4} (r_0 - h) (3r_0^2 + 2r_{\text{cap}}^2) \right]$ $W_1 = \frac{\pi^2}{4} r_0^3 \left[ 1 - \frac{2}{\pi} \arctan\left(\frac{r_0-h}{r_{\text{cap}}}\right) - \frac{2r_{\text{cap}}}{\pi r_0^2} (r_0 - h) \right] + \frac{1}{3}\pi r_{\text{cap}}^3$ $W_2 = \frac{\pi^2}{4} r_0^2 \left[ 1 - \frac{2}{\pi} \arctan\left(\frac{r_0-h}{r_{\text{cap}}}\right) - \frac{2r_{\text{cap}}}{\pi r_0^2} (r_0 - h) \right] + \frac{\pi}{3} r_{\text{cap}}^2 \left[ \frac{\pi}{2} + \arcsin\left(1 - \frac{h}{r_0}\right) \right]$ $W_3 = \frac{\pi^2}{4} r_0 \left[ 1 - \frac{2}{\pi} \arctan\left(\frac{r_0-h}{r_{\text{cap}}}\right) - \frac{2r_{\text{cap}}}{\pi r_0^2} (r_0 - h) \right] + \frac{2\pi}{3} r_{\text{cap}} \left( 2 - \frac{h}{r_0} \right)$
Truncated hypercone	$W_0 = \frac{\pi}{3} h \frac{r_1^4 - r_0^4}{r_1 - r_0} \quad W_1 = \frac{\pi}{3} \left[ r_0^3 + r_1^3 + (r_0^2 + r_0 r_1 + r_1^2) \sqrt{h^2 + (r_0 - r_1)^2} \right]$ $W_2 = \frac{\pi}{3} (r_0 + r_1) \left\{ h + (r_0 - r_1) \arcsin \left[ \frac{r_0 - r_1}{\sqrt{h^2 + (r_0 - r_1)^2}} \right] \right\} + \frac{\pi^2}{6} (r_0^2 + r_1^2)$ $W_3 = \frac{\pi}{3} \left[ 2(r_0 + r_1) + \frac{h^2 + 2(r_0 - r_1)^2}{\sqrt{h^2 + (r_0 - r_1)^2}} \right]$
24-cell	$W_0 = 2a^4 \quad W_1 = 2\sqrt{2}a^3 \quad W_2 = \frac{2}{3}\pi\sqrt{3}a^2 \quad W_3 = 8 \left[ 3 \arccos\left(\frac{1}{3}\right) - \pi \right] a$
120-cell	$W_0 = \frac{15}{512}\sqrt{5} (1 + \sqrt{5})^8 a^4 \quad W_1 = \frac{15}{2} (15 + 7\sqrt{5}) a^3$ $W_2 = 3\pi\sqrt{25 + 10\sqrt{5}} a^2 \quad W_3 = 100 \left[ 3 \arccos\left(\frac{1}{\sqrt{5}}\right) - \pi \right] a$
600-cell	$W_0 = \frac{25}{4} (2 + \sqrt{5}) a^4 \quad W_1 = \frac{25}{2}\sqrt{2} a^3$ $W_2 = 25\sqrt{3} \left[ \arccos\left(\frac{1}{4}\right) - \frac{\pi}{3} \right] a^2 \quad W_3 = 60 \left[ 5 \arccos\left(-\frac{1}{3}\right) - 3\pi \right] a$

## B Analytical values for virial coefficients of hard bodies

Tab. A-4: Virial coefficients of  $D$ -dimensional spheres and  $(D-1)$ -dimensional spherical plates with radius  $r_0$  in  $\mathbb{R}^D$  [69, 113, 118].

	$D$	2	3	4
Sphere	$B_2^*$	2	4	8
	$B_3^*$	3.128017...	10	32.40575...
	$B_4^*$	4.257854...	18.364768...	77.74518...
Spherical plate	$B_2/r_0^D$	1.273239...	4.934802...	13.69084...
	$\tilde{B}_3$	0.514202...		

Tab. A-5: Reduced, analytical second virial coefficients  $B_2^*$  of planar dumbbells in  $\mathbb{R}^2$  and dumbbells in  $\mathbb{R}^3$  and reduced, semi-analytical second virial coefficients  $B_2^*$  of hyperdumbbells in  $\mathbb{R}^4$  with aspect ratio  $\nu$  [2].

$\nu$	$B_2^*$		
	Planar dumbbell	Dumbbell	Hyperdumbbell
1.1	2.003878...	4.014344...	8.041278116 (11)
1.2	2.014986...	4.055424...	8.159328006 (2)
1.3	2.032859...	4.121570...	8.3491846 (5)
1.4	2.057422...	4.212539...	8.609761190 (8)
1.5	2.088983...	4.329352...	8.9429226 (4)
1.6	2.128300...	4.474324...	9.35274172 (5)
1.7	2.176762...	4.651243...	9.84454201 (5)
1.8	2.236842...	4.865757...	10.4230371 (9)
1.9	2.313355...	5.126040...	11.0879331 (13)
2.0	2.420637...	5.443918...	11.8209372 (15)

Tab. A-6: Reduced second virial coefficients  $B_2^*$  of convex solids with aspect ratio  $\nu$  in  $\mathbb{R}^2$  [3].

$B_2^*$					
$\nu$	Stadium	Ellipse	Planar spindle	Rectangle	Rhombus
1	2	2	2	2.273239 ...	2.273239 ...
2	2.178285 ...	2.188827 ...	2.223832 ...	2.432394 ...	2.591549 ...
3	2.457112 ...	2.508168 ...	2.612345 ...	2.697652 ...	3.122065 ...
4	2.756799 ...	2.864039 ...	3.044973 ...	2.989436 ...	3.705634 ...
5	3.064270 ...	3.236269 ...	3.495466 ...	3.291831 ...	4.310422 ...
6	3.375488 ...	3.617522 ...	3.954929 ...	3.599530 ...	4.925821 ...
7	3.688796 ...	4.004379 ...	4.419528 ...	3.910261 ...	5.547284 ...
8	4.003389 ...	4.394994 ...	4.887340 ...	4.222887 ...	6.172535 ...
9	4.318828 ...	4.788275 ...	5.357295 ...	4.536776 ...	6.800313 ...
10	4.634854 ...	5.183522 ...	5.828751 ...	4.851549 ...	7.429859 ...

Tab. A-7: Reduced second virial coefficients  $B_2^*$  of convex solids of revolution with aspect ratio  $\nu$  in  $\mathbb{R}^3$  [58, 73].

$B_2^*$			$B_2^*$		
$\nu$	Spherocylinder	Ellipsoid	$\nu$	Ellipsoid	Lens
2	4.6	4.538486 ...	1/2	4.538486 ...	4.792694 ...
3	5.5	5.453748 ...	1/3	5.453748 ...	6.123448 ...
4	6.454545 ...	6.477898 ...	1/4	6.477898 ...	7.581452 ...
5	7.428571 ...	7.552003 ...	1/5	7.552003 ...	9.087395 ...
6	8.411764 ...	8.654088 ...	1/6	8.654088 ...	10.616259 ...
7	9.4	9.773725 ...	1/7	9.773725 ...	12.157786 ...
8	10.391304 ...	10.905217 ...	1/8	10.905217 ...	13.707019 ...
9	11.384615 ...	12.045146 ...	1/9	12.045146 ...	15.261282 ...
10	12.379310 ...	13.191323 ...	1/10	13.191323 ...	16.819006 ...

Tab. A-8: Reduced second virial coefficients  $B_2^*$  of convex, uniaxial solids of revolution with aspect ratio  $\nu$  in  $\mathbb{R}^4$  [4].

$\nu$	$B_2^*$		$\nu$	$B_2^*$	
	Hyperspherocylinder	Hyperellipsoid		Hyperellipsoid	Hyperlens
2	9.602518...	9.263435...	1/2	9.263435...	10.21107...
3	11.934231...	11.414980...	1/3	11.414980...	13.81911...
4	14.385623...	13.825608...	1/4	13.825608...	17.71034...
5	16.878455...	16.355484...	1/5	16.355484...	21.69561...
6	19.390485...	18.952106...	1/6	18.952106...	25.72150...
7	21.912971...	21.590481...	1/7	21.590481...	29.76806...
8	24.441780...	24.256959...	1/8	24.256959...	33.82638...
9	26.974704...	26.943363...	1/9	26.943363...	37.89195...
10	29.510455...	29.644467...	1/10	29.644467...	41.96228...

Tab. A-9: Reduced second virial coefficients  $B_2^*$  of regular, convex polytopes in  $\mathbb{R}^2$ ,  $\mathbb{R}^3$ , and  $\mathbb{R}^4$ , including the quasiregular polytopes in  $\mathbb{R}^3$  with their dual geometries and limiting the number of side for polygons up to eleven [117, 118, 142].

Polygon	$B_2^*$	Polyhedron	$B_2^*$	Polychoron	$B_2^*$
Triangle	2.653986...	Tetrahedron	7.703715...	5-cell	23.36594...
Tetragon	2.273239...	Cube	5.5	8-cell	13.79061...
Pentagon	2.156328...	Octahedron	5.318988...	16-cell	12.56631...
Hexagon	2.102657...	Dodecahedron	4.560508...	24-cell	10.05559...
Heptagon	2.073029...	Icosahedron	4.457632...	120-cell	8.50003...
Octagon	2.054786...	Cuboctahedron	4.662978...	600-cell	8.32916...
Nonagon	2.042697...	Rhombic dodecahedron	4.674234...		
Decagon	2.034251...	Icosidodecahedron	4.298816...		
Hendecagon	2.028106...	Rhombic triacontahedron	4.269441...		

## C Numerical results for virial coefficients of hard bodies

Tab. A-10: Reduced virial coefficients  $B_n^*$  of  $D$ -dimensional spheres in  $\mathbb{R}^D$ . Values from [10, 92].

$D$	2	3	4
$B_5^*$	5.33689664 (64)	28.22437 (2)	146.2451 (5)
$B_6^*$	6.363026 (11)	39.8152 (2)	253.388 (6)
$B_7^*$	7.352080 (28)	53.3418 (6)	375.07 (6)
$B_8^*$	8.318668 (62)	68.526 (4)	609.2 (7)
$B_9^*$	9.27236 (29)	85.83 (3)	767 (11)
$B_{10}^*$	10.2155 (32)	105.6 (2)	1420 (110)
$B_{11}^*$	11.195 (19)	126.4 (7)	
$B_{12}^*$	12.01 (11)	160 (40)	
$B_{13}^*$	12.94 (66)		
$B_{14}^*$	14.9 (42)		

### Virial coefficients of hard, anisotropic particles in two-dimensional space

Tab. A-11: Reduced virial coefficients  $B_n^*$  of planar dumbbells with aspect ratio  $\nu$ . First row: This work [2], second row: Values from [111, 114].

$\nu$	$B_3^*$	$B_4^*$	$B_5^*$	$B_6^*$	$B_7^*$	$B_8^*$
1.1	3.13810 (8)	4.27453 (22)	5.35881 (29)	6.3893 (7)	7.3813 (26)	8.347 (10)
1.2	3.16723 (8)	4.32297 (21)	5.4240 (6)	6.4673 (9)	7.4692 (30)	8.447 (9)
1.3	3.21481 (6)	4.40338 (18)	5.5334 (5)	6.5990 (10)	7.6190 (28)	8.607 (13)
	3.22 (4)					
1.4	3.28142 (8)	4.51748 (17)	5.6902 (6)	6.7906 (9)	7.8385 (26)	8.865 (12)
1.5	3.36863 (5)	4.66972 (14)	5.9024 (5)	7.0523 (12)	8.142 (4)	9.190 (18)
	3.370 (7)	4.68 (3)	5.9 (2)			
1.6	3.47997 (7)	4.86783 (21)	6.1823 (5)	7.4011 (8)	8.551 (5)	9.661 (17)
1.7	3.62098 (10)	5.12428 (20)	6.5516 (7)	7.8673 (11)	9.099 (4)	10.276 (21)
	3.62 (4)					
1.8	3.80149 (10)	5.46156 (29)	7.0474 (6)	8.5030 (17)	9.857 (5)	11.17 (4)
1.9	4.04045 (7)	5.92374 (24)	7.7458 (6)	9.4182 (16)	10.967 (6)	12.46 (5)
2.0	4.39398 (9)	6.64200 (30)	8.8815 (8)	10.9668 (29)	12.913 (6)	14.78 (7)
	4.394 (9)	6.64 (4)	8.9 (2)			

Tab. A-12: Reduced virial coefficients  $B_n^*$  of stadia with aspect ratio  $\nu$ . First row: This work [3], second row: Values from [115].

$\nu$	$B_3^*$	$B_4^*$	$B_5^*$	$B_6^*$	$B_7^*$	$B_8^*$
2	3.58548 (9)	4.96478 (20)	6.1581 (4)	7.1502 (15)	8.022 (4)	8.86 (4)
	3.5843 (15)	4.961 (11)	6.15 (5)			
3	4.35851 (11)	6.1491 (4)	7.3115 (11)	7.7567 (26)	7.911 (15)	8.35 (12)
	4.3566 (19)	6.142 (15)	7.29 (8)			
4	5.27623 (15)	7.5506 (5)	8.2301 (18)	6.829 (7)	4.689 (27)	4.4 (4)
	5.2766 (23)	7.543 (21)	8.20 (12)			
5	6.31242 (20)	9.1236 (8)	8.537 (4)	2.833 (11)	-4.75 (9)	-5.9 (13)
	6.3071 (29)	9.121 (29)	8.64 (18)			
6	7.45958 (20)	10.8501 (10)	7.824 (4)	-6.292 (24)	-24.97 (20)	-24 (4)
	7.456 (4)	10.81 (4)	7.79 (26)			
7	8.71429 (23)	12.7211 (12)	5.630 (6)	-23.21 (5)	-62.0 (5)	-46 (11)
8	10.0755 (5)	14.7273 (21)	1.411 (12)	-51.39 (6)	-124.4 (7)	-80 (14)
	10.076 (5)	14.69 (7)	1.0 (6)			
9	11.5423 (6)	16.8625 (18)	-5.428 (11)	-95.13 (10)	-222.9 (10)	-99 (26)
10	13.1142 (6)	19.1200 (21)	-15.582 (14)	-159.37 (13)	-370.8 (21)	-100 (50)
	13.119 (7)	19.12 (10)	-15.7 (10)			

Tab. A-13: Reduced virial coefficients  $B_n^*$  of ellipses with aspect ratio  $\nu$ . First row: This work [3], second row: Values from [115].

$\nu$	$B_3^*$	$B_4^*$	$B_5^*$	$B_6^*$	$B_7^*$	$B_8^*$
2	3.59622 (10)	4.94310 (24)	6.0753 (5)	7.0261 (9)	7.946 (5)	9.01 (4)
	3.5961 (15)	4.950 (11)	6.06 (5)			
3	4.46471 (10)	6.1635 (6)	6.9348 (9)	6.787 (5)	6.668 (20)	7.89 (15)
	4.4647 (19)	6.169 (16)	6.97 (8)			
4	5.54971 (17)	7.6062 (6)	6.8812 (19)	2.735 (9)	-1.22 (7)	3.1 (6)
	5.5475 (25)	7.588 (24)	6.86 (14)			
5	6.81920 (30)	9.1990 (10)	4.988 (5)	-9.108 (24)	-22.73 (20)	-2.5 (21)
	6.817 (4)	9.19 (4)	4.94 (22)			
6	8.26395 (28)	10.9071 (9)	0.181 (8)	-34.32 (5)	-68.4 (5)	3 (5)
	8.264 (4)	10.89 (5)	0.2 (4)			
7	9.8800 (4)	12.7066 (16)	-8.790 (12)	-80.67 (9)	-153.7 (10)	67 (17)
8	11.6664 (5)	14.5789 (27)	-23.359 (11)	-157.95 (15)	-298.6 (19)	270 (50)
	11.642 (6)	14.43 (9)	-23.9 (8)			
9	13.6219 (5)	16.5092 (19)	-45.157 (26)	-278.94 (25)	-530 (5)	810 (90)
10	15.7462 (8)	18.478 (4)	-76.00 (5)	-458.9 (4)	-884 (6)	1880 (190)
	15.748 (9)	18.4 (2)	-75.8 (15)			

Tab. A-14: Reduced virial coefficients  $B_n^*$  of planar spindles (lenses) with aspect ratio  $\nu$  [3].

$\nu$	$B_3^*$	$B_4^*$	$B_5^*$	$B_6^*$	$B_7^*$	$B_8^*$
2	3.70315 (8)	5.1400 (4)	6.3479 (7)	7.3334 (19)	8.240 (5)	9.21 (4)
3	4.79564 (11)	6.7005 (5)	7.3796 (12)	6.761 (7)	6.330 (17)	8.52 (24)
4	6.17692 (21)	8.4973 (5)	6.5653 (26)	-1.036 (13)	-7.13 (8)	6.7 (8)
5	7.81020 (27)	10.4278 (14)	2.078 (8)	-24.495 (23)	-46.42 (23)	23 (5)
6	9.6857 (4)	12.4518 (17)	-8.162 (9)	-75.81 (7)	-132.9 (7)	132 (13)
7	11.8001 (5)	14.5403 (27)	-26.594 (19)	-171.73 (17)	-298.7 (15)	490 (110)
8	14.1516 (7)	16.6740 (27)	-55.978 (30)	-334.08 (29)	-592 (4)	1440 (120)
9	16.7395 (9)	18.829 (4)	-99.44 (4)	-591.0 (4)	-1070 (5)	3540 (170)
10	19.5631 (9)	20.987 (4)	-160.55 (6)	-976.2 (7)	-1811 (13)	7700 (600)

Tab. A-15: Reduced virial coefficients  $B_n^*$  of rectangles with aspect ratio  $\nu$ . First row: This work [3], second row: Values from [113].

$\nu$	$B_3^*$	$B_4^*$	$B_5^*$	$B_6^*$	$B_7^*$	$B_8^*$
1	3.98333 (10)	5.94843 (25)	7.9507 (6)	9.7521 (15)	11.103 (5)	11.766 (22)
	3.98 (2)	5.94 (8)				
2	4.43409 (14)	6.6993 (4)	8.8470 (8)	10.542 (4)	11.543 (7)	11.64 (6)
	4.44 (2)	6.72 (8)				
3	5.24381 (13)	8.0503 (4)	10.2095 (10)	10.994 (6)	10.231 (18)	7.97 (17)
4	6.21777 (22)	9.6715 (7)	11.3221 (19)	9.343 (12)	3.75 (6)	-2.98 (30)
	6.22 (3)	9.7 (5)				
5	7.31910 (19)	11.4963 (7)	11.756 (5)	3.743 (15)	-12.26 (16)	-27.6 (15)
	7.31 (4)	11.4 (8)				
6	8.53585 (21)	13.4993 (9)	11.067 (5)	-8.22 (4)	-43.74 (30)	-71 (5)
	8.53 (6)	14 (2)				
7	9.8632 (4)	15.6678 (16)	8.765 (7)	-29.59 (6)	-98.9 (6)	-136 (9)
8	11.2984 (4)	17.9906 (19)	4.283 (9)	-64.30 (8)	-188.8 (11)	-222 (13)
9	12.8406 (5)	20.4600 (21)	-3.021 (19)	-117.06 (14)	-326.4 (18)	-321 (25)
10	14.4890 (5)	23.0705 (21)	-13.814 (20)	-193.51 (23)	-529.8 (29)	-440 (60)

Tab. A-16: Reduced virial coefficients  $B_n^*$  of rhombi with aspect ratio  $\nu$ . First row: This work [3], second row: Values from [113].

$\nu$	$B_3^*$	$B_4^*$	$B_5^*$	$B_6^*$	$B_7^*$	$B_8^*$
1	3.98335 (11) 3.98 (2)	5.94841 (21) 5.94 (8)	7.9505 (6)	9.7530 (17)	11.104 (4)	11.776 (19)
2	4.90794 (16)	7.4813 (4)	9.6767 (13)	11.048 (5)	11.507 (17)	11.12 (15)
3	6.64549 (21)	10.1098 (7)	10.397 (4)	5.477 (12)	0.02 (9)	8.1 (7)
4	8.86529 (29)	13.0689 (11)	5.109 (7)	-26.741 (24)	-57.39 (27)	36 (6)
5	11.5232 (7)	16.2044 (14)	-11.408 (14)	-116.26 (10)	-217.1 (9)	300 (21)
6	14.6075 (5)	19.441 (4)	-45.40 (4)	-309.06 (20)	-571.9 (30)	1330 (90)
7	18.1136 (7)	22.722 (5)	-104.20 (5)	-669.1 (4)	-1262 (8)	4480 (170)
8	22.0399 (8)	26.000 (5)	-196.29 (6)	-1281.3 (10)	-2486 (16)	11700 (1000)
9	26.3854 (11)	29.214 (9)	-331.29 (13)	-2255.0 (14)	-4530 (40)	27300 (1600)
10	31.1492 (15)	32.330 (16)	-519.81 (14)	-3725.0 (23)	-7790 (70)	57900 (2400)

Tab. A-17: Reduced virial coefficients  $\tilde{B}_n$  of infinitesimal thin needles. First row: This work [3], second row: Values from [113], third row: Values from [115].

$n$	3	4	5	6	7	8
$\tilde{B}_n$	0.514547 (19)	-0.031027 (19)	-0.28816 (5)	-0.22659 (9)	-0.03464 (25)	0.1012 (8)
	0.514202 ...	-0.031 (7)				
	0.5145 (3)	-0.031 (1)	-0.288 (2)			

## Virial coefficients of hard, anisotropic particles in three-dimensional space

Tab. A-18: Reduced virial coefficients  $B_n^*$  of dumbbells with aspect ratio  $\nu$ . First row: This work [2], second row: Values from [104].

$\nu$	$B_3^*$	$B_4^*$	$B_5^*$	$B_6^*$	$B_7^*$	$B_8^*$
1.1	10.0604 (4)	18.4943 (13)	28.422 (7)	40.077 (22)	53.70 (12)	68.8 (17)
	10.060307 (25)	18.49433 (15)	28.42184 (59)	40.0883 (27)	53.659 (15)	69.093 (88)
1.2	10.2345 (4)	18.8709 (11)	28.998 (5)	40.876 (24)	54.77 (17)	69.5 (25)
	10.234601 (25)	18.87081 (15)	28.99836 (65)	40.8812 (30)	54.774 (16)	70.273 (90)
1.3	10.5189 (4)	19.4908 (16)	29.956 (6)	42.209 (24)	56.52 (20)	72.5 (22)
	10.518960 (22)	19.49162 (11)	29.95581 (44)	42.2099 (16)	56.5327 (89)	72.406 (54)
1.4	10.91708 (29)	20.3695 (14)	31.316 (6)	44.09 (4)	59.10 (22)	74.8 (19)
	10.917214 (27)	20.36946 (17)	31.31624 (76)	44.1084 (37)	59.093 (20)	75.23 (12)
1.5	11.4401 (4)	21.5372 (18)	33.130 (6)	46.645 (27)	62.6 (4)	80 (5)
	11.440035 (29)	21.53740 (18)	33.12783 (83)	46.6552 (41)	62.617 (24)	79.95 (15)
1.6	12.1064 (5)	23.0452 (23)	35.473 (8)	49.98 (5)	67.3 (4)	85 (4)
	12.106367 (26)	23.04531 (14)	35.47086 (60)	49.9702 (25)	67.208 (15)	85.52 (10)
1.7	12.9450 (6)	24.9723 (24)	38.459 (11)	54.23 (6)	73.4 (5)	92 (6)
	12.945143 (34)	24.97247 (22)	38.4561 (11)	54.2213 (58)	73.273 (38)	92.50 (26)
1.8	13.9994 (4)	27.4366 (15)	42.251 (9)	59.63 (8)	81.1 (8)	99 (11)
	13.999401 (37)	27.43608 (25)	42.2500 (13)	59.6389 (75)	81.184 (50)	103.47 (37)
1.9	15.3326 (5)	30.6094 (23)	47.095 (14)	66.65 (10)	91.8 (8)	111 (16)
	15.332444 (40)	30.60935 (29)	47.0961 (16)	66.6526 (98)	92.005 (74)	113.51 (54)
2.0	17.0399 (8)	34.763 (4)	53.338 (16)	75.91 (13)	106.6 (19)	140 (40)
	17.039851 (46)	34.76134 (34)	53.3373 (21)	75.797 (13)	106.79 (10)	132.22 (82)

Tab. A-19: Reduced virial coefficients  $B_n^*$  of prolate spherocylinders with aspect ratio  $\nu$ . First row: This work, second row: Values from [104].

$\nu$	$B_3^*$	$B_4^*$	$B_5^*$	$B_6^*$	$B_7^*$	$B_8^*$
2	12.4156 (4)	22.6885 (19)	32.904 (9)	45.35 (7)	62.2 (5)	74 (9)
	12.41560 (4)	22.6882 (4)	32.906 (2)	45.33 (1)	61.75 (7)	78.4 (5)
3	16.1835 (7)	27.9829 (30)	36.235 (18)	59.01 (20)	85.1 (25)	40 (60)
	16.18331 (9)	27.9805 (6)	36.231 (4)	58.96 (3)	85.5 (3)	55 (2)
4	20.4055 (11)	31.772 (5)	37.51 (6)	97.8 (7)	60 (12)	-210 (220)
	20.4056 (2)	31.775 (1)	37.511 (7)	97.89 (6)	59.2 (6)	-210 (30)
5	24.9257 (19)	33.127 (11)	41.30 (11)	181.7 (10)	-250 (50)	-900 (800)
	24.9248 (2)	33.128 (2)	41.30 (2)	181.8 (1)	-253 (1)	339 (11)
6	29.677 (4)	31.387 (12)	55.70 (20)	315 (5)	-1320 (60)	2000 (5000)
	29.6758 (2)	31.389 (2)	55.63 (2)	312.3 (2)	-1323 (2)	2220 (30)
7	34.620 (4)	26.053 (16)	90.9 (5)	452 (10)	-3750 (280)	15000 (9000)
	34.6205 (2)	26.057 (3)	90.98 (3)	454.5 (3)	-3788 (4)	15230 (60)
8	39.737 (7)	16.714 (28)	160.2 (7)	525 (20)	-8400 (500)	48 (24) $\times 10^3$
9	44.994 (8)	3.002 (17)	277.4 (13)	370 (40)	-14700 (800)	14 (6) $\times 10^4$
	44.9960 (3)	3.008 (4)	277.24 (6)	366.7 (8)	-15000 (20)	145400 (300)
10	50.394 (9)	-15.37 (5)	458.5 (20)	-260 (70)	-23700 (1700)	32 (9) $\times 10^4$

Tab. A-20: Reduced virial coefficients  $B_n^*$  of prolate ellipsoids of revolution with aspect ratio  $\nu$ . First row: This work, second row: Values from [100,103].

$\nu$	$B_3^*$	$B_4^*$	$B_5^*$	$B_6^*$	$B_7^*$	$B_8^*$
2	12.0913 (6)	21.9537 (16)	32.248 (7)	45.91 (5)	64.1 (6)	82 (5)
	12.09 (4)	21.6 (3)	31.9 (7)			
3	15.8348 (8)	27.0134 (21)	35.664 (19)	60.26 (20)	85 (3)	70 (50)
	15.8357 (6)	27.005 (4)	35.70 (3)	60.0 (3)	83 (3)	
4	20.3006 (14)	30.575 (4)	36.50 (7)	101.7 (7)	39 (10)	-100 (260)
	20.3026 (9)	30.568 (6)	36.5 (2)	101.3 (5)	21 (4)	
5	25.2587 (15)	31.157 (7)	40.02 (11)	198.0 (17)	-400 (50)	-10 (1500)
	25.256 (2)	31.153 (9)	39.9 (1)	197 (2)	-401 (10)	
6	30.5968 (30)	27.642 (17)	57.42 (25)	359 (5)	-1890 (110)	2 (6) $\times 10^3$
	30.6 (4)	28.0 (6)	61 (3)			
7	36.252 (4)	19.141 (18)	104.7 (6)	540 (12)	-5700 (400)	19 (28) $\times 10^3$
	36.252 (2)	19.13 (2)	105.4 (8)	524 (4)	-5936 (9)	
8	42.174 (6)	4.883 (26)	202.3 (10)	589 (21)	-12600 (700)	10 (6) $\times 10^4$
	42.2 (5)	5.2 (2)	200 (8)			
9	48.331 (9)	-15.76 (4)	374.0 (14)	260 (50)	-23100 (1700)	24 (11) $\times 10^4$
10	54.691 (9)	-43.32 (5)	647.2 (26)	-840 (70)	-35000 (4000)	49 (28) $\times 10^4$
	54.692 (4)	-43.34 (5)	648 (1)	-900 (30)	-36900 (600)	

Tab. A-21: Reduced virial coefficients  $B_n^*$  of oblate ellipsoids of revolution with aspect ratio  $\nu$ .  
 First row: This work, second row: Values from [58].

$\nu$	$B_3^*$	$B_4^*$	$B_5^*$	$B_6^*$	$B_7^*$	$B_8^*$
4/5	10.21019 (25)	18.7637 (15)	28.736 (6)	40.458 (27)	54.35 (16)	69.8 (18)
	10.2101 (4)	18.7641 (12)	28.735 (12)	40.435 (21)	54.32 (12)	84 (4)
2/3	10.7169 (4)	19.7345 (16)	29.940 (7)	41.898 (28)	56.57 (25)	73.4 (15)
	10.7166 (6)	19.7359 (24)	29.940 (8)	41.90 (6)	56.53 (16)	74.3 (17)
1/2	12.2648 (5)	22.7288 (13)	33.225 (8)	45.00 (4)	61.67 (24)	85 (7)
	12.2653 (8)	22.7280 (24)	33.226 (19)	45.02 (7)	61.88 (12)	82.4 (27)
1/3	16.7417 (6)	31.4863 (30)	38.524 (17)	39.19 (20)	56.6 (18)	114 (28)
	16.7412 (9)	31.486 (5)	38.53 (4)	39.3 (4)	56.39 (10)	94 (13)
1/4	22.6447 (8)	43.221 (5)	34.47 (5)	-14.0 (6)	-15 (5)	80 (100)
	22.6462 (16)	43.222 (10)	34.51 (6)	-13.9 (10)	-10 (4)	120 (40)
1/5	29.8426 (12)	57.823 (8)	10.57 (9)	-170.1 (11)	-241 (22)	300 (400)
	29.8431 (20)	57.823 (13)	10.53 (9)	-170.4 (28)	-227 (8)	170 (140)
1/6	38.2949 (13)	75.390 (15)	-46.14 (13)	-513.2 (20)	-720 (40)	100 (900)
	38.2943 (13)	75.389 (21)	-46.09 (26)	-513 (5)	-764 (11)	400 (400)
1/7	47.9885 (16)	96.066 (16)	-151.1 (19)	-1154 (5)	-1730 (70)	500 (4000)
	47.9872 (26)	96.077 (25)	-150.9 (4)	-1156 (16)	-1670 (50)	700 (2200)
1/8	58.9149 (21)	120.035 (16)	-322.8 (4)	-2247 (7)	-3320 (200)	-700 (9000)
	58.916 (4)	120.05 (4)	-322.9 (8)	-2247 (9)	-3350 (130)	-300 (4000)
1/9	71.0768 (29)	147.49 (4)	-582.5 (7)	-3979 (15)	-5800 (400)	-2000 (12000)
	71.075 (5)	147.50 (5)	-582.1 (11)	-3988 (26)	-5700 (400)	2000 (10000)
1/10	84.467 (5)	178.59 (5)	-953.7 (9)	-6601 (24)	-9400 (700)	3000 (23000)
	84.465 (5)	178.61 (6)	-953.2 (11)	-6583 (29)	-9760 (120)	4000 (19000)

Tab. A-22: Reduced virial coefficients  $B_n^*$  of lenses with aspect ratio  $\nu$ . Values from [58].

$\nu$	$B_3^*$	$B_4^*$	$B_5^*$	$B_6^*$	$B_7^*$	$B_8^*$
4/5	10.3219 (6)	19.0350 (23)	29.190 (13)	41.06 (5)	54.88 (8)	70.91 (15)
2/3	11.1016 (8)	20.6321 (17)	31.344 (10)	43.66 (6)	58.26 (12)	74.8 (25)
1/2	13.50721 (26)	25.519 (4)	36.864 (12)	48.65 (10)	65.9 (5)	85 (5)
1/3	20.5892 (12)	39.798 (6)	41.34 (7)	21.17 (23)	48 (4)	184 (26)
1/4	30.1398 (17)	59.162 (9)	13.94 (11)	-160.5 (13)	-163 (28)	490 (230)
1/5	41.9838 (24)	83.784 (14)	-78.11 (26)	-718.6 (16)	-933 (24)	1800 (900)
1/6	56.078 (4)	114.06 (5)	-275.2 (5)	-1965 (7)	-2780 (220)	4400 (1300)
1/7	72.397 (6)	150.51 (8)	-627.0 (11)	-4377 (25)	-6600 (400)	8000 (9000)
1/8	90.926 (8)	193.61 (9)	-1189.0 (20)	-8490 (40)	-13900 (600)	20 (18) $\times 10^3$
1/9	111.66 (11)	243.91 (14)	-2030.0 (23)	-15140 (70)	-26000 (1300)	5 (5) $\times 10^4$
1/10	134.610 (6)	301.62 (14)	-3225 (6)	-25230 (70)	-41100 (2400)	10 (5) $\times 10^4$

Tab. A-23: Reduced virial coefficients  $B_n^*$  of cylinders with aspect ratio  $\nu$ . Values from [57].

$\nu$	$B_3^*$	$B_4^*$	$B_5^*$
1/10	$\approx 60.64$	$\approx 127.8$	$\approx -359$
1	$\approx 13.72$	$\approx 25.3$	$\approx 34$
3	$\approx 19.98$	$\approx 31.6$	$\approx 36$
10	$\approx 55.99$	$\approx -37.7$	$\approx 547$

Tab. A-24: Reduced virial coefficients  $B_n^*$  of regular polyhedra. Values from [105, 106].

	Tetrahedron	Cube	Octahedron
$B_3^*$	33.02466 (7)	18.30341 (5)	17.00537 (5)
$B_4^*$	80.7479 (8)	41.8485 (5)	36.9035 (3)
$B_5^*$	85.025 (8)	70.709 (2)	58.149 (2)
$B_6^*$	-90.62 (8)	88.33 (2)	67.07 (1)
$B_7^*$	-326.1 (8)	63.5 (1)	49.9 (1)
$B_8^*$	193 (8)	-37 (1)	17.6 (8)
$B_9^*$	1284 (80)		

Tab. A-25: Reduced virial coefficients  $\tilde{B}_n$  of spherical plates. First row: This work, second row: Values from [103].

$n$	3	4	5	6	7	8
$\tilde{B}_n$	0.444625 (16)	0.019968 (17)	-0.06035 (5)	-0.01791 (7)	0.00148 (10)	0.0004 (4)
	0.44464 (2)	0.01993 (2)	-0.060339 (3)	-0.01730 (5)	0.00157 (7)	

## Virial coefficients of hard, anisotropic particles in four-dimensional space

Tab. A-26: Reduced virial coefficients  $B_n^*$  of hyperdumbbells with aspect ratio  $\nu$  [2].

$\nu$	$B_3^*$	$B_4^*$	$B_5^*$	$B_6^*$	$B_7^*$	$B_8^*$
1.1	32.6898 (15)	78.486 (9)	147.59 (11)	256.1 (9)	378.9 (29)	610 (80)
1.2	33.5071 (14)	80.636 (10)	151.46 (7)	263.2 (13)	386 (5)	620 (120)
1.3	34.8407 (14)	84.156 (12)	157.88 (10)	275.7 (11)	398 (6)	680 (160)
1.4	36.7060 (16)	89.070 (15)	166.78 (10)	293.2 (18)	417 (7)	740 (170)
1.5	39.1485 (18)	95.493 (12)	178.48 (10)	317.8 (17)	439 (11)	880 (200)
1.6	42.2394 (19)	103.548 (14)	193.02 (13)	349.5 (19)	461 (15)	900 (400)
1.7	46.0677 (28)	113.371 (13)	210.69 (21)	392 (4)	463 (15)	1000 (500)
1.8	50.7204 (22)	124.972 (20)	231.15 (21)	444 (5)	450 (30)	1900 (800)
1.9	56.2473 (25)	138.046 (30)	253.9 (4)	515 (6)	380 (50)	2400 (1400)
2.0	62.4926 (25)	151.288 (18)	276.4 (5)	594 (11)	220 (80)	2200 (2700)

Tab. A-27: Reduced virial coefficients  $B_n^*$  of hyperspherocylinders with aspect ratio  $\nu$  [1].

$\nu$	$B_3^*$	$B_4^*$	$B_5^*$	$B_6^*$	$B_7^*$	$B_8^*$
2	42.7361 (20)	96.325 (14)	174.58 (16)	340 (4)	373 (15)	1200 (500)
3	57.9720 (29)	108.70 (4)	270.5 (5)	444 (19)	-640 (130)	11000 (6000)
4	74.454 (9)	104.28 (5)	564.3 (13)	-850 (40)	3600 (500)	39000 (23000)
5	91.606 (11)	81.18 (7)	1213.2 (22)	-7000 (130)	59200 (1600)	-38 (13) $\times 10^4$
6	109.188 (21)	39.09 (14)	2363 (7)	-23500 (400)	288 (6) $\times 10^3$	-33 (4) $\times 10^5$
7	127.076 (25)	-21.31 (16)	4161 (12)	-57500 (600)	925 (12) $\times 10^3$	-141 (10) $\times 10^5$
8	145.19 (4)	-99.59 (24)	6723 (27)	-119000 (1100)	2337 (20) $\times 10^3$	-45 (4) $\times 10^6$
9	163.52 (5)	-194.71 (24)	10180 (40)	-215600 (1900)	504 (7) $\times 10^4$	-121 (7) $\times 10^6$
10	182.00 (9)	-306.7 (6)	14581 (30)	-360000 (4000)	978 (14) $\times 10^4$	-274 (13) $\times 10^6$

Tab. A-28: Reduced virial coefficients  $B_n^*$  of prolate, uniaxial hyperellipsoids of revolution with aspect ratio  $\nu$ .

$\nu$	$B_3^*$	$B_4^*$	$B_5^*$	$B_6^*$	$B_7^*$	$B_8^*$
2	40.2748 (17)	91.834 (14)	171.97 (13)	327.5 (15)	374 (12)	1000 (400)
3	54.041 (4)	105.184 (29)	247.0 (4)	409 (9)	-200 (80)	8500 (2800)
4	70.020 (7)	103.02 (5)	476.0 (12)	-440 (50)	2400 (400)	34000 (30000)
5	87.265 (9)	80.01 (6)	1032.5 (19)	-5180 (120)	41600 (1100)	-21 (11) $\times 10^4$
6	105.321 (15)	33.94 (13)	2121 (6)	-19570 (290)	225 (5) $\times 10^3$	-23 (4) $\times 10^5$
7	123.968 (16)	-35.85 (23)	3944 (9)	-52000 (500)	788 (17) $\times 10^3$	-122 (17) $\times 10^5$
8	143.04 (4)	-129.18 (30)	6694 (22)	-113500 (1200)	217 (4) $\times 10^4$	-43 (5) $\times 10^6$
9	162.41 (5)	-245.56 (23)	10550 (40)	-218400 (2300)	499 (5) $\times 10^4$	-115 (17) $\times 10^6$
10	182.09 (6)	-384.0 (5)	15680 (40)	-383000 (4000)	1031 (13) $\times 10^4$	-29 (4) $\times 10^7$

Tab. A-29: Reduced virial coefficients  $B_n^*$  of oblate, uniaxial hyperellipsoids of revolution with aspect ratio  $\nu$ .

$\nu$	$B_3^*$	$B_4^*$	$B_5^*$	$B_6^*$	$B_7^*$	$B_8^*$
4/5	33.2168 (15)	79.561 (10)	148.98 (7)	259.6 (7)	384 (10)	660 (270)
2/3	35.1908 (14)	84.079 (11)	155.40 (10)	273.6 (12)	401 (15)	590 (270)
1/2	41.3178 (23)	98.345 (11)	172.29 (18)	310.4 (25)	456 (13)	1000 (250)
1/3	59.5237 (26)	141.562 (21)	190.6 (4)	343 (9)	430 (50)	2600 (1600)
1/4	84.202 (4)	201.58 (6)	127.8 (10)	130 (40)	-330 (180)	2000 (6000)
1/5	114.911 (6)	278.38 (8)	-104.4 (19)	-690 (50)	-3300 (500)	6000 (29000)
1/6	151.539 (10)	372.95 (11)	-618.8 (28)	-2630 (90)	-10100 (2200)	2 (9) $\times 10^4$
1/7	194.058 (10)	486.46 (13)	-1555 (4)	-6420 (200)	-26800 (2300)	-4 (24) $\times 10^4$
1/8	242.448 (16)	620.35 (16)	-3084 (10)	-12800 (400)	-57 (8) $\times 10^3$	-2 (4) $\times 10^5$
1/9	296.710 (22)	775.93 (24)	-5387 (13)	-23400 (700)	-111 (11) $\times 10^3$	-3 (12) $\times 10^5$
1/10	356.853 (19)	954.44 (25)	-8694 (23)	-39200 (1200)	-186 (23) $\times 10^3$	-14 (17) $\times 10^5$
1/20	1281.91 (6)	4327.6 (24)	-164700 (400)	-114 (4) $\times 10^4$	-66 (25) $\times 10^5$	-1 (46) $\times 10^7$
1/50	7596.6 (4)	43720 (50)	-6843 (17) $\times 10^3$	-97 (4) $\times 10^6$	-12 (7) $\times 10^8$	-5 (26) $\times 10^{10}$
1/100	29932.9 (19)	295100 (400)	-11137 (20) $\times 10^4$	-292 (14) $\times 10^7$	-34 (26) $\times 10^9$	7 (50) $\times 10^{12}$